POLITECNICO
MILANO 1863

DEPARTMENT OF ENERGY
DOCTORAL PROGRAM IN ENERGY AND NUCLEAR SCIENCE AND TECHNOLOGY

INVESTIGATION ON NEAR-CRITICAL DOUBLE-LAYER TARGETS FOR ENHANCED LASER-DRIVEN ION ACCELERATION

Doctoral Dissertation of:
Andrea Pazzaglia

Supervisor:
Prof. Matteo Passoni

Tutor:
Prof. Carlo S. Casari

The Chair of the Doctoral Program:
Prof. Vincenzo Dossena

Year 2020 – Cycle XXXII

Abstract

The laser technology development in the last years enabled to generate ultra-intense and ultra-short laser pulses with intensity easily exceeding $10^{19}\ W/cm^2$; the interaction of these last with matter produces almost instantly a plasma and a wide range of non-linear phenomena. Among all the possible laser-plasma interaction scenarios, laser-driven ion acceleration, consisting in the production of high energy ions ($MeVs/nucleon$) when the laser is focused onto a thin solid target ($<\ 100\ \mu m$), is increasingly attracting interest from the scientific community.

Indeed, the compact size of the accelerator and the peculiar properties of the accelerated particles (e.g. high ion density per bunch, ultrafast duration) could be exploited in the next future for appealing applications, for example in the nuclear science (e.g. bright neutron sources, fast ignition inertial fusion), in the material science (e.g. Ion Beam Analysis) and in the medical field (e.g. radioisotopes generation, hadron-therapy).

Nevertheless, laser-driven ion acceleration schemes generally exhibit low laser conversion efficiency into energetic particles. A viable route to overcome this limitation is to use a Double-Layer Target (DLT) with a near-critical front layer, made of an extremely low density solid material (about one thousandth of the solid density); both theoretical and experimental works proved the effectiveness of this solution for the increasing of the proton energy and the total particles number, but the full potential of this solution is still not achieved.

Therefore, this thesis work aims at investigating and optimizing the near-critical DLT through an integrated experimental-theoretical approach: the target parameters which improve at most the acceleration efficiency are theoretically found, then proper targets are produced and characterized with peculiar material science techniques and finally the latter are tested in an international laser acceleration experiment.

Contents

Introduction

The advent in the 1960 of the laser technology enabled to produce monochromatic and coherent electromagnetic waves opening new physics and engineering branches. In the following years, the development of the *Q-switch* and the *Mode-Locking*, capable to generate short pulses with exponentially increasingly power (up to GWs), allowed discovering non-linear effects of the laser-matter interaction, now widely used in several fields. In the mid-1980s Donna Strickland and Gérard Mourou proposed the *Chirped Pulse Amplification* (CPA) technology, for which they received the Nobel prize in Physics in 2018: a breakthrough technology with the capability of generating ultra-short pulses ($< 1\ ps$) and high power (to date up to tens of PWs) which enables to reach intensities, when they are focused to few μm^2, easily exceeding $10^{19}\ W/cm^2$.

In the ultra-intense laser-matter interaction, the electromagnetic fields are much greater than the typical atomic fields, resulting in a prompt ionization of matter which transforms it into a plasma. In addition, the fields push the plasma electron to high velocities within a single wave cycle and the interaction is dominated by highly non-linear and relativistic phenomena.

Besides the novelty and interest of this regime which is still largely unexplored, the laser-plasma interaction is an appealing branch of physics because of the possible useful applications; indeed, great longitudinal electric fields are generated, which are capable to accelerate charged particles to high energies in very compact length scales compared to conventional accelerators.

In the last decades, electron bunches were accelerated up to $4\ GeV$ energy with a plasma length less than $10\ cm$; also burst of radiation secondary sources, X and γ rays, has been realised with compact scales.

In 2000 three independent works reported the acceleration high energy protons (up to tens of MeV) produced by the interaction of ultra-intense pulses with solid thin films ($< 100\ \mu m$); the protons bunch was featured by a very short duration ($< 1\ ps$), a broad thermal-like spectrum with a cut-off at high energy, and emission at the normal of the solid foil target with an ultra-low emittance.

These peculiar properties could be exploited in a number of appealing applications, such

as in the material science, for the *Ion Beam Analysis*, in the nuclear science, for the production of secondary sources with unique properties of brightness and for the fast ignition inertial fusion and also in the medical field, since hadronteraphy or radioisotopes production could be achieved.

The new physical mechanism, known as laser-driven ion acceleration, was then deeply studied in following years by a growing community of theoretical and experimental scientists and large number of results have been achieved. Most of them have been interpreted within the generally accepted *Target Normal Sheath Acceleration* model (TNSA). The latter explains the ions acceleration phenomenon with a series of consequent events: the interaction of high intensity electromagnetic fields with the front side of the foil, which is a high density plasma, generates relativistic electrons which are injected inside the target; when the hot electrons reach the rear interface they form strong longitudinal electric fields due to the charge separation (in the order of TV/m), capable of accelerating, perpendicularly to the interface, high energy light ions (e.g. Hydrogen, Carbon), present as impurities.

Despite the attractive features of the laser-driven ions, the control over the process is still not completely fulfilled, because large part of the involved pulse energy is not converted into plasma particles: for example, a consistent fraction of the laser pulse is reflected by the solid target and also a big quantity of high energy photons, both X and γ, are produced. In fact, the total TNSA ions total energy hardly exceed the one percent of the pulse one.

One way to overcome this limitation is to increase the intensity of the laser source in order to enhance the hot electrons production; nevertheless, the CPA state of the art requires great costs and large scale laser sources to overcome the PW peak power, and hence reduces the appealing features of compactness and cheapness of the laser-driven accelerator. In addition PW-class facilities can rarely operate at high *repetition rate* (RR), $> 1\ Hz$, which is an essential element to be addressed for future applications.

Another way to enhance the acceleration process, keeping at the same time the compact source ($100s\ TW$ lasers) and the high repetition rate ($10\ Hz - 1\ kHz$), is to exploit advanced target configurations, featured by an increased conversion efficiency. A consistent part of the scientific community dealt with this topic in the last decade and numerous solutions have been proposed as well.

In this framework targets from all the aggregation states have realized: gas, liquid, cryogenic and nanostructured solid targets demonstrated to have both their peculiar advantages and disadvantages. Just to mention a few, the gas, liquid and cryogenic ones are in principle capable to reach higher repetition rates (up to $1\ kHz$), nonetheless they require complex experimental apparatus and in general give rise to lower ions energy with respect to solid targets; while the latter show their limitations in the reduced theoretical RR ($10\ Hz$ at the state of the art) and in the production of fast solid/liquid debris, dangerous for the laser optics, and electromagnetic pulses, detrimental for the electronic devices.

Among the advanced solid targets, one promising solution is to use a *Double-Layer Target* (DLT) composed by a thin solid foil substrate and a near-critical density layer, where the

critical density marks the threshold of transparency for an electromagnetic wave propagating inside a plasma. In this regime the laser pulse coupling with matter is increased and the result is a more energetic and dense ion bunch; this point has been proved experimentally many times with a proton energy enhance (with respect to standard target) up to three-fold. For this reason DLTs could represent a way to deal with the above-mentioned efficiency issue and also with the repetition rate problem, because the solid substrate provides the mechanical robustness necessary for an ion beam realization.

Nevertheless the critical density corresponds, for the widely used Ti:Sapphire lasers, to about one thousandth of the solid bulk density and therefore highly porous materials must be used for this purpose; many issues are related to this point, since not only the near-critical layer must be proper produced with advanced material science techniques, but it has also to be accurately characterized with unconventional measurements.

In addition, all the near-critical layer parameters, as the thickness, mean density, uniformity grade, are essential in the interaction and they must be finely chosen to optimize the DLT performances; since with the laser acceleration experiments only few parameters can be tested at time, to achieve the best DLT properties a theoretical approach which guides the target production is of great utility. In this framework, numerical tools play an important role in the experiments realization and interpretation: in particular, *Particle-In-Cell* (PIC) simulations can solve the Maxwell-Vlasov equations and for this reason are largely used to help the experimental and theoretical work.

Motivations and aims of the thesis

The main aim of this thesis work is to investigate the near-critical DLT solution for laser-driven ion acceleration, through an approach which integrates the theoretical description of the acceleration phenomenon with the advanced target, the production and characterization of optimized DLTs and their test in a dedicated experiment, carried out in collaboration with an international facility.

The theoretical description of the laser-DLT interaction is based on the analysis of PIC simulations and in the formulation of a proper model which takes into account the essential aspects of the involved physical mechanisms; the latter is used to obtain the DLT density and thickness values which maximize the performances for the specific laser source.

The technique for the nanostructured near-critical material production is then investigated with the aim of increasing the control over the material properties; in addition, also an unconventional characterization technique is developed, to assure a better feedback over the production activity.

Finally DLTs with proper parameters are produced and tested in an acceleration experiment in collaboration with an international facility; the results are analysed in order to verify the effectiveness of the used targets and they are interpreted at the light of the gained insight about the interaction.

This thesis was founded by the *European Research Council* (ERC) project ENSURE

(*Exploring the New Science and engineering unveiled by Ultraintense ultrashort Radiation interaction with mattEr*, https://www.ensure.polimi.it/).

Structure of the thesis

The PhD thesis is organized as follows:

Part I: In the first part an introduction to laser-driven ion acceleration is provided, starting from a brief overview of the ultra-intense laser technology and the physical mechanism which are involved in the laser-plasma interaction. Some crucial advanced target strategies are then presented, with a particular emphasis on the near-critical Double-Layer Target solution. In particular, it is also given an introduction on the production and characterization of Carbon nanofoams, which are used in this field as a near-critical material.

Part II: The second part is dedicated to the theoretical investigation, carried out with Particle-In-Cell simulations and analytical methods, on the ultra-intense laser interaction with near-critical plasmas and the subsequent ion acceleration in the double layer case. The aim of this part is to shed a light on the interaction process and to extract informations which can guide the experimental activities. A first analysis is given onto idealized uniform plasmas in order to determine the optimal parameters of the DLT in a simplified condition; while secondly, the focus is shifted to the simulation of more realistic nanostructured plasmas and their effect in the ions acceleration compared to the ideal uniform ones.

Part III: The third part deals with the experimental investigation on the production and characterization of nanofoams which are used as near-critical layers in DLTs. Firstly the advancements on the density/uniformity characterization method are presented; therefore, the nanofoam growth process is investigated and a new aggregation model is proposed and experimentally demonstrated, with the final aim of better controlling the materials properties. Finally, a first investigation on nanofoams produced by Pulsed Femtosecond Laser Deposition are shown.

Part IV: This part describes the experimental investigation on nanofoam-based Double-Layer Targets for the enhanced laser-driven ion acceleration. The production of DLTs and the related issues are firstly presented, therefore the results of a laser-acceleration campaign (carried out at the Helmholtz-Zentrum Dresden-Rossendorf) are reported; the enhancement in the laser absorption and ion acceleration is interpreted on the basis of the theoretical insights gained in Part II.

Part V: Finally, the last part draws the conclusion of this PhD work and the future perspectives for future research.

Publications and research activity

The contents of this thesis were published in the following peer reviewed papers:

- Prencipe, I., Metzkes-Ng, J., **Pazzaglia, A.**, Dellasega, D., Fedeli, L., Formenti, A., Garten, M., Kluge, T., Kraft, S., Laso Garcia, A., Maffini, A., Obst-Huebl, L, Rehwald, M., Russo, V., Sobiella, M.m Zeil, K., Schramm, U., Cowan, T.E. and Passoni, M. *Experimental investigation on ultra-intense laser interaction with fractal-like near-critical plasmas*. In preparation. Personal contribution: participation to the experimental campaign and contribution to data analysis.

- **Pazzaglia, A.**, Fedeli, L., Formenti, A., Maffini, A. and Passoni, M. *A theoretical model of laser-driven ion acceleration from near-critical double layer targets*. Under review at Communications Physics. Personal contribution: writing of the manuscript and figure production, contribution to PIC simulations production and analysis, model development.

- Fedeli, L., Formenti, A., **Pazzaglia, A.**, Arioli, F.M., Tentori, A. and Passoni, M. *Enhanced laser-driven hadron sources with nanostructured double-layer targets*. New Journal of Physics 22.3 (2020): 033045. Personal contribution: development of virtual foam nanostructures and contribution to PIC simulation analysis.

- Passoni, M., Arioli, F., Cialfi, L., Dellasega, D., Fedeli, L., Formenti, A., Giovannelli, A., Maffini, A., Mirani, F., **Pazzaglia, A.**, Tentori, A., Vavassori, D., Zavelani-Rossi, M. and Russo, V. *Advanced laser-driven ion sources and their applications in materials and nuclear science*. Plasma Physics and Controlled Fusion 62.1 (2019): 014022. Personal contribution: writing and figure production of the 'Production and characterization of nanostructured carbon foams' and 'Electron heating in DLT configuration' sections.

- Maffini, A., **Pazzaglia, A.**, Dellasega, D., Russo, V. and Passoni, M. *Growth dynamics of pulsed laser deposited nanofoams*. Physical Review Materials 3.8 (2019): 083404. Personal contribution: contribution to the production and characterization of nanofoams, to data analysis and model development.

- **Pazzaglia, A.**, Maffini, A., Dellasega D., Lamperti, A. and Passoni, M., *Reference-free evaluation of thin films mass thickness and composition through energy dispersive x-ray spectroscopy*. Materials Characterization 153 (2019): 92-102. Personal contribution: writing of the manuscript and figure production, development of the model.

- Fedeli, L., Formenti, A., Cialfi, L., **Pazzaglia A.** and Passoni, M. *Ultra-intense laser interaction with nanostructured near-critical plasmas*. Scientific reports 8.1 (2018): 3834. Personal contribution: development of virtual foam nanostructures and contribution to PIC simulation analysis.

- Besozzi, E., Maffini, A., Dellasega, D., Russo, V., Facibeni, A., **Pazzaglia, A.**, Beghi, M. and Passoni, M. *Nanoseconds laser pulses for mimicking thermal effects on tungsten materials in ITER-relevant conditions*. Nuclear Fusion 58.3 (2018): 036019. Personal contribution: contribution to the model development.

And in the following conference proceedings:

- Formenti, A., Fedeli, L., Cialfi, L., **Pazzaglia, A.**, Maffini, A., and Passoni, M. Ultra intense laser interaction with nanostructured targets. 45th EPS conference 4-page paper (2018). Personal contribution: development of virtual foam nanostructures and contribution to PIC simulation analysis.
- Fedeli, L., Mirani, F., Maffini, A., Formenti, A., **Pazzaglia, A.**, Tentori, A., Dellasega, D., Russo, V. and Passoni, M. Laser-plasma based hadron sources for materials science applications. 45th EPS conference 4-page paper (2018). Personal contribution: development of virtual foam nanostructures and contribution to PIC simulation analysis.

During my PhD I have attended these conferences and schools with the following personal contributions:

- **Oral contribution** at the 'Conference on High Intensity Lasers and attosecond science in Israel', Tel Aviv, Israel, December 2019
- **Oral contribution** at the '4th Targetry for High Repetition Rate Laser-Driven Sources Workshop', Milano, Italy, June 2019
- **Oral contribution** at the 'Laser-Plasma Accelerator Workshop', Split, Croatia May 2019
- **Oral contribution** at the 'Target Fabrication Workshop 7', Darmstadt, Germany, September 2018
- **Oral contribution and poster presentation** at the 6th School 'Intl. School on Lasers in Materials Science', Venezia, Italy, July 2018
- Attendance at the school 'Ultrafast and Intense Laser Metrology', Bordeaux, France, December 2017
- **Poster presentation** at the 8th School 'Atoms and Plasmas in Super-Intense Laser fields', Erice, Italy, July 2017
- **Poster presentation** at the 'Target Fabrication Workshop 6', London, UK, May 2017

During my PhD I have been the P.I. of the IscraC 225000 CPU hours project "GARLIC" at CINECA supercomputer (Italy).

Part I

Laser-driven ion acceleration basic concepts and state of the art

CHAPTER 1

Introduction to laser-driven ion acceleration

This chapter offers an overview on the ultra-intense laser-matter interaction phenomena and the laser-driven ion acceleration basic concepts. At this purpose Section 1.1 overlooks the evolution of the laser technology over the years which enabled to generate ultra-intense laser pulse; consequently the principal mechanisms of interaction between matter and these kind of lasers is illustrated in Section 1.2. Finally, 1.3 gives an introduction to laser-driven ion acceleration (within the *Target Normal Sheath Acceleration* framework), with a particular emphasis on the experimental observations and the theoretical models developed to described the phenomenon.

1.1 Ultra-intense laser pulse technology

The advent of the first laser, theorized by Albert Einstein in 1917 [1] and realized in 1960 [2], gave birth to new branches of physics which exploited the appealing properties of this particular light source: the temporal and spatial coherence and the monochromaticity. In the following years (see Figure 1.1), the development of the laser technology enabled to generate pulses with short duration, with the *Q-switching* first ($\sim ns$) [3] and the *Mode-Locking* later ($\sim fs$) [4], which were characterized by high electromagnetic fields, with intensity above $10^{10}\ W/cm^2$. This capability allowed the discovery of several highly important light-matter interaction phenomena; to mention a few, the second harmonic generation was discoverd in 1961 thanks to the high intensity of a ruby laser focused onto a quartz crystal [5] and the branch of non-linear optics became widespread since the laser electric field reached the values in the order of the atomic electric fields, in the order of $10^8\ V/m$.

The *Q-switch* technology is based on a controllable attenuator inside the laser resonant cavity which enables to variate the quality factor *Q*. When the round-trip losses are increased (low *Q*) the gain medium is pumped till a strong population inversion is reached. The losses

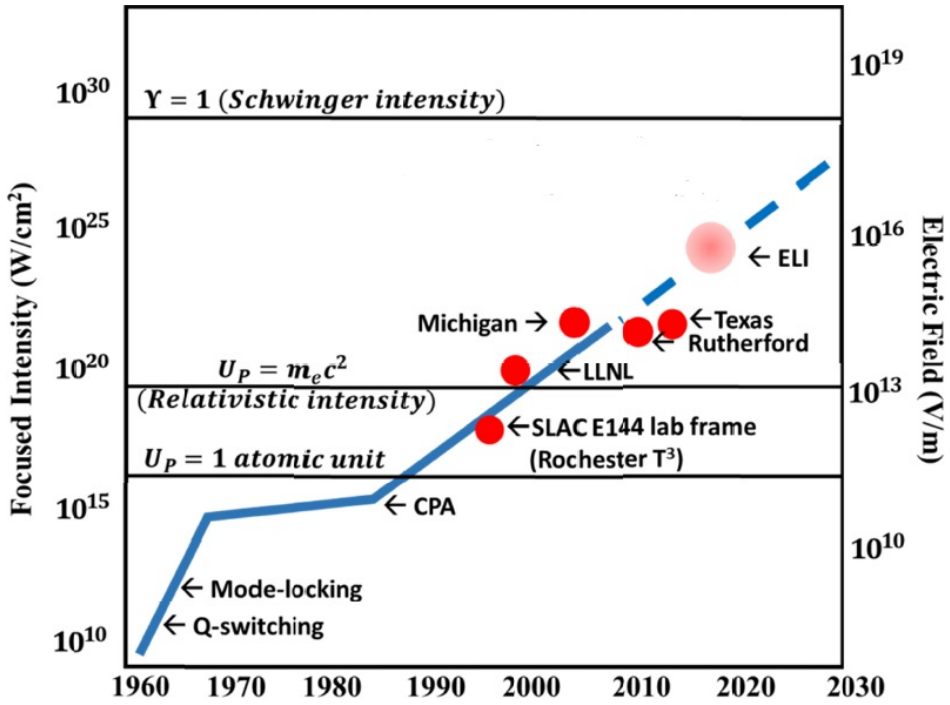

Figure 1.1: Evolution of the highest focused intensities over the years. CPA and solid-state laser technology have pushed the present peak intensity to the range of $10^{22}\ W/cm^2$. The European ELI project will scale this up more than one order of magnitude in the near future. The three horizontal lines show the intensity for the ponderomotive (quiver) energy U_p of an electron in the focus of an $800nm$ (Ti:Sapphire) laser to be equal to one atomic unit; or for U_p to be equal to the electron rest mass; or for the Schwinger intensity $Y = 1$ where the vacuum becomes unstable and light is directly converted to matter.

are then promptly reduced and the energy accumulated in the lasing medium is emitted in a strong and short pulse.

On the other hand, *Mode-Locking* exploits a fixed phase relation in the longitudinal cavity modes to construct an interference which generates a train of ultra-short pulses with temporal temporal duration down to few fs, which is inversely proportional to the gain medium bandwidth. Very common mode-locked oscillators are the Ti:Sapphire lasers, emitting in the infrared ($\lambda \sim 800\ nm$) high intensity pulses with duration higher than $5\ fs$, repetition rate above ten MHz and mean power up to the W level.

The pulses intensity can be further increased by other amplification stages, consisting a in pumped gain medium which gives more energy to the ultra-short pulse with the stimulated emission mechanism. Nevertheless, the amplification through multiple stages can be repeated only to a limiting threshold given by the non-linear effects, which degrade the beam properties, and the damaging threshold of the solid active medium ($\sim GW/cm^2$).

This limit in the maximum laser power remained a major problem from the 70' for over a decade (see Figure 1.1), since in the mid 80' Donna Strickland and Gèrard Mourou proposed a breakthrough technology, the *Chirped Pulsed Amplification* (CPA) [6], for which they received the Nobel prize in Physics in 2018.

The CPA mechanism, depicted in Figure 1.2, consists in the stretching of an ultra-short pulse ($< ps$) to nanoseconds through a grating, which induces a high dispersion of the laser frequencies into a *chirped* pulse. The lower intensity allows enhancing the beam energy with

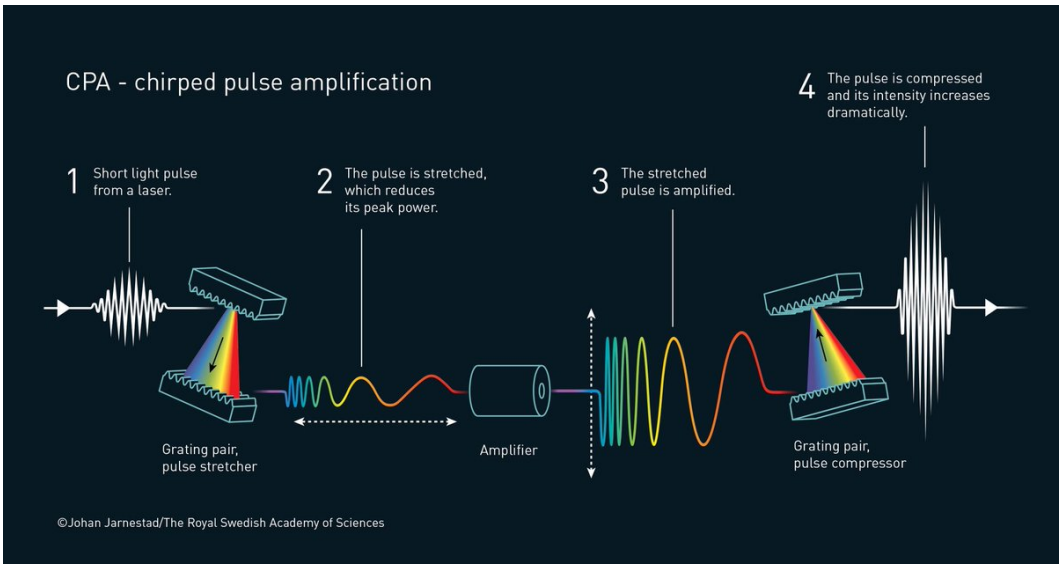

Figure 1.2: Scheme of the Chirped Pulse Amplification technology.

multiple amplification stages, preventing at the same time the damaging of the active media. Finally, the pulse is compressed again with another grating with reversed dispersion to have a high energy and ultra-short pulse. Thanks to this technology the nowadays ultra-intense laser pulses can reach peak power above the petawatts and intensities above $10^{22}\ W/cm^2$ [7, 8], which is roughly equivalent to focusing all the sunlight power that hits the Earth onto a single grain of sand, for a duration of few femtoseconds.

In the world (see Figure 1.3a) the number of the laser facilities capable to exceed the PW peak power are not numerous; among them the *European Extreme Light Infrastructure* project (ELI), implemented in four sites of the continent, should be mentioned since it is rapidly approaching the full operation capabilities, spread in different branches of the ultra-intense laser field, with the foreseen highest intensity of $10^{23-24}\ W/cm^2$.

On the other hand, several and continuously-growing ultra-intense laser facilities ($I > 10^{19}\ W/cm^2$) are present to date in the world (see Figure 1.3b). Their technology could be divided in two main categories: fs and ps ultra-intense laser pulses.

The first are typically based on Ti:Sapphire oscillators and CPA stages which generate $15 - 100\ fs$ pulses with energy in the order of Joules; the repetition rate can be relatively high, since up to $1\ kHz$ frequency can be achieved. On the other hand 'long' ps pulses are generally generated by Nd:YAG-based active media and very energetic pulses, easily exceeding $100\ J$; since the pumping procedure requires longer times, the repetition rate can be very low, from $0.1\ Hz$ till one shot per-day.

1.2 Ultrahigh intensity laser-matter interaction

The fast development in the last decades of ultrahigh intensity laser facilities in the world enabled to study the matter-interaction mechanisms in highly nonlinear and relativistic regimes. The physical phenomena induced in this interaction are extremely rich and far beyond the aims of this work; for this reason only the key notions to understand the laser-driven ion

(a)

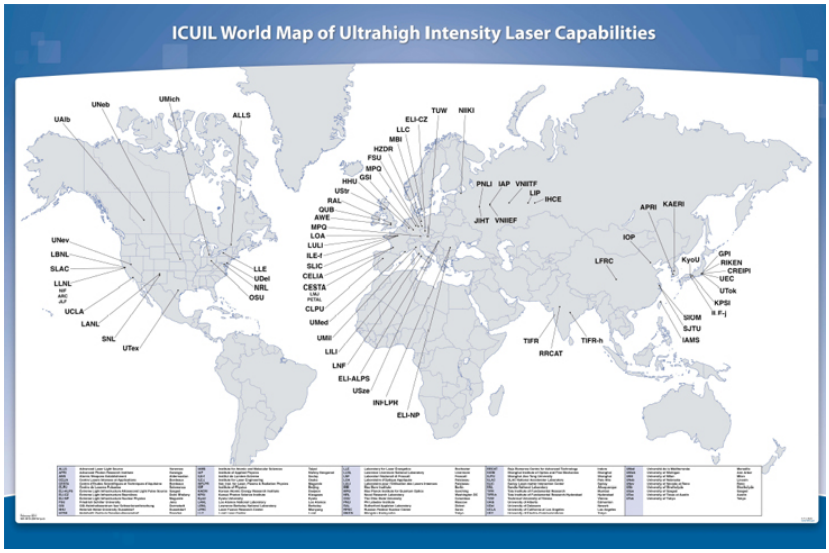

(b)

Figure 1.3: (a) Petawatt-class laser in the world. (b) Ultra-intense laser ($I > 10^{19}\ W/cm^2$) in the world.

acceleration will be given.

Since the intensity required to ionize a material is generally in the range $10^{13-14}\ W/cm^2$, ultra-intense pulses with $I > 10^{19}\ W/cm^2$ have the prompt effect (within a single laser cycle) of inducing a phase transition to the plasma state. The two principal and competitive mechanisms which induce ionization (see Figure 1.4a) are the *Tunnel Ionization* (TI), consisting in the distortion of the atomic field by the electric field of the laser pulse, and the *Multi-Photon Ionization* (MPI), consisting in the direct overcoming of the atomic electron binding energy by the non-linear action of multiple photons. The weight of the two can be evaluated by the *Keldysh parameter*:

$$\gamma_k \sim \sqrt{\frac{E_{ion}}{U_p}} \tag{1.1}$$

Where E_{ion} is the *ionization energy* and U_p is the *ponderomotive potential*, defined as $U_p = \frac{q^2}{4m\omega^2}|\mathbf{E_0}|^2$, which will be discussed later. If $\gamma_k \ll 1$, corresponding to long wavelengths or very strong fields, the ponderomotive potential bends the atomic potential well

and TI becomes dominant; conversely, if $\gamma_k \gg 1$, MPI becomes the principal ionization effect, indeed the lower photon wavelength is related to a higher energy and a decreased number of photons required to overcome the ionization energy. In order to make simple estimations, we can express the Keldysh parameter as a function of the laser intensity and wavelength, which reads as $\gamma_k \sim \sqrt{\frac{E_{ion}[eV]}{9.5 \cdot 10^{-14} I[W/cm^2]\lambda[\mu m]}}$. For typical first ionization energies around $10\ eV$, a Ti:Sapphire laser with an intensity higher than $10^{14}\ W/cm^2$ induces principally Tunnel Ionization. Without entering in the details of calculations, the theoretical ionization rate for this mechanism is reported for H_2 in Figure 1.4b; the figure shows that for intensity higher than $10^{15}\ W/cm^2$ this rate is higher than $1\ fs^{-1}$ which is comparable to a single wave cycle duration.

Nevertheless, it should be pointed out that this framework holds for weekly bounded electron, while for the strong bounded ones (where the ionization energy can be higher than $10\ keV$) the physical mechanism can be more complicated involving not only MPI and TI, but also electron collisions and plasma kinetic effects.

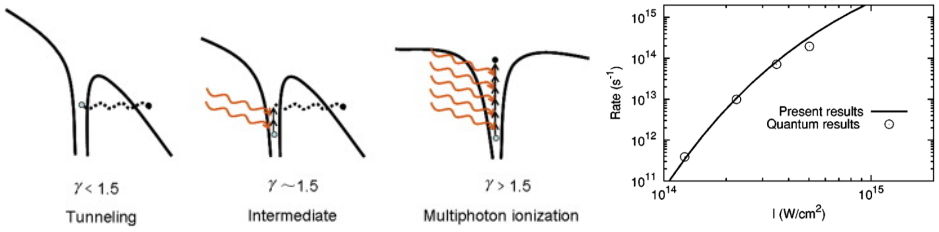

Figure 1.4: (a) Scheme of tunnel ionization (left), multiphoton ionization (right) and a mixed condition (centre). (b) Theoretical ionization rate for H_2 from [9]

An ultra-intense laser thus promptly ionizes the matter and the interaction is dominated by the electromagnetic effects of a plasma. It is well known that a light wave interacting with a cold plasma is characterized by a dispersion relation given by [10]

$$\omega^2 = \omega_p e^2 + k^2 c^2 \tag{1.2}$$

Where $\omega_p e = \sqrt{\frac{4\pi e^2 n_e}{m_e}}$ is the electron population plasma frequency, with n_e the electron plasma density.

According to Equation 1.2, an electromagnetic wave is able to propagate inside a plasma if its frequency overcomes $\omega_p e$; while in the opposite condition only an evanescent wave penetrates the plasma (with a length scale in the order of the skin depth $\lambda_{sd} = c/\omega_p e$), leading to total wave reflection. The propagation condition can be also expressed in terms of the plasma density, once the laser wavelength is fixed. The threshold for the two behaviours is called critical density and it is defined as:

$$n_c = \frac{m_e \omega^2}{4\pi e^2} \tag{1.3}$$

If n_e is lower than then the critical density the wave can propagate for long distances

and the plasma is called *under-dense* or *under-critical*; for typical infra-red laser wavelength (in the order of $1\ \mu m$) this condition is valid for atmospheric pressure gasses. On the other hand for $n_e > n_c$ the plasma is called *over-dense* or *over-critical*, which is common for solid state materials, where $n_e \gg 100 n_c$. Finally, a plasma which matches its frequency to the electromagnetic wave, $n_e \sim n_c$, is referred as a *near-critical* plasma; this condition introduces very complex interaction phenomena, since the laser-plasma coupling is increased and many non-linear and unstable effects arise. Because of the very rich research topic and its relevance in this thesis work, a deeper description of these mechanisms will be given in Section 2.2.

In the ultra-high intensity regime the physical phenomena can be still further complicated, since not only the non-linear effects become important, but the electrons speed can approach the light speed, inducing relativistic effects during the interaction. To estimate the relativistic phenomena relevance, the wave amplitude expressed by the vector potential $\mathbf{A}$, should be normalized to the electron rest energy which reads as:

$$\mathbf{a} = \frac{e\mathbf{A}}{m_e c^2} \tag{1.4}$$

This quantity is quite convenient since the transversal electron oscillation momentum $\mathbf{p}_\perp$ due to the laser electric field is given by $\mathbf{p}_\perp / mc = \mathbf{a}$; approximating the total electron momentum to the transversal one, the Lorentz factor can be calculated as $\gamma = \sqrt{1 + \mathbf{a}^2}$. The pulse peak intensity can be related to the normalized peak amplitude with the relation $a_0 = \sqrt{\frac{I[W/cm^2]\lambda^2[\mu m^2]}{1.37 \cdot 10^{18}}}$; thus, if the condition $a_0 > 1$ holds (valid for ultra-intense pulses), the mean electron Lorentz factor exceeds the unity and the relativistic effects become very relevant.

One particularly important relativistic effect is given by the increasing of the electron inertia, since the plasma frequency decreases accordingly; the critical density definition must be thus modified by substituting γm_e to the electron mass, namely:

$$n_c^{rel} = \gamma \frac{m_e \omega^2}{4\pi e^2} \tag{1.5}$$

The latter equation states that the relativistic critical density in high intensity regimes can be several times higher than the classical one, valid in low intensity condition. For this reason a classically over-dense plasma could become transparent due to relativistic effect, when ultra-high intensity lasers are exploited.

Another crucial non-linear effect, arising in non-homogeneous laser fields, is the *ponderomotive force*. This force pushes the particles from areas of higher wave amplitude to zones of weaker fields strength; this happens because the net force acting on the particles changes during the oscillation period and, after a complete cycle, the fields inhomogeneity makes the particle to move to area of weaker fields.

The non-relativistic relation for the ponderomotive force is expressed by:

$$\mathbf{f_p} = -\nabla \left(\frac{q^2}{4m\omega^2} |\mathbf{E_0}| \right) = -\nabla U_p \tag{1.6}$$

Where U_p is defined as the *ponderomotive potential* which is related to the electromagnetic fields energy density; thus the charged particles, under the ponderomotive potential, tends to escape from high energy density space regions to lower ones. It should be pointed out that the magnitude of this force is inversely proportional to the particle mass and therefore the plasma electrons are more sensible to this effect with respect to plasma ions which can be considered, as a first approximation, not affected by the ponderomotive force.

We also remark that the ponderomotive potential can be expressed in a relativistic framework ($a_0 > 1$), to give the following relation:

$$U_p = mc^2(\gamma - 1) \sim mc^2(\sqrt{a_0^2/\mathcal{P} + 1} - 1) \tag{1.7}$$

Where $\mathcal{P}$ can assume different values for different laser polarization condition ($\mathcal{P} = 2$ for linear polarization and $\mathcal{P} = 1$ for circular polarization). Equation 1.7 states that the ponderomotive potential is proportional to the rest mass of the charged particle and that its magnitude is a monotonic function of the normalized amplitude a_0, with a linear asymptote, $U_p \sim mc^2 \frac{a_0}{\sqrt{\mathcal{P}}}$, valid in the ultra-relativistic regime ($a_0 \gg 1$). This result is particularly relevant since ponderomotive scalings have been reported for the electrons mean energy during the laser interaction with overcritical plasmas.

In particular, an ultra-intense pulse can be absorbed by a steep solid materials (which at low intensity totally reflects the wave) by the so-called *electron heating* mechanisms; an energetic and relativistic supra-thermal electron population is generated, featured by a broad momenta distribution (as shown in Figure 1.5).

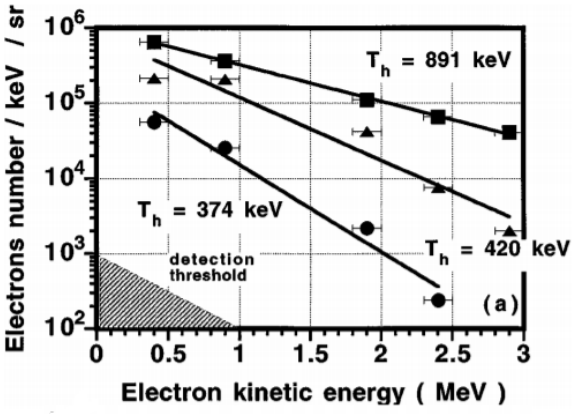

Figure 1.5: Experimental hot electron distributions in the MeV range obtained by irradiating a 30 μm solid CH target at $9 \cdot 10^{18},\ 3 \cdot 10^{18},\ 2 \cdot 10^{18}\ W/cm^2$ intensity, measured along the laser propagation axis in the forward direction. From [11].

The electron heating phenomenon takes place when the plasma density is sufficiently high to reflect the radiation and form a small length scale evanescent wave (in the order of the skin

depth λ_{sd}); in this framework only the superficial electrons interact with the fields and they can be extracted in the vacuum by the component of the Lorentz force perpendicular to the interface. Once in the vacuum, these particles can be re-injected into the high density plasma, with a energy in the order of the quiver motion, where the fields are highly damped and no retraction force is exerted.

Two main mechanism can be distinguished if the electric part or the magnetic one of the Lorentz force are considered, namely the *Brunel effect* and the $\mathbf{j} \times \mathbf{B}$ *heating* respectively.

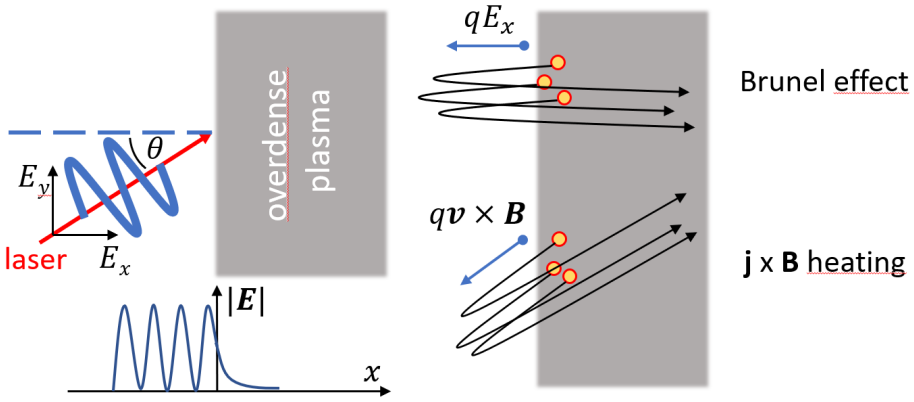

Figure 1.6: Scheme of the two main electron heating mechanism in the interaction of an ultra intense laser pulse with an overdense plasma.

The Brunel effect, called also *vacuum heating*, is represented in Fig. 1.6: the laser interacts with the plasma surface with a non-zero incidence angle and with a linear polarization in the plane of reflection (called *P-polarization*); in this condition a not-vanishing component of the electric field is perpendicular to the vacuum-plasma interface and it is capable to accelerate electrons outside the plasma and, at the end of the wave cycle, to re-inject them into the surface. Since the fields are damped over the skin depth (much lower than the laser wavelength) by the over-critical plasma, the retraction force is not capable to slow down the electrons, which start to travel towards the bulk. Since the Brunel effect requires an electric field component normal to the surface, it is highly damped when the incidence is normal or when laser is in circular polarization or in linear *S-polarization* (where the $\mathbf{E}$ field is perpendicular to the reflection plane).

In the $\mathbf{j} \times \mathbf{B}$ heating the electrons acceleration is similar but the driving force is given by the magnetic part of the Lorentz force, namely $q\mathbf{v}/c \times \mathbf{B}$. The electrons are firstly accelerated by the laser electric field to high speed and therefore they are pushed by the magnetic force along the laser propagation direction; since the phenomenon is due to both the electric and magnetic fields, it is characterized by a non-linear behaviour; thus, the frequency domain of the hot electrons bunches is 2ω instead of the ω domain of the Brunel effect. In addition, since the force is effective when the particles velocity is near the speed of light, the heating mechanism is efficient when the electron motion is relativistic, when $a_0 \gg 1$. In contrast to Brunel effect, the $\mathbf{j} \times \mathbf{B}$ heating is efficient also at normal incidence or S-polarization; while in C-polarization condition, the oscillating part of the magnetic Lorentz force vanishes, with

the main effect of damping the electrons acceleration.

A semi-empirical relation has been proposed to estimate the hot electron temperature T_h acquired by the overall effect of the two mechanisms [12], which reads:

$$T_h = C_1(a_0, pol)m_ec^2\left[\sqrt{1+\frac{a_0^2}{2}}-1\right] + C_2(a_0, pol)m_ec^2\left[\sqrt{1+f^2\frac{a_0^2}{2}sin^2\theta}-1\right]tan\theta \tag{1.8}$$

Where the first term represents the contribute from the $\mathbf{j}\times\mathbf{B}$ heating and the second the Brunel effect; C_1 and C_2 are semi-empirical parameters which depend on the polarization condition and the laser intensity, while θ is the incidence angle and f is the amplification factor due to the laser reflection. As mentioned before, the electrons temperature is roughly proportional to the ponderomotive potential, even if the mechanisms of acceleration are quite different from the motion of a particle under the ponderomotive force. Indeed, this proportionality is due to the electrons kinetic energy acquired in a single laser cycle $(\gamma_{osc}-1)m_ec^2$, (see Section 1.1). It should be also pointed out that these semi-empirical parameters, determined by proper numerical simulations, tend to reach constant values for intensities above $a_0 > 8$, with C_1 larger than C_2; therefore indicating that at ultra-relativistic intensities the $\mathbf{j}\times\mathbf{B}$ heating becomes predominant.

1.3 Laser-driven ion acceleration by Target Normal Sheath Acceleration (TNSA)

Ion acceleration induced by the interaction of ultra intense laser pulses with thin solid targets is a peculiar physical phenomenon discovered for the first time in 2000 with three indipendent works [13–15].

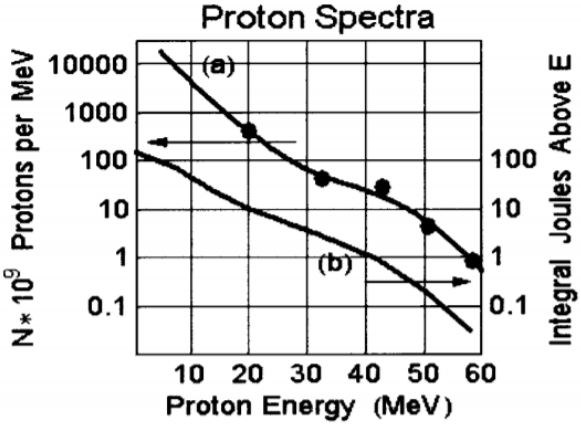

Figure 1.7: Proton energy spectrum for a 423 J shot at normal incidence on 100 μm CH. From [14].

In all the three reported cases the irradiation of a micro-metric plastic or metallic foil from short laser pulses with intensity higher than $10^{18}\ W/cm^2$ resulted in the acceleration of protons with a broad exponential spectrum with a cut-off energy up to tens of $MeV/nucleon$ (as shown in Figure 1.7). The ions bunch, with particles number higher than 10^9 up to 10^{13}, was directed perpendicularly to the target and with a cone of few tens of degrees from a point-like source.

These interesting results immediately fascinated the scientific community both for the curiosity about the phenomenon itself, both for the appealing applications which could be dealt with an innovative laser-driven ion source [16]. Indeed, the compact size and the relatively cheapness of the accelerator and the peculiar properties of the accelerated particles (e.g. high ion density per bunch, ultrafast duration) could be exploited, for example, in the nuclear science (e.g. bright neutron sources, fast ignition inertial fusion), in the material science (e.g. Ion Beam Analysis) and in the medical field (e.g. radioisotopes generation, hadron-therapy) [17, 18].

In the few years following the first experimental observations, a big effort has been devoted to understand the phenomenon with new experiments and theoretical models; in particular, after some debates, the *Target Normal Sheath Acceleration* model [19] was widely accepted as an explanation for most of the experimental data.

The TNSA scheme describes the acceleration phenomenon with chained mechanisms represented in Figure 1.8: the ultra intense laser pulse, interacting with the solid target promptly generates an over-dense plasma which reflects the electromagnetic fields. As explained in the previous section, when the fields overcome relativistic intensities ($a_0 > 1$) the superficial plasma electrons are heated through the Brunel effect and the $\mathbf{j} \times \mathbf{B}$ heating and they start to travel inside the solid target. The high current is counter-balanced by a return current of cold electron moving in the opposite direction. When the fast electrons arrive at the rear side of the solid, they try to escape forming a charge unbalance capable of generating strong electrostatic fields; these latter therefore ionize and accelerate to $MeVs$ energy the ions present at the rear surface. Since contaminants are generally present at this interface, ions with composition different from the target itself can be found; in fact the highest energy ions are typically protons likely coming from dirt or water contaminants.

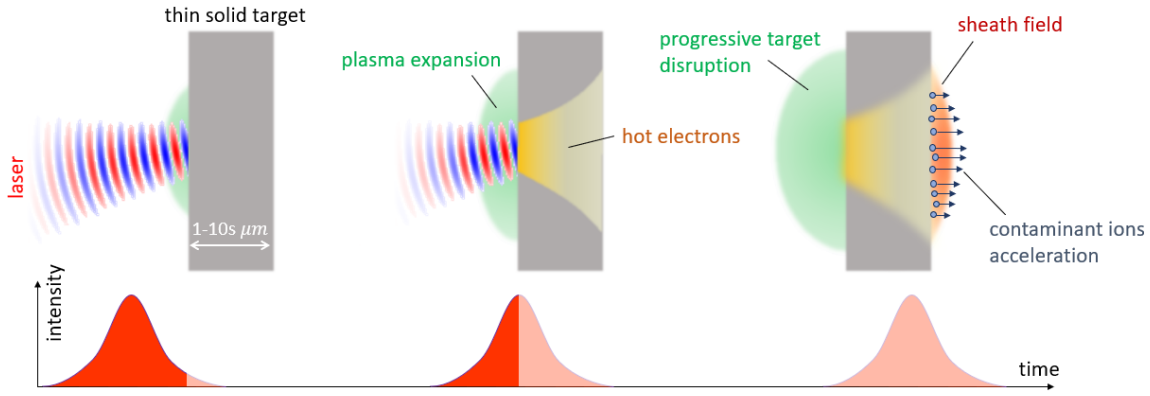

Figure 1.8: Scheme of the Target Normal Sheath Acceleration model.

Exploiting the TNSA model some simple estimations over the phenomenon can be carried out: considering that the hot electron population is generated by the above-mentioned heating mechanisms, their energy distribution is similar to a Maxwellian with temperature in the order of the ponderomotive potential, namely $T_h \sim m_e c^2(\sqrt{1 + a_0^2/p} - 1) \sim m_e c^2 a_0/\sqrt{\mathcal{P}}$,

where the last approximation is valid at high intensity. Imposing the energy flux balance, the initial density of electrons can be retrieved, $\eta I = n_h v_h T_h$ with η the conversion efficiency of the laser into energetic particles and $v_h \sim c$; in a similar way the total number of electrons is estimated by the energy balance $\eta \epsilon_p = N_h T_h$. Therefore assuming a laser irradiance $I\lambda^2 = 10^{20}\ \mu m^2 W/cm^2$ and a 10 % of conversion efficiency, we find $T_h \sim 5.1 m_e c^2 \sim 2.6 MeV$ and $n_h \sim 8 \cdot 10^{20}\ cm^{-3}$, which is lower than the critical density; the relative current density is consequently $\mathbf{j_h} \sim e n_h c \sim 3.8 \cdot 10^{10}\ A/cm^2$. This huge current must be locally neutralized by a cold electrons return current opposite in direction, otherwise the generated electric or magnetic fields should be strong enough to interrupt the hot electrons motion.

The hot electrons attempting to escape in vacuum at the rear side of the target form a charge unbalance and a strong sheath electric field E_s which back-holds the electrons. E_s can be thus estimated by imposing that the sheath potential energy is equal to the hot electrons temperature $eE_sL_s \sim T_h$, with L_s the extension of the sheath, well approximated by the Debye length $\lambda_D = \sqrt{T_h/4\pi e^2 n_h}$. Finally the electrostatic field can be calculated as $E_s \sim \sqrt{4\pi n_h T_h}$ which, for the above case, corresponds to $E_s \sim 6\ TV/m$, a great field capable to instantaneously ionize the contaminant ions and accelerate them along the sheath potential, with a maximum energy given by $\epsilon_i^{max} = Z_i e E_s L_s = Z_i T_h \sim Z \cdot 2.6\ MeV$.

These simple estimations are useful also to indicate the ions energy scaling laws with respect to the laser parameters; indeed, since the electrons temperature scales with the ponderomotive energy, also the ions maximum energy follows the irradiance scaling, which means an energy growth with the square root of the intensity and linearly with the wavelength. Nonetheless, it should be pointed out that the wavelength dependence is not decoupled with the peak intensity, since the duration of an ultra-short pulse is limited below by the wave single cycle length; also the focal spot dimension w_0, which strongly affects the peak intensity, can be reduced at most to the diffraction limit $w_0 \sim \lambda$. Thus, estimating the intensity as $I \sim \epsilon_p/\tau w_0^2$, we can assume that the temporal duration $\tau \sim k_\tau \lambda/c$ is proportional to the single cycle duration and the spot waist to the wavelength $w_0 \sim k_{w_0}\lambda$ (where k_τ and k_{w_0} are proportionality constants in the order of $1 - 10$); therefore, it is straightforward to demonstrate that the irradiance is inversely proportional to the wavelength (when the pulse energy is fixed) $I\lambda^2 \sim \epsilon_p c/k_\tau k_{w_0}\lambda$. The ions energy ponderomotive scaling is consequently given by $\epsilon_i^{max} \propto \sqrt{\epsilon_p/\lambda} \propto \sqrt{P}$ where P is the peak laser power, which is a commonly reported value in laser facilities, as introduced in Section 1.1.

The scaling law of the maximum proton energy with respect to the pulse power is reported in Figure 1.9 for a number of different ultra-intense laser pulse facilities; it should be pointed out that two different power laws are showed, for relatively 'long' and 'short' pulses (which are the two main different facilities explained in Section 1.1). The 'long' pulses facilities scaling law is in a good agreement with the ponderomotive scaling; in addition a higher energy than the 'short' ones is observed over the wide range of existing experimental data; conversely, the $\sim fs$ laser category is characterized by a power law intermediate between the square root and the linear one. These substantial differences, not foreseen by

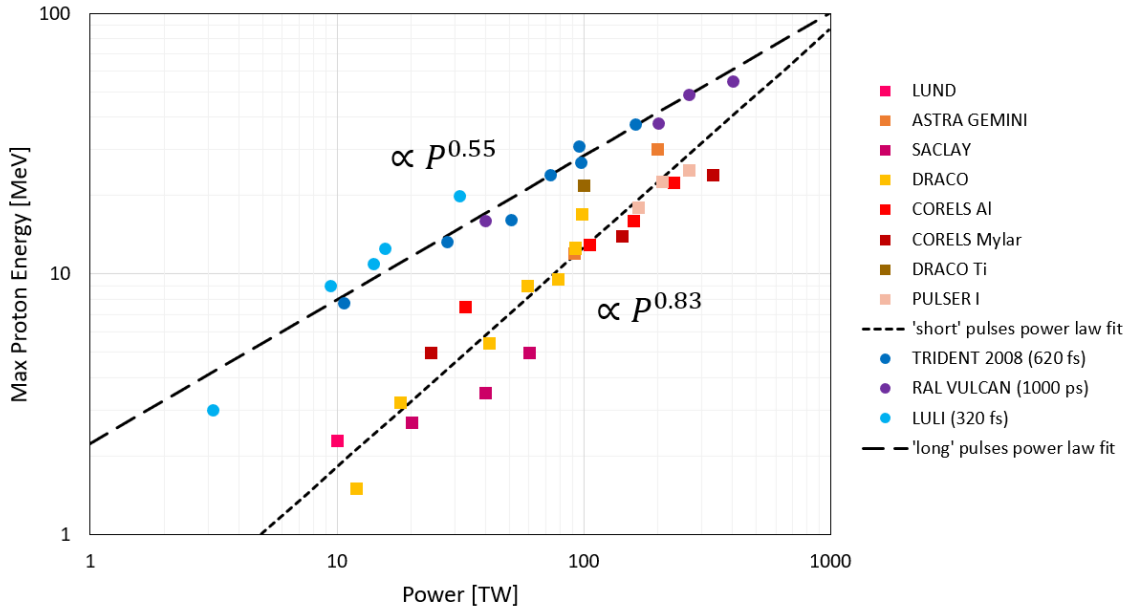

Figure 1.9: Maximum proton energy against the laser falicity pulse peak power. The data of 'short' ($\sim fs$) pulses are from: Lund Al target [20], Astra Gemini 2 μm Al target [21] [22], Saclay 1.5 μm Al target [23], Draco 5 μm Al target [24] and 3 μm Ti target [25], CoReLs 0.75 μm Al target [26] and 0.75 μm Mylar target [27], Pulser I 0.05 μm polymer target [28]. The data of 'long' ($\sim ps$) pulses are from: Trident, 15 μm Al target [29], Ral Vulcan 10 μm Al target [30], Luli 20 μm Al target [31].

the above-mentioned TNSA estimations, highlight the complexity of the laser acceleration phenomenon, which requires more advanced models to be finely understood.

To tackle the analytical modelling problem, it is useful to reduced its complexity by describing the system in one-dimensional approximation and by dividing the mechanism into more fundamental sub-parts: the electron heating, the hot electron transport in the target and the ion acceleration, through the sheath field generation. As depicted in Figure 1.10, these different phenomena are characterized by time scales ranging from few fs to several ps. Indeed the electron heating, due to the above-mentioned Brunel and $\mathbf{j} \times \mathbf{B}$ mechanisms, happens during the single wave cycle (few fs for Ti:Sapphire lasers) and continues for the whole duration of the laser pulse; the electron transport phenomenon temporal duration can be estimated by the time in which the relativistic particles, generated at the surface, reach the rear side of the target, namely $\tau_{tr} \sim d_t/c$, which corresponds again to few fs for a micrometric foil target. The sheath field generation and ion acceleration can be studied in different time scales, where different ions properties can be described: in those cases in which the acceleration occurs within the inverse of the hot electrons plasma frequency ($1/\omega_{pe} \sim 10\ fs$), the ions dynamics can be neglected and the analytical models fall into the *quasi-stationary* framework. Otherwise, if the ions dynamic is considered, the time scale is longer ($1/\omega_{pi} \sim 1\ ps$) and *fluid* models are used.

Quasi-stationary models assume that on the time scale of plasma electrons frequency the target ions are immobile, the hot electrons population is isothermal and that the accelerated light ions are sufficiently low in number not to perturb the evolution of the sheath field. These assumptions are reasonable for the estimation of the maximum energy of the contam-

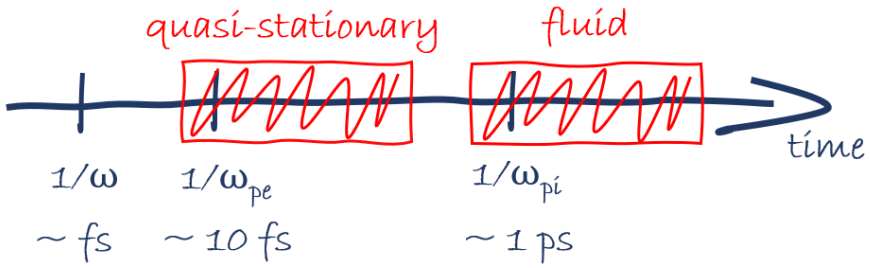

Figure 1.10: Time scales in TNSA models.

inant layer light ions, especially if short pulses are used. Conversely, the quasi-stationary models lack of precision for the determination of the ions energy spectrum and the heavy ions evolution, because the occurring phenomena happen at longer time scale.

In these limits, the Poisson equation can be coupled with the Boltzmann distribution with temperature T_h fixed a priori (e.g. using the ponderomotive scaling) to obtain a relation for the potential in the space:

$$\phi(x) = -\frac{2T_h}{e}\left[ln\left(1+\frac{x}{\sqrt{2\mathrm{e}}\lambda_D}\right)-1\right] \tag{1.9}$$

The latter equation (notice that e is the Nepero number while e is the elementary charge) allows determining the sheath electrostatic field at the vacuum interface as $E(0) = \sqrt{\frac{2}{\mathrm{e}}}\frac{T_h}{e\lambda_D}$ which justifies the rough calculations for the TNSA field. Nevertheless, this mathematical description leads to a divergent potential at infinite distance from the target, therefore to infinite light ions energy. This non-physical effect is due to the use of the Boltzmann distribution which implies the existence of electrons with infinite energy.

To avoid this unphysical result, a cut-off in the particles energy must be introduced, for example by using scaling laws based on experimental data; another elegant solution was proposed in References [32, 33], where the cut-off is not imposed a priori, but it is calculated in a self-consistent way from the consideration that only the 'low-energy' part of the particles spectrum is retained from the potential (*trapped electrons*). Conversely, the 'high-energy' electrons escape from the system in a time that is well lower than the time scale of interest. This point is analytically deployed by integrating a proper relativistic distribution, the Maxwell-Juttner, over the trapped electrons, which posses negative energy $W = m_e c^2(\gamma - 1) - e\phi$.

The resultant potential is then vanishing at infinite distance and a maximum energy for light ions can be analytically obtain, which reads:

$$\epsilon_i^{max} = ZT_h\left[\varphi^* - 1 + \frac{\beta(\zeta,\varphi^*)}{I(\zeta,\varphi^*)\mathrm{e}^{\zeta+\varphi^*}}\right] \tag{1.10}$$

Where $\zeta = m_e c^2/T_h$ is the inverse of the normalized temperature, $\varphi = e\phi/m_e c^2$ the normalized potential, $\beta(\zeta,\varphi^*) = \sqrt{(\varphi+\zeta)^2-\zeta^2}$, $I(\zeta,\varphi^*) = \int_0^{\beta(\zeta)} \mathrm{e}^{-\sqrt{\zeta^2-p^2}}dp$, and φ^*

is the value of the normalized potential deep inside the target. It should be remarked that Equation 1.10 justifies the maximum energy estimation of the TNSA model, since it depends only on the electron temperature and φ^*. The latter quantity physically represents the normalized maximum electrons energy, which can be obtained by a semi-empirical relation, $\varphi^* = 4.8 + 0.8\log(\epsilon_p)$ [33], or by a finer model which takes into account the electrons recirculation and the target thickness [34].

In those cases where the ion acceleration mechanism takes place over long time scales (in the order of the inverse of the ions plasma frequency) or under conditions which do not fulfil the quasi-static models assumptions, the target ions dynamic must be considered. The simplest approach consists in a one-dimensional fluid model, based on the quasi-neutral plasma approximation. It should be firstly highlighted that this approximation does not require a vanishing sheath field, indeed the fluid description allows a uniform field along the plasma and non-uniform fields over length scales in the order of the Debye length.

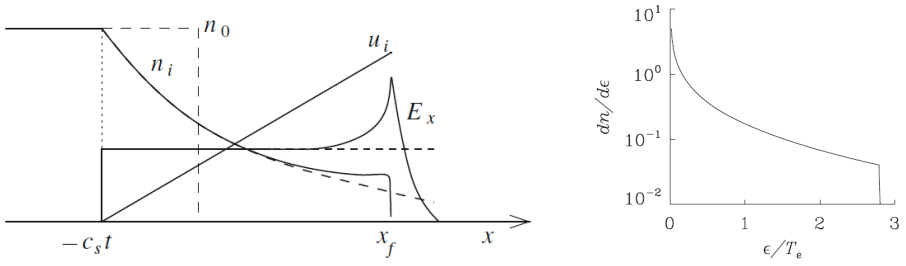

(a) **(b)**

Figure 1.11: (a) Scheme of the one-dimensional fluid model. (b) Ion spectrum for a cut-off energy of $\epsilon = 2.8T_h$.

The model, outlined in Figure 1.11a, consists in considering the acceleration process as an isothermal plasma expanding in vacuum, with a rarefaction wave described by the classical self-similar solutions for the ions density n_i and velocity u_i fields:

$$n_i = n_0 \text{exp}\left(-\frac{x}{c_s t} - 1\right), \quad u_i = c_s + \frac{x}{t} \tag{1.11}$$

Where x/t is the self-similar variable and $c_s = \sqrt{ZT_h/m_i}$ is the ion sound velocity. Equation 1.11 is singular at $t = 0$ because the model is not able to describe the charge unbalance of the first stages of acceleration. In addition, this equation allows diverging ions speed at finite times; to solve the latter issue the quasi-neutrality approximation must be invoked to determine the ion front position as a function of time. Exploiting that the non-uniformity scale of the density field $n_i/|\partial n_i|$ must be in the order of the Debye length, the ion front speed can be evaluated as $u_f = 2c_s ln(\omega_{pi} t)$. This speed is still divergent for infinite time because in the plasma is approximated as isothermal, which implies an infinite reservoir of energy for the acceleration; to avoid this divergence some authors considered a finite acceleration time, scaling with the pulse duration through a semi-empirical law $t_{max} = 1.3\tau_p + \tau_{offset}$ [35]. Other solutions of this unphysical constrain make use of the adiabatic

plasma expansion in vacuum, which consistently implies a decreasing electron temperature in time [36, 37].

One interesting feature of the fluid model is the capability of finding an analytical ions spectrum, with properties very similar to the ones experimentally measured. Indeed, the spectrum at the final acceleration time t_{max} is:

$$\frac{dn_i}{d\epsilon_i} = \frac{n_0/T_h}{\sqrt{2\epsilon_i/T_h}} \exp\left(-\sqrt{\frac{2\epsilon_i}{T_h}}\right), \quad \epsilon_i \leq \epsilon_i^{max} = \frac{1}{2} m_i u_f(t_{max})^2 \tag{1.12}$$

An example is plotted in Fig. 1.11b, where the exponential-like tail should be observed.

CHAPTER 2

Enhanced ion acceleration through advanced targets

This second chapter deals with the vast framework of advanced targets for enhanced ion acceleration, with the main aim of introducing some crucial concept more than reviewing the literature.

The advanced targets, developing during the last decade, aim at the enhancement of the acceleration mechanism performances, principally the ions maximum energy and the total particles number.

Different approaches to the problem can be adopted; here we describe two main categories, in Section 2.1 the advanced target which increase the ions energy by improving the hot electrons transport. While Section 2.2 describes some of the strategies which can be exploited to increase the hot electron absorption.

2.1 Role of the electrons transport in TNSA

The enhancement of the laser-accelerated ions energy can be obtained by improving the hot electron transport inside the target; since the accelerating quasi-static field can be estimated as $E_s \sim \sqrt{4\pi n_h T_h}$ (see Section 1.3), the TNSA performances can be increased by simply controlling the hot electrons density n_h and temperature T_h, which tend to decrease during their transport towards the rear side of the target.

Nevertheless, the relativistic electron transport in dense materials is a very complex phenomenon which is studied mainly for the *Inertial Confinement Fusion* (ICF) applications [38]. Some of the mechanisms studied for ICF are particularly interesting also in the laser acceleration field, indeed it has been showed that, making reference to Figure 2.1a, hot electrons travelling inside a dense material generate extremely high density currents which are neutralized by a return current of cold electrons (conductive electrons in metals or ionized electrons in dielectrics); these currents are associated to self-generated magnetic and elec-

tric fields which can slow down the fast particles. In addition, the electrons can undergo to collisions which diminish the particles energy and broadens the spatial distribution.

Measurements, shown in Figure 2.1b, have demonstrated that the fast electrons travel inside the target with roughly a cone shape with opening angle in the order of tens of degrees.

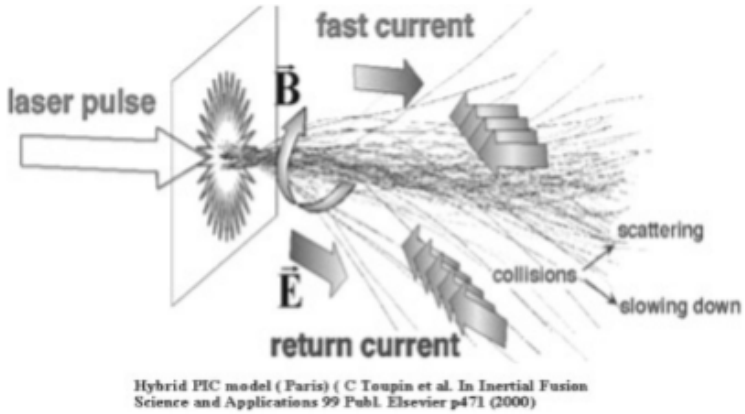

(a)

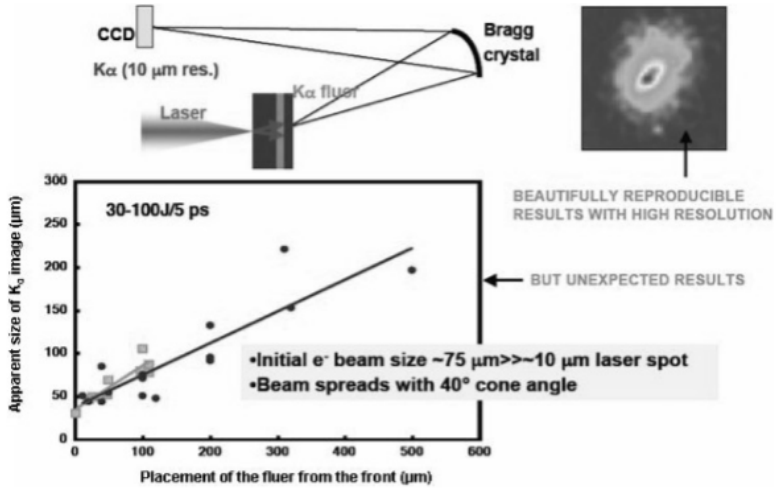

(b)

Figure 2.1: (a) A schematic of the electron transport into dense materials . (b) Scheme of the measurements of the propagation of hot electrons inside an Al target; the measurement consists in the acquisition of characteristic X-rays, by a bent Bragg crystal, produced in thin layers positioned at different lengths inside the Al target. From [38].

In order to enhance the TNSA performances, it is therefore of high importance to reduce the electron cooling and angular spread in the solid target.

Different strategies have been developed: the simplest one is to decrease the solid target thickness, since for thinner solids the detrimental transport effects are intrinsically reduced. Figure 2.2a shows an example of the results obtained by decreasing the target thickness; it should be noticed that for the data represented by empty markers, the lower thickness is beneficial for the cut-off protons energy. On the contrary, for the full points we observe an opposite behaviour; this is explained by the different irradiation condition, namely high

and low contrast respectively. The laser contrast is defined by the ratio between the peak intensity over the intensity of the pre-pulse (which can affect the target several ps before the main peak interaction); since in the first case the laser has an ideal temporal profile (high contrast, HC) the TNSA mechanism develops without non-idealities and gives better results for reduced thickness targets. On the other hand, in the low contrast case (LC) the main pulse is preceded by a low intensity pre-pulse which destroys the solid before the main peak arrival.

These observation also indicates that, in the laser-driven ion acceleration, the quality of the incident laser pulse is an essential aspect to be considered.

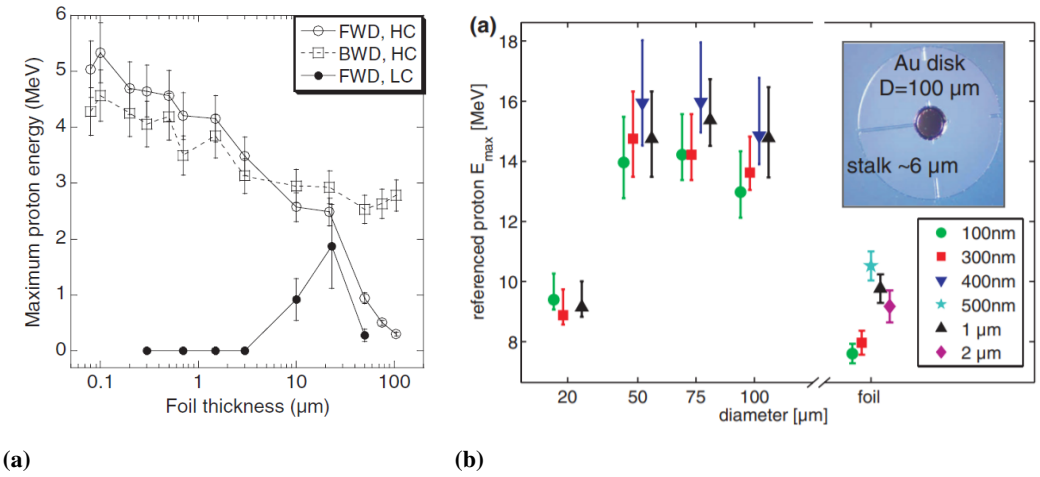

Figure 2.2: (a) Experimental maximum proton energies obtained with standard solid target with different thickness values; FWD refers to protons observed along the forward direction while BWD to backward direction. LC stands for low contrast, HC for high contrast. From [39]. (b) Experimental maximum proton energies obtained by RMTs (showed in the inset) with different thickness and diameter are reported. From [40].

Another possible solution for the improvement of the electron transport is to exploit foils with finite lateral dimension, called *Reduced Mass Targets* (RMT). The configuration, represented in the inset of Figure 2.2b, generally consists in a small disk solid foil with $10s\ \mu m$ lateral extension and sub-μm thickness; the target is supported by one or more micrometric stalks. The finite lateral dimension enables to use the recirculation effects to confine the hot electrons into a reduced volume; this allows increasing the charged particles density and consequently generating a stronger and more uniform sheath field. Figure 2.2b reports experimental results obtained with RMTs; a clear maximum energy enhancement is observed for $50 - 100\ \mu m$ diameter disks up to a factor of 1.5 with respect to standard foils. The smaller disk ($20\ \mu m$ diameter) shows instead a lower cut-off energy; this could be explained by the fact that for small lateral dimension the edge sheath fields become comparable to the normal one, which is detrimental for TNSA because the target tends to be destroyed and the accelerating field is highly distorted. It should be also noticed that an optimal RMT thickness is observed at about $400\ nm$ and for lower and higher values worse performances are reported; also in this case this is probably an effect of the pulse contrast, since at lower thickness the pre-pulse could disrupt the RMT.

2.2 Role of the electrons absorption in TNSA

Another large fraction of the advanced targets which enable to increase the ions energy can be grouped in the category of the enhanced electron absorption.

Because the accelerating field depends on the electrons density and temperature, a direct route to enhance the ion properties consists in increasing the hot electrons conversion efficiency with engineered targets. It should be remarked that the following strategies are not in contradiction with the ones of Section 2.1, indeed they can be considered as complementary solutions that could be exploited in a synergistic way.

One possibility is to use a *grating* target (see Figure 2.3a), having a periodical surface modulation with sub-wavelength depth, to exploit the surface resonant wave excitation to increase both the hot electrons number and their temperature [41]. Experimental results demonstrated the increase of the protons energy at the resonant angle condition up to $5\ MeV$ compared to highest energy of $4\ MeV$ obtained at larger angle for the flat target [42].

Similar results have been reported for nanostructured targets, composed by a flat solid covered by a mono-layer of sub-micron spheres as shown in Figure 2.3b; due to the improved laser-target coupling, a proton energy increase of a factor about 1.6 was observed at low incidence angle [43]. However, measurements with the same target at high incidence angle evidenced an absence of ions energy enhancement [44].

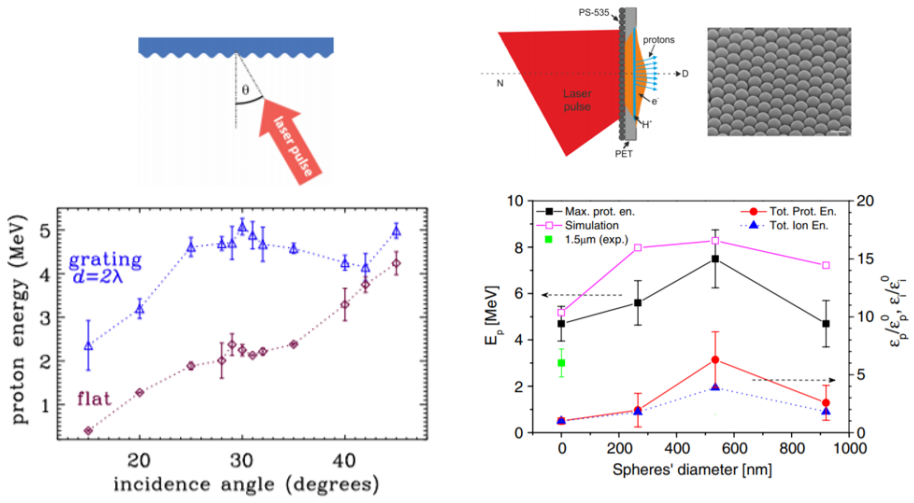

(a) **(b)**

Figure 2.3: (a) Grating target scheme (top) and relative proton energy results at different incidence angle (bottom). From [42]. (b) Micro-spheres target scheme (top) and relative proton energy measurements with different spheres diameter (bottom). From [43].

The use of *shaped* target is another viable route to increase the electrons temperature; *micro-cones target*, represented in Figure 2.4a, allowed achieving in 2011 a new proton energy record [45] of $67.5\ MeV$ against the long-lasting record obtained in 2000 of $58\ MeV$ [14] (note that the nowadays record is $94\ MeV$, from a PW-calss ps pulse interacting with a $75\ nm$ solid foil [46]). In the micro-cones target experiment, carried out with relatively long

pulses ($700\ fs$), the proton energy enhancement factor of 1.35 was justified by the *direct laser-light-pressure acceleration* of electrons. The mechanism consists in the extraction of electrons from the cone surface and in their acceleration to super-ponderomotive energies by the direct action of the wave electromagnetic fields.

Finally, one last strategy, particularly important for this thesis work, is the near-critical *Double Layer Target* (DLT) (see Figure 2.4b), consisting in a low density layer attached to the front of a standard flat solid foil. The main idea of this advanced target is the exploitation of the critical density layer to increase the electron absorption, since, conversely to standard targets, the laser can propagate inside the plasma and generate volumetric hot electrons.

The propagation of an ultra-intense pulse inside a near-critical plasma is a very complex topic because of the strong light-matter coupling, characterized by highly non-linear and relativistic phenomena; for this reason, the problem is mainly studied by means of numerical tools, as PIC simulations [47, 48]. Thanks to this tool and to several experimental observation, various interdependent phenomena have been identified: a plasma channel is formed due to the ponderomotive force which pushes the electrons outside the channel and produces a radially dependent refractive index triggering a focusing waveguide (always referred as *self-focusing*, SF) [49, 50]. The plasma channel is also strongly magnetized in the angular direction due to the high electron currents; the magnetic field therefore pinches the relativistic electrons in a straitghforward direction [51]. The electrons are accelerated to superponderomotive energies because of the *Direct Laser Acceleration* phenomenon (DLA), through the betatron resonance (a mechanism similar to the one happening within the micro-cone targets) [47, 48, 52, 53].

Independent experimental works, which observed an ion energy enhancement with the DLT configuration, were interpreted at the light of the above-mentioned phenomena. In some cases, the principal effect was attribuited to the increase of the electron absorption [26, 54, 55], in other works, by the generation of superponderomotive electrons [56] and also by the *Radiation Pressure Acceleration* (RPA) of the target ions [57, 58] (a particular laser-driven acceleration mechanism consisting in the direct acceleration of a thin target by the pulse radiation pressure [59]).

Due to presence of all these interdependent phenomena, probably the acceleration enhancement is due to a combination of all of them. A possible physical picture could be the following: the pulse relativistic self-focusing enables to push the target by radiation pressure while generating at the same time high energy electrons in the solid target; simultaneously, the great number of relativistic electrons produced in the near-critical plasma contribute to form a very strong sheath field which boosts the ions energy. Nonetheless, it should be remarked that the weight of these phenomena on the ion acceleration has still not been deeply investigated.

Beyond the DLT-laser interaction physics, it should be highlighted that this kind of target requires advanced production techniques. Indeed, the critical density for a Ti:Sapphire laser corresponds to a mass density in the order of few mg/cm^3 considering a completly ionized

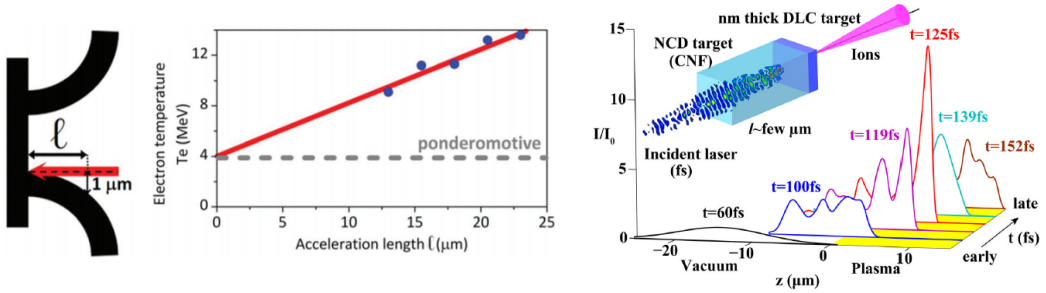

(a) **(b)**

Figure 2.4: (a) Microcone target (on the left) and hot electrons temperature with respect to the cone length. From [45]. (b) Near-critical double layer target scheme (top) and laser envelope evolution during the interaction calculated by PIC simulation; relativistic pulse shaping should be observed, which increases the peak amplitude by a factor of 10. From [49].

material; this extremely low density, down to 0.1 % of the bulk, can be realised by few methods.

One possibility is to exploit very dense gas jets [60] which, at the state of the art, are characterized by relatively long lengths (hundreds of microns) and long density gradients; in addition to the difficulty to finely control the gas properties down to the μm and to the complex apparatus, this solution is hardly compatible with a solid target in the DLT configuration (which is necessary for the enhanced TNSA mechanism).

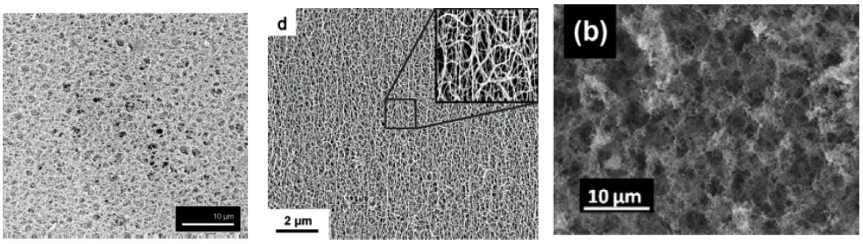

(a) **(b)** **(c)**

Figure 2.5: (a) SEM image of a Cellulose Triacetate foam [61]. (b) SEM image of a Carbon Nanotubes foam [62]. (c) SEM image of a Carbon nanofoam [63]

The other viable route is to exploit very porous nanostructured materials, featured by a void fraction higher than 99 %. The desired properties of such a solid near-critical material are the following:

- a controllable low density ($\sim mg/cm^3$)
- a controllable thickness down to the laser wavelength ($\sim \mu m$)
- a non-uniformity scale lower than the laser wavelength ($< 1\ \mu m$) in order to be considered homogeneous for the interaction
- the possibility to attach the nanostructure to any kind of standard solid target

Nowadays no material satisfies all the above-mentioned properties, nevertheless three types of nanostructure have been successfully exploited in laser-interaction experiments

thanks to their properties almost matching the ones of the *ideal* near-critical solid material:

Cellulose Triacetate foam (TAC, $C_{12}H_{16}O_8$) can be produced by a chemical method with a mean density down to $2\ mg/cm^3$ (which corresponds to $0.7\ n_c$ for fully ionized atoms) and it is characterized by a uniform 3D network structure consisting of $1-2\ \mu m$ pores, $0.1\ \mu m$ thick and $1\mu m$ long fibers; its minimum thickness is in the order of $100\ \mu m$ (see Figure 2.5a) [61, 64, 65].

Single walled Carbon nanotubes foam (CNT) can be synthesized thorough a Chemical Vapour Deposition technique (CVD) directly onto solid targets with a mean density of about $3\ mg/cm^3$ (which corresponds to $0.4\ n_c$ for fully ionized atoms) [62]; since the CVD method implies high operation temperature ($600\ C^\circ$) only refractory targets can be used as substrate (e.g. Diamond Like Carbon, DLC). This particular foam is composed by highly uniform 3D network of nanometric carbon nanotubes with a uniformity scale lower than $1\ \mu m$, which can be produced with thickness down to hundreds of nm (see Figure 2.5b).

Carbon nanofoam (CNF) is produced by the Pulsed Laser Deposition technique (PLD) with a mean density down to $7\ mg/cm^3$ (which corresponds to $1.2\ n_c$ for fully ionized atoms); the nanofoam is characterized by a fractal 3D structure of small Nanoparticles (NP) with diameter of about $10-20\ nm$ and a uniformity scale in the order of few μm [55, 63]. This material can be deposited onto any type of substrate (without any particular limitation) with a thickness down to few μm (see Figure 2.5a).

The latter nanostructured material is particularly relevant for this thesis work since the near-critical DLTs dealt in this manuscript are based on Carbon nanofoam attached to thin solid substrates. Chapter 3 describes in detail the C nanofoam-based DLT realization and the laser-acceleration experimental results obtained before this thesis work.

CHAPTER 3

Nanofoam-based near-critical Double Layer Targets (DLTs)

This chapter deals with the Carbon nanofoam-based Double Layer Targets for the enhancement of laser ion acceleration; in particular all the knowledge acquired before the start of this PhD thesis is presented.

The first Section describes the production technique, the *Pulsed Nanosecond Laser Deposition* (ns-PLD), and the synthesis parameters used to realize the material; Section 3.2 presents the characterization methods which allow measuring the more important properties of the nanostructure, as the morphology, the mean density and the thickness.

Finally, in 3.3 the ion acceleration experimental and theoretical results are deepened and the open points of the research field, which are tackled in this PhD thesis, are summarized in Section 3.4.

3.1 Pulsed Nanosecond Laser Deposition (ns-PLD) of nanofoams

Carbon nanofoam (CNF) is a very porous nanostructured material produced by the *Pulsed Nanosecond Laser Deposition* technique (ns-PLD).

Figure 3.1 shows the schematic of this technique, which consists in the ablation of a target by a ns-duration laser pulse; the ablated species expand into a vacuum chamber with controllable pressure of an ambient gas and are collected by a substrate on which the film is formed.

More in detail the machine used at the *Micro- and Nanostructured Materials Laboratory* (NanoLab), in the Politecnico di Milano, to deposit Carbon nanofoams exploits a Nd:YAG *Q-switch* laser ($\lambda = 1064\ nm$) with $7\ ns$ duration and $100 - 1000\ mJ$ energy pulses. The wavelength can be modified through second harmonic crystal to 532 and $266\ nm$. When the laser is focused onto the target with a $1\ mm$ diameter spot, intensities up to $10^{10}\ W/cm^2$

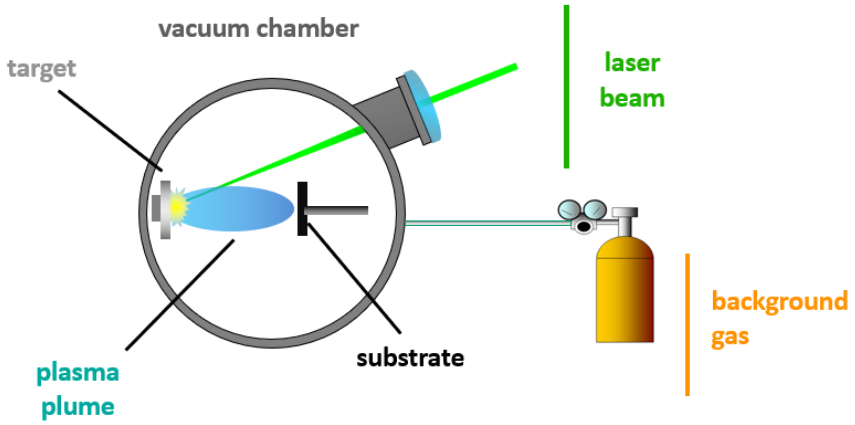

Figure 3.1: Schematic of the ns-PLD technique.

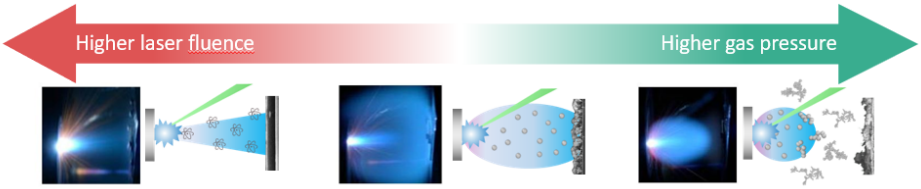

Figure 3.2: Schematic of the ns-PLD deposition regimes as a function of the laser fluence and the background gas pressure.

can be reached; in this regime the laser deposits its energy to electrons lying in a characteristic length (which is roughly the maximum length between the heat transfer length and the skin depth defined in Section 1.2), which generally assumes values in the order of tens of nanometers. The electrons are removed from the atoms potential by multiphoton ionization (see Section 1.1) and start to oscillate in the laser field, with a characteristic time scale of $1 - 100\ fs$; in longer times the electrons give energy to the target atoms with non-linear processes as electron-phonon collisions, which heat the solid and vaporize it. The ablated gas can be weakly ionized and it expands into the chamber atmosphere/vacuum with a particular luminescent cloud, called *plasma plume*.

Two opposite regimes can be distinguished with respect to the chamber atmosphere condition: a *vacuum-like* expansion, when the laser *fluence* (i.e. pulse energy over spot area) is high and the background pressure is negligible, where the plasma plume is directional and the ablated atomic/ionized species are quite energetic ($\sim\ 10\ eV$); and a *shock* expansion, when the fluence is lower and the pressure is high, where the plasma launches a shock wave inside the background gas and is progressively slowed and cooled down. Between the two regimes we can find intermediate regions without a net threshold.

The vacuum-like deposition is featured by a more peaked distribution of material on the substrate. To deposit uniform films (i.e. with constant thickness over large areas), the substrate must be rotated off the plasma plume axis; the resulting film (see left side of Figure 3.2) is composed by energetic atoms and therefore shows a high compactness and generally an amorphous structure. For increasing atmosphere pressure and decreasing laser fluence,

the ablated species are less energetic and are slowed down by the collisions with the gas; this results in a broader lateral distribution in the deposited material and in the generation of more porous films.

In this last condition a particular phenomenon can occur: the formation of *nanoparticles* (NP). When the target vapour cools down during the expansion, if it is sufficiently spatially confined, a supersaturated condition can be achieved and spherical liquid particles aggregate to form NPs [66]; it was demonstrated that the supersaturated gas ionization plays an essential role in the high rate NPs formation [67]. The materials generated by these nanoparticles are particularly porous (see intermediate image of Figure 3.2).

At very low laser fluence ($\sim 1\ J/cm^2$) and high gas pressure ($\sim 100s\ Pa$) particular nanostructures were deposited from Carbon target at NanoLab, called Carbon nanofoams (CNF), featured by a very porous and a fractal geometry [63]. The smaller components of these materials were found to be spherical-like NPs with $10 - 20\ nm$ radius (see Figure 3.3), which aggregate to form a 3D complex network rich in voids.

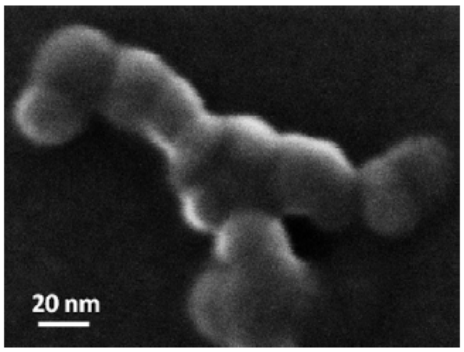

Figure 3.3: HR-STEM image of the nanoparticles composing the Carbon nanofoam. From [63]

One of the more interesting features of the CNF nanostructure is the wide range of deposited morphologies with respect to the PLD parameters, as illustrated by Figure 3.4. In particular, it was observed that the background pressure plays a relevant role in determining the porosity of the nanostructure: a cauliflower-like shape is found for lower pressure values (tens of Pa) and a more open structures in the hundreds of Pa range. In addition, it was studied the effect of the composition of background atmosphere exploiting two different inert gases: Helium and Argon. The foam deposition in Helium is featured by a slow variation of the structure with respect to the pressure, while for the Argon case, the CNF shape changes more dramatically. This can be explained by the different gases atomic mass number (4 for He, and 40 for Ar); indeed, a higher gas mass results in a higher transferred momentum in collision with the ablated species and in a stronger confinement of the plasma plume. In the latter condition the target high energy atoms quickly reach the supersaturation condition forming a large number of NPs which are essential to form the CNF structure.

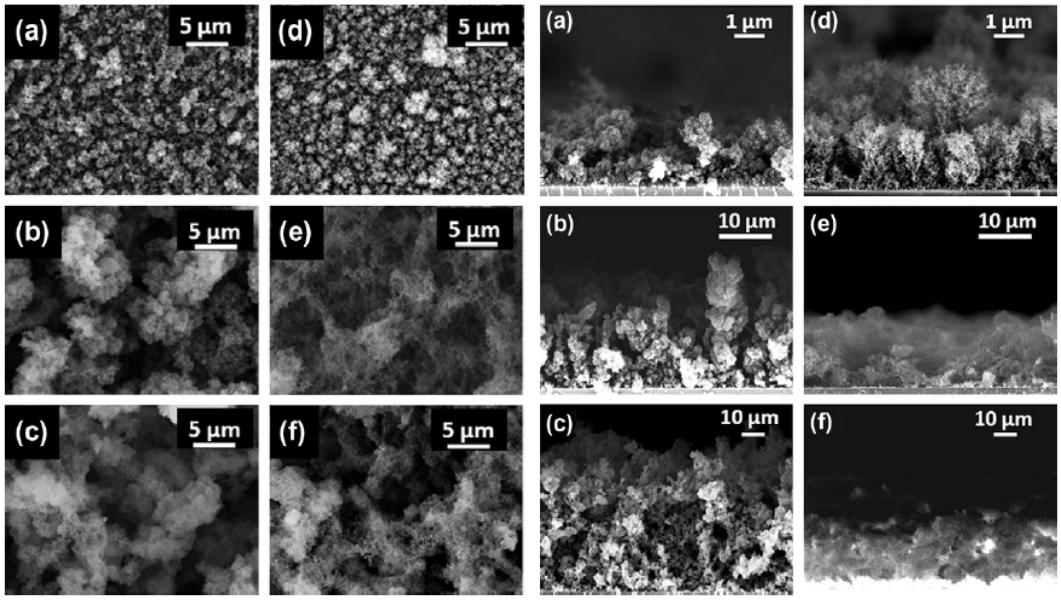

Figure 3.4: SEM top view (left panel) and cross section (right panel) of Carbon nanofoams produced in different background gas: Helium (a, b, c) and Argon (d, e, f); at different pressure values: 30 Pa (a, d), 100 Pa (b, e), 500 Pa (c, f). From [63]

3.2 Characterization of nanofoams

The Carbon nanofoam more relevant properties for the laser-acceleration field are probably the mean density, the thickness, the NPs dimension and the uniformity (as introduced in Section 2.2). Different characterization techniques were exploited to achieve these objectives.

As shown in Section 3.1 the *Scanning Electron Microscope* (SEM) is used to extract qualitative informations about the foam structure shape and uniformity through top view images. SEM cross section images are instead exploited to measure the film thickness; while the *High Resolution Scanning Transmission Electron Microscope* (HR-STEM) is used to determine the NPs radius.

More complex is the measurement of the Carbon nanofoam mean density, because standard balances could lead to high measurement errors. Indeed, the material is generally produced on small area samples ($\sim 1\ cm^2$) with few μm thickness; if the Carbon critical density is considered ($5.6\ mg/cm^3$), a total film mass can be estimated as about $0.5\ \mu g$ which is comparable to the weight error of the more advanced micro-balances.

Only *Quartz Crystal Microbalances* (QCM) are capable to reach lower error values (down to tens of ng/cm^2); nevertheless, they can't be exploited to determine the mean foam density since the oscillations produced by the quartz crystal are damped in the nanofoam structure and the QCM measurements are therefore unreliable.

For this reason, a technique for the measurement of thin films areal density (or mass thickness, defined as the sample density multiplied for its thickness) based on *Energy Dispersive X-ray Spectroscopy* (EDS) is used. EDS is an analytical technique used to measure the elemental composition of a sample surface [68]; it is based on the excitation of characteristic

X-rays through the ionization of atoms inner-shells by $1 - 30\ keV$ energy electrons. The electron beam which allows producing the X-rays is typically the one used in the Scanning Electron Microscope, hence the two characterization technique are often coupled (as in the case of the SEM-EDS present at Nanolab).

Exploiting EDS to measure films mass thickness, known as quantitative *Electron Probe Micro-Analysis* (EPMA), was proposed for the first time in 1960 by Sweeney, Seebold and Birks [69]. It is an appealing technique because of the non-destructive measurement, the common experimental apparatus and the high spatial resolution. The technique consists in calculating the ratio (called *k-ratio*) of the X-rays intensity of the sample elements from the ones of a homogeneous reference sample with known composition. It is then possible to relate the film mass thickness to the k-ratio through the knowledge of the distribution function of the production of X-rays in the sample depth, generally called $\phi(\rho z)$, where ρ is the sample density and z the depth [70].

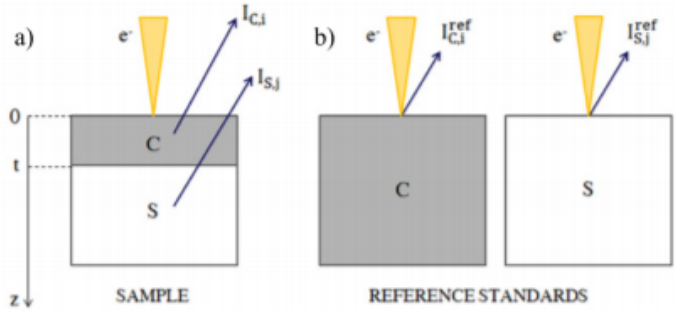

Figure 3.5: Scheme of the quantitative Electron Probe Micro-Analysis. (a) X-ray emission from a coating with thickness t and density ρ and from a substrate due to the incident electron beam. (b) X-ray emission from reference standards for the coating method and the substrate method. From [71].

In particular two method can be distinguished by the choice of the reference sample, as illustrated in Figure 3.5: the *coating method* if the reference sample has the same composition of the analysed coating or the *substrate method* in the opposite case [71]. For the first method the following equation must be numerically inverted to find the film mass thickness $\tau = \rho t$:

$$k_C = \frac{I_{C,i}}{I^{ref}_{C,i}} = \frac{\int_0^{\tau} c_{C,i}\phi_{C,i}(\rho z)\exp(-\chi_{C,i}\rho z)d(\rho z)}{\int_0^{\infty} c_{ref,i}\phi_{ref,i}(\rho z)\exp(-\chi_{ref,i}\rho z)d(\rho z)} \tag{3.1}$$

Where I is the X-ray measured intensity, c the atomic concentration, $\chi = (\mu/\rho)1/\cos(\alpha)$ is the X-rays mass attenuation factor obtained from the absorption coefficient μ and the angle α of the detector with respect to the interface of the sample; the subscripts refer to the element i and the analysed sample C or the reference sample ref. The k-ratio numerator thus represents the total amount of characteristic X-rays generated in the coating detected when the layered sample is irradiated by the EDS electrons; the denominator on the other hand represents the ones measured when a reference sample with the same composition of the film is irradiated.

The substrate method is similar and the equation to be inverted reads as:

$$k_S = \frac{I_{S,i}}{I_{S,i}^{ref}} = \frac{\exp(-\chi_{C,i}\tau)\int_{\tau}^{\infty} c_{S,i}\phi_{S,i}(\rho z)\exp[(-\chi_{S,i}(\rho z-\tau)]d(\rho z)}{\int_0^{\infty} c_{ref,i}\phi_{ref,i}(\rho z)\exp(-\chi_{ref,i}\rho z)d(\rho z)} \tag{3.2}$$

Equations 3.1 and eq:1.14 can be accurately solved if proper models for the X-ray production distribution $\phi(\rho z)$ are adopted; several semi-empirical models can be used (described in detail in References [71–75]) which fit experimental ϕ distribution starting from few sample properties as the atomic and mass number and the electron energy. The so-called RE method [76] is in particular exploited to evaluate the mass thickness τ of Carbon nanofoam films deposited onto Silicon substrates; consequently, the mean foam density is calculated by simply diving τ by the thickness measured by SEM cross section images.

It should be pointed out that the EDS method suffers from a time-consuming procedure. Firstly, the EDS measurements must be carried out at many electron energy values (both for the analysed sample and the reference one), because, as shown in Figure 3.6a, the retrieved mass thickness is energy-independent only in a limited electron energy range, called plateau. For example, in the showed case, the substrate method measurement are valid only in the $13 - 22\ keV$ range, while for the coating method case the measurements are stable in the $18 - 29\ keV$ plateau.

This time-consuming procedure is also affected by a limited accuracy, particularly when the film and the substrate have a high difference in the $\phi(\rho z)$ (as in the case of large variations in the atomic number). Indeed, the large part of the semi-empirical models for $\phi(\rho z)$ (included the one used for the foam characterization) calculates the X-ray generation distribution under the hypothesis of homogeneous sample, and does not introduce correction for the layered case.

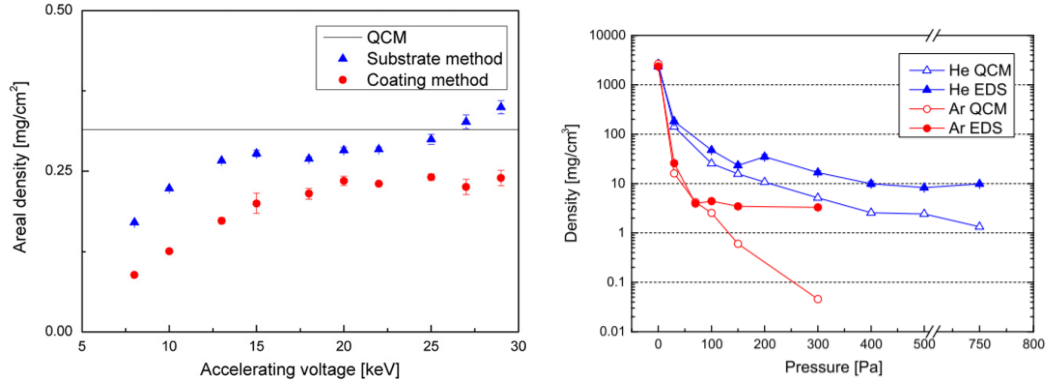

(a) **(b)**

Figure 3.6: (a) Mass thickness of a thin Ag film on Au substrate measured as a function of the electron accelerating voltage. (b) Density of Carbon nanofoams as a function of the background gas pressure in the PLD chamber calculated by the substrate method. From [71].

Despite these measurements limitations, the substrate method was effectively exploited to measure the C nanofoam density. Figure 3.6b shows these results compared the QCM measurements; it should be pointed out that for higher density values (about $30\ mg/cm^3$)

the two techniques give similar results, while at lower density the QCM returns non-realistic low values, which are explained by the above-mentioned damping of the quartz crystal oscillations.

It is possible also to observe in Figure 3.6a the differences in the deposited foams with respect to the background gas mass number; indeed, Argon gas allows producing lower (and near-critical) densities materials because it confines more efficiently the ablated species (as explained in Section 3.1).

3.3 Laser ion acceleration from nanofoam-based targets

Two ultra-intense laser ion acceleration experiments were carried out before the start of this PhD thesis work; different target and laser conditions were investigated during the experimental campaigns which are here summarized.

The first experiment was performed at the *Saclay Laser Interaction Center Facility* [54], using the *UHI100* laser, which delivers intense pulses at a central wavelength of $790\ nm$. The pulse energy ($2\ J$) was focused onto the target with $10°$ angle of incidence onto a $3.5\ \mu m$ focal spot (FWHM) with a temporal duration of $25\ fs$; which resulted in a peak intensity of $5 \cdot 10^{19}\ W/cm^2$. The experiment tested the near-critical CNF-DLT configuration (shown in Figure 3.7a) with a $7\ mg/cm^3$ mean density (corresponding to $1.2\ n_c$), measured by the EDS method, and $12\ \mu m$ thickness, measured by cross section SEM image. Maximum proton energies were measured by a Thomson Parabola spectrometer [77] in the DLT and bare target configurations in a wide intensity range $5 \cdot 10^{16-19}\ W/cm^2$ (obtained by increasing the laser spot size) with low and high contrast (10^8 and 10^{12} respectively).

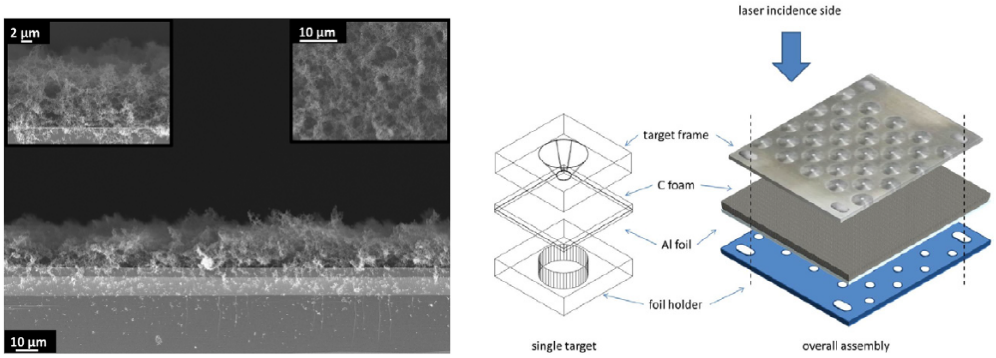

(a) **(b)**

Figure 3.7: (a) SEM image of the Carbon nanofoam used in the first experiment ($7\ m/cm^3$ density, $12\ \mu m$ thickness) [54]. (b) Schematic of the holder assembly used in the second experiment [55].

The proton energies obtained in the low contrast condition, shown in Figure 3.8, were always lower than the ones at high contrast, for both the foam-based and bare targets. This was a consequence of the detrimental effects of the target early pre-expansion due to the pre-pulse (see Section 2.1). The proton energies measured in presence of the DLT were sensibly higher than the ones of standard target at lower intensities (up to a factor of 3) and in some cases showing MeV protons in conditions were no accelerated ions were reported in

the bare target case. Nevertheless, in the high contrast condition, the highest intensity on target produced slightly higher ions energies for the standard target. This is a quite peculiar behaviour which was interpreted with the following argument: at low intensity the Carbon foam is not fully ionized during the interaction, therefore its density is below the critical threshold which enables the laser pulse to propagate and to efficiently heat the foam electrons. Conversely, when the laser intensity becomes relevant ($> 10^{18}\ W/cm^2$) the Carbon nanofoam is fully ionized and the resulting plasma is slightly over-dense, which prevents the pulse to propagate and to heat volumetric electrons. This effect is weakly mitigated in the low contrast condition, since the foam pre-expansion enables to decrease its density below the critical threshold.

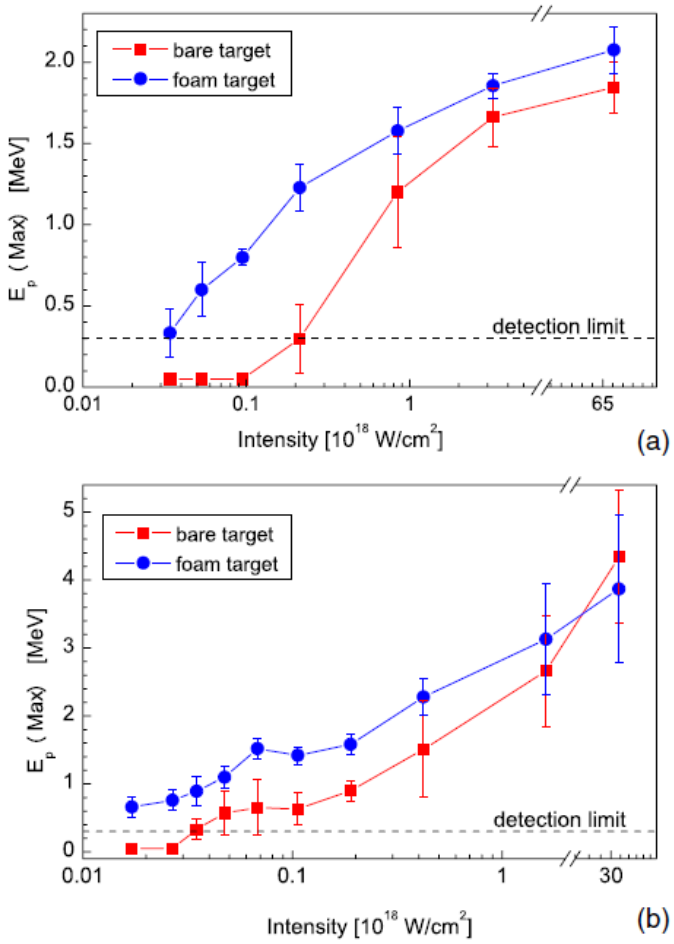

Figure 3.8: Maximum proton energies obtained for the DLT (blues dots) and standard target (red squares) in the $5 \cdot 10^{16-19}\ W/cm^2$ intensity range with low contrast (top) and high contrast condition (bottom). From [54].

The second experiment was carried out at the *Center for Relativistic Laser Science* (CoReLS), *Institute for Basic Science* (IBS) in Korea, operating a $30\ fs$, petawatt Ti:sapphire laser [26, 55]. The laser pulse energy (up to $7.4\ J$), deposited onto a $5\ \mu m$ focal spot with $30°$ angle of incidence, allowed achieving $4.5 \cdot 10^{20}\ W/cm^2$ intensity. The high temporal contrast was kept higher than 10^{11} with a double plasma mirror system. The experiment aimed at testing the foam DLT (represented in Figure 3.7b) performaces in a wide range of parameters

and conditions: linear (S and P) and circular polarization was studied for the bare and foam targets in the $1 - 4.5 \cdot 10^{20}\ W/cm^2$ intensity range (obtained by changing the pulse energy); the Carbon nanofoam was produced with 7 mg/cm^3 and thickness $8 - 12 - 18 - 36\ \mu m$; finally also a foam with a higher density ($24.5\ mg/cm^3$) with $12\ \mu m$ thickness was tested.

A Thomson Parabola spectrometer was used to detect the ion energy spectra (protons and fully ionized Carbon in particular) for the different irradiation conditions. The effect of the foam thickness and the pulse polarization on the ion maximum energies is reported in Figure 3.9a; it should be noticed that for the $0\ \mu m$ point (which corresponds to the standard target) the maximum energy was highly sensible to the pulse polarization. This was a reasonable result because the Brunel effect, as explained in Section 1.3, is an electron heating mechanism, efficient when linear P-polarization is used; moreover, the energy obtained in C-polarization was particularly low because also the $\mathbf{j} \times \mathbf{B}$ heating was damped. On the contrary, the polarization didn't affect the ions energy in the DLT case; this was a consequence of the volumetric electrons heating taking place in the near-critical layer, which is less sensible to the pulse polarization.

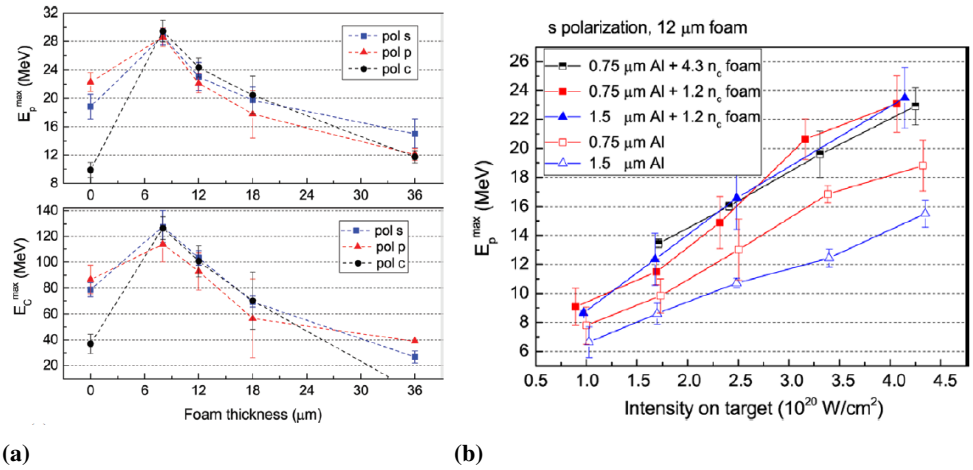

Figure 3.9: (a) Maximum proton (top) and fully ionized Carbon ions (bottom) energies as a function of the DLT foam thickness (0 stands for standard target), for different pulse polarization conditions. (b) Maximum proton energy for variable standard target (open markers) and DLT parameters (full markers). From [55]

It should be also observed that the nanofoam thickness is a crucial parameter in the DLT, since for the $8\ \mu m$ case the ions energy was higher with respect to the standard target, in P-polarization, for a factor of about 1.3; while for higher thickness the maximum energy was comparable or even lower than the reference target.

Finally, Figure 3.9b shows the results obtained by different target properties in the $1 - 4.5 \cdot 10^{20}\ W/cm^2$ intensity range. The Aluminum substrate thickness was changed from $0.75\ \mu m$ to $1.5\ \mu m$, showing worse performances in the thicker case, which is consistent with the arguments explained in Section 2.1. Instead, proton energies obtained with DLTs were comparable for different substrate thickness and even for different mean density values ($1.2\ n_c$ and $4.3\ n_c$). Here the over-critical foam performed well, in contrast to what observed in the first experiment; this was a consequence of the relativistic effects of the ultra-high

pulse intensity. Indeed the used intensity ($a_0 = 16$) forces electrons to relativistic motion with a Lorentz factor approximated by $\gamma = \sqrt{1 + a_0^2/2} \sim 11$; as a consequence the relativistic critical density increases by an order of magnitude and the classically over-dense foam becomes transparent.

All these observations demonstrated that the foam-based DLT can be exploited to enhance the ion acceleration phenomenon; nevertheless, a careful attention must be given to the optimization of the near-critical layer, in particular in the choice of the mean density, which must be relativistically under-dense, and in the choice of the thickness. The two reported experiments highlighted also that a deeper comprehension of acceleration process with the DLT is needed (for example to determine in a theoretical way the optimal foam parameters) and that the performances could be still increased.

3.4 Thesis motivations, goals and personal contribution

Before the start of this PhD thesis, Carbon nanofoam has been successfully used to enhance the laser-driven ion acceleration mechanism, through the near-critical Double Layer Target solution.

Nevertheless, several questions are still open and deserve a deeper investigation. Firstly, it is not completely clear how does the near-critical layer enhance the ions energy (see Section 2.2); Part II is dedicated to answer this question exploiting the numerical simulations tool. An analytical model, validated and tuned through Particle-In-Cell simulations, is proposed in Chapter 4 to describe, in a minimal fashion and under ideal conditions, the laser-DLT interaction, the volumetric hot electrons heating and the ions acceleration energy. The presented model is solved to determine the optimal theoretical parameters (thickness and density) of the near-critical layer and also the highest theoretical ion energy enhancement. Chapter 5 is aimed at analysing the acceleration phenomenon in more realistic conditions, through simulations with a near-critical nanostructured plasma, resembling the CNF.

The tasks that I personally carried out to accomplish the Part II goals were the performing of the PIC simulations and the development of the analytical model of Chapter 4. While in Chapter 5, I developed the nanostructure model used in the realistic PIC simulations (performed by Dr. Luca Fedeli and Ms. Arianna Formenti) and contributed to their processing and analysis.

Secondly, the ns-PLD has been introduced as a peculiar technique for the production of ultra-low density C nanofoam (see Section 3.1), which is characterized by the SEM and the EDS methods (see Section 3.2). As yet introduced, the latter technique suffers from some methodological and accuracy limitations, while the foam deposition process is still largely unexplored. Part III deals with these points, starting from the description of an improved technique for the high-accuracy film mass thickness EDS-based measurements (Chapter 6). The new technique and the SEM are thus exploited to study the foam growth mechanism; Chapter 7 goal is to present this work and a CNF aggregation model, which has the main outcome to determine the main material features and to introduce new methods to control

the nanofoam density. The CNF deposition is further studied by an innovative PLD technique, developed for this purpose, which uses ultra-short laser pulses: the Pulsed Femtosecond Laser Deposition (fs-PLD). The last chapter of Part III, Chapter 8, is devoted to the description of the first experimental activities with the fs-PLD, with a particular emphasis on the comparison to the standard ns-PLD and on the promising features of the deposited nanofoams.

My personal tasks in Part III consisted in the development of the EDS-based technique (Chapter 6) and in its validation with experimental benchmarks realized by Dr. David Dellasega and Dr. Alessandro Maffini, and characterized with the X-Ray Reflectivity technique by Dr. Alessio Lamperti. While in Chapter 7 I produced, characterized and developed the aggregation model in collaboration with Dr. Alessandro Maffini. I personally carried out all the first experimental activities with the fs-PLD described in Chapter 8.

Finally, because the performed laser acceleration experiments didn't find a clear optimal condition for the highest ion energy enhancement, an additional experiment is carried out and described in Part IV. Chapter 9 is aimed at describing the DLT production methodology and the related manufacturing issues; while Chapter 10 presents the acceleration experiment, carried out in collaboration with an international facility. In particular, this chapter aims at showing an ion energy enhancement higher than the previously reported ones, and to give an interpretation of the results at the light of the theoretical framework introduced in Part II.

This last Part was the outcome of a collaboration between the ENSURE group and the Helmoltz Zentrum Dresden-Russeldorf laser acceleration group. My tasks for the experiment fulfilment consisted in the production and characterization of the nanofoam-based DLTs and the relative manufacturing issues, in collaboration with Dr. Alessandro Maffini and Dr. David Dellasega (Chapter 9). In addition, I participated to the laser acceleration experiment and helped to data collection and analysis; while I personally developed all the result interpretations presented in the last section of Chapter 10.

Part II

Theoretical investigation on ion acceleration from DLTs

CHAPTER 4

Ion acceleration with uniform near-critical plasmas

This chapter describes the numerical and theoretical work about the laser driven ion acceleration phenomenon when the near-critical Double-Layer Target is used; in particular, in this chapter ideal conditions are considered, namely a uniform near-critical layer and laser normal incidence. Section 4.1 introduces the *Particle-In-Cell* (PIC) numerical tool and summarizes the simulations carried out for this work. In Section 4.2, a theoretical model for the description of the laser-DLT interaction and ion acceleration is described and optimal near-critical layer parameters are estimated.

4.1 Parametric Particle-In-Cell scan

The plasma behaviour under the great fields of ultra-intense lasers is characterized by thermal non-equilibrium (i.e. the species velocity distribution can't be properly described by Maxwellians) and physical quantities such as temperature and pressure are not defined. In this regime a plasma kinetic description must be adopted by solving the Vlasov equation or the Boltzmann equation (when the collisions have a relevant role) [78]. Nevertheless, these equations are impossible to solve in an analytical way for the laser-plasma and ion acceleration framework due to their high complexity; for this reason numerical methods are exploited, in particular *Particle-In-Cell* (PIC) simulations are a standard tool for the study of the laser-plasma interaction at time scales comparable to the laser cycle duration.

PIC simulations approach describes the plasma as a collection of particles (e.g. electrons and ions) moving under the influence of external electric and magnetic fields (laser) and internal ones (generated by the charges motion) [79, 80]. The PIC method roughly consists in the following steps (see Figure 4.1): the relativistic equations of motion are integrated numerically in a time step Δt for all the plasma particles, then the positions and momenta are used to calculate the charge density ρ and the density current $\mathbf{j}$ over a spatial grid with

Δx discretization; finally, the electric and magnetic fields ($\mathbf{E}$ and $\mathbf{B}$) are calculated over the grid by the Maxwell equations, which are used to calculate the Lorentz forces acting onto the particles in the following numerical cycle.

Since real systems are featured by an extremely large number of particles, the electrons and ions are approximated by so-called *macro-particles* (also referred as *quasi-particles* or *super-particles*); these computational particles represent a large number of real ones (e.g. millions of electrons or ions). This rescaling is allowed because the Lorentz force depends on the charge-to-mass ratio, therefore the macro-particle follows the same trajectory of a real one. The number of real particles contained in a single macro-particle must be chosen in order that sufficient statistic is collected on the phase space. A thumb rule can be adopted, in particular when a PIC simulation is initialized: the number of macro-particles in each grid cell must be higher or equal than the ratio n_e/n_c. In this way densities lower than the critical one can be properly resolved even when a grid cell is occupied by only one macro-electron.

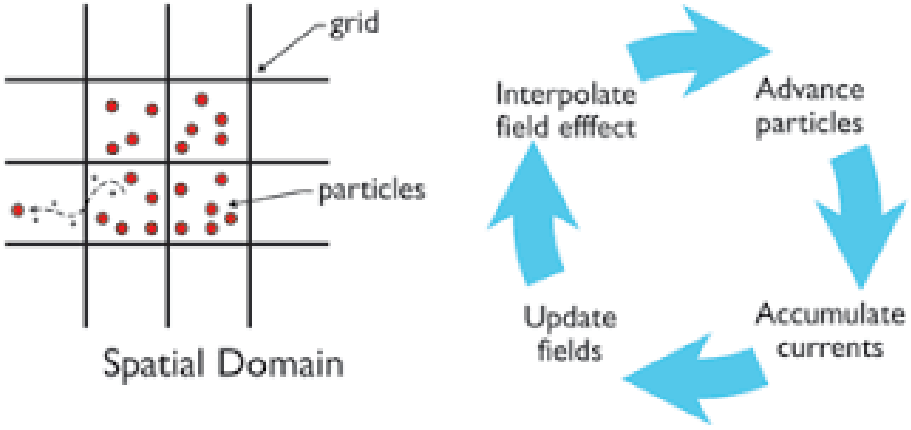

Figure 4.1: Scheme of the PIC simulation method; on the left the spatial grid and the macro-particles are represented, while on the right the PIC temporal evolution is illustrated.

The PIC numerical method must satisfy some requirements for the proper description of the plasma physics and to assure the numerical stability. The *Courant-Friedrichs-Lewy* (CFL) condition states that an explicit numerical method is stable when $\Delta t < \Delta x/c$ (in one dimension) [81]; in addition, the spatial discretization should be able to resolve the more important plasma length scales, namely the electrons skin depth $\lambda_{sd} = c/\omega_{pe}e$ and Debye length $\lambda_D = \sqrt{T_e/4\pi n_e e^2}$ while the temporal step should be chosen to describe phenomena faster than the inverse of the plasma frequency $\Delta t < 1/\omega_{pe}$. It should be pointed out that, for a relativistic plasma, all these requirements can be simplified: indeed, the ratio $\lambda_{sd}/\lambda_D = \sqrt{\gamma m_e c^2/T_e}$ tends to $\sqrt{\gamma/(\gamma-1)} \to 1$ when relativistic effects become relevant due to the high intensity ($a_0 > 2 \to \gamma \sim a_0/\mathcal{P}$, see Chapter 1) [82]. For this reason the spatial discretization condition is satisfied when $\Delta x < \lambda_{sd}$ and it can be expressed as a function of the laser wavelength λ and the electrons density:

$$\frac{\lambda}{\Delta x} > 2\pi\sqrt{\frac{n_e}{\gamma n_c}} \tag{4.1}$$

Where the latter ratio is commonly referred as the *points per lambda* parameter (ppl) or also *points per wavelength* (ppw). On the other hand, the time discretization constrains are fulfilled if the above-mentioned CFL condition is respected, namely:

$$\Delta t < \frac{\Delta x}{c} < \frac{\lambda_{sd}}{c} = \frac{1}{\omega_{pe}} \tag{4.2}$$

Note that in Equations 4.1 and 4.2 only the electron plasma parameters are used, because the more crucial laser-plasma interaction phenomena are mediated only by these particles, which are lighter that the ions, evolving in longer time scales. With the same argument, it is possible to justify the general use of fewer macro-particles for the ions with respect to electrons in the PIC simulations.

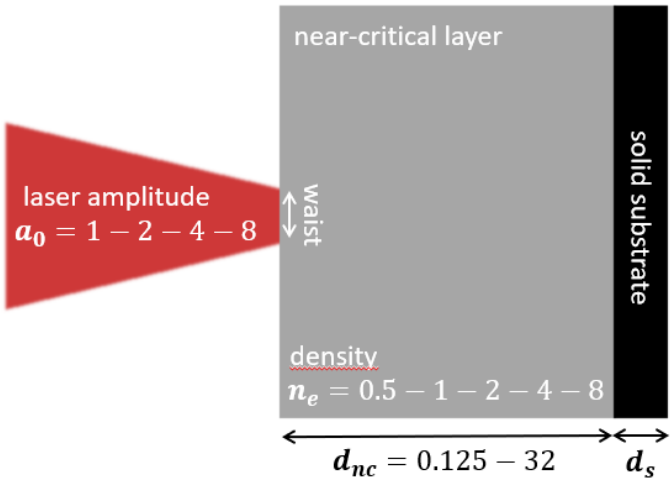

Figure 4.2: Scheme of the PIC simulations parametric scan. The laser, with variable intensity, is focused onto the DLT with uniform near-critical layer, with variable density and thickness (given in normalized units).

In this PhD work, several PIC simulations are performed with the open-source, massively parallel code Piccante [83], to study the laser-DLT interaction and the consequent ion acceleration. As illustrated in Figure 4.2, a parametric scan is carried out in two dimensions with variable laser intensity equal to $a_0 = 1 - 2 - 4 - 8$ at fixed normal incidence and linear P-polarization; also the near-critical layer properties are changed, in particular the density values are $n_e = 0.5 - 1 - 2 - 4 - 8\ n_c$ and the thickness varies in the range $d_{nc} = 0.125 - 32\ \lambda$ in order to have a mass thickness $\mu_{nc} = d_{nc} n_e$ equal to $1 - 2 - 4 - 8 - 16\ n_c \lambda$.

The laser pulse has a cos^2 temporal profile (to approximate an ideal high contrast pulse) and a Gaussian transverse profile and it is focused at the vacuum-plasma boundary. The fields temporal duration is characterized by a *Full-Width-Half-Maximum* (FWHM) of $15\ \lambda/c$. These parameters, if scaled to Ti:Sapphire lasers, correspond to a $28.5\ fs$ pulse, providing a peak intensity in the range $2.2{\cdot}10^{18}\ W/cm^2 < I < 1.4{\cdot}10^{20}\ W/cm^2$ which is found in small-medium scale ultra-intense laser facilities (see Chapter 1). A $4\ \lambda$ waist and a $200\lambda \times 120\lambda$ box are used, with a resolution of 64 ppl which respect the condition of Equation 4.1. 10 macro-electrons per cell are used for the near-critical layer and 64 macro-electrons are used for the

solid density layer, with density fixed to $64\ n_c$ and thickness $0.5\ \lambda$. In all the simulated cases the plasma is fully pre-ionized and the the charge/mass ratio of the ions is 0.5 (e.g. C^{6+}); the electron population is initialized with a small temperature (few eVs) to avoid numerical artefacts.

The first analysis on these simulations consists in the calculation of the accelerated maximum proton energy for different intensity, density and thickness; it should be remarked that in 2D simulations the ions energy does not reach a saturation value with time, yet it continues to increase with a logarithmic trend [84]. This is an effect of the reduced dimensionality of the simulations, since in 2D the laser has an infinite width over one dimension and the macro-particles represent infinite cylinders in real space. In addition, the expanding sheath electrons have a $1/r$ density decrease trend, instead of the $1/r^2$ one of the real 3D space (with r the distance from the rear surface of the target). Thus, a widely accepted way to solve this problem is to fix the simulation time and to compare the final proton energies for the different simulations without the necessity of considering the absolute energy values as realistic (indeed 2D simulations generally overestimate the accelerated proton energies).

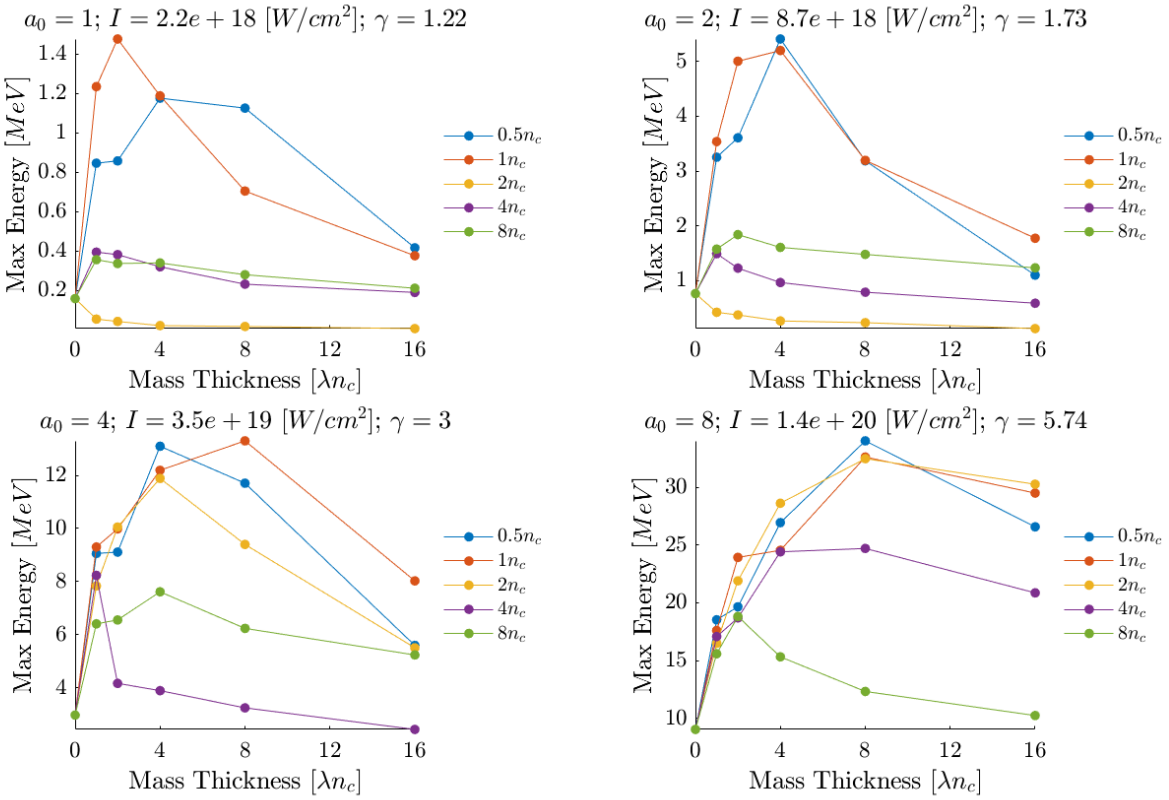

Figure 4.3: Maximum proton energies obtained from the PIC simulations parametric scan represented as a function of the near-critical layer mass thickness $\mu_{nc} = d_{nc}n_e$.

The results, summarized in Figure 4.3, bring to several interesting observations. Firstly, it should be noticed that the DLT does not enhance the proton energy in every condition, yet in some cases it is detrimental for the ions acceleration. In particular, it appears that the threshold for this behaviour is given by the relativistic transparency factor $\bar{n} = n_e/\gamma n_c$:

when $\bar{n} < 1$, which means that the normalized density is lower than γ (reported in the graph titles), the near-critical layer is transparent and the DLT is able to improve the acceleration process with high ion energy enhancement factors (defined as the ratio of proton energy with DLT to the one with standard target $\epsilon_p^{max}/\epsilon_{p,std\ targ}^{max}$), up to almost one order of magnitude.

Conversely, when $\bar{n} > 1$ a particular phenomenon occurs and a sudden detrimental effect is seen, while for increasing $\bar{n}$ the proton energy starts to grow again (without reaching the high enhancement factors of the $\bar{n} < 1$ case).

In the *transparent regime* ($\bar{n} < 1$) an optimal value of the near-critical layer mass thickness can be observed and it appears that, at fixed intensity, this optimal μ_{nc} is similar for different densities. In addition, it should be observed that the best mass thickness for $a_0 = 1$ is about $2\ \lambda n_c$, while for $a_0 = 8$ its value clearly grows to about $8\ \lambda n_c$, with a monotonic increase for the intermediate intensities. The more intuitive explanation of this result is that for high a_0 the near-critical layer becomes more and more transparent and the laser is able to propagate more inside it and generate a larger number of hot electrons.

In order to shed a light onto this effect, other dedicated simulations are performed to study the propagation of the laser pulse into a semi-infinite near-critical plasma. They consist in 2D simulations with a uniform plasma, a $4\ \lambda$ waist and a $100\lambda \times 60\lambda$ box, with a resolution of 20 points per wavelength and 9 macro-electrons per cell. The density is varied in the values $0.5 - 1 - 2\ n_c$ and the laser amplitude in the range $a_0 = 2 - 4 - 8$.

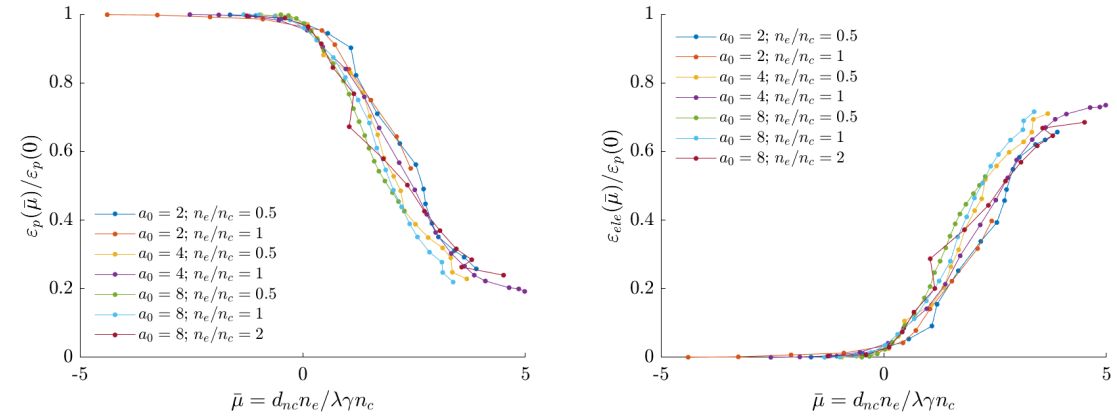

(a) **(b)**

Figure 4.4: (a) Normalized laser pulse energy along the mass propagation length in a semi-infinite uniform near critical layer (normalized to $\lambda\gamma n_c$). (b) Normalized total hot electrons energy along the mass propagation length in a semi-infinite uniform near critical layer (normalized to $\lambda\gamma n_c$).

The laser pulse energy along the propagation inside the plasma is recorded (see Figure 4.4a) as well as the total hot electrons energy (see Figure 4.4b). The more interesting feature of the analysed data is that a proper normalization of the variables enables to collapse the points to a self-similar curve. The ordinate (laser/electrons energy) is normalized in an intuitive manner to the initial pulse energy; the abscissa instead is normalized in a more complex way. Owing to the fact that an optimal mass thickness is observed for the proton energies, the pulse propagation length is multiplied by the electron density to give a mass

propagation length $x_{nc}n_e$; both the quantities are normalized to their natural units, namely λ for the length and n_c for the density. Nevertheless, it is also considered the effect of the relativistic transparency including γ in the normalization factor, hence normalizing the density to the relativistic critical density. As a result the abscissa is expressed by the *relativistic normalized mass thickness* $\bar{\mu} = x_{nc}n_e/\lambda\gamma n_c$. It seems quite evident that both the laser pulse energy and the total hot electrons energy follow a self-similar trend with respect to this relativistically normalized path length, confirming that for higher intensity simulations the near-critical layer is more transparent to the incoming radiation; it appears also that the sum of the two energies approaches one, which can be interpreted as the pulse propagating into the plasma loses energy only in heating fast electrons. Thus the ions population does not acquire high energy and they can be considered almost immobile within the analysed time scales ($\sim 10s\ fs$).

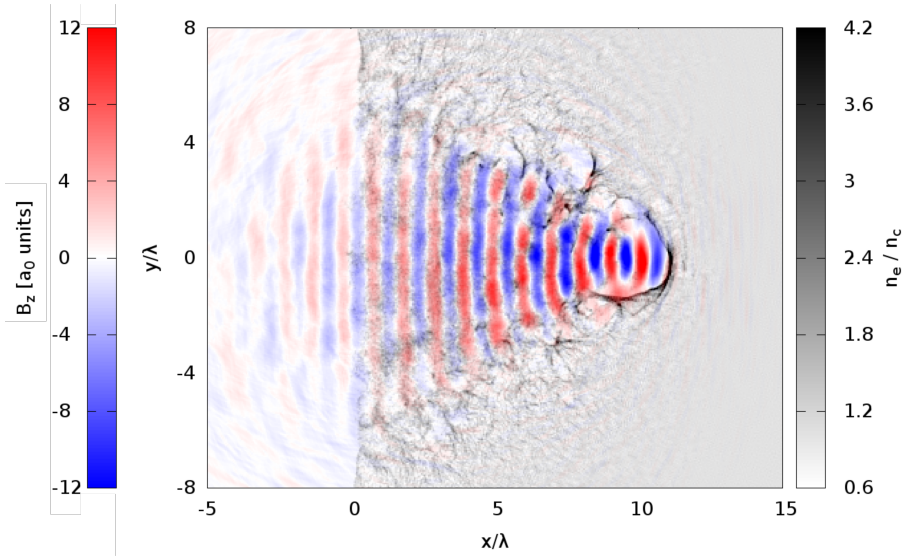

Figure 4.5: The figure shows the transverse component of the magnetic field of an ultra-intense laser with $a_0 = 8$, propagating inside a uniform near-critical plasma with $n_e/n_c = 1$ ($\bar{n} = 0.17$) at the time 20 λ/c after the beginning of the interaction; the pulse self focusing should be noticed.

The semi-infinite plasma simulations were also used to study a peculiar phenomenon widely observed in the PIC simulation with uniform slightly under-critical plasmas: the *self-focusing* (SF). The self-focusing consists in the plasma-driven focalisation of the incoming radiation due to ponderomotive and relativistic effects (see Figure 4.5); as introduced in Chapter 1, the ponderomotive force pushes the electrons outside the higher intensity regions and, at the same time, the peak fields move the electrons to ultra-relativistic energies. Both the effects cause the plasma to form a channel with radially dependent refractive index, in particular with larger values inside the channel [85]. This behaviour is similar to a gradient index lens [86] which has the capability to focalise a laser pulse without the need of a rounded lens and the property to reduce the aberrations typical of the spherical lenses. The relativistic self-focusing was studied in several experimental and numerical works [47, 49, 50, 57] and in some cases it was indicated as the more important effect in the ions energy enhancement obtained with near-critical DLTs.

The quantitative analysis of the self-focusing in the performed 2D simulations evidences that also this process has a self-similar behaviour. The waist along the path is represented in Figure 4.6a (calculated as the $1/e$ peak intensity threshold), as a function of the *relativistic path length*, defined as $\bar{x} = x\sqrt{\bar{n}}/\lambda$. This varible was proposed in some work [49,87] and its self-similarity is justified by theoretical reasons [88]. Due to the initial waist reduction with respect to $\bar{x}$, the laser intensity increases accordingly; Figure 4.6b shows the pulse amplitude amplification (defined as $a(\bar{x})/a_0$) as a function of the relativistic pulse propagation length, which is denoted again by a self-similar trend.

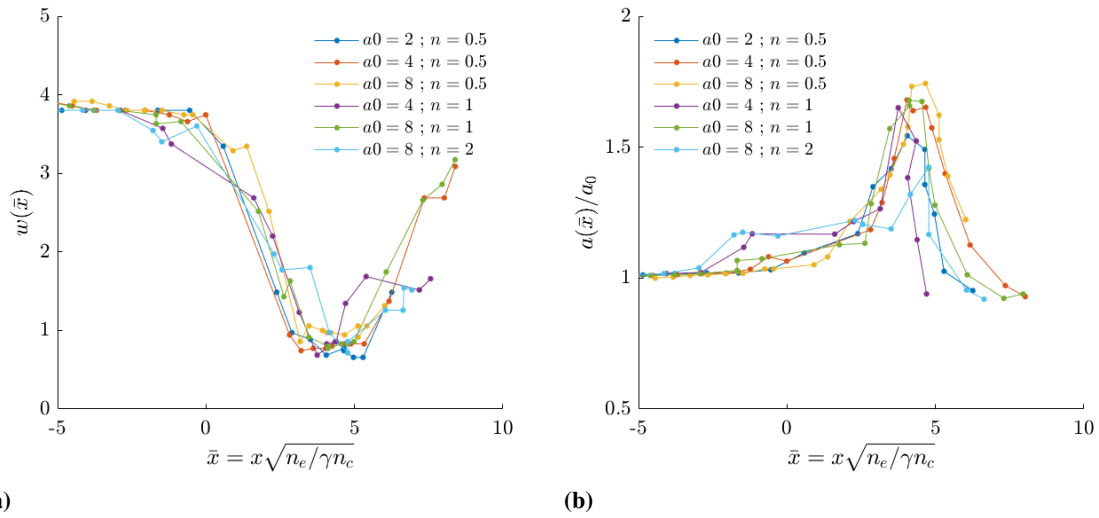

Figure 4.6: Figure (a) shows the laser waist and Figure (b) the pulse amplitude amplification inside a uniform plasma at different pulse relativistic path length values.

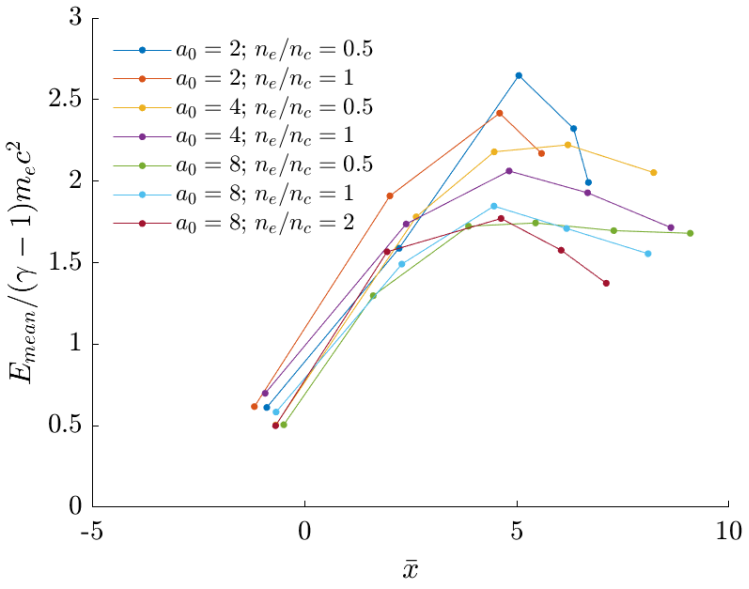

Figure 4.7: It is shown the near-critical layer hot electron mean energy for different laser propagation length.

Finally the hot electron mean energy E_{mean}, which is a good estimation of the electrons temperature if the distribution is exponential, is calculated and represented in Figure 4.7 as

a function of $\bar{x}$ and normalized to the ponderomotive scaling $(\gamma - 1)m_e c^2$. It is possible to observe that the electrons mean energy increases with the near-critical layer thickness due to SF; in addition, the maximum temperature is obtained when the lowest waist and the highest amplitude amplification are reached. This is a crucial result, since TNSA analytical models require the knowledge of the hot electrons temperature to estimate the accelerated ions maximum energy. Therefore, a model which estimates the electron temperatures for different near-critical layer properties is capable to calculate the maximum proton energies; for this reason in the next Section a model which tries to describe these observation and scalings is presented.

4.2 A theoretical model for the laser-DLT interaction and ion acceleration

It should be remarked that the interaction of an ultra-intense laser pulse with a near-critical plasma is a complex phenomenon, characterized by a strong coupling between the electromagnetic fields and the plasma; indeed, when the transparency factor is lower than one, $\bar{n} = n_e/\gamma_0 n_c < 1$, the laser can propagate inside the plasma and drills a channel which induces relativistic-ponderomotive SF. In this process the laser generates volumetric hot electrons (see Figure 4.8b), that have a higher number of particles and a higher mean energy with respect to the solid target superficial ones. Furthermore, the strong currents in the channel generate a high magnetic field which confine the electrons in a directional motion and finally, part of the electrons are pushed by the laser at the boundary of the channel inducing a temporal shaping of the pulse which undergoes into a contrast increase and a duration reduction.

In this complex framework, only the essential mechanisms for a sufficiently accurate description of the interaction are considered and the analysis is restricted to the simple conditions adopted in the simulations of the previous Section (depicted in Figure 4.8d): normal incidence, P-polarization and homogeneous plasma. The validity of the model outside this ideal framework will be discussed in the next chapter. Owing to the observations of the laser and electron energy trends, it is also assumed that the laser pulse duration is short enough that the plasma ions are almost motionless during the interaction.

4.2.1 Laser-DLT interaction: pulse propagation and electron heating

One of the most important effects of the propagation of a ultra-intense pulse in a near-critical plasma is the above-mentioned SF; this phenomenon has been studied by some works, and a simple relation has been proposed for the minimum laser waist w_m which the laser can achieve within this regime [49, 87], namely:

$$w_m = \frac{\lambda}{\pi\sqrt{\bar{n}}} \tag{4.3}$$

In order to describe the laser waist evolution along the pulse propagation length x inside

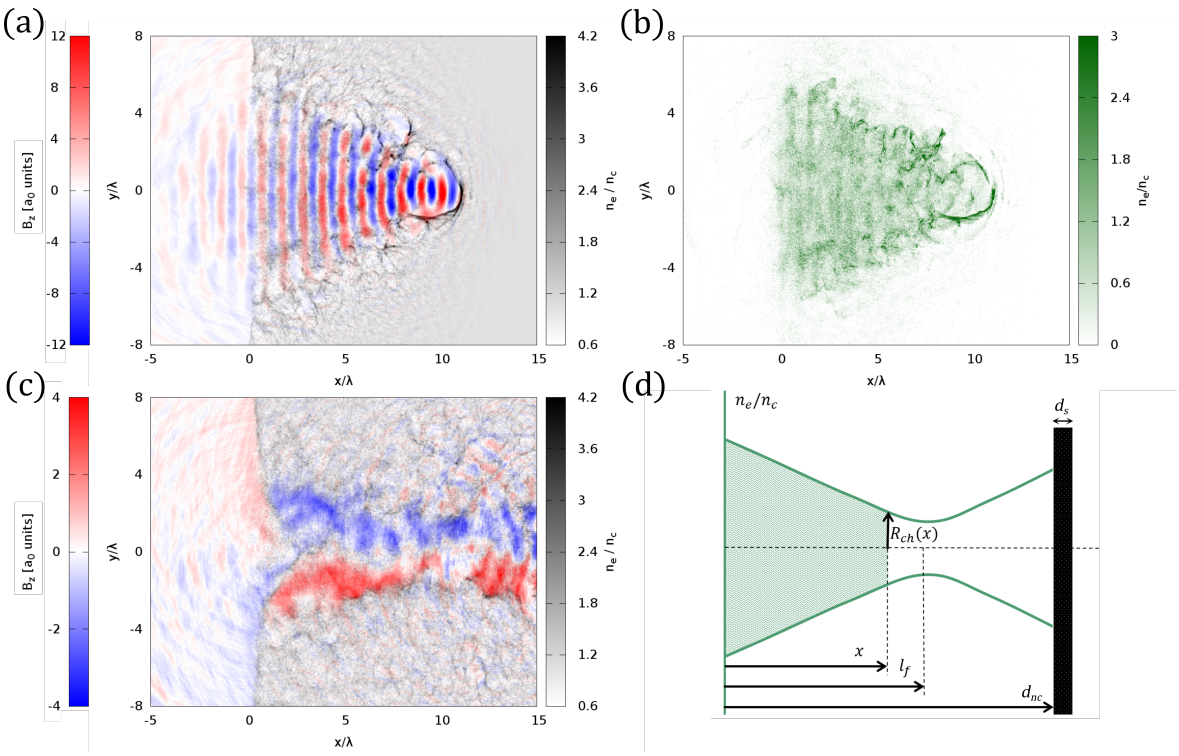

Figure 4.8: Figure (a) shows the transverse component of the magnetic field of an ultra-intense laser with $a_0 = 8$ amplitude, propagating inside a uniform near-critical plasma with $n_e/n_c = 1$ ($\bar{n} = 0.17$) at the time 20 λ/c after the beginning of the interaction; the pulse self-focusing should be noticed. Figure (b) shows the hot electrons density (with energy higher then $m_e c^2$) for the latter case. Figure (c) shows the transverse magnetic field for the latter case at the time 36 λ/c after the beginning of the interaction; the magnetization of the channel should be noticed. Figure (d) shows the scheme of the theoretical model described in this Section.

the plasma, a thin-lens approximation is proposed:

$$w(x) = w_m \sqrt{1 + \left(\frac{x - l_f}{x_R}\right)^2} \tag{4.4}$$

$$x_R = \frac{\pi}{\lambda} w_m^2 \tag{4.5}$$

$$l_f = \sqrt{x_R \left(\frac{\pi}{\lambda} w_0^2 - x_R\right)} \tag{4.6}$$

Where w_0 is the initial laser pulse waist, x_R the Rayleigh length, and l_f the SF focal length, namely the position at which the laser is more strongly focused in the plasma. This kind of description is highly approximative, because the plasma more likely acts as a gradient-index lens instead of a rounded thin lens; nevertheless, making reference to Figure 4.9, we observe a good agreement between the waist described by Equation 4.4 and the waist measured in 2D PIC simulations, within pulse propagation length in the order of the SF focal length ($x \lesssim 2l_f$). At longer distances complex instabilities are induced, such as filamentation, which distort the laser ideal gaussian shape.

It is worth mentioning that $l_f \sim w_0/\sqrt{\bar{n}}$ when $w_0 \gg w_m$ (which is a reasonable approximation), thus the SF focal length is invariant with respect to the relativistically normalized

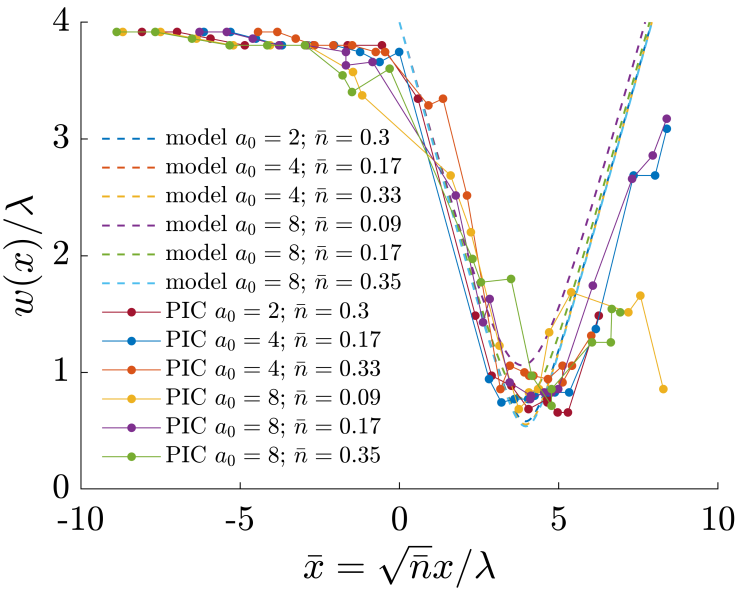

Figure 4.9

Figure 4.10: The figure shows the laser waist evolution calculated from 2D PIC simulation of a pulse propagating inside a uniform plasma at different normalized propagation length. The full lines and points refer to 2D PIC simulations with intensity ranging in $a_0 = 2 - 8$ and plasma density in $n_e/n_c = 0.5 - 2$, while the broken lines refer to the proposed model.

space variable $\bar{x} = \sqrt{\bar{n}}x/\lambda$ (defined in the previous Section), as can be seen in the approximate expression of the Equation 4.4:

$$\frac{w(\bar{x})}{\lambda} \sim \sqrt{\frac{1}{\pi^2 \bar{n}} + \left(\bar{x} - \frac{w_0}{\lambda}\right)^2} \tag{4.7}$$

This approximate expression emphasizes that for constant transparency factor, the waist evolution inside the plasma is self-similar also for different values of intensities and it depends only onto the $\bar{x}$ variable and the w_0 parameter. Consequently, we expect that the pulse, propagating inside the channel, loses part of the energy to heat the electrons and it increases its intensity due to SF, according to the following equation for the normalized amplitude (in 2D geometry):

$$\bar{a}(x) = \frac{a(x)}{a_0} = \sqrt{\frac{\bar{\varepsilon}_p(x)}{w(x)/w_0}} \tag{4.8}$$

Where $\bar{a}\,(x)$ is defined as the normalized amplification factor and $\bar{\varepsilon}_p\,(x) = \varepsilon_p(x)/\varepsilon_{p0}$ as the normalized laser energy, with ε_{p0} the initial pulse energy. The pulse temporal shaping effects are neglected, because the temporal amplitude amplification has a minor importance with respect to the SF; indeed, the temporal duration can reduce up to a factor of 2 [49], while the SF waist can reach the diffraction limit, implicating a waist reduction which can easily exceed a factor of 10. In order to calculate the laser energy loss in the propagation it can be assumed that all the electrons inside the channel are heated by the pulse with the

well-known ponderomotive scaling described in Section 1.2:

$$d\varepsilon_p = -n_e C_{nc,2D} \left(\gamma\left(x\right) - 1\right) m_e c^2 2R_{ch}(x) dx \tag{4.9}$$

Where R_{ch} is the plasma channel radius, $\gamma\left(x\right) = \sqrt{1 + a\left(x\right)^2/2}$ is the Lorentz factor in P-polarization at a given pulse propagation length, while $C_{nc,2D}$ is a constant which allows to estimate the mean electron energy as $C_{nc,2D}\left(\gamma\left(x\right) - 1\right) m_e c^2$ (as introduced in Section 1.2); thus it takes into account all the complex details of the energetic electrons acceleration in the interaction. It should be remarked that, due to the magnetization of the plasma channel, the hot electrons tend to co-move with the laser and will maintain a directional motion. Considering the laser pulse distribution as an ideal gaussian, both in time and space, its initial linear energy density in 2D geometry can be expressed as $\varepsilon_{p0} = m_e c^2 n_c a_0^2 w_0 \tau c \pi/4$ [89], where τ is the fields temporal duration ($1/e$ for the fields) and c the light speed; the FWHM temporal duration and the focal spot over the intensity (which are the parameters generally indicated in the experiments) can be retrieved by $\tau_{FWHM}^I = \sqrt{2\log(2)}\tau$ and $w_{FWHM}^I = \sqrt{2\log(2)} w_0$. Then, the normalized energy loss assume the following form:

$$\frac{\partial \bar{\varepsilon}_p\left(x\right)}{\partial x} = -\frac{4 n_e C_{nc,2D}\left(\gamma\left(x\right) - 1\right) 2R_{ch}\left(x\right)}{n_c a_0^2 \pi w_0 \tau c} = -\frac{8 C_{nc,2D} r_c}{\pi \tau c} \frac{n_e}{a_0 n_c} \frac{\gamma\left(x\right) - 1}{a_0} \frac{w\left(x\right)}{w_0} \tag{4.10}$$

Where we introduced the ratio of the plasma channel radius to the waist $r_c = R_{ch}(x)/\, w\left(x\right)$. It should be observed that, at increasing pulse propagation length x, the laser waist decreases while the $\left(\gamma\left(x\right) - 1\right)$ factor increases accordingly; then the two factors tend to cancel each other out and the energy loss roughly depends onto $n_e/a_0 n_c$ which tends to the transparency factor $\bar{n}$ at high intensity. As a consequence, we expect that the normalized energy will be almost invariant with respect to the normalized mass length $\bar{\mu} = \bar{n} x/\lambda$, which is exactly the self-similar curve observed in Section 4.1 for the laser and hot electrons energy evolution.

Equation 4.10 is a differential equation dependent on the laser waist equation (Equation 4.4) and can be numerically solved, coupled with Equation 4.8, with a finite difference method. In order to do so, the initial condition $\bar{\varepsilon}_p\left(0\right)$ must be imposed. When $\bar{n}$ is low, a reasonable approximation could be to impose it to 1, nevertheless if we consider also the cases where the density is near the relativistic critical threshold we have to consider that part of the laser pulse can be reflected. It is well known that an electromagnetic wave is reflected by an overcritical interface while it is transmitted in an under-critical medium. In the near-critical case a mixed condition is verified, since a plasma can be at the same time relativistically under-critical and transparent ($n_e/\gamma_0 n_c < 1$), but classically overcritical and thus opaque ($n_e/n_c > 1$). Indeed, if we consider a gaussian pulse amplitude envelope in 2D, $a\left(t, y\right) = a_0 e^{-t^2/\tau^2} e^{-y^2/w_0^2}$, the laser tails give to electrons a not relativistic quiver motion and they are reflected by the overcritical plasma. On the contrary, near the fields peak the electron motion is relativistic and the plasma is transparent. Making reference to Figure 4.11a, to calculate the transmittance we firstly find the threshold of this process given by the condition $n_e/\gamma\left(t, y\right) n_c = 1$. Roughly approximating the Lorentz factor as

$\gamma(t,y) \sim a(t,y)/\sqrt{2}$, the following relation can be obtained:

$$\frac{n_e}{\gamma_0 n_c} = \frac{\gamma(t,y)}{\gamma_0} = e^{-\frac{t^2}{\tau^2}} e^{-\frac{y^2}{w_0^2}} \tag{4.11}$$

With a change of variables ($t/\tau = \xi$ and $y/w_0 = \chi$) and taking the natural logarithm of the latter equation we obtain:

$$\xi^2 + \chi^2 = -\log(\bar{n}) \tag{4.12}$$

To calculate the fraction of energy transmitted we use the more convenient polar coordinates $r^2 = \xi^2 + \chi^2$, since Equation 4.13 represents a circumference, and we integrate the electromagnetic energy density from $r = 0$ to the transparency threshold $r = -\log(\bar{n})$:

$$\mathcal{T}_{2D} = \frac{\int_0^{\sqrt{-log(\bar{n})}} r e^{-2r^2} dr}{\int_0^{+\infty} r e^{-2r^2} dr} = 1 - \bar{n}^2 \tag{4.13}$$

This relation is in agreement with the trend given by 2D PIC simulation as shown in Figure 4.11b even if it underestimates the absolute values at high $\bar{n}$, when a_0 is low.

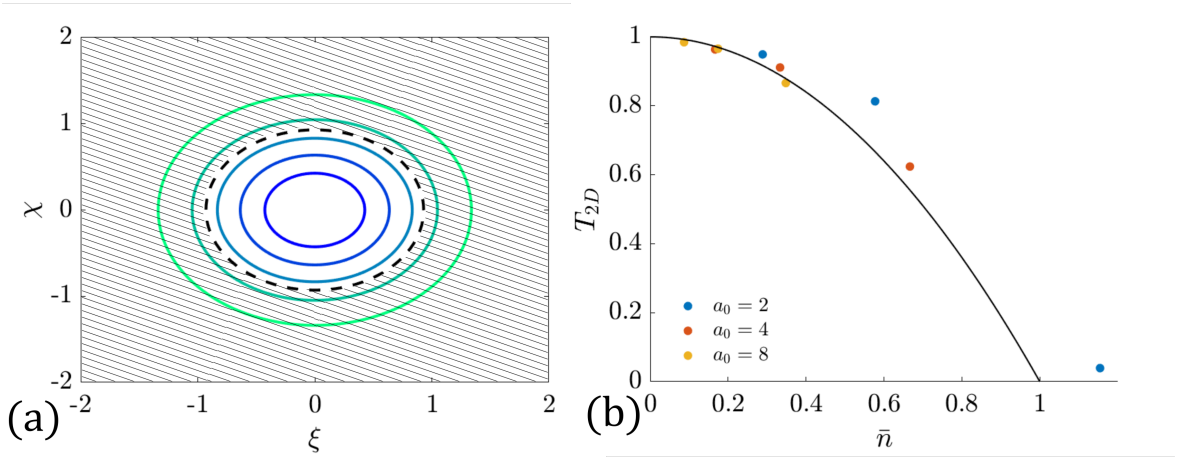

Figure 4.11: Figure (a) shows the level plot of the gaussian amplitude in normalized units. The dashed black line marks the threshold obtained from Equation 4.13; the hatched part of the plot represents the tails of the pulse which are reflected by the overcritical plasma. Figure (b) represents the transmitted energy obtained from Equation 4.13 (full line) and from 2D PIC simulations (points).

Once the initial condition is set, Equations 4.8 and 4.10 are numerically solved and the pulse energy loss during the propagation and the relative amplitude can be compared with the PIC simulation results, in Figure 4.12a and Figure 4.12b. The free parameters r_c and $C_{nc,2D}$ are fixed to values which minimize the difference between the model and the PIC trends; the showed trends are in good agreement for all the cases expect for the energy loss curve of $a_0 = 2,\ n = 1\ n_c$. This discrepancy is quite reasonable considering that the amplitude is low and and the calculated transmittance is not very accurate (as observed in Figure 4.11b).

It should be observed that both the simulations and the model show a self-similar trend for the waist, the normalized amplification factor and the normalized energy when the abscissa is properly normalized: for w and $\bar{a}$ we use the relativistic normalized path length $\bar{x}$, which

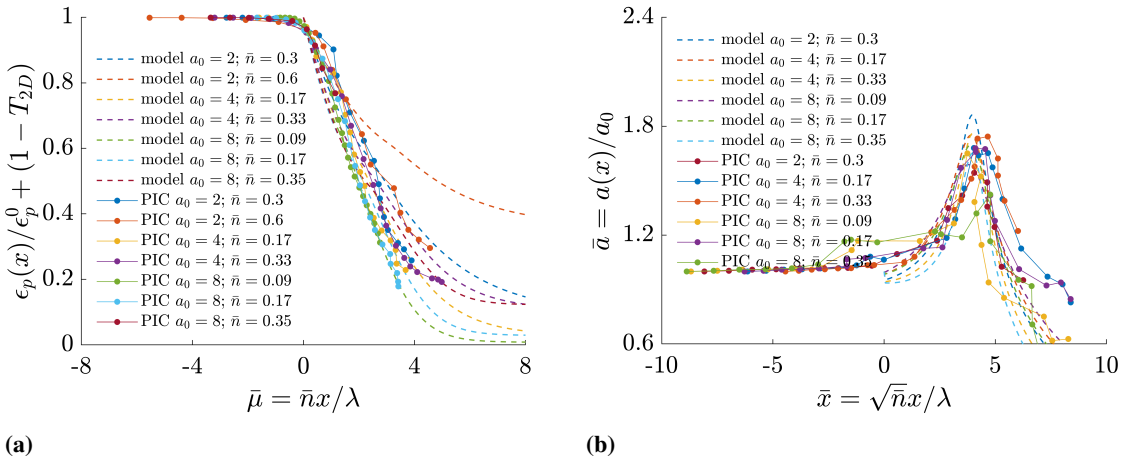

(a) **(b)**

Figure 4.12: The figure shows in (a) the laser energy evolution and in (b) the normalized amplitude of a pulse propagating inside a uniform plasma at different normalized propagation length. The full lines and points refer to 2D PIC simulations with intensity ranging in $a_0 = 2 - 8$ and plasma density in $n_e/n_c = 0.5 - 2$, while the broken lines refer to the proposed model.

can be easily explained by the dependence on Equation 4.8, while for $\bar{\varepsilon}_p$ we use the above-mentioned normalized mass path length $\bar{\mu}$, that is useful to describe the energy loss.

In this picture, it is possible to calculate the total number of hot electron N_{nc} involved in the interaction at a given x position, by integrating the electron density inside the plasma channel:

$$\frac{\partial N_{nc}(x)}{\partial x} = n_e 2R_{ch}(x) \tag{4.14}$$

Thus, the hot electron mean energy E_{nc} is retrieved, exploiting the assumption that all the laser energy is given to electrons:

$$E_{nc}(x) = \frac{(\mathcal{T}_{2D} - \bar{\varepsilon}_p(x))\,\varepsilon_{p0}}{N_{nc}(x)} \tag{4.15}$$

The former equation can be rewritten in a more readable form if we carry out some approximation; in the ultra-relativistic case ($a_0 \gg 1$), namely at high intensity, the normalized amplitude is proportional to the Lorentz factor ($a_0 \sim \sqrt{2}\gamma_0$) and we can firstly express the energy loss equation (Equation 4.10) as:

$$\frac{\partial \bar{\varepsilon}_p(x)}{\partial x} \sim -\bar{n}\frac{8C_{nc,2D}r_c}{\pi\tau c}\bar{a}(x)\frac{w(x)}{w_0} = -\bar{n}\frac{8C_{nc,2D}r_c}{\pi\tau c}\sqrt{\bar{\varepsilon}_p(x)}\sqrt{\frac{w(x)}{w_0}} \tag{4.16}$$

Equation 4.16 can be analitically integrated with the variable separation method to give:

$$\bar{\varepsilon}_p(x) = \left(\sqrt{\mathcal{T}_{2D}} - \bar{n}\frac{4C_{nc,2D}r_c}{\pi\tau c}\int_0^x \sqrt{\frac{w(x)}{w_0}}dx\right)^2 \tag{4.17}$$

Thus for little propagation lengths ($x \lesssim l_f$) Equation 4.16 can be rewritten with the

	2D	3D	Physical meaning
C_{nc}	1.7	1.1	Corrective factor to the ponderomotive scaling for near-critical hot electrons temperature
C_s	0.24	0.18	Corrective factor to the ponderomotive scaling for substrate hot electrons temperature
r_c	2.0	2.1	Ratio of the channel radius (formed by ponderomotive force) to the pulse waist
$\tilde{n}$	$1.2 \cdot 10^{-3} n_c$	$5 \cdot 10^{-2} n_c$	Hot electron density normalization constant which scales the estimated proton energy

Table 4.1: The free parameters of the proposed model for the two-dimensional and three-dimensional cases are reported, on the right column the physical meaning is briefly described.

following approximate form:

$$\frac{E_{nc}(x)}{(\gamma_0 - 1) m_e c^2} \sim C_{nc,2D} \frac{\int_0^x \sqrt{w(x)/w_0} dx}{\int_0^x w(x)/w_0 dx} \tag{4.18}$$

This expression shows that the mean electron energy can be normalized to the ponderomotive scaling $(\gamma_0 - 1) m_e c^2$, while the normalization over the propagation length is given by $w(x)$, namely the relativistically normalized space variable $\bar{x}$. The comparison of the calculated E_{nc} with the one obtained from the PIC simulation, shown in Fig.3a, is satisfactory since not only the absolute values are retrieved but also the general trend, which is another indication that all the model approximations used up to this point can be considered acceptable.

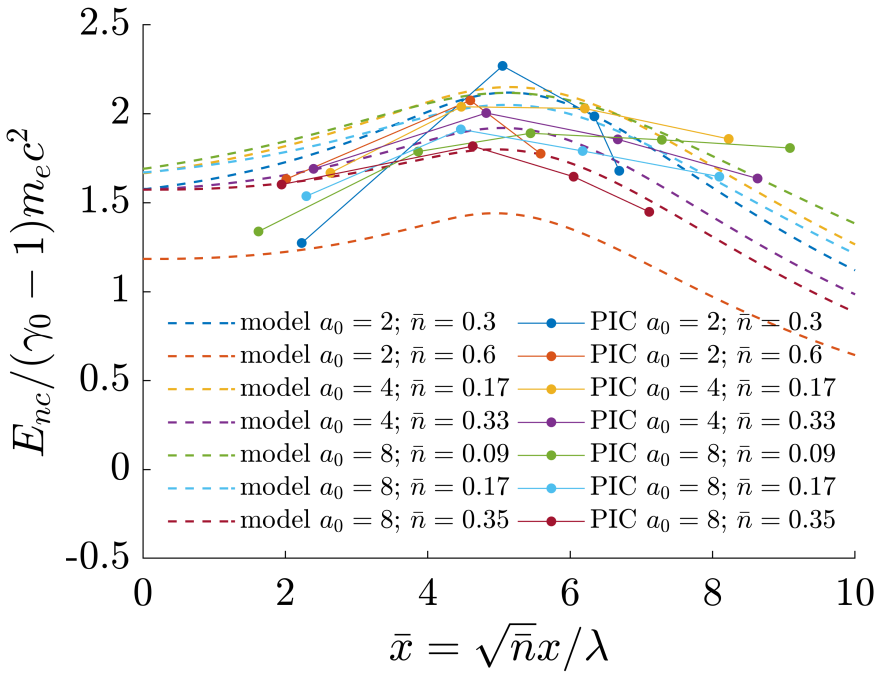

Figure 4.13: The figure shows the near-critical layer hot electron mean energy for different laser propagation length; The full lines and points refer to 2D PIC simulations with intensity ranging in $a_0 = 2 - 8$ and plasma density in $n_e/n_c = 0.5 - 2$, while the broken lines refer to the proposed model.

In these calculations we fixed the free parameters $C_{nc,2D}$ and r_c (the values are summa-

rized in Table 4.1) in order to fit the pulse energy loss, the normalized amplitude and the mean electron energy. We point out that both the parameters can't assume arbitrary values; indeed it should be observed in Figure 4.8a that the channel radius at $x = 0$ is about 6λ, corresponding to $r_c \sim 1.5$, which is quite in agreement with the fitted value, equal to 2.0. Also the $C_{nc,2D}$ parameter has a reasonable value, in the order of 1, justified by the ponderomotive scaling. Moreover, note that the parameters variation does not affect the trend of the obtained curves, but especially their amplitude.

Up to now, we have described the laser interaction with a semi-infinite near-critical plasma and the volumetric electron heating. Nonetheless, if we want to describe the laser-DLT interaction, we have to take into account the effect of a thin solid substrate of a given d_s thickness coupled with a near-critical plasma with d_{nc} length.

To do so, we have to consider that the laser pulse can arrive at the substrate with some residual energy and produce hot electrons at the substrate interface, with a mean energy given by a ponderomotive scaling, as done for Equation 4.9:

$$E_s\left(d_{nc}\right) = C_{s,2D}\left(\gamma^*\left(d_{nc}\right) - 1\right) m_e c^2 \tag{4.19}$$

Where $C_{s,2D}$ is a constant which includes the physical details of the superficial interaction and γ^* is the mean Lorentz factor at a given near-critical plasma thickness d_{nc}, considering the amplification factor f_{amp} due to the pulse reflection, $\gamma^*\left(d_{nc}\right) = \sqrt{1 + \left(f_{amp} a(d_{nc})\right)^2 / 2}$. The amplification factor can be calculated taking into account the laser absorption η into the substrate hot electrons $f_{amp} = 1 + \sqrt{1 - \eta}$.

The dependance of the hot electron absorption efficiency on the laser intensity is an issue addressed in several works [90–93]. Here, in order to assure the consistency with the 2D PIC simulation results, we fit the absorption efficiency in the range $a_0 = 1 - 16$ from bare solid target simulations, giving the linear relation $\eta = 0.00388\, a_0 + 0.04257$. The η factor is also used to calculate the number of hot electrons accelerated in the substrate with a energy balance equation:

$$\eta \varepsilon_p\left(d_{nc}\right) = N_s\left(d_{nc}\right) E_s\left(d_{nc}\right) \tag{4.20}$$

Finally, we remark that the near-critical layer electron population is generated directionally in the magnetized plasma and it tends to mix together with the substrate one; thus, it is reasonable to introduce a single mixed population with a mean energy $E_{DLT}\left(d_{nc}\right)$ obtained as a weighted average of the two:

$$E_{DLT}\left(d_{nc}\right) = \frac{N_s\left(d_{nc}\right) E_s\left(d_{nc}\right) + N_{nc}\left(d_{nc}\right) E_{nc}\left(d_{nc}\right)}{N_s\left(d_{nc}\right) + N_{nc}\left(d_{nc}\right)} \tag{4.21}$$

The free parameter $C_{s,2D}$ is fixed by fitting the hot electron temperature and the proton energy from the simulations with the bare solid target ($d_{nc} = 0$), where the other two free parameters, $C_{nc,2D}$ and r_c, are irrelevant.

The comparison of the model results and the PIC simulations, in Figure 4.14, shows also in this case a good agreement for $\bar{d}_{nc} \lesssim 2\sqrt{\bar{n}} l_f/\lambda \sim 2w_0/\lambda$; furthermore, it should

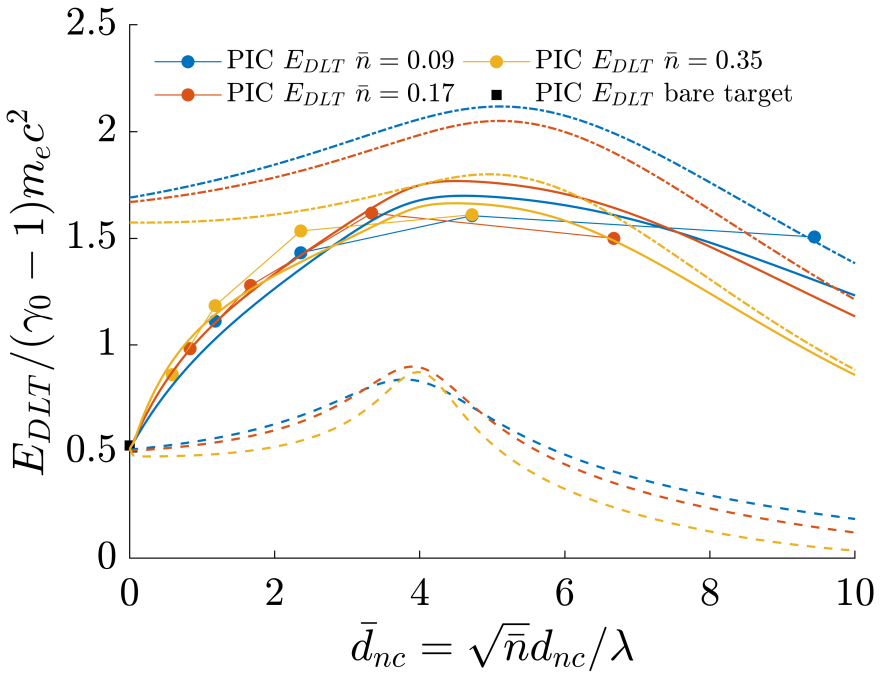

Figure 4.14: The figure shows the averaged hot electron energy inside a double layer target with a near-critical layer of thickness d_{nc} and a thin solid substrate, at the moment in which the pulse has been reflected by the substrate. The full lines and points refer to 2D PIC simulations with intensity $a_0 = 8$ and plasma density in $n_e/n_c = 0.5 - 2$, while the other lines refer to the hot electron energies calculated by our model relative to the substrate (dashed lines), the near-critical layer (dotted lines) and the weighted average (continuous lines).

be observed that the mean electron energy of the mixed population tends, for increasing $\bar{d}_{nc}$ values, to the near-critical layer electrons energy. This is consistent with the fact that the volumetric heating of the near-critical layer produces a number of particles largely exceeding the number of the surface-generated substrate electrons.

4.2.2 Proton acceleration by the near-critical DLT

Once the hot electron temperature is retrieved an analytical TNSA model can be exploited to estimate the maximum protons energy. The quasi-stationary model, introduced in Section 1.3, is adopted due to its quite accurate quantitative predictions; in particular Equation 1.10 is used in the following approximate form, valid when $\varphi^*/T_h \gg 1$:

$$\epsilon_p^{max} = T_h \left[log\left(\frac{n_{h0}}{\widetilde{n}}\right) - 1 \right] \tag{4.22}$$

Where T_h and n_{h0} are respectively the hot electron temperature and density inside the target, $\widetilde{n}$ a normalization constant that is used as a fitting parameter; it should be highlighted that the validity condition $\varphi^*/T_h \gg 1$ has the physical meaning of imposing that the hot electrons distribution is Maxwellian with a cut-off energy much higher than its temperature, which is a very common and reasonable condition.

The hot electron temperature is therefore approximated as the averaged energy, namely $T_h \sim E_{DLT}(d_{nc})$, which is an exact result when the electron spectrum is perfectly expo-

nential. While, to calculate the hot electron density, we consider that they are approximately spread uniformly in a box (in the 2D geometry) with heigh length equal to the substrate thickness d_s and the side length in the order of two-times the laser diameter, $n_{h0} = [N_s(d_{nc}) + N_{nc}(d_{nc})]/d_s 2w_0$.

The calculation of the proton energy estimation requires, as a consequence, to fix an additional free parameters, $\widetilde{n}$. Its numerical values can be easily obtained by fitting the proton energy from the simulations with the bare solid target ($d_{nc} = 0$).

The proton energy calculated by the above-mentioned method are compared to the PIC data in Figure 4.15a, where it should be observed a reasonable agreement; the data were represented with the abscissa axis normalized to $\sqrt{\bar{n}} d_{nc}/\lambda$, as done previously. The fact that, for different values of the transparency factor, the proton energies lie onto an almost self-similar curve is an indication that the proton energy is roughly proportional to the mixed population temperature and it follows the same relativistic normalization. Another indication of this point is that, making reference to Figure 4.15b, all the points tend to collapse to the self-similar curve, when the maximal energy is normalized by the ponderomotive scaling $(\gamma_0 - 1)m_e c^2$.

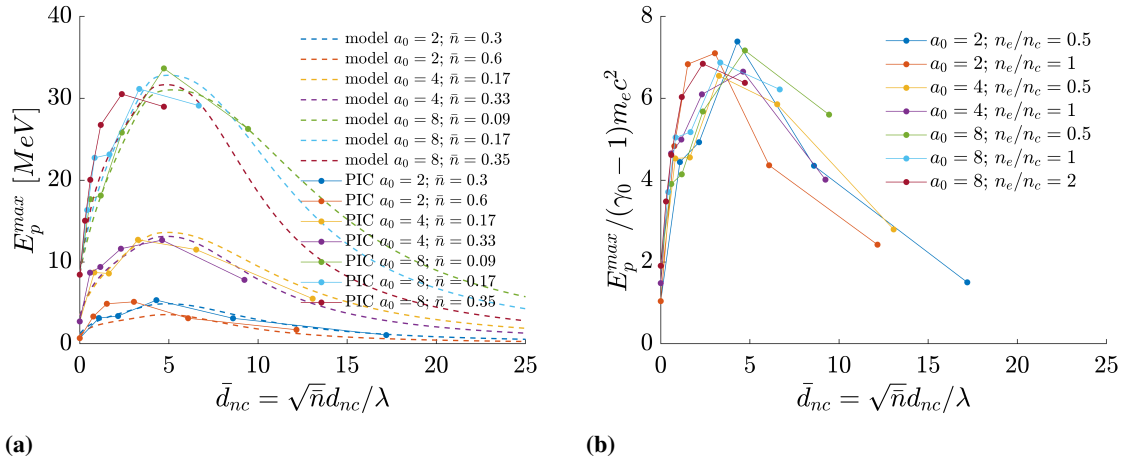

Figure 4.15: The figures show the maximum proton energy obtained in two-dimensional PIC simulations with fixed substrate thickness and spot size and variable near-critical layer thickness d_{nc} and density n_e, with intensity ranging in $a_0 = 2-8$. In (a) the simulation results are compared with the maximum proton energy predicted by the proposed model; in (b) the proton energy is normalised to the ponderomotive scaling.

It should be noticed that the maximum of the self-similar curve is situated at about the laser initial waist values $w_0 = 4\lambda$; the explanation of this behaviour is given by the following considerations: the proton energy reaches the highest values when the mixed population temperature reaches the maximum, which is obtained when both the near-critical layer and substrate electrons are heated by the pulse at the peak amplitude value, namely at the SF focal length.

It is then quite straightforward to estimate the optimal normalized thickness for the near-critical layer: $\bar{d}_{nc}^{opt} \sim \sqrt{\bar{n}} l_f/\lambda \sim w_0/\lambda$, which justifies the results yet reported in References [49, 56–58, 87, 94] .

Since the proposed model has been validated with the numerical observations from 2D

PIC simulations it is straightforward to extent the described two-dimensional model in 3D geometry. This step enables to describe realistically the ion acceleration process and could be useful to predict experimental results; in particular the new set of equations is:

$$\bar{a}\left(x\right)=\sqrt{\frac{\bar{\varepsilon}_p\left(x\right)}{\left(w\left(x\right)/w_0\right)^2}} \tag{4.23}$$

$$\frac{\partial\bar{\varepsilon}_p\left(x\right)}{\partial x}=-\frac{4\sqrt{2}C_{nc,3D}{r_c}^2}{\sqrt{\pi}\tau c}\frac{n_e}{a_0 n_c}\frac{\gamma\left(x\right)-1}{a_0}\left(\frac{w\left(x\right)}{w_0}\right)^2 \tag{4.24}$$

$$\varepsilon_{p0}=m_e c^2 n_c a_0^2 w_0^2 \tau c\pi\frac{1}{4}\sqrt{\frac{\pi}{2}} \tag{4.25}$$

$$\mathcal{T}_{3D}=\mathrm{erf}\Big(\sqrt{-2\log\left(\bar{n}\right)}\Big)-\frac{4}{\sqrt{2\pi}}\bar{n}^2\sqrt{-\log\left(\bar{n}\right)} \tag{4.26}$$

$$\frac{\partial N_{nc}\left(x\right)}{\partial x}=n_e\pi R_{ch}\left(x\right)^2 \tag{4.27}$$

$$n_{h0}=\frac{N_s\left(d_{nc}\right)+N_{nc}\left(d_{nc}\right)}{d_s\pi{w_0}^2} \tag{4.28}$$

Where a new set of the free parameters $C_{nc,3D}$, $C_{s,3D}$, r_c, $\widetilde{n}$ must be used. The criterion to fix these parameters values is the same explained for the two-dimensional case and the 3D values are reported in Table 4.1. The fact that $C_{nc,3D}$ and $C_{s,3D}$ are both lower than $C_{nc,2D}$ and $C_{s,2D}$ could be explained with the following argument: at equal pulse peak a_0 the mean amplitude in the laser-plasma interaction is lower in 3D with respect to 2D. This dimensionality effect has been reported also in Reference [12].

The numerical solution consists in a finite difference method as done for the 2D case. In Figure 4.16, 3D simulations proton cut-off energies are compared to the model results for intensity equal to $a_0 = 4$. Also in this case the model is quite accurate even if the higher density case ($\bar{n} = 0.5$) shows a lower agreement, probably due to the error in the transmittance prediction as illustrated in Figure 4.11b. It should be noticed that in three dimensions the proton energies do not lie onto a self-similar curve. This is an effect of the higher dimensionality: for high density near-critical plasmas the pulse reflection is increased with respect to the two-dimensional case and, in addition, also the laser attenuation and amplification increase with a non-linear trend (see Equations 4.23 and 4.24). It is worth mentioning that the 3D simulations were carried out only at one intensity value (due to the high computational cost) and thus the self-similarity can't be observed for equal $\bar{n}$ and different a_0 values.

4.2.3 Determination of optimal near-critical layer parameters

The highest proton energy is observed when the pulse intensity reaches a maximum due to SF, which enables to determine in a simple way the optimal near-critical layer thickness; nevertheless it is also shown that in the 3D case the transparency factor plays an important

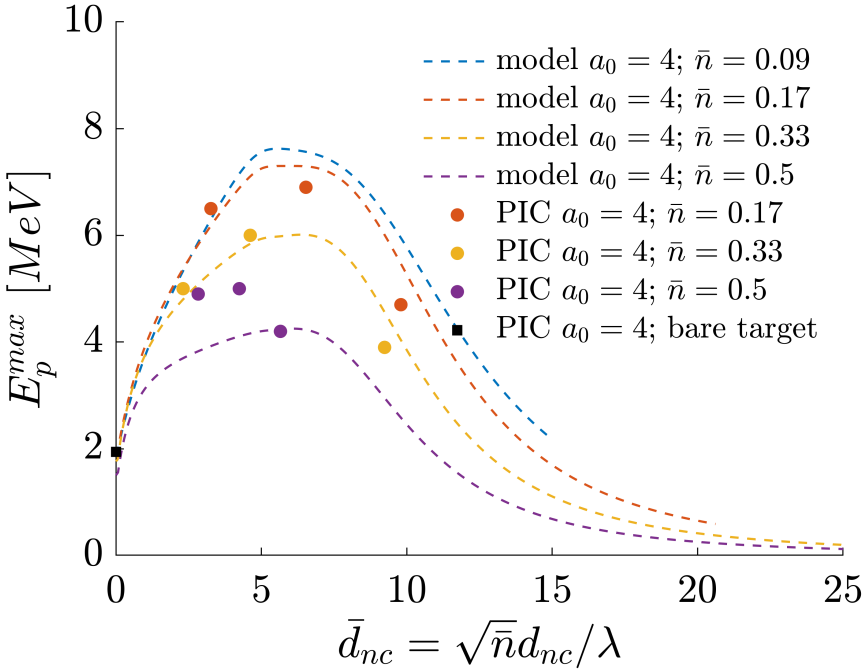

Figure 4.16: The figure shows the maximum proton energy obtained in 3D PIC simulations with fixed substrate thickness and spot size and variable near-critical layer thickness d_{nc} and density n_e, with intensity equal to $a_0 = 4$. The simulation are compared with the predictions of the proposed model.

role in the determining the proton enhancement factor.

The dependence on $\bar{n}$ is justified by the following qualitative arguments: the SF intensity amplification in 3D not trivially depends on the transparency factor because, when $\bar{n}$ tends to one, Equation 4.3 predicts the highest pulse self-focusing, but at the same time, Equation 4.24 predicts the highest pulse energy absorption. Conversely, when $\bar{n}$ tends to 0 the SF is absent while the transmitted part of the pulse $\mathcal{T}_{3D}$ (Equation 4.26) reaches the highest value and the energy absorption is minimal. As a consequence the transparency factor which maximizes the ions energy will be a trade-off between these two opposed behaviours.

In order to find the optimum, the set of Equations 4.23, 4.24, 4.25, 4.26, 4.27, 4.28 is solved in an approximate analytical way.

It should be firstly observed that Equation 4.22 predicts a linear dependence of the proton energy onto the hot electron temperature, and weaker logarithmic dependence onto the hot electrons density. Thus, the ion energy enhancement factor (defined as the ration of the cut-off proton energy obtained with the DLT to the one obtained with the standard target) can be roughly estimated by the hot electrons enhancement factor, defined as $\bar{E}_{DLT}(x) = E_{DLT}(x)/E_s(0)$. Thus the DLT temperature equation (Equation 4.21) should be analytically solved. Combining Equations 4.20, 4.21, 4.23 and 4.27 and noting that $N_s(d_{nc})\, E_s(d_{nc}) = \eta \varepsilon_p(d_{nc})$ and $N_{nc}(d_{nc})\, E_{nc}(d_{nc}) = \mathcal{T}_{3D} - \varepsilon_p(d_{nc})$, the following re-

lation can be found:

$$\bar{E}_{DLT}(x) = \frac{E_{DLT}(x)}{E_s(0)} = \frac{(\eta-1)\,\bar{a}(x)^2\left(\frac{w(x)}{w_0}\right)^2 + \mathcal{T}_{3D}}{\eta\bar{a}(x)\left(\frac{w(x)}{w_0}\right)^2 + \bar{n}\frac{2\sqrt{2}r_c^2 C_{s,3D}\sqrt{f_{amp}}}{\sqrt{\pi}\tau c}\int_0^x\left(\frac{w(x)}{w_0}\right)^2 dx} \tag{4.29}$$

To solve the latter equation an explicit relation for $\bar{a}(x)$ should be found. To do so, we restrict the analysis to the ultra-relativistic case ($a_0 \gg 1$)) where Equation 4.24 reduces to:

$$\frac{\partial\bar{\varepsilon}_p(x)}{\partial x} \sim -\bar{n}\frac{2\sqrt{2}C_{nc,3D}{r_c}^2}{\sqrt{\pi}\tau c}\frac{a(x)}{a_0}\left(\frac{w(x)}{w_0}\right)^2 = -\bar{n}\frac{2\sqrt{2}C_{nc,3D}{r_c}^2}{\sqrt{\pi}\tau c}\frac{w(x)}{w_0}\sqrt{\bar{\varepsilon}_p(x)} \tag{4.30}$$

This equation can be solved by the variable separation method to obtain an analytical solution for the laser energy attenuation:

$$\sqrt{\bar{\varepsilon}_p(x)} = \sqrt{\mathcal{T}_{3D}} - \bar{n}\frac{\sqrt{2}C_{nc,3D}{r_c}^2}{\sqrt{\pi}\tau c}\int_0^x\frac{w(x)}{w_0}dx \tag{4.31}$$

Therefore also the normalized amplification factor can be obtained, substituting Equation 4.31 into Equation 4.23:

$$\bar{a}(x) = \frac{w(x)}{w_0}\left(\sqrt{\mathcal{T}_{3D}} - \bar{n}\frac{\sqrt{2}C_{nc,3D}{r_c}^2}{\sqrt{\pi}\tau c}\int_0^x\frac{w(x)}{w_0}dx\right) \tag{4.32}$$

As stated in the previous Subsection, the highest amplitude should be expected at the SF length; as a consequence, also the highest temperature of the DLT hot electron population is found at:

$$d_{nc}^{opt} = l_f \sim \frac{w_0}{\sqrt{\bar{n}}} \tag{4.33}$$

This assumption is also reasonably justified by the heat map of Figure 4.17a, which represents the enhancement factor numerically calculated as a function of the near-critical layer density and thickness; indeed the black dashed line, representing d_{nc}^{opt}, well predicts the numerical optimal thickness.

By substituting this value into Equation 4.32, an amplification factor which depends only on the normalized density $\bar{n}$ is retrieved:

$$\bar{a}\left(\bar{d}_{nc}^{opt}\right) = \frac{w_0}{w_m}\left(\sqrt{\mathcal{T}_{3D}} - \bar{n}\frac{\sqrt{2}C_{nc,3D}{r_c}^2}{\sqrt{\pi}\tau c}\frac{w_m x_R}{2w_0}\left[\frac{l_f}{x_R}\sqrt{1+\left(\frac{l_f}{x_R}\right)^2} + \sinh^{-1}\left(\frac{l_f}{x_R}\right)\right]\right) \tag{4.34}$$

In which the $\int_0^x w(x)/w_0\,dx$ integral is solved explicitly from Equation 4.4. The term in the square brackets tends to $(l_f/x_R)^2$ when l_f/x_R increases (when $l_f/x_R > 2$, which is equivalent to $\bar{n} \geq \lambda^2/2{w_0}^2$, the relative error is under 50%), thus the normalized amplitude

amplification can be expressed as:

$$\bar{a}(\bar{d}_{nc}^{opt}) \sim \pi\sqrt{\bar{n}}\frac{w_0}{\lambda}\left(\sqrt{\mathcal{T}_{3D}} - \sqrt{\bar{n}}\frac{\sqrt{2}C_{nc,3D}{r_c}^2}{2\sqrt{\pi}\tau c}w_0\right) \tag{4.35}$$

Now Equation 4.34 can be used to express the normalized enhancement factor as a function of $\bar{n}$ only; in addition, owing to the fact that η is often quite low, we can approximate it to 0, which is equivalent to state that E_{DLT} tends to E_{nc} at the SF focal length, a reasonable assumption due to the much larger number of hot electrons generated in the near-critical layer compared to the ones of the substrate:

$$\bar{E}_{DLT}(\bar{d}_{nc}^{opt}) \sim \frac{E_{nc}\left(\bar{d}_{nc}^{opt}\right)}{E_s\left(0\right)} = \frac{-\left(\sqrt{\mathcal{T}_{3D}} - \sqrt{\bar{n}}\frac{C_{nc,3D}{r_c}^2}{\sqrt{2\pi}\tau c}w_0\right)^2 + \mathcal{T}_{3D}}{\sqrt{\bar{n}}\frac{2\sqrt{2}r_c^2 C_{s,3D}\sqrt{f_{amp}}}{\sqrt{\pi}\tau c}\frac{w_0}{3}\left(1 + \frac{3\lambda^2}{\pi^2 w_0^2 \bar{n}}\right)} \tag{4.36}$$

Furthermore, we exploit that the transmittance $\mathcal{T}_{3D}$ approaches the unity when the transparency factor is sufficiently low, approximately $\bar{n} < 1/4$. This assumption will be verified a posteriori.

To find the normalized density which optimizes the enhancement factor, we calculate the derivative of Equation 4.36 and impose it to zero. The derivative numerator is proportional to $\bar{n}^{3/2} + 3\varpi\bar{n}^{1/2} - 4\varpi/\iota$, where $\varpi = 3\lambda^2/\pi^2 w_0^2$ and $\iota = C_{nc,3D}r_c^2 w_0/\sqrt{2}\pi\tau c$ are constants. Since ϖ approaches zero and $\bar{n}$ is assumed low, the term $3\varpi\bar{n}^{1/2}$ is a second order infinitesimal term and can be neglected (also this approximation will be verified a posteriori) in order to easily find the zeros of the derivative, which reads as:

$$\bar{n}^{opt} \sim \left(\frac{4\varpi}{\iota}\right)^{2/3} = \left(\frac{12\sqrt{2}\lambda^2\tau c}{\pi^{3/2}{r_c}^2 C_{nc,3D}{w_0}^3}\right)^{2/3} \tag{4.37}$$

The above-mentioned three approximation conditions can be consequently verified a posteriori in order of appearance:

- $\bar{n} > \lambda^2/2w_0^2$: exploiting Equation 4.37, the condition is equal to $\tau > \pi^{3/2}r_c^2 C_{nc,3D}\lambda/12\sqrt{2}c \sim 1.6\lambda/c$ (where the latter numerical value is calculated with the retrieved free parameters values). This corresponds to a FWHM temporal duration of $5\ fs$ which is generally verified in experimental conditions.

- $\bar{n} < 1/4$: from this condition we find $w_0/\lambda > \sqrt[3]{24.4\tau c/C_{nc,3D}{r_c}^2\lambda}$. Using the free parameters and fixing the FWHM temporal duration at $28.5\ fs$, the latter inequality reads as $w_0 > 3.5\lambda = 2.8\ \mu m$, which is an often respected condition in real laser systems. Note that the inequality depends weakly on the pulse temporal duration, because it lies under a cubic root.

- $3\varpi\bar{n}^{1/2} \ll 4\varpi/\iota$: by substituting Equation 4.37 into the inequality, we obtain that $\tau \gg 3^{3/2}C_{nc,3D}r_c^2\lambda/2^{5/2}\pi^{3/2}c$; using again the numerical values of the free parameters we find $\tau \gg 0.8\lambda/c$ which is always verified when the first condition is respected.

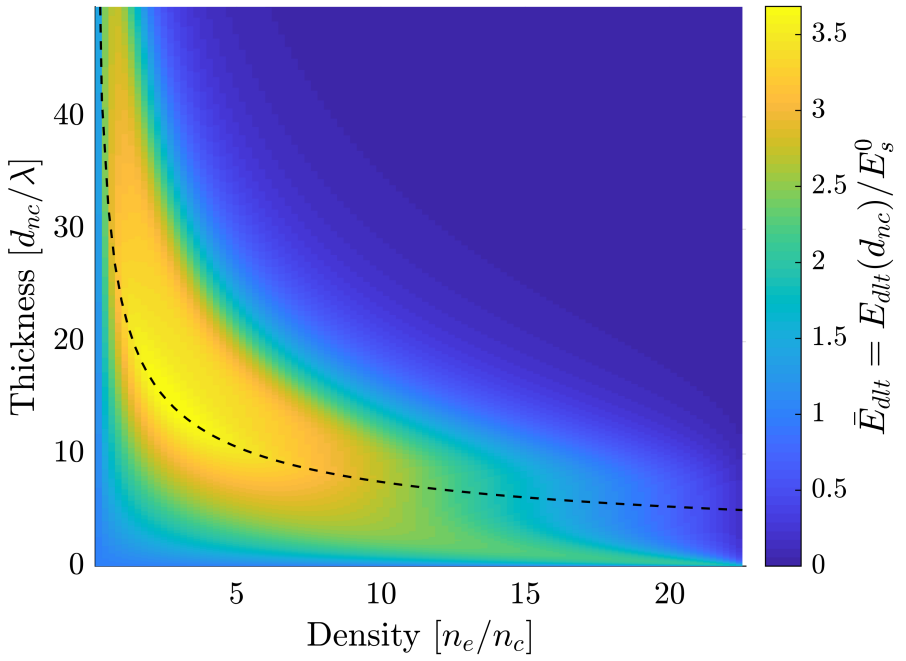

(a)

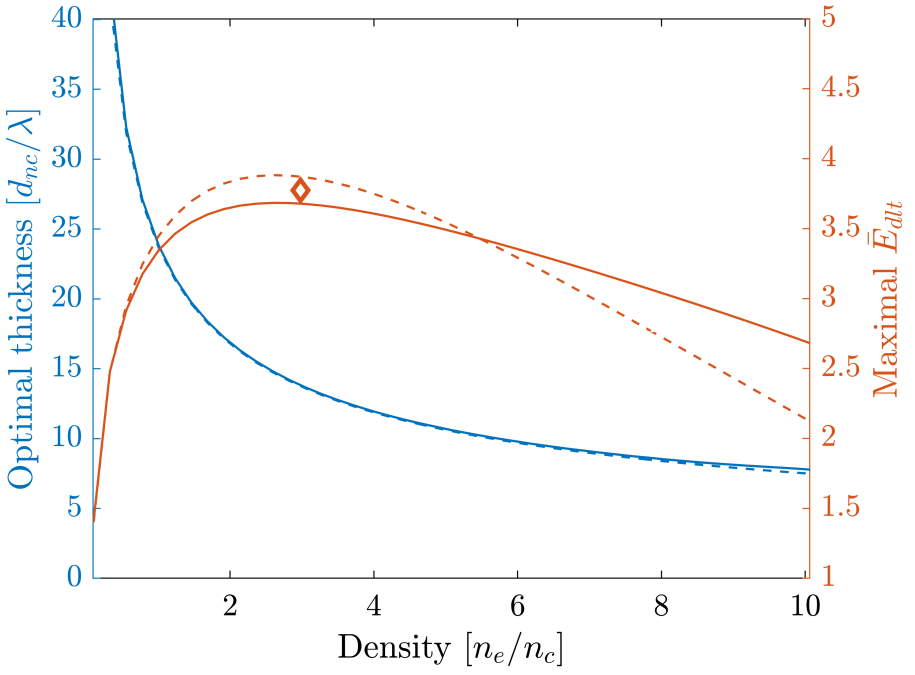

(b)

Figure 4.17: Figure (a) shows the enhancement factor $\bar{E}_{DLT} = E_{DLT}(d_{nc})/E_s(0)$ obtained by solving numerically the 3D-model as a function of density n_e/n_c and thickness d_{nc} of the near-critical density layer; the SF focal length l_f is represented with a black dashed line. Figure (b) shows the optimal thickness (solid blue curve) and the relative enhancement factor $\bar{E}_{DLT}$ (solid red curve) as a function of the density, calculated numerically from the data of Figure (a) and the SF focal length l_f (dashed blue curve) and the $\bar{E}_{DLT}$ values calculated from Equation 4.36; the red diamond represents the values obtained by Equation 4.37 and Equation 4.38.

As a final step, the found optimal near-critical layer thickness and density can be used to determine also the optimal value of the enhancement factor. Substituting $\bar{n}^{opt}$ in Equation

4.36 and neglecting again the factor ϖ, we obtain:

$$\bar{E}_{DLT}^{opt} \sim \frac{3}{2}\frac{C_{nc,3D}}{C_{s,3D}f_{amp}}\left[1-\frac{1}{\pi}\left(\frac{\sqrt{3}C_{nc,3D}r_c^2\lambda}{2\tau c}\right)^{2/3}\right] \tag{4.38}$$

The comparison of the optimal values estimated by Equations 4.37, 4.38 with the numerical solution of the 3D model are satisfactory, as shown in Figure 4.17b. The former equation is quite straightforward in the interpretation, because when the square brackets term approaches the unity (for $\tau \gg \sqrt{3}C_{nc,3D}r_c^2\lambda/2\pi^{3/2}c \sim 0.8\lambda/c$, which is equal to the third condition), $\bar{E}_{DLT}^{opt}$ tends to a constant equal to $3C_{nc,3D}/4C_{s,3D} \sim 4.6$, which can be read as the ratio of the hot electron temperatures of a near-critical plasma (DLT) and an overcritical one (standard solid foil), evaluated by the corrected ponderomotive scaling.

Thus, within the validity ranges of the proposed model and once the optimal thickness and density are chosen, the maximal enhancement value remains invariant with respect to the laser parameters, namely the intensity, the focal spot and the temporal duration. The obtained $\bar{E}_{DLT}^{opt}$ numerical value appears quite reasonable to the light of the experimental results achieved until now, since enhancement from 1.5 to 3 has been yet reported. Nevertheless, the found equations can be considered as a useful tool to carry out experiments which aim at increasing the DLT performances at best.

It should be pointed out that the basic assumptions of considering normal incidence, uniform plasmas and P-polarization will be dealt and relaxed in the next chapter.

CHAPTER 5

Ion acceleration with realistic nanostructured plasmas

This chapter describes the work inherent the simulation of the ultra-intense laser interaction with realistic near-critical target. In this framework, a realistic simulation should take into account all the possible non-ideal phenomena: for example, the target nanostructure, the plasma ionization during the interaction, the target pre-expansion due to pre-pulses and the non-ideal laser pulse shape. Nevertheless, considering all the above-mentioned effects is a demanding task; in addition, it could be not convenient to simulate the most realistic situation because the different non-ideal phenomena could affect the results in an interdependent way, which is a condition which gives few physical insights on the process.

For these reasons, a PIC simulation campaign aimed principally at studying the nanostructure effect was performed, maintaining all the other usual non-realistic approximation, such as an ideal pulse profile, a fully ionized plasma and an infinite pulse contrast (absence of pre-pulses).

In Section 5.1 the foam nanostructure is approximated by an extension of a standard aggregation model, the *Diffusion Limited Cluster-Cluster Aggregation* (DLCCA). This virtual structure is used in PIC simulations to study, in Section 5.2, the interaction differences between ideal uniform semi-infinite near-critical plasmas and realistic ones; here the validity of the theoretical model described in the previous Chapter is discussed. Finally, in Section 5.3, PIC simulations with realistic nanostructured DLTs are described, with a focus onto the ion acceleration process.

5.1 Nanostructure model

The nanofoam material, introduced in 3.1, is featured by a complex fractal-like structure composed by small nanoparticles with $10 - 20\ nm$ diameter; to reproduce its nanostructure

different computer-based aggregation models can be exploited, such the *Diffusion Limited Aggregation* (DLA) [95] or the *Diffusion Limited Cluster-Cluster Aggregation* (DLCCA) [96]. The last one is particularly useful to describe the structure of soot [97] or colloidal aggregates [98] which closely resemble the nanofoam structure, as shown in Figure 5.1; therefore, it is the one adopted to reproduce the foam virtual structure.

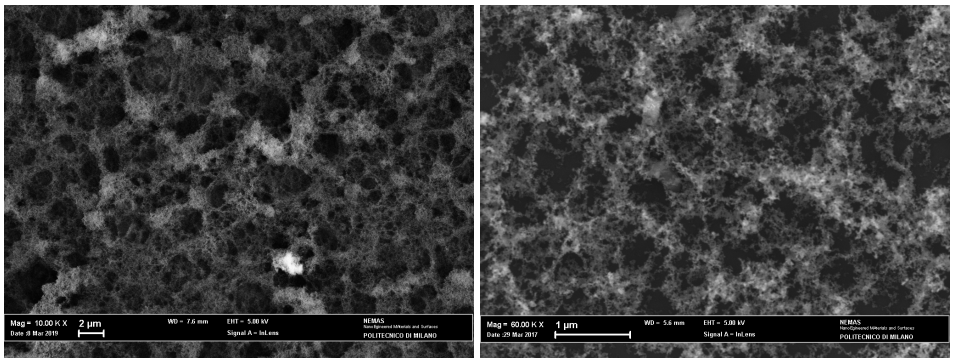

(a) **(b)**

Figure 5.1: (a) SEM image of a Carbon nanofoam. (b) SEM image of a soot film deposited by the flame of a normal candle.

The DLCCA model is based on the hypothesis that spherical particles, called clusters, moving with Browning motion into a fluid (liquid/gas) have the possibility to stick together and form aggregates; this hypothesis is valid in the PLD foam deposition conditions and are discussed deeply in Chapter 7.

In its original version, DLCCA starts with a collection of N monodisperse spherical particles (clusters), randomly disposed into a periodic cubic mesh with size L, normalized to the cluster diameter (see the block diagram of Figure 5.2a). Then, these particles are moved in each numerical cycle along one random direction over the regular mesh, to simulate the Brownian diffusing motion; once the spheres touch each other, they stick together to form a rigid dimer, which can undergo random motion as well. Since Brownian diffusion is due to the stochastic collisions of the clusters with the fluid molecules, the probability that a large aggregate move due to diffusion is lower with a square root trend $\propto 1/\sqrt{N}$. This effect is taken into account by a random number extraction between 0 and 1, if the number value is lower than $1/\sqrt{N}$ the cluster is moved, while in the opposite case it is kept motionless for the whole numerical cycle.

The mechanism is repeated for a number of cycles, until all the particles in the box aggregate together in a large fractal structure (see Figure 5.3). The resultant DLCCA aggregate therefore simulates the micro-metric fractal aggregate composing the C nanofoam (for a detailed description of the aggregation phenomenon see Chapter 7).

The original version is generally called *on-lattice* DLCCA because the particles are able to move only onto the regular mesh nodes; a more realistic and computational demanding version is the *off-lattice* DLCCA [99], where the clusters can freely move in the 3D space. The latter is a more realistic model for the foam structure, nevertheless the computational cost is quite high due to the non-linear scaling of the problem with the particles number N:

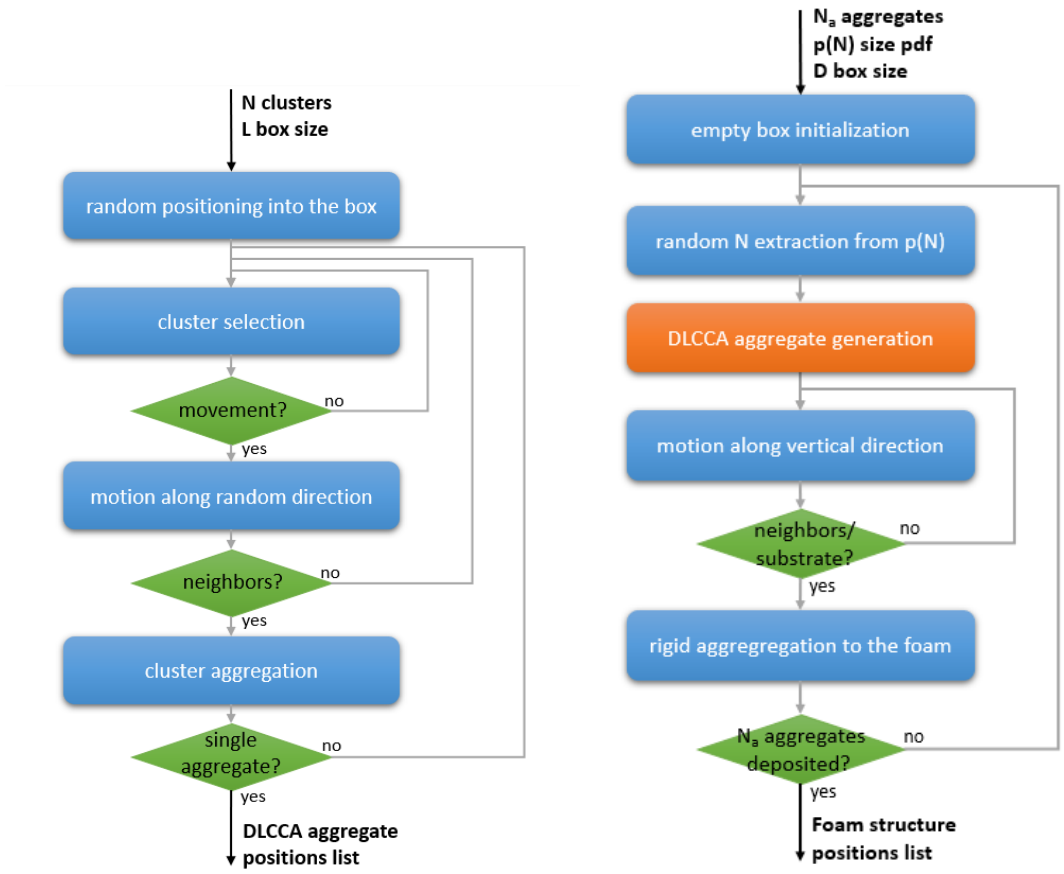

Figure 5.2: Block diagrams of the DLCCA model (a) and the foam structure assembling model (b). In (b) the orange block encloses the code described in the (a) diagram.

in each cycle the distance between each cluster must be calculated in order to find neighbours, thus the number of operations grows with the N^2 scaling law.

The problem can be reduced in computational cost by adopting a less physical but more efficient algorithm: the particles are initialized in a list and in every iteration two clusters are chosen randomly to aggregate in a small temporary box, through the DLCCA algorithm; once the two are aggregated, the list dimension is reduced by one and the procedure is repeated until all the clusters are aggregated in a single fractal [100]. Despite the physical intuitive interpretation is lost with this algorithm, it was demonstrated that the final result is the same [101]: it was observed that the probability that a large cluster aggregates to a small cluster is roughly similar to the one of two clusters with the same dimension. As a consequence, the aggregation process can be split in subsequent aggregations with two clusters at time. Note that this is a valid approximation only when the initial concentration $c = N/L^3$ is sufficiently low, $c < 0.01$, where n-body collisions (with $n > 2$) are reasonably neglected.

This last method is exploited to generate the nanofoam structure with an algorithm represented in the block diagram of Figure 5.2b. The off-lattice DLCCA code is used to generate a large number of virtual aggregates N_a, with cluster number N extracted randomly by a pre-chosen *probability density distribution* (pdf), $p(N)$. This pdf is generally a decreasing

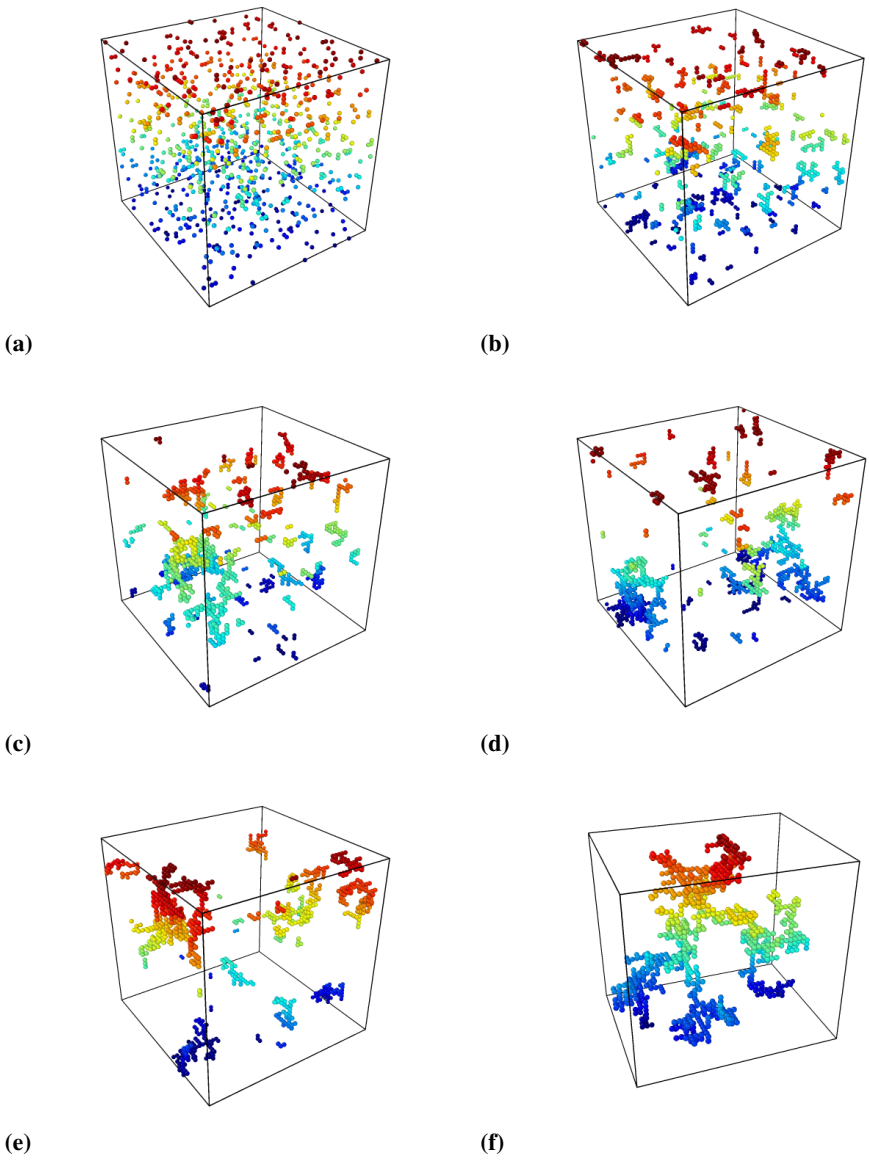

Figure 5.3: Representation of the on-lattice DLCCA algorithm cycles, with initial clusters number $N = 1000$ and box dimension $L = 50$. The cycle number is equal to 0 in (a), 50 in (b), 100 in (c), 150 in (d), 200 in (e) and the final DLCCA aggregate in (f).

exponential taken from experimental data (see Chapter 7) or fixed to arbitrary values to reproduce a wanted filling factor (defined as the fraction of particle occupied space over the box volume). The formed aggregates are singularly deposited into another periodic simulation box with size D through a vertical motion starting from the box top; once one of the aggregate particles is found near the substrate or another pre-deposited cluster, a bond is generated and the DLCCA structure starts to move circularly around this fulcrum as a rigid body. This procedure is repeated until three bonds are formed. The foam structure is then updated and another DLCCA aggregate is generated and deposited.

The final virtual foam structure is shown in Figure 5.4 for increasing number of deposited aggregates N_a; initially (Figure 5.4a) the single DLCCA aggregates are separated in space and are distinguishable, while for higher number of N_a a continuous fractal 3D structure is

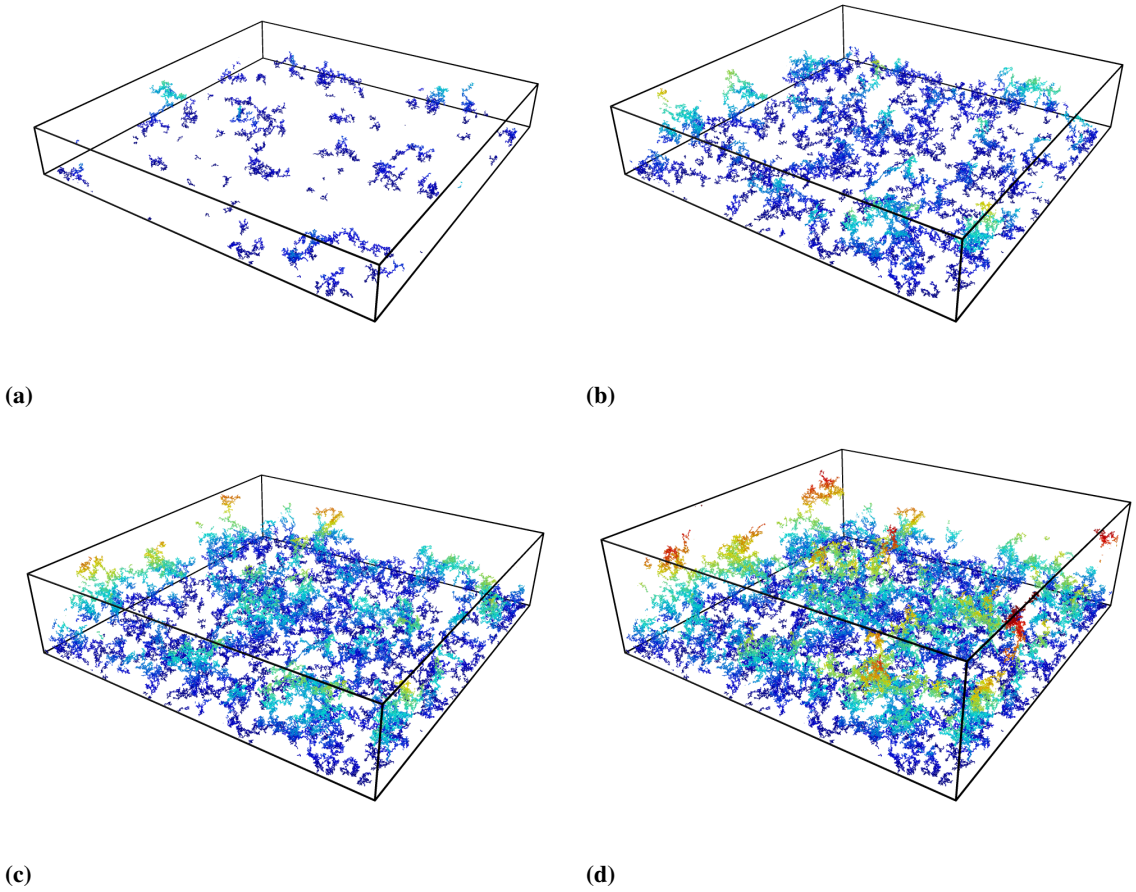

Figure 5.4: Representation of the foam off-lattice DLCCA deposition algorithm steps with $N_a = 1100$, $D = 1000$, exponential $p(N)$ with 1100 expected value. The deposited aggregates number is equal to 100 in (a), 400 in (b), 700 in (c), 1100 in (d).

formed. Once the required foam heigh is reached, the particles position list can be used to generate the nanostructured plasma in the PIC simulations; to reduce the PIC computational costs the simulated NPs diameter is set to a higher value of the measured one. Indeed, the PIC simulations calculation time non-linearly depends on the spatial resolution; a generally accepted resolution is 50 points per lambda which corresponds to $\Delta x = 16nm$. Because the single NP must be resolved with some grid points, its numerical diameter must be sufficiently higher than Δx; a reasonable trade-off consists in using $80\ nm$ diameter as shown in Figure 5.5, which is therefore $4 - 8$ times larger the real one ($10 - 20\ nm$). To do so, the DLCCA spheres diameter is set to $0.075\ \lambda$ in the aggregation algorithm (where the particles barely touch each other) and it is inflated up to a diameter of $0.1\lambda = 80\ nm$.

To further reduce the PIC computational effort, the mean density of the numerical NP is set to a value inferior than the real one ($40\ n_c$ against $\sim 300\ n_c$). Combining the lower density and the higher radius, this is physically equal to approximate a fractal chain of smaller real NPs with a single less dense and bigger numerical NP; consequently, the PIC simulation neglects all fractal structure effects taking place at scales smaller than $80\ nm$. It should be pointed out that this choice should not be detrimental for the interaction phenomenon

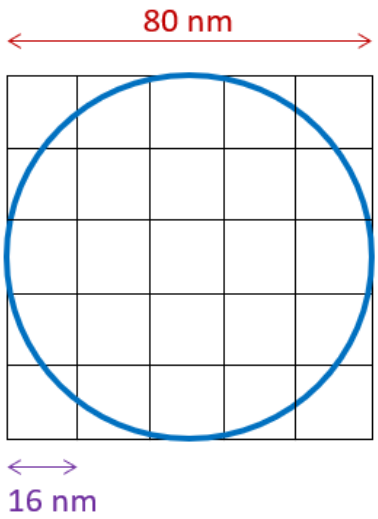

Figure 5.5: 2D scheme of the virtual foam nanoparticle and the PIC simulation grid.

description, because such small scales are rapidly homogenized by the laser pulse ponderomotive force; in addition, pre-pulses, not included in the PIC simulations but often present in real laser systems, have the effect of an additional pre-expansion of the NPs, further justifying the approximation.

5.2 Laser interaction with realistic near-critical plasmas

Ion acceleration in the TNSA regime is particularly dependent on the hot electrons properties (temperature and density); we have seen in previous Sections that electrons produced in the near-critical layer have a fundamental role in the acceleration due their higher number and energy. To study the differences between an ideal uniform near-critical plasma and a more realistic one, it is very useful to simulate the interaction of the laser pulse with a semi-infinite plasma and to analyse the hot electron heating mechanism and the pulse propagation phenomenon in the different conditions: in particular, the different polarization effect and the different plasma idealisation (nanostructured/uniform) consequences on the interaction are presented in this Section.

In more detail, 3D PIC simulations are performed with the Piccante code (see Section 4.1), by varying the following parameters singularly:

- Polarization: the pulse polarization is changed to P-polarization and C-polarization taking the pulse energy constant.
- Intensity: the pulse, normally incident onto the plasma, has amplitude values equal to $a_0 = 5 - 15 - 45$ in P-polarization. The corresponding simulations with C-polarization are performed keeping the pulse energy constant, thus the reported value of a_0 should be divided by a $\sqrt{2}$ factor for this condition (notice that exploiting this choice $\bar{n}$ is equal for P- and C-pol).

- Plasma structure: the near-critical plasma is described by an ideal uniform slab with $3\ n_c$ density or a DLCCA nanostructure with the same mean density.

The laser pulse has an idealized cos^2 temporal profile (approximating a high contrast laser) and a Gaussian transverse profile and it is focused at the vacuum-plasma boundary. The waist is 5λ, while the temporal duration is $15\ \lambda/c$ (FWHM of the fields). These parameters, if scaled to Ti:Sapphire lasers, correspond to a $28.5\ fs$ beam focused into a $4\ \mu m$ spot, providing a peak intensity in the range $5 \cdot 10^{19}\ W/cm^2 < I < 3.2 \cdot 10^{21}\ W/cm^2$. For the simulations with a uniform plasma, a $90\ \lambda \times 50\ \lambda \times 50\ \lambda$ box is used, with a resolution of 20 points per wavelength. A uniform plasma slab fills a $50\ \lambda \times 50\ \lambda \times 50\ \lambda$ region with a density of $3\ n_c$. 12 macro-electrons per cell, sufficient to resolve the critical density, are used. For the simulations with the DLCCA plasma, a $80\ \lambda \times 30\ \lambda \times 30\ \lambda$ box is used, with a resolution of 50 points per wavelength. The plasma fills a $40\ \lambda \times 30\ \lambda \times 30\ \lambda$ region with an average density of $3\ n_c$. The local density is $\sim\ 60\ n_c$, with a filling factor of $\sim\ 5\%$. 64 macro-electrons per cell, sufficient to resolve the critical density, are used. In all the simulations the plasma is fully pre-ionized and the the charge/mass ratio of the ions is equal to 0.5 (e.g. C^{6+}). The electron population is initialized with a small temperature (few eVs) to avoid numerical artefacts.

Figure 5.6 shows a snapshot of the laser-plasma interaction after about $90\ fs$ its beginning, in the uniform case (Figure 5.6a) and in the nanostructured one (Figure 5.6b). The differences in the propagation of the laser pulse in the two cases are evident: the laser in the uniform plasma is strongly self-focused, as yet deeply discussed in Chapter 4, while in the DLCCA case the pulse is more scattered and it appears that no focusing is present. It should be pointed out that this intuitive observation should be taken due precautions; indeed, the comparison of Figures 5.6c and 5.6d shows that, even if clean SF is not present in the DLCCA plasma, an amplification of the fields amplitude with similar values is still present.

To study more in detail the interaction differences with respect to the plasma structure, the total electrons energy absorption as a function of time is analysed. The results, summarized in Figure 5.7a, show that different polarization condition, plasma structure and even intensity have the effect of changing the hot electrons absorption mechanism: for example, the low intensity case ($a_0 = 5$), which is characterized by a high opacity ($\bar{n} = 0.8$), exhibits a larger absorption rate for the DLCCA case with respect to the homogeneous one. This absorption enhancement (observed also in 2D PIC parametric simulations [102]) can be explained considering that the uniform plasma, due to the density near the relativistic critical threshold, reflects large part of the incoming radiation (as described in Section 4.2); conversely, the DLCCA structure lets the laser propagate through its voids deeper in the target, enhancing absorption.

In addition, differences in the absorption rate are seen with respect to the pulse polarization, only for the uniform plasma case: in C-polarization and normal incidence, electron heating mechanisms are suppressed, leading to a more efficient formation of a denser reflecting surface at the vacuum-plasma boundary; this involves a reduced absorption with respect

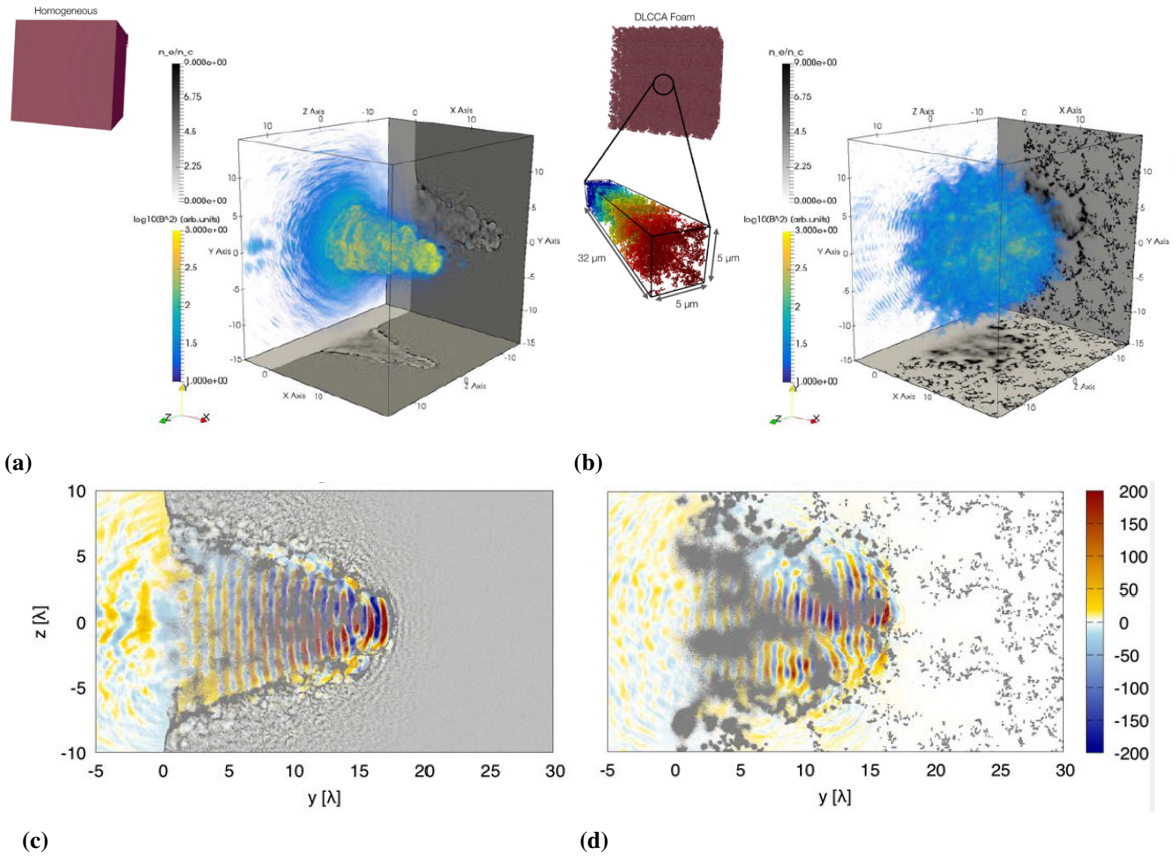

Figure 5.6: Propagation of a P-polarized, $a_0 = 15$, laser pulse in a uniform plasma (a) and in a DLCCA foam plasma (b), at a time of $t = 30\ \lambda/c$ after the beginning of the interaction. Slices of $y = 0$ and $z = 0$ of the electron density are represented in grey scale, while the square modulus of the magnetic field $|B|^2$ is showed in color. Cross-section of the pulse at $z = 0$ of the z component of the magnetic field for $a0 = 45$ and a homogeneous plasma (c) and a DLCCA foam plasma (d). The electron density is shown in greyscale, while the magnetic field is represented in color.

to P-pol. On the contrary, the dependence of the absorption onto the polarization vanishes for the nanostructured plasma, because the rough DLCCA surface removes all the angular dependencies of the electron heating phenomena (see Chapter 1).

At higher intensity the absorption curves tend to assume similar trends for all the cases (P/C-pol, uniform/DLCCA plasmas), with a total superposition for the $a_0 = 45$ case; in the latter condition, the near-critical plasma is relativistically very transparent ($\bar{n} = 0.1$) and the intense pulse is able to homogenize the nanostructure in rapid times leading to similar propagation mechanism. This is a very relevant phenomenon for this PhD work, since the equations for the optimal near-critical layer density and thickness (Equations 4.33 and 4.37, see Section 4.2) are valid under the $\bar{n} < 1/4$ condition; because in the 3D simulations, for $\bar{n} \lesssim 0.3$, the DLCCA and uniform cases are featured by the same electron absorption rate, the results obtained in the previous Chapter for ideal homogeneous near-critical layers can be considered valid also for the more realistic nanostructured ones.

Another quite peculiar mechanism is observed in the plasma ions kinetic energy absorption represented in the bottom of Figure 5.7a (not to be confused with the TNSA accelerated ions, not simulated in these 3D PIC with semi-infinite plasma); the ion energy absorption re-

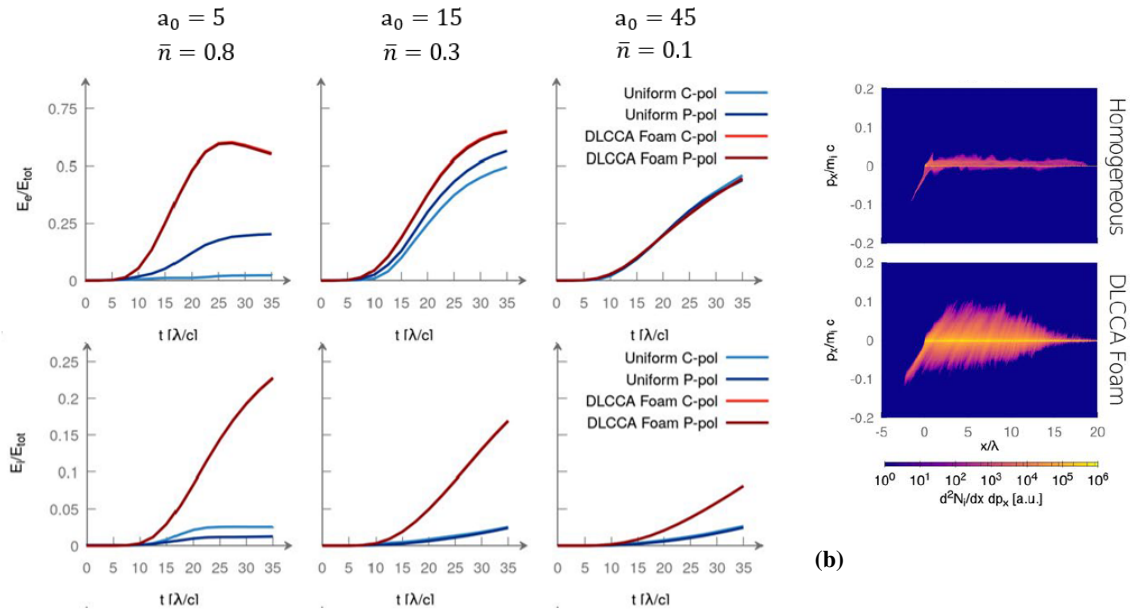

Figure 5.7: (a) Time evolution of the energy absorption of the laser pulse into electrons (top) and ions (bottom) kinetic energy for uniform and DLCCA plasma, linear and circular polarization. (b) Projection of the ion phase space on the (x, px) plane for uniform plasma (top) and DLCCA plasma (bottom), with $a_0 = 15$, P-polarization at time $40\ \lambda/c$).

mains well below 5% in all the homogeneous plasma cases, while it is remarkably enhanced with foams, up to 20% for $a_0 = 5$. This is a direct consequence of the explosion (*Coulomb Explosion*, CE [103]) of the nanoparticles constituting the DLCCA plasma, whose signature can be found in the ion phase space, as shown in Figure 5.7b. In the enhanced TNSA from DLTs, Coulomb Explosion should be considered principally a detrimental phenomenon, because the CE ions energy is generally low and the spatial distribution isotropic; in addition, the CE subtracts energy from the hot electrons useful for the TNSA process. It should be highlighted that this mechanism can't completely be eliminated in realistic plasmas composed by nanoparticles, nevertheless it can be suppressed by the fast homogenization which takes place at low $\bar{n}$ or, alternately, by the experimental realization of smaller nanoparticles (see Part III).

Finally one last effect is worth of mention: as a general feature, the DLCCA plasma allows for a more efficient acceleration of mildly energetic electrons (i.e. with a kinetic energy $\lesssim 0.1 E_{co}$, where E_{co} is the cut-off energy). On the other hand, the plasma nanostructure has a detrimental effect on the acceleration of the high-energy electrons. At $a_0 = 5$ the effect is rather weak and the spectra are comparable, while at $a_0 = 15$ and $a_0 = 45$ they exhibit great differences, being the electron cut-off energies significantly reduced with foams. This also affects the mean kinetic energy of the most energetic component of the electron spectra T_h, shown in Figure 5.8a; at $a_0 = 45$, the uniform plasma electrons temperature can exceed three times the DLCCA one (see Figure 5.8b).

This observation could be explained by the quenching of the *Direct Laser Acceleration*

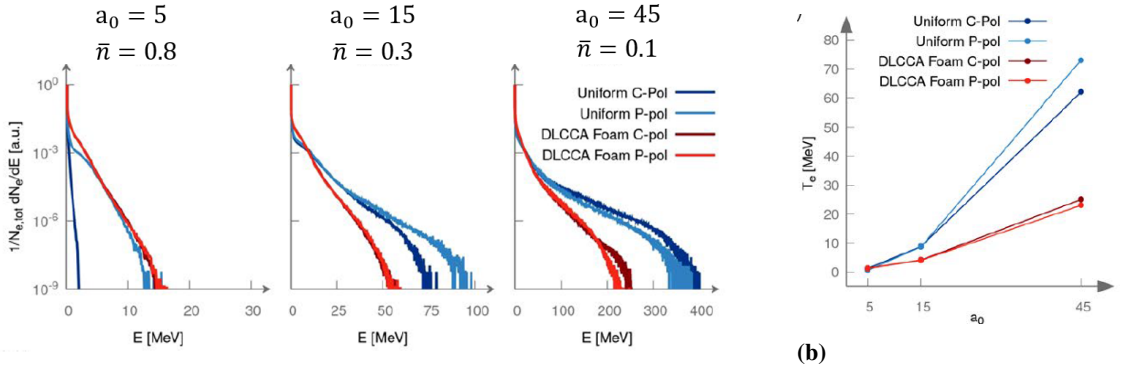

Figure 5.8: (a) Electron energy spectra at time 30 λ/c for uniform and DLCCA plasmas, linear and circular polarization. (b) Temperature of the tail of the electron energy spectrum as a function of a_0 for uniform and foam targets, linear and circular polarization.

(DLA) of the electrons. DLA is a resonant process in which the hot electrons in the tail of the energy distribution are in phase with the electromagnetic field and are accelerated to high energies [47, 104]. It is reasonable to expect that perturbing the electromagnetic field distribution, as observed in Figure 5.6 for the nanostructured plasma, would result in a detuning of the resonance condition and in a reducing of the electron temperature. Owing to this fact, the near-critical layer mean energy, calculated by the model of Section 4.2, should be multiplied by a corrective factor $E_{ns} = \alpha_{ns} E_{nc}$, less than 1, to take into account the inferior electron temperature in the nanostructured case with respect to the ideal uniform one; because the total energy absorbed by electrons is similar in the two cases (when we fulfil the transparency condition), the amount of the nanostructured foam electrons must be increased accordingly, $N_{ns} = N_{nc}/\alpha_{ns}$. The main consequence, predicted by Equation 4.38, is that the ion energy enhancement in a DLT configuration (approximated by $3C_{nc,3D}/4C_{s,3D}$) should be reduced by about the α_{ns} factor; this prediction is discussed with more detail in the next Section and compared with experimental data in Section 10.3.

5.3 Ion acceleration from nanostructured DLTs

Realistic PIC simulations were performed also in the DLT configuration to study the ion acceleration process at the light of the gained insights from the 2D ideal simulations and models and the 3D PIC with semi-infinite plasma. In particular, the numerical work is restricted to few relevant conditions, due to the high computational cost of the realistic 3D PIC, which are here summarized:

- Intensity: laser pulse amplitude fixed to $a_0 = 4$, which corresponds to an intensity of about $3.5 \cdot 10^{19}\ W/cm^2$ typical of widespread medium-scale laser facilities. P-polarization and normal incidence are used, to compare the results with the previous simulations.

- Plasma structure: both uniform and nanostructured near-critical plasma are used, with

fixed thickness ($d_{nc} = 4\ \lambda$) and variable mean density ($n_e = 1 - 1.5 - 1.75 - 2.3 - 3\ n_c$ for the uniform and $n_e = 1.5 - 2.3\ n_c$ for the DLCCA).

- Substrate properties: the substrate is idealized by a very thin solid foil ($d_s = 0.5\ \lambda$) with constant thickness in all the simulations.

With more detail, the numerical box is $100\ \lambda \times 60\ \lambda \times 60\ \lambda$, with periodic boundary conditions. The total simulation duration is $80\ \lambda/c$. The laser beam has a Gaussian spatial profile with a waist equal to $5\ \lambda$ and a cos^2 temporal profile with a fields FWHM equal to $15\ \lambda/c$. Concerning the target, ions are initialized perfectly cold, while electrons are initialized with a very small temperature (few eV). The substrate density is set to $40\ n_c$ and 40 macro-electrons per cell and 2 macro-ions with $Z/A = 0.5$ per cell are used. The spatial resolution is 20 points per wavelength in each direction, which is sufficient to resolve the relativistic skin depth; convergence tests are performed with 40 points per wavelength to assure that the ions energy remains unaltered by the spatial resolution. With this discretization the DLCCA nanoparticles are resolved by few grid nodes (from 4 to 8), since their diameter is twice the spatial grid size; nevertheless, it is observed in the convergence tests that the pulse propagation, the electron heating and ion acceleration is weakly affected by the chosen spatial discretization (as shown in Figure 5.9). Because in the TNSA mechanism the accelerated ions come from a contaminant layer, an hydrocarbon layer is simulated at the rear of the solid target with $0.05\ \lambda$ thickness and an electron density of $7\ n_c$, a proton density of $1\ n_c$ and a fully ionized carbon density of $6\ n_c$ (64 macro-particles per cell per species are used).

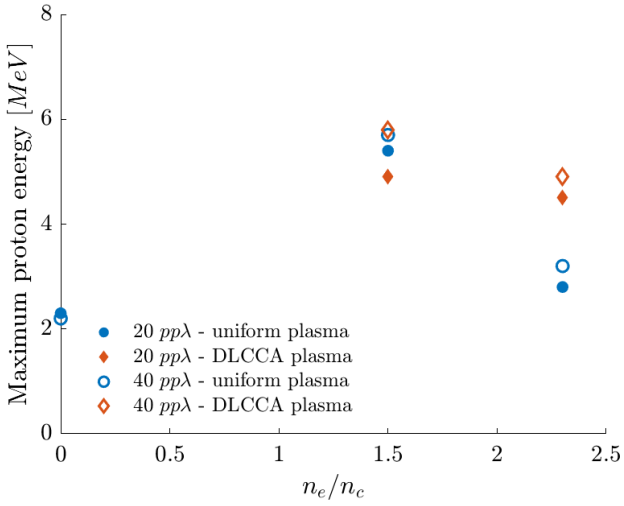

Figure 5.9: Maximum proton energy (from 3D PIC simulations) as a function of the mean density of the near-critical layer of DLTs with different plasma structure (blue uniform, orange DLCCA), where $n_e/n_c = 0$ corresponds to bare target. Notice that the different spatial resolution weakly affects the maximum proton energy.

The 3D PIC simulations confirm several yet discussed observation as well they reveal interesting effects observable only in the DLT configuration. Figure 5.10 shows the laser-DLT interaction and protons acceleration in the nanostructured plasma case (with mean density $n_e = 1.5\ n_c$); it is possible to observe that the DLCCA structure tends to homogenize during

the laser propagation, as seen in the previous Section, while the laser pulse is both disordered and amplified by the near-critical plasma. Even if the relativistic transparency factor $\bar{n} = 0.5$ is quite high, it appears that the pulse is almost not reflected by the nanostructured surface, thanks to the presence of structure voids.

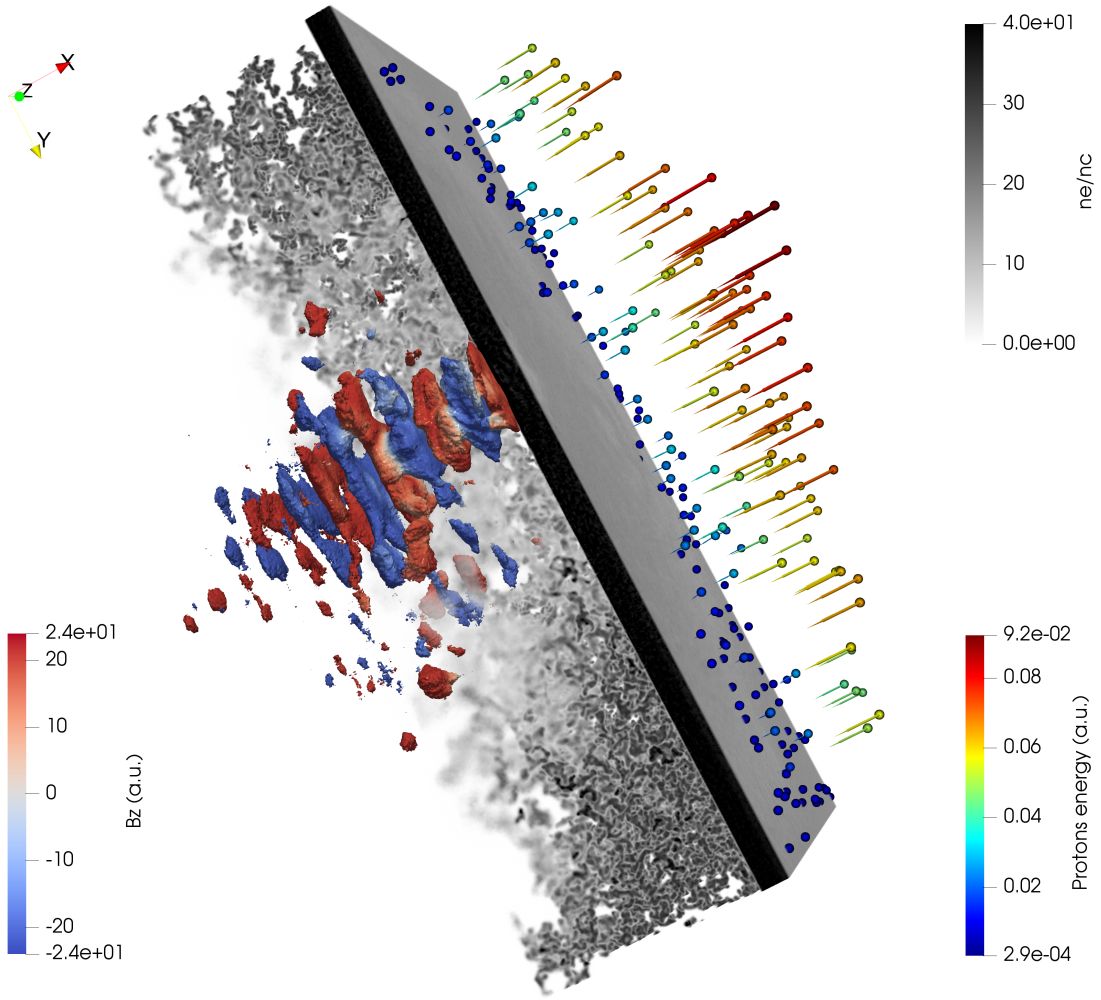

Figure 5.10: 3D PIC simulation snapshot at time 20 λ/c after the beginning of the interaction; electron density is represented in gray scale, electromagnetic energy density isosurface is represented in color scale, accelerated protons at the end of the simulations are represented with spheres.

The pulse propagation is thus quite unaffected by the presence of the substrate; as a consequence, it is expected that the hot electron heating should be similar to the one of the semi-infinite case, reported in the previous Section. However, the presence of the solid foil introduces a new electron population to be considered, which can play a role in the TNSA field formation and in the ion acceleration. To study this effect, electron spectra from the near-critical layer and the substrate are retrieved from the simulations and represented in Figure 5.11 for five conditions: bare target, DLCCA/uniform DLTs with mean density $n_e/n_c = 1.5$ (Figure 5.11a) and $n_e/n_c = 2.3$ (Figure 5.11b). Several evidences are here summarized:

- **Substrate electrons temperature enhancement**: comparing the dotted lines represen-

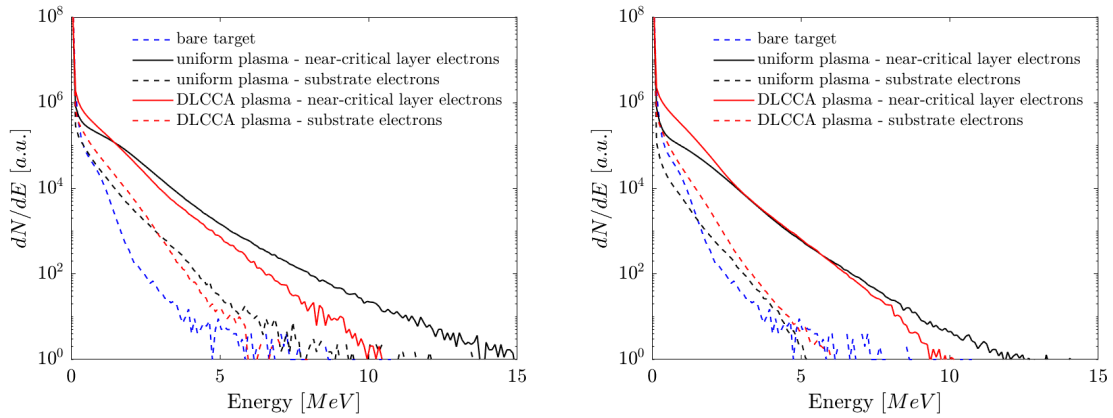

Figure 5.11: (a) Near-critical layer (full lines) and substrate (broken lines) electron energy spectra at time 40 λ/c for uniform (black) and DLCCA (red) plasmas with mean density $n = 1.5\ n_c$ and for bare target (blue line). (b) Near-critical layer (full lines) and substrate (broken lines) electron energy spectra at time 40 λ/c for uniform (black) and DLCCA (red) plasmas with mean density $n = 2.3\ n_c$ and for bare target (blue line).

tative of the substrate electrons spectra, it is observed that the distribution temperature is higher in presence of the near-critical layer (both uniform and nanostructured); this is an indication that self-focusing takes place and, even if the laser is partially absorbed in the propagation in the first layer, the local intensity on target is higher, with the resulting effect of producing more energetic particles (as discussed in the model of Section 4.2).

- **Near-critical layer vs substrate electrons**: it is quite evident that the hot electrons temperature of the near-critical layer (both nanostructured and uniform) is substantially higher of the substrate one; this is due to the different heating mechanism which is more efficient when volumetric interaction occurs. This point confirms the results of Section 4.2, where the near-critical layer empirical weight of the ponderomotive scaling C_{nc} was found to be larger than the one relative to the substrate C_s. In addition, the first layer hot electrons number is larger by almost one order of magnitude with respect to the second layer ones; thus it is expected that the TNSA accelerating field will be principally due to the near-critical hot electrons.

- **Uniform vs DLCCA plasma**: some differences are noticed in the particles distributions for different plasma structures. The temperature has the highest value in the uniform case with the lower density, which is justified by the presence of the DLA resonant mechanism which accelerates electrons to high energies; conversely, the nanostructured plasma allows increasing the total number of hot electrons, in particular in the low energy area of the spectrum. In addition, the DLCCA spectra are less sensitive to the density value with respect to the uniform case. This can be explained by the higher reflectivity sensitivity to $\bar{n}$ in the uniform case with respect to the nanostructured one.

Furthermore, the maximum proton energy in the different simulated conditions are represented in Figure 5.12 and normalized to the bare target value. As easily expected, the proton

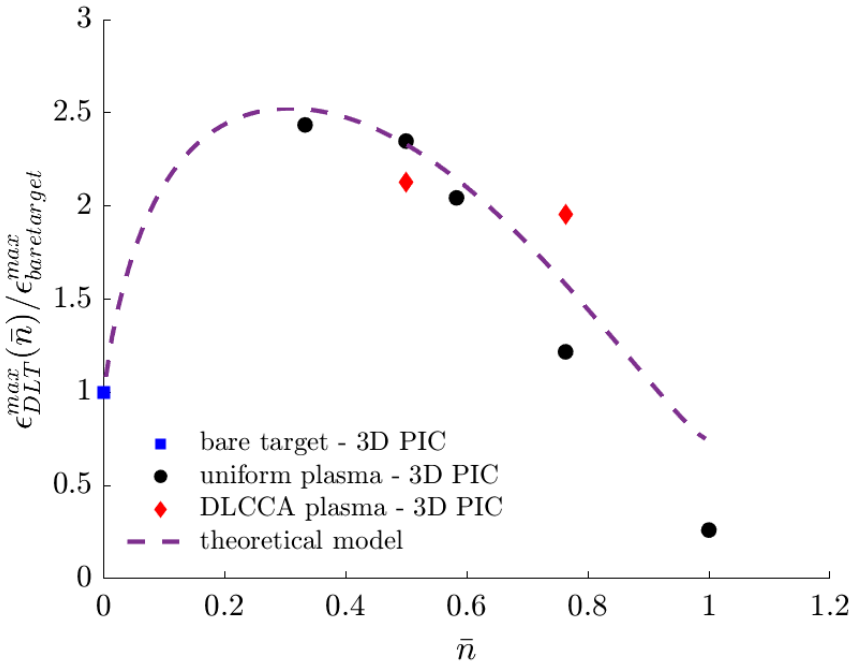

Figure 5.12: Maximum proton energy obtained by 3D PIC simulation from DLTs with variable density and structure (uniform in black and nanostructured in red) normalized to the bare target maximum proton energy. The broken line is the enhancement factor $\bar{E}_{DLT} = E_{DLT}/E_s$ calculated by solving numerically the 3D model of Section 4.2 and taking the ratio of Equation 4.21 to Equation 4.19

energy in the DLT case is higher with respect to the bare target in all the conditions, except the uniform $\bar{n} = 1$ case, which is the one where the maximum in the reflectivity occurs. The enhancement factors are in good agreement with the values numerically calculated from the model of Section 4.2. It should be pointed out that the maximum enhancement factor (about 2.5), obtained with uniform plasma and $n_e/n_c = 1$, is lower than the theoretical optimal value of about 4 predicted by Equation 4.38; indeed, in this PIC simulation campaign only the density was varied keeping fixed the thickness. As explained in Section 4.2, to obtain the highest enhancement factors both density and thickness should be carefully optimized.

Figure 5.12 also indicates that the proton energy obtained with the nanostructured DLT quite deviates from the predicted values and it is less sensitive to the density variations, due to the laser propagation into the foam voids. To support this interpretation the quasi-static model (Equation 4.22) is exploited to estimate the proton maximum energy from the hot electrons temperature and total number retrieved from the simulations.

The results, shown in Figure 5.13, are calculated by approximating the hot electron temperatures as the mean energies of the relativistic part of the spectra ($E > 0.511\ MeV$); in addition only the contribution from the near-critical layer electrons was considered. The $\tilde{n}$ parameter was fixed to $3.4 \cdot 10^3$ in the code units.

The quasi-static model reproduces the observed proton energies with a reasonable approximation; in particular, the more evident trends are captured: the cut-off proton energy from the DLCCA plasma are quite almost independent onto the mean density, on the contrary a reduced energy is observed in the uniform case for higher $\bar{n}$. This indicates that, even if the

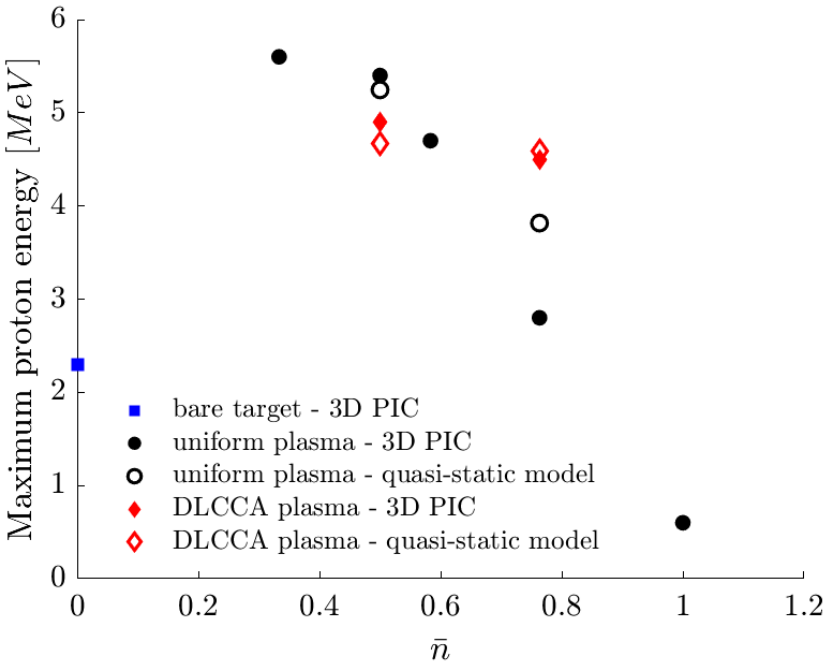

Figure 5.13: Maximum proton energy obtained by 3D PIC simulation from DLTs with variable density and structure (uniform in black and nanostructured in red) normalized to the bare target maximum proton energy. The empty markers refer to proton energies calculated from the quasi-static model (Equation 4.22) using the electron temperatures and numbers from the spectra of Figure 5.11.

nanostructured DLT produces lower energy electrons (due to DLA suppression), the high transmittance and the high number of heated particles enables to form strong accelerating sheath fields and high proton energy enhancements.

In conclusion, high ions energy enhancements with the foam-based DLT (over than 2) are theoretically predicted. Nevertheless, to reach these values a proper control of the near-critical layer must carried out; in particular, the density and thickness have to be tuned in such a way that the laser pulse is slightly reflected and highly converted to volumetric and energetic electrons. Because the theoretical optimal near-critical layer properties depend onto the laser source parameters (intensity, spot size, temporal duration), the near-critical material must be experimentally produced with specific parameters for different experiments; hence, the production technique has to be very versatile and should be able to produce nanofoams in a wide range of densities and thickness. Finally, it is observed in the simulations that non-uniform nanostructures have a little detrimental effect onto the ion energy enhancement, therefore evaluating and optimizing the uniformity grade should be a highly important experimental challenge.

Part III

Experimental investigation on near-critical nanofoams

CHAPTER 6

Advancements in the nanofoams characterization

In this chapter the advancements in the nanofoam characterization are described. The previous Part highlighted that the near-critical layer of the DLT must be produced with precise values of mean density and thickness, in order to obtain the best performances in the enhanced acceleration of laser-driven ions. In addition, the thickness and density optimal values depend onto the particular laser source (in particular the pulse intensity, temporal duration and spot size), thus foams have to be produced with finely tunable properties.

As seen in Section 3.2, the nanofoam mean thickness can be accurately measured by the SEM cross section method; nevertheless no technique allows estimating the thickness spatial uniformity. On the other hand, the foam mean density measurement based on *Energy Dispersive X-ray Spectroscopy* (EDS) relies on empirical or semi-empirical models based on databases of measurements, limited by a low flexibility and by the intrinsic uncertainty of the experimental data. The EDS method also suffers from methodological limitations (see Section 3.2 for details): firstly, the measurement procedure needs a standard reference sample having the same composition of the substrate or the film, which is not always available; secondly, the method needs many acquisitions at different accelerating voltage to find the plateau, which involves a time-consuming procedure.

In Section 6.1 a new method which solves all these issues is proposed: a reference-free measurement, which is based onto a fully theoretical model, enables to obtain film mass thickness values for any kind of material. The theoretical model describes the electron transport in multilayer solids and the consequent X-ray emission by the solution of the Boltzmann equation; its solution uses well characterized physical parameters summarized in Section 6.2. This innovative method is tested with benchmark techniques and an uncertainty analysis is carried out in order to quantify its error (Section 6.3). Finally, the method is applied to the nanofoams case in Section 6.3, where a new characterization capability is shown: the mass thickness mapping, useful to quantify the nanofoam non-uniformity. Nanofoams are there-

fore characterized in different PLD parameter conditions to build an accurate database of the material material density which can exploited for the DLT production.

6.1 Reference-free film mass thickness measurement through Energy Dispersive X-ray Spectroscopy

The aim of the here-proposed method is the retrieval of thin film mass thickness τ and compositions $C_{F,k}$ in a film-substrate geometry, from EDS measurements, without the need of reference samples and multiple voltages measurements. As introduced in Section 3.2, the standard method for the mass thickness determination consists in the measurements of the ratio of characteristic X-rays emitted from the multilayer sample with respect to a reference homogeneous sample, known as *k-ratios* ($k_F = I_F/I_F^{ref}$ or $k_S = I_S/I_S^{ref}$), where the F and S subscripts refer to the film and substrate layers respectively), and from the knowledge of the in depth X-ray generation distributions $\phi(\rho z)$. A different approach is developed in this thesis work: the measurement of different ratios, called *K-ratios* (with a capital 'K' to distinguish it from the conventional k-ratio), of film X-ray intensities over the substrate ones which enables, when the substrate composition $C_{S,j}$ is known (which is a common situation), to overcome the need of reference samples. The method consists of relating the K-ratios to the thin film mass thickness τ and composition $C_{F,k}$ (see Figure 6.1a). This is done through the following equation:

$$K_{k,j} = \frac{I_{F,k}}{I_{S,j}} = \frac{\varepsilon_k C_{F,k} \int_0^{\tau} \phi_{F,k}(\rho z) \exp(-\chi_{F,k}\rho z) d(\rho z)}{\varepsilon_j C_{S,j} \exp(-\chi_{F,j}\tau) \int_{\tau}^{\infty} \phi_{S,j}(\rho z) \exp(-\chi_{S,j}\rho z) d(\rho z)} \tag{6.1}$$

Where $I_{F,i}$ is the intensity of measured X-rays generated in the film by the *k-th* element while $I_{S,j}$ is the substrate intensity of the *j-th* element; ε_k and ε_j are the detector efficiencies at the X-ray energies of the *k-th* and *j-th* elements respectively; $C_{F,k}$ and $C_{S,j}$ are the atomic fractions of *k-th* and *j-th* elements in the film and in the substrate, $\chi = \mu/(\rho\, cos\alpha)$ is the attenuation coefficient (α is the angle of the detector with respect to the interface of the sample) and the subscripts refer respectively to the layer and the X-ray energy.

Thus, if the $\phi(\rho z)$ distributions are known, Equation 6.1 can be numerically solved to obtain, from measured K-ratios, the film mass thickness τ and the film atomic composition $C_{F,k}$; the calculation of the X-ray generation as a function of depth is not straightforward because it depends on the complex physics of electrons multiple scattering with the additional problem of the multilayer geometry, which can introduce strong perturbations to the $\phi(\rho z)$ curves compared to a homogeneous bulk sample. Consequently a theoretical approach should be used to describe the electron transport into multilayer samples and then to derive accurate $\phi(\rho z)$ functions; in particular a kinetic approach is adopted. It should be pointed out that Equation 6.1 is based on the spatial one dimensional approximation, namely that all the quantities depend only on the sample depth variable, which is valid in the cases where τ and $C_{F,k}$ vary slowly with respect to the lateral distribution of X-ray generation (roughly assuming values in the $1 - 100\ nm$ range).

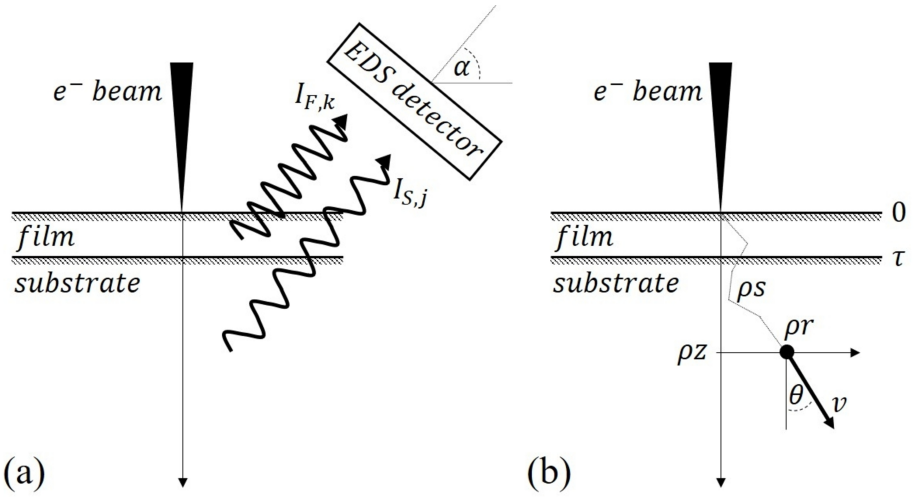

Figure 6.1: Scheme of the problem geometry. In (a) the characteristic X-rays emission and measurement is represented, while in (b) a sample electron trajectory is shown, with the variables that are used in the analytical treatment of the electron transport.

The X-ray generation depth distribution $\phi(\rho z)$ can be calculated with a kinetic approach from the knowledge of the electron distribution function $F(\vec{r}, \vec{p}, t)$, which solves the Boltzmann transport equation. We exploit the problem symmetries, by reference to Figure 6.1b, to neglect the lateral spatial coordinates x and y; then, if we express the momentum by the energy and the orientation, within the spherical coordinates, we can also neglect the azimuthal angle φ. In addition, it is useful to relate the time to the path travelled by an electron via its velocity. In these new coordinates the number of variables of the electron distribution function are thus reduced from 7 to 4: one spatial dimension, two momentum dimensions and one time variable, $F(\vec{r}, \vec{p}, t) \rightarrow F(z, \vartheta, E, vt = s)$, where z is the depth, ϑ the angle of the velocity vector with respect to the z axis, E the energy and s the path length travelled by the electron. Finally, it is more convenient to express the spatial variables in terms of mass and we obtain $F(\rho z, \vartheta, E, \rho s)$. Accordingly, the $\phi(\rho z)$ function is calculated as an integration of the distribution function over all the variables except ρz, with a weight function which represents the microscopic ionization cross section σ_{ion}, multiplied by the fluorescence yield ω, the atomic fraction C and the atoms number density, namely the number of atoms per unit volume:

$$\phi_{F/S,i}(\rho z) = \frac{\omega_{F/S,i} C_{F/S,i} N_{av}}{A_{F/S,i}} \int_0^{Ve} \int_0^{\rho s_R} \int_0^{\pi} F(\rho z, \theta, E, \rho s)\, \sigma^{ion}_{F/S,i}(E)\, sin\theta d\theta d(\rho s)\, dE \tag{6.2}$$

Where N_{av} is the Avogadro number and A the atomic weight (in mg/mol units), Ve is the initial electron energy (in keV units), which corresponds to the accelerating voltage times the electron charge, while ρs_R is the electron mass range (which can be calculated using an empirical relation or the stopping power integration [105]) in mg/cm^2 units. Then $\phi(\rho z)$ has the units of $1/(mg/cm^2)$ and, considering that each energetic electron carries e charge, we can also normalize the distribution to the electron gun current and express it in

$1/(\mu A\ mg/cm^2)$ units. In order to make feasible the determination of F via the Boltzmann transport equation, some useful assumptions can be exploited, in order to further simplify the equation:

- The electrons collide with atoms in two decoupled ways: elastic and inelastic collisions
- The elastic collisions change the electron trajectories without affecting the electron energies (we neglect the atom recoil energy)
- The inelastic collisions make the electrons lose energy without affecting their trajectories (the momentum transfer is negligible with respect to elastic collisions)

These assumptions are generally considered reasonable (see Reference [106] for a detailed justification) and they enable to separate the electron distribution function:

$$F\left(\rho z, \vartheta, E, \rho s\right) = f\left(\rho z, \vartheta, \rho s\right) g\left(E, \rho s\right) \tag{6.3}$$

Including this relation in the Boltzmann equation and applying the variable separation method we obtain two coupled transport equations:

$$\frac{\partial f}{\partial\left(\rho s\right)} = -\vec{u} \bullet \nabla_{\rho r} f + \left(\frac{\partial f}{\partial\left(\rho s\right)}\right)_{coll} \tag{6.4}$$

$$\frac{\partial g}{\partial\left(\rho s\right)} = \left(\frac{\partial g}{\partial\left(\rho s\right)}\right)_{coll} \tag{6.5}$$

Where $\vec{u} = \vec{v}/v$ and $\nabla_{\rho r} = \frac{\partial}{\partial \rho x}\hat{i} + \frac{\partial}{\partial \rho y}\hat{j} + \frac{\partial}{\partial \rho z}\hat{k}$ is the gradient operator with respect to the mass coordinates. From Equation 6.4, expressing the integral of collisions and expanding in power series [107], an equation which describes the elastic multiple scattering process can be derived:

$$\frac{\partial f(\rho z, \theta, \rho s)}{\partial(\rho s)} = -cos\theta \frac{\partial f(\rho z, \theta, \rho s)}{\partial(\rho z)} + \frac{1}{sin\theta}\frac{\partial}{\partial\theta}\left(sin\theta \frac{\partial}{\partial\theta}\left(\frac{f(\rho z, \theta, \rho s)}{\rho\lambda_{tr}(\rho z, \bar{E})}\right)\right) \tag{6.6}$$

Where $\rho\lambda_{tr}$ is the mass transport mean free path, which is a functional of the differential elastic cross section $\partial\sigma_e\left(\theta, E\right)/\partial\theta$:

$$\frac{1}{\rho\lambda_{tr}}\left(E\right) = \frac{N_{av}}{A_r}\int \pi\left(1 - cos\theta\right)\frac{\partial\sigma_e\left(\theta, E\right)}{\partial\theta}\sin\theta d\theta \tag{6.7}$$

The dependence of the transport mean free mass path on the depth variable is due to the multilayer geometry, so this parameter follows a piecewise trend along ρz. It should be noted that the coupling between the two transport equation is mediated by the $\rho\lambda_{tr}$ parameter because it is evaluated at the mean energy $\bar{E} = \int E\ g\left(E, \rho s\right) dE$ which is calculated from the solution of Equation 6.5, which describes the electron energy loss process. The energy transport problem could be solved with the *continuous slowing down approximation* (CSDA), which enables to express the energy with a one-to-one relation to the path length; however,

this treatment oversimplifies the problem, where the electron energy spectrum broadens after few inelastic collisions and consequently the energy straggling plays an important role. Thus, in order to take into account the energy straggling we can express Equation 6.5 with the following relation:

$$\frac{\partial g\left(E,\rho s\right)}{\partial\left(\rho s\right)}=-g\left(E,\rho s\right)\int_{0}^{E}\frac{\partial\sigma_{i}\left(E,W\right)}{\partial W}dW+\int_{0}^{Ve-E}\frac{\partial\sigma_{i}\left(E+W,W\right)}{\partial W}g\left(E+W,\rho s\right)dW \tag{6.8}$$

Where Ve is the initial electron energy, while $\partial\sigma_i\left(E,W\right)/\partial W$ is the differential inelastic scattering cross section which expresses the probability of an electron of energy E to lose energy W in an inelastic collision. In the literature several approaches have been proposed to describe the straggling distribution as a function of the path travelled by charged particles, as the Gaussian model or the Landau distribution [108]. These models, however, suffer from some limitations, as the low accuracy at high travelled path and the difficulty in including the multilayer geometry in the calculation; for this reason we decided to adopt the convolution method which is widely regarded as the most accurate approach to calculate the exact theoretical straggling distribution, being only limited by the accuracy of the numerical solution and the uncertainty on the knowledge of the differential inelastic scattering cross section.

The convolution method consists in calculating via a numerical method the energy spectrum after a given path $\Delta\rho s$, as the sum of the energy loss spectra due to n_{ic} inelastic collisions, multiplied for the related probability, given by the Poisson distribution. In detail, the treatment is based on the calculation of the mass inelastic mean free path:

$$\frac{1}{\rho\lambda_{ic}}\left(\bar{E}\right)=\frac{N_{av}}{A_{r}}\int_{0}^{\bar{E}}\frac{\partial\sigma_{i}\left(\bar{E},W\right)}{\partial W}dW \tag{6.9}$$

And then calculating the mean number of inelastic collision in a given mass path length as $n_{ic}=\Delta(\rho s)/\rho\lambda_{ic}$. Thus, starting from a initial monoenergetic distribution, after n_{ic} collisions the energy spectrum will be given by the n_{ic}-fold convolution of the differential inelastic cross section:

$$w^{0}\left(E\right)=\delta\left(E-eV\right) \tag{6.10}$$

$$w^{k+1}\left(E\right)=\int_{0}^{E}\frac{\partial\sigma_{i}\left(E,W\right)}{\partial W}w^{k}\left(E+W\right)dW \tag{6.11}$$

And taking into account also the statistics of collision number, namely the Poisson distribution, we finally obtain the equation that describes the electron energy straggling:

$$g(\rho s+\Delta(\rho s),E)=\int_{0}^{E}g(\rho s,E')\sum_{k=0}^{\infty}\frac{{n_{ic}}^{k}e^{-n_{ic}}}{k!}w^{k}\left(E'\right)dE' \tag{6.12}$$

It should be noted that this equation is coupled with the spatial transport equation (6.6) because of the multilayer geometry, which is addressed in detail the next Section.

6.2 Electron transport model solution

6.2.1 Numerical solution

Equations 6.6 and 6.11 are coupled and their solution is carried out numerically at the same time. Equation 6.6 is solved with an explicit finite difference scheme: a first order accuracy upwind scheme on the ρz axis and a centered second order accuracy scheme on the θ axis [109]. The scheme is solved onto the grid $\rho z \times \theta$, with 80×40 cells over the ranges $[0, \rho s_R] \times [0, \pi]$, with the following initial and boundary conditions:

$$f(\rho z, \theta, \rho s) = \delta(\rho z)\,\delta(\theta) \quad \text{at } \rho s = 0 \tag{6.13}$$

$$f(\rho z, \theta, \rho s) = 0 \quad \text{at } \rho z = 0 \quad \text{and } 0 \leq \theta < \pi/2 \quad \text{and } \rho s > 0 \tag{6.14}$$

$$f(\rho z, \theta, \rho s) = 0 \quad \text{at } \rho z = \rho s_R \tag{6.15}$$

$$\frac{\partial f(\rho z, \theta, \rho s)}{\partial \theta} = 0 \quad \text{at } \theta = 0,\ \pi \tag{6.16}$$

The first condition is the initial one, where electrons are all at the surface point without angular dispersion; the meaning of the second condition is that there is not injection of new electrons at the surface after the initial 'time' (when $\rho s = 0$) , while it is possible to have electrons escaping from the surface at any 'time' ($f(\rho z, \theta, \rho s) \neq 0$ at $\rho z = 0$ and $\pi/2 < \theta \leq \pi$ and $\rho s > 0$); the third condition imposes that the electron distribution function vanishes at the electron range and the fourth condition expresses that the net distribution angular flux is null at the boundaries, because of the angular symmetry. In order to assure stability to the method, some shrewdness must be carried out. In fact, the electron flow direction changes in the θ axis in correspondence to the $\pi/2$ value and so also the direction of the finite derivative in the ρz axis (first term on the right hand side of Equation 6.6) must change at that grid line. In addition, it should be noticed that the second term of the right hand side of Equation 6.6 plays the role of a diffusion term with a not-constant coefficient $1/\rho\lambda_{tr}\left(\rho z, \bar{E}\right)$ in 'time' and space, which increases dramatically when the energy decreases, namely when ρs increases; to ensure the numerical scheme stability, the *Courant-Friedrichs-Lewy* condition must be fulfilled at each step, namely introducing a variable $\Delta(\rho s)$ step which decreases with the path length: $\Delta(\rho s) < \left(1/\Delta(\rho z) + 2/(\rho\lambda_{tr})_{max}\Delta\theta^2\right)^{-1}$ [109]. The solution in a multilayer geometry is accounted by changing with a piecewise function the value of the $1/\rho\lambda_{tr}\left(\rho z, \bar{E}\right)$ coefficient along the ρz axis. Nevertheless, if the jump discontinuity is too high, some instabilities can arise; for this reason we have expressed all the variables as the mass ones, in a way that the differences of film and subtrate densities do not contribute to this discontinuity and make the solution method more stable.

The numerical solution of Equation 6.11 is straightforward and is carried out over the energy grid, uniformly spaced by $0.05\ keV$. However it should be noted that in the film-substrate geometry we have to distinguish the energy distributions in the different layers, because of their different energy loss, and we have to evaluate the g functions for each layer, namely g_F in the film and g_S in the substrate; in addition, it must be also considered

that the flow of electrons from one layer to another one tends to mix the energy spectra. This phenomenon is taken into account calculating the fraction of electrons, r_F and r_S, respectively coming from the film to the substrate and from the substrate to the film at each path step:

$$r_F(\rho s) = \frac{\int_0^{\frac{\pi}{2}} f(\tau, \theta, \rho s)\, sin\theta cos\theta d\theta d(\rho z)}{\int_\tau^{\rho s_R} \int_0^{\pi} f(\rho z, \theta, \rho s)\, sin\theta d\theta d(\rho z)} \tag{6.17}$$

$$r_S(\rho s) = \frac{\int_{\frac{\pi}{2}}^{\pi} f(\tau, \theta, \rho s)\, sin\theta cos\theta d\theta d(\rho z)}{\int_0^{\tau} \int_0^{\pi} f(\rho z, \theta, \rho s)\, sin\theta d\theta d(\rho z)} \tag{6.18}$$

We first calculate the unperturbed energy distributions in the film and the substrate, $g^0_{S/F}$; then we take into account the mixing phenomenon by averaging the film and substrate distributions by the fractions r_F and r_S:

$$g_F(\rho s, E) = (1 - r_F(\rho s))\ g^0_F(\rho s, E) + r_S(\rho s)\, g^0_S(\rho s, E) \tag{6.19}$$

$$g_S(\rho s, E) = (1 - r_S(\rho s))\ g^0_S(\rho s, E) + r_F(\rho s)\, g^0_F(\rho s, E) \tag{6.20}$$

Once the electron distribution, $F = fg$, is calculated, it is possible to calculate the $\phi(\rho z)$ functions for both the film and the substrate with Equation 6.2, remembering that also the microscopic ionization cross section and the fluorescence yield are described by piecewise functions. As we can see from the example in Figure 6.2, the model enables to calculate the $\phi(\rho z)$ functions in a multilayer geometry with a good agreement with respect to a standard Monte Carlo code (PENEPMA [110]), with two main advantages, namely the faster calculation (about one minute for our model against about two hours for the Monte Carlo code, for a standard personal computer) and the smooth feature of the analytical curve. In addition, it is possible to observe the perturbation in the distributions due to the multilayer geometry with respect to the single layer case. For example, in the shown case, the electron transport features change because of the jump discontinuity in the $1/\rho\lambda_{tr}\left(\rho z, \bar{E}\right)$ coefficient at the τ interface; the diffusion coefficient is higher in the substrate than in the film, then the electrons tend to be more backscattered by the substrate toward the film, and thus the film electron density and $\phi(\rho z)$ distribution increases, with respect to the single layer case.

Finally, once the film mass thickness and composition is fixed, the knowledge of the $\phi(\rho z)$ functions in the film-substrate geometry can be used to simulate the values of the $K_{k,j}$ ratios; the problem is then to minimize the difference between the calculated ratios with the measured ones by EDS, $\widetilde{K}_{k,j}$, namely to minimize the chi squared factors:

$$\chi^2{}_{k,j} = \left(K_{k,j} - \widetilde{K}_{k,j}\right)^2 \tag{6.21}$$

Two different algorithm can be used: the first one is based on the so-called *gradient descent algorithm* [111] which consists of calculating the gradients of the simulated $K_{k,j}$ ratios with respect to the mass thickness and composition and then to obtain, with a linear regression, the next-iteration values of mass thickness and composition; with few iterations this

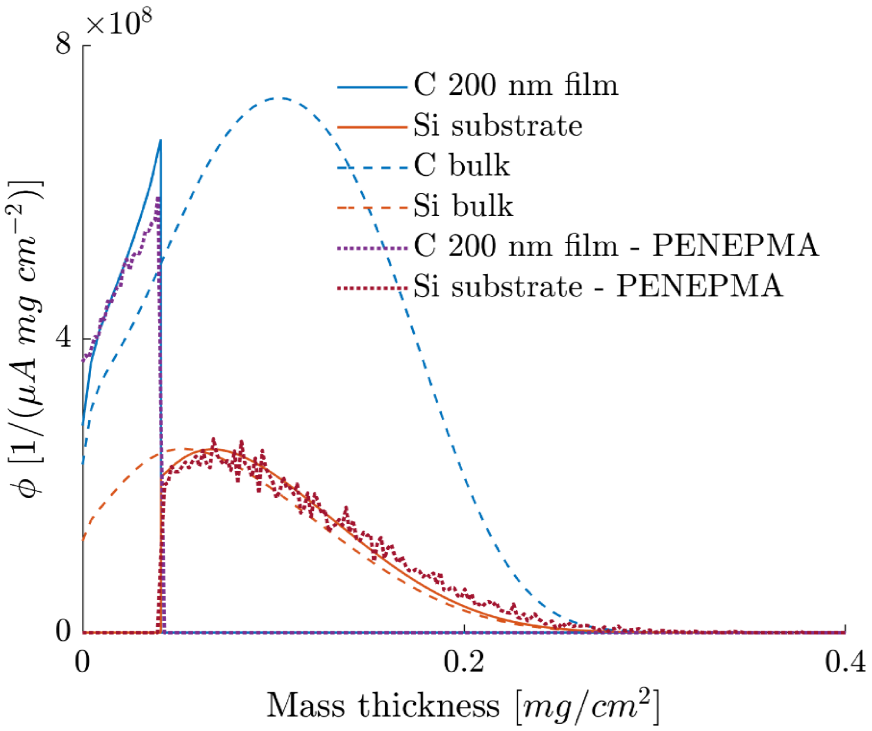

Figure 6.2: The figure shows the calculated $\phi(\rho z)$ distributions by the electron transport model and by PENENPMA (with $2 \cdot 10^6$ trajectories) at an accelerating voltage of 10 kV, in 3 different geometries: a single semi-infinite layer of bulk Carbon by our model (blue dashed curve), a single semi-infinite layer of bulk Silicon by our model (orange dashed curve), a film-substrate geometry made by a bulk density, 200 nm thick, Carbon film on a semi-infinite Silicon substrate by our model (blue and orange continuous curves) and by PENENPMA (violet and red points curves). It should be noted that in the film-substrate geometry the $\phi(\rho z)$ functions are perturbed with respect to the single semi-infinite samples. In addition, the distribution calculated with our model are in good agreement with ones calculated with the Monte Carlo code.

method enables to reach low values of ${\chi^2}_{k,j}$ and obtain a measurement of τ and $C_{F,k}$. The second algorithm consists of calculating the $K_{k,j}$ ratios over a regular grid of mass thickness and composition, in order to obtain a discrete function $K_{k,j}^{m,n,p}(\tau^m, C_k^n, C_j^p)$; then this function is interpolated cubically to retrieve the values of mass thickness and composition which minimize the ${\chi^2}_{k,j}$. The first algorithm is more useful for a fast calculation of film mass thickness and composition in a standard single point measurement, while the second algorithm is necessary when we want to obtain a two-dimensional mass thickness and composition mapping, as the case shown in Section 6.4.

The whole model, consisting in the electron transport solution, in the $\phi(\rho z)$ and in the algorithm for the evaluation of film mass thickness and composition of film-substrate systems, was implemented in a MATLAB application, which requires a low calculation time (a single measurement calculation runs in few minutes in a standard computer), called "EDs for areal Density & composItion Evaluation" (EDDIE).

6.2.2 Physical parameters

The model relies on a number of different physical parameters and, in order to obtain enough accurate outputs, namely the mass thickness and composition, they must be calculated with

high precision models or database. In this subsection these adopted models are briefly described.

Electron elastic scattering: as described in Section 6.1, one of the more important physical input that enables to describe the electron multiple elastic scattering process is the transport mean free path, which appear in equation 6.6. We rely on the calculations based on the solution of the Dirac equation, in the approximation of 'static field', which means that the atomic electron density has spherical symmetry, and the differential cross section is evaluated with the relativistic Dirac-Hartree-Fock potential, that is considered the more reliable model for the atomic potential [112, 113]. The static field approximation is considered very reliable in this case, because the momentum transfer is higher for the collisions with the close bounded electrons; in this way, the solid state potential, which greatly varies from one material to another, can be neglected and the multiple scattering phenomenon is independent from the aggregation state. The values of the transport mean free path calculated from the Dirac-Hartree-Fock differential cross section are tabulated in a recent NIST database [114], that covers the primary electron energy range of $0.05 - 300\ keV$.

Electron inelastic scattering: the other crucial aspect of the model is the electron energy loss described by Equation 6.11; so it is of great importance to have a reliable model for the differential inelastic cross section $\partial\sigma_i\left(E, W\right)/\partial W$. Some analytical model for the inelastic cross section exist, but only for quite simple systems, like Hydrogen or free electron gas [115], and are nevertheless complex to calculate; thus, it seems to us reasonable to make use of a semi-empirical model which combines a sufficient grade of accuracy with the possibility to obtain the differential inelastic cross section for any kind of material with low calculation time [116].

X-rays generation, attenuation and detection: finally, it is fundamental for the calculation of X-ray generation in the sample, to know the electron microscopic ionization cross section $\sigma_{ion}\left(E\right)$ and the fluorescence yield factor ω, which appear in Equation 6.2; and it is of equal importance to know the X-rays mass attenuation coefficient μ/ρ and the detection efficiency ε, present in Equation 6.1. We used a recent analytical formula for the ionization cross section [117] that approximates with 1% of error the theoretical ionization cross section calculated from the relativistic *distorted-wave Born approximation* (DWBA) which consistently accounts the effect of distortion of the projectile wavefunctions caused by the electrostatic atom field and the exchange effects which arise from the indistinguishability of the projectile and the target electrons. The resulting ionization cross sections have been compared to available experimental data, to other theoretical calculations and to empirical and semi-empirical formulas, showing that the DWBA provides a better description of recent measurements. The fluorescence yield ω, defined as the probability that an ionized atom emits a characteristic X-ray, is given by empirical fits of experimental data as a function of the atomic number and the ionized shell. Some reliable databases exist that collect all these data [118, 119], and we decided to use the most recent one. Nevertheless, some uncertainties still exists for low atomic number elements because the few experimental data obtained in

that range quite differ from the tabulated data of the recent databases [120, 121]; we noticed that for $Z \leq 8$ the older database values for fluorescence yield are more consistent with experimental data, for this reason we decided to integrate these values in the more recent database. The X-rays mass attenuation coefficients μ/ρ are tabulated for all elements over the energy range $0.05 - 30\ keV$ [122] and their values are considered very reliable because they are based on a large quantity of experimental data and established theoretical calculations. The X-rays detection efficiency ε depends on the intrinsic detector energy response and the detector window transmittance; these quantities depend on the characteristic X-ray energy and nominal values are given by the detector manufacturer. Nevertheless, these values vary for each detector and they can also change with the aging of the instrument; for this reason some uncertainty should be expected on this parameter.

6.3 Model validation

6.3.1 Uncertainty and sensitivity analysis

The model explained in Section 6.1 for the film mass thickness and composition evaluation is sensible to the physical parameters accuracy; the estimation of τ and $C_{F,k}$ error bars requires an uncertainty analysis, which consists in the propagation of the parameters error onto the final output. Furthermore, a sensitivity analysis allows addressing the physical parameters which contribute more to the measurement uncertainty, in order to pave the way to further improvements in the future.

This task is carried out by the preparation (by the ns-PLD introduced in Section 3.1) and characterization of 4 samples composed by a thick substrate (considered semi-infinite) and a film. The samples compositions were chosen in order to cover a wide range of atomic numbers ($Z_F = 6,\ 7,\ 8,\ 74;\ Z_S = 14,\ 42$): Sample 1 is composed of a compact metallic, $64\ nm$ thick, Tungsten film and a metallic Molybdenum substrate, Sample 2 is composed of a compact, $99\ nm$ thick, Carbon film and a Silicon wafer substrate, Sample 3 is an amorphous, $102\ nm$ thick, Tungsten film with Oxygen inclusions on a Molybdenum substrate and Sample 4 is a porous amorphous, $135\ nm$ thick, Tungsten, Oxygen and Nitrogen based film on a Molybdenum substrate. $\widetilde{K}_{k,j}$ ratios were calculated from EDS measurements of each sample at different accelerating voltages; the measurement conditions were fixed to $120\ s$ acquisition time and we selected the K lines for Carbon, Oxygen, Nitrogen and Silicon, while we used the sum of L_α and L_β lines for Molybdenum and M_α line for Tungsten.

Firstly, a Monte Carlo uncertainty and sensitivity analysis (depicted in Figure 6.3a) is carried out [123], using as inputs the experimental $\widetilde{K}_{k,j}$ ratios measured from Sample 1 at the accelerating voltages of $10,\ 20,\ 30\ kV$. We assume a gaussian distribution function on physical parameters errors, with reasonable standard deviation values assumed from the relative cited literature works and summarized in Table 6.1, and a Poisson distribution on the $\widetilde{K}_{k,j}$ ratios error; then we extract at each Monte Carlo iteration a different value for each physical parameter following its error distribution, and we obtain different τ and $C_{F,k}$ values

at each iteration. With a sufficiently high number of iterations (in the shown case $N_{it} = 200$) we achieve to find an uncertainty distribution on the output values and consequently we can estimate the standard deviation, namely the error bar.

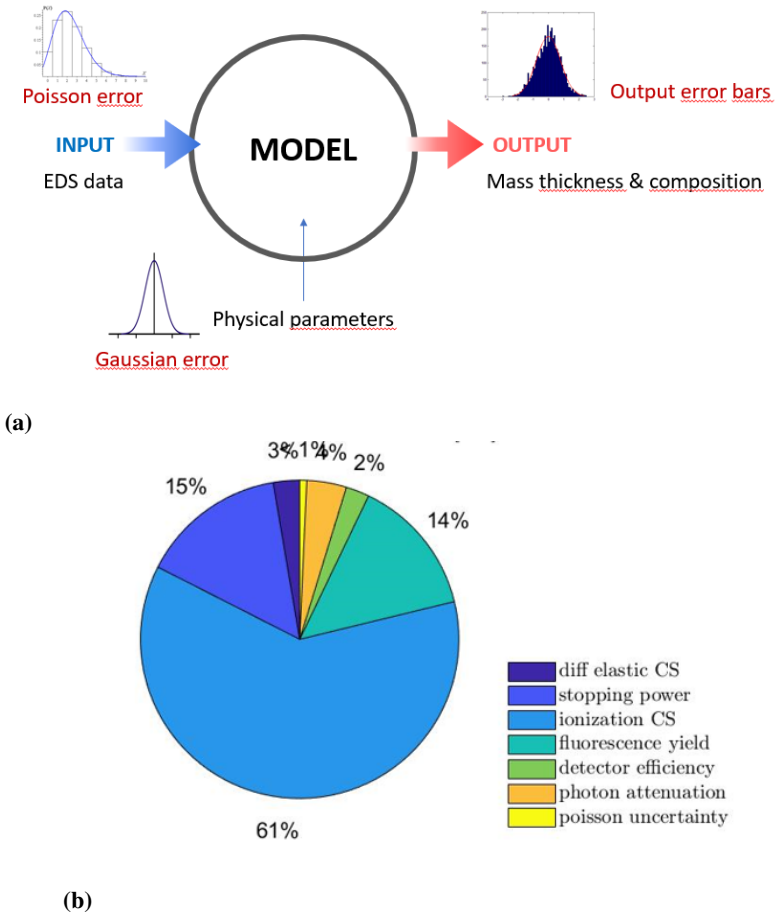

Figure 6.3: (a) Scheme of the Monte Carlo uncertainty analysis. (b) An example of variance decomposition pie chart.

From the results of Table 6.1, it should be noted that higher accelerating voltage measurements intrinsically have higher error values. Moreover, we carry out the output variance decomposition in order to determine which physical parameters contribute more to the output uncertainty. For example, in the case of Table 6.1, the parameters that contribute more to the mass thickness error are the inelastic scattering cross section, which decreases with voltage, the ionization cross section and the fluorescence yield, which increase with accelerating voltage; thus, to further improve the model, the accuracy of these three parameters should be increased.

Moreover the Monte Carlo sensitivity analysis enables to estimate the linearity of the model with respect to the errors; in the above mentioned case, we see that this factor is always near 1 and we can reasonably conclude that the model error behaviour is quite linear. This useful result can be exploited to simplify the uncertainty analysis, in fact in the linear error models the partial derivative analysis can be carried out, which is simpler and faster to perform compared to the Monte Carlo method. Thus, the error bars reported in the following

Accelerating Voltage [kV]	**10**	**20**	**30**	
Output std. deviation [$\mu g/cm^2$]	14.9	17.5	18.5	
Model linearity	1.07	0.98	1.04	
Variance Decomposition				**Assumed Relative Std Deviation**
Elastic scattering CS	0.01	0.03	0.00	0.10
Inelastic scattering CS	0.50	0.15	0.11	0.20
Ionization CS	0.39	0.61	0.58	0.10
Fluorescence yield	0.03	0.14	0.11	0.05
Detector efficiency	0.06	0.02	0.13	0.05
Photon attenuation	0.01	0.04	0.07	0.025
Poisson uncertainty	0.00	0.01	0.00	0.01

Table 6.1: Results of the Monte Carlo uncertainty and sensitivity analysis ($N_{it} = 200$) carried out with inputs from Sample 1, with accelerating voltage equal to $10,\ 20,\ 30\ kV$. On the last column the assumed relative standard deviations on the parameters are shown (CS stands for cross section).

Accelerating Voltage [kV]	**4**	**5**	**6**	**8**	**10**	**12**	**14**	**16**
Output std. deviation [$\mu g/cm^2$]	2.1	2.5	2.8	3.7	4.1	4.8	4.5	5.9
Variance Decomposition								
Elastic scattering CS	0.00	0.00	0.00	0.00	0.00	0.00	0.01	0.05
Inelastic scattering CS	0.77	0.58	0.50	0.37	0.42	0.40	0.33	0.11
Ionization CS	0.14	0.23	0.31	0.43	0.35	0.39	0.37	0.35
Fluorescence yield	0.04	0.07	0.09	0.09	0.10	0.09	0.11	0.18
Detector efficiency	0.04	0.07	0.09	0.09	0.10	0.09	0.11	0.18
Photon attenuation	0.00	0.02	0.01	0.01	0.01	0.01	0.05	0.11
Poisson uncertainty	0.00	0.02	0.01	0.01	0.02	0.02	0.02	0.02

Table 6.2: Results of the partial derivative variance decomposition analysis, carried out with inputs from Sample 2.

figures are obtained with this method. In order to confirm the results of the Monte Carlo variance decomposition we carry out the partial derivative variance decomposition also on Sample 2. The results, summarized in Table 6.2, confirm that the errors increase with the measurement accelerating voltage; in addition it should be noted that also in this case the parameters which are more significant for the error generation are the inelastic cross section, the ionization cross section, the detector efficiency and the fluorescence yield. In addition, we see a strong correlation of the increasing uncertainty with the ionization cross section, as the Monte Carlo analysis highlights for the case of Sample 1. For this reason we expect that increasing, with new measurements and better models, the accuracy of the ionization cross section will result in a strong improvement of the new technique.

6.3.2 Experimental benchmarking

The new technique is experimentally validated by the comparison of measurements with other standard and reliable techniques. The 4 prepared samples were characterized (film mass thickness and compositions) with standard techniques, namely the EDS for the composition measurements (carried out at $5\ kV$) and the *X-Ray Reflectometry* (XRR) and standard weighting techniques for the mass thickness evaluation. In particular the XRR is a standard technique which enables to calculate with high accuracy the electronic density and the thickness of planar thin films and it consists in the collection of monochromatic X-rays reflected

by the multilayer sample.

In order to validate the technique reliability we made EDS measurements at many values of accelerating voltage for each sample and we collected the results in Figures 6.4, 6.5, 6.6. For the Samples 1, 2, 3 (Figures 6.4, 6.5) we used the XRR technique measurements as a benchmark thanks to its high precision and the data reported on the abscissa is the mass thickness, while for Sample 4 we used a standard weighting procedure, because the high roughness of this sample prevents the use of XRR, and the reported data in the abscissa is the density; because the new technique enables to retrieve the mass thickness, the density was calculated by $\rho = \tau/t$, where the film thickness t was measured with cross section SEM image.

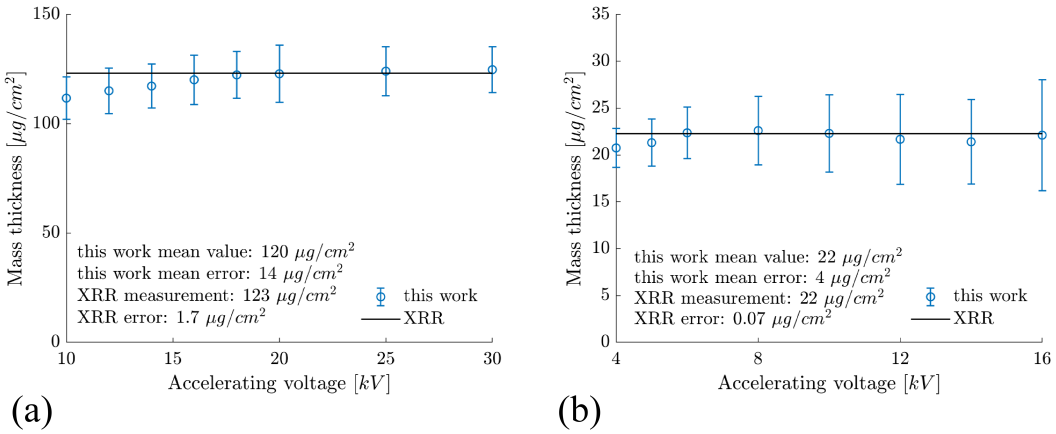

Figure 6.4: Figure (a) shows the mass thickness of Sample 1 (Tungsten, 64 nm thick, film onto Molybdenum substrate), measured by our method (points in blue) at different accelerating voltages, and by the XRR (line in black). Figure (b) shows the mass thickness of Sample 2 (Carbon, 99 nm thick, film onto Silicon substrate), measured by our method (points in blue) at different accelerating voltages, and by the XRR (line in black). On the graphs the mean value obtained by our method, the mean value of its error bars, the value measured by XRR and its error are displayed.

All the measured samples prove that the new method mass thickness measurements agree with the benchmarks inside the error bars, calculated with the uncertainty analysis. We see that at low voltages measurements there is a correlation between the mass thickness and the accelerating voltage and we believe that it is caused by the effect of the inaccuracy of inelastic cross sections at low energy values; this point is justified by the fact that at low voltages the sensitivity analysis shows a prevailing role in error generation by this physical parameter (see Table 6.1 and 6.2). Nevertheless all the measurement fluctuations with respect to the accelerating voltage are all less then the error bars; accordingly, it is reasonable to state that the new technique can be used, at the limit, with only one accelerating voltage measurement, as opposed to other EDS-based methods which need many voltages to obtain accurate results. The mass thickness errors, calculated by the uncertainty analysis, show lower absolute values for the case of Sample 2 with respect to the other ones. This effect is probably caused by lower values of accelerating voltages used for Sample 2 characterization (as explained in Section 4.1, the error slowly increases with the accelerating voltages), and

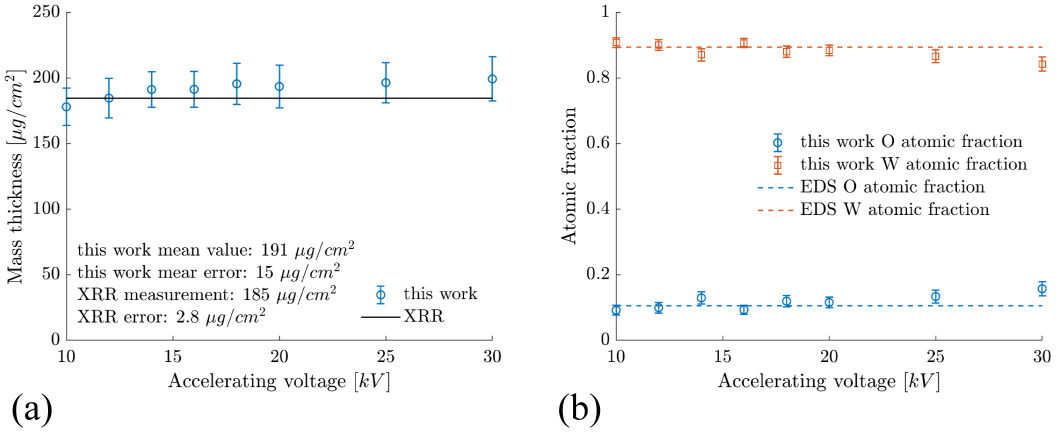

Figure 6.5: Figure (a) shows the mass thickness and figure (b) the composition of Sample 3 (Tungsten with Oxygen inclusions, 102 nm thick, film onto Molybdenum substrate), measured by our method (points in blue and orange) at different accelerating voltages, and by the XRR (line in black) and EDS (blue and orange dashed lines). On the figure (a) the mean value obtained by our method, the mean value of its error bars, the value measured by XRR and its error are displayed.

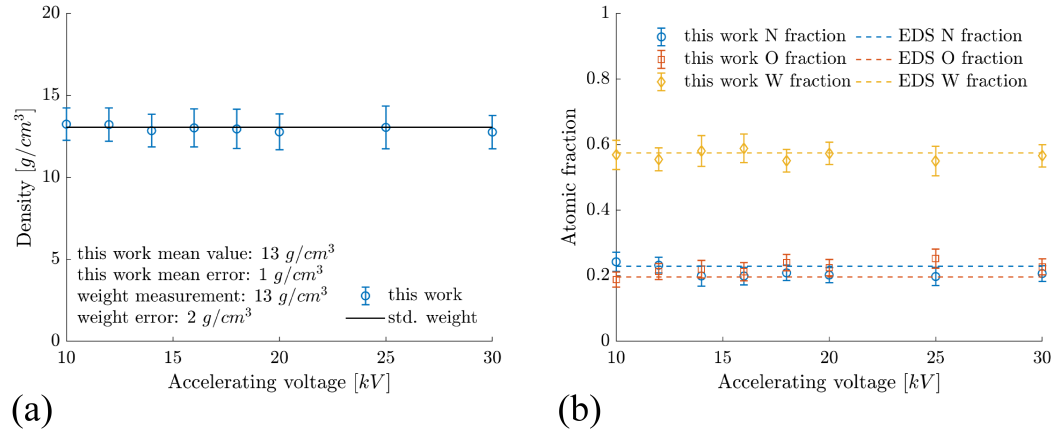

Figure 6.6: Figure (1) shows the density and figure (b) the composition of Sample 4 (Tungsten with Nitrogen and Oxygen inclusions, 135 nm thick, film onto Molybdenum substrate), measured by our method (points in blue, orange and yellow) at different accelerating voltages, and by the standard weight measurement (line in black) and EDS (blue, orange and yellow dashed lines). On the figure (a) the mean value obtained by our method, the mean value of its error bars, the value measured by XRR and its error are displayed.

by the lower mass thickness of the film (lower by a $1/5$ factor with respect to the other samples). In all the cases, the mass thickness errors are higher by at least of one order of magnitude with respect to XRR errors, but it should be taken into account that the method does not suffer from limitations due to film roughness, as for the case of Sample 4 which could not be characterized by XRR; in addition, our technique enables to retrieve at the same time the film composition, which is not determined by XRR. Moreover, we point out that the error bars values lie in the range $2 - 20$ $\mu g/cm^2$, in all the shown cases. This value is comparable to the resolution of nuclear standard techniques ($\sim$ 10 $\mu g/cm^2$) such as *Rutherford Backscattering Spectrometry* (RBS) [124] and *Time Of Flight – Elastic Recoil*

Detection Analysis (TOF-ERDA) [125]. Finally, it should be noted that the composition measurements of Sample 3 and 4 (Figures 6.5 and 6.6) are in agreement with the standard EDS composition measurement within few percentage points. Nevertheless, there are some little deviations from the benchmark for higher accelerating voltage values; the variance decomposition analysis (data not shown) indicates that, also in this case, the ionization cross section increases with the accelerating voltage and it is responsible for about the 50% of the error. In addition, we observe that the errors are higher for the Sample 4 with respect to Sample 3, probably for the higher number of elements in that film. Thus, we believe that the knowledge of the ionization cross section parameter should be enhanced in order to finely characterize the composition of films with a large number of elements.

6.4 Application to the nanofoams characterization

Finally the new technique is applied to the nanofoam characterization, in particular a new tools is exploited: the mapping of mass thickness and composition. A Carbon nanofoam is deposited onto a Silicon substrate with a mean density near $20\ mg/cm^3$ and a mean thickness of $5\ \mu m$; this CNF is featured by with a very high roughness ($\pm\ 3\ \mu m$ over the μm lateral scale), which makes this kind of material very difficult to characterize with standard techniques, such as XRR or high sensitivity balances, as introduced in Section 3.2.

The capability of measuring EDS map from a surface over a grid is exploited to retrieve two-dimensional profiles of $\widetilde{K}_{k,j}$ ratios with a fixed accelerating voltage value ($5\ kV$), which are used, through our method, to retrieve a film mass thickness and composition maps. Figure 6.7 shows the mass thickness and composition measurements in comparison with the relative SEM image; it should be observed that the method enables to obtain a mass thickness map (with pixel dimension equal to $300\ nm$) which is in agreement with the qualitative information given by the electron microscope image. As the mass thickness map highlights the film roughness features, we can consequently state that the EDS measurement resolves the film mass thickness variation over the pixel scale; this means that the film respects the hypothesis of slowly varying mass thickness along the transversal direction. This innovative capability is quite important for the application to DLTs in the laser-driven ion acceleration field, because it enables to quantify the film uniformity, which is an important property in the laser-nanostructure interaction (see Section 5.2).

Another interesting feature is relative to the nanofoam chemical composition, from EDS both Carbon and Oxygen signal is measured and the new method enables to reconstruct the composition map along the transversal direction. In Figure 6.7c it is represented the nanofoam Carbon atomic fraction map; the mean Carbon concentration is about 80%, nevertheless it is observed a higher Oxygen fraction (which is the complementary of the Carbon one) where lower mass thickness is measured. This measurement can be interpreted with the following argument: the foam, thanks to its porosity, adsorbs atmosphere gas into its matrix; where the nanostructure is more open, the density is lower and consequently also the mass thickness and in these positions the more porous material allows for a higher adsorption.

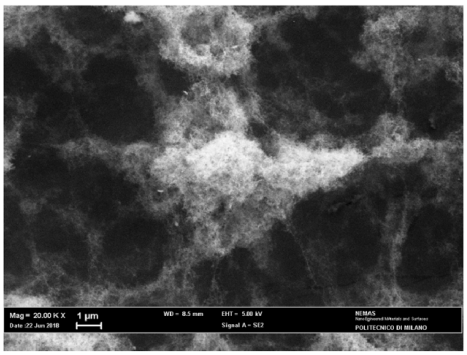

(a)

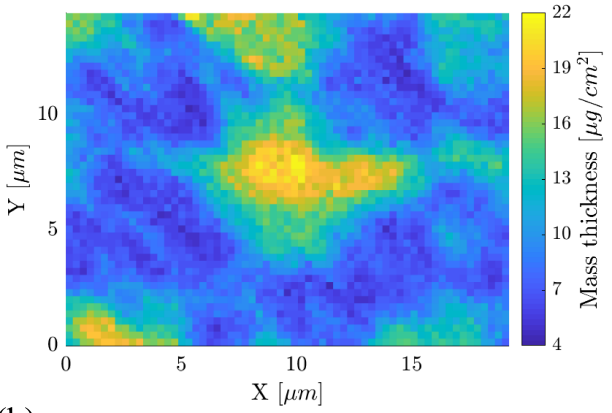

(b)

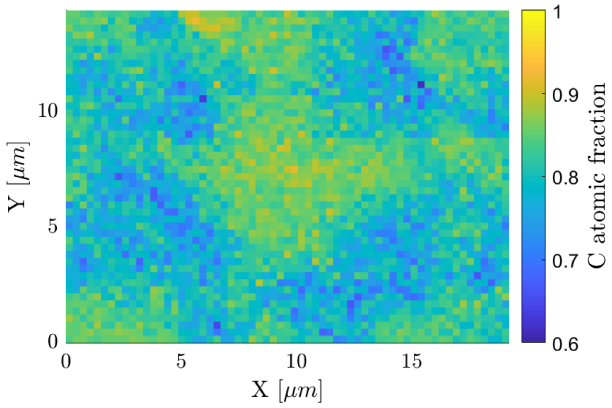

(c)

Figure 6.7: Figure (a) shows a SEM image of a Carbon nanofoam film. Figure (b) shows the film mass thickness map and figure (c) the Carbon atomic fraction map retrieved with the EDDIE software in the measurement condition of 5 kV accelerating voltage and 300 nm pixel dimension. The spatial resolution is sufficient to highlight the high roughness feature of the film.

EDDIE software was used also to characterize ns-PLD-produced foams with different process parameters, in order to build a database useful to deposit near-critical materials with controlled and proper characterized mean density and thickness. Firstly, the ns-PLD laser parameters are fixed to 150 mJ energy on target and 3.4 mm spot diameter to obtain a fluence

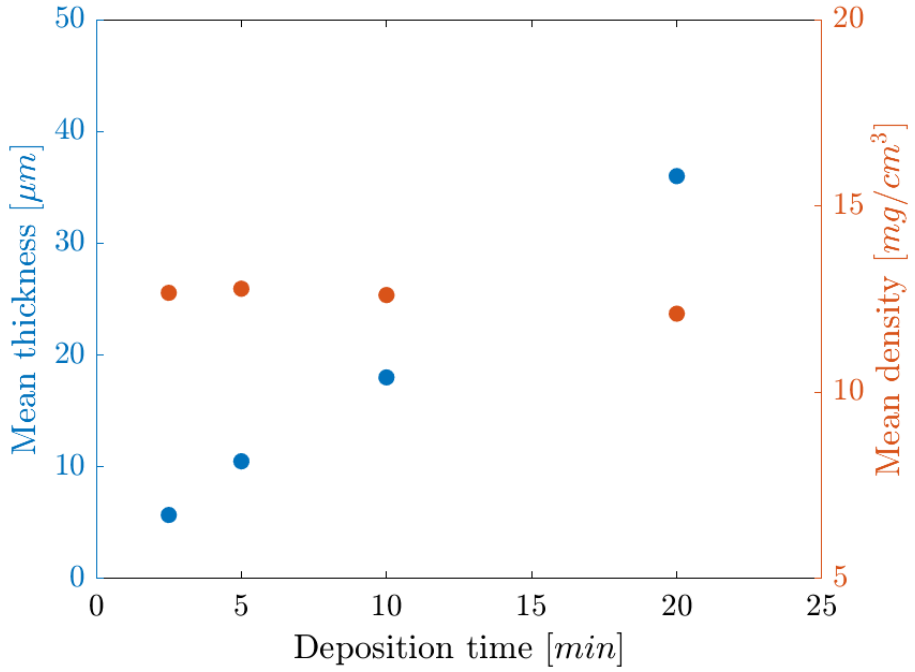

Figure 6.8: EDS-measured foam mean density (orange, right ordinate) and SEM-measured mean thickness (blue, left ordinate) as function of the deposition time. Pulse energy is fixed to 150 mJ, spot diameter to 3.4 mm and Argon ambient gas pressure to 700 Pa.

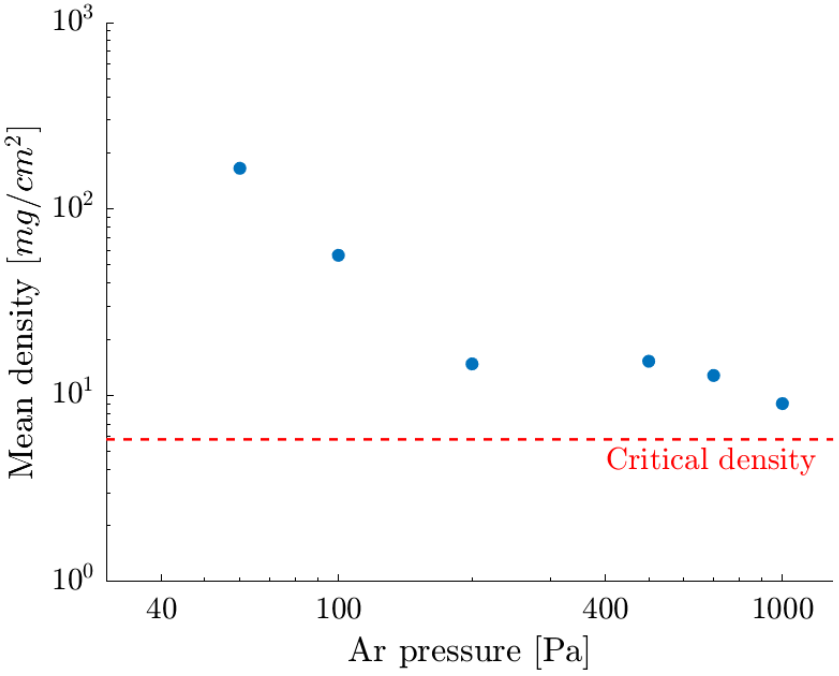

Figure 6.9: EDS-measured foam mean density as function of the Argon gas pressure. Pulse energy is fixed to 150 mJ, spot diameter to 3.4 mm and deposition time to 5 minutes.

on target equal to 1.65 J/cm^2; Argon is used as ambient gas with relatively high pressure equal to 700 Pa. Within these conditions nanofoam is produced with different deposition time (see Figure 6.8); it is observed that the mean density (roughly equal to 12.5 mg/cm^3) does not depend on the deposition time, while the thickness increases linearly with time.

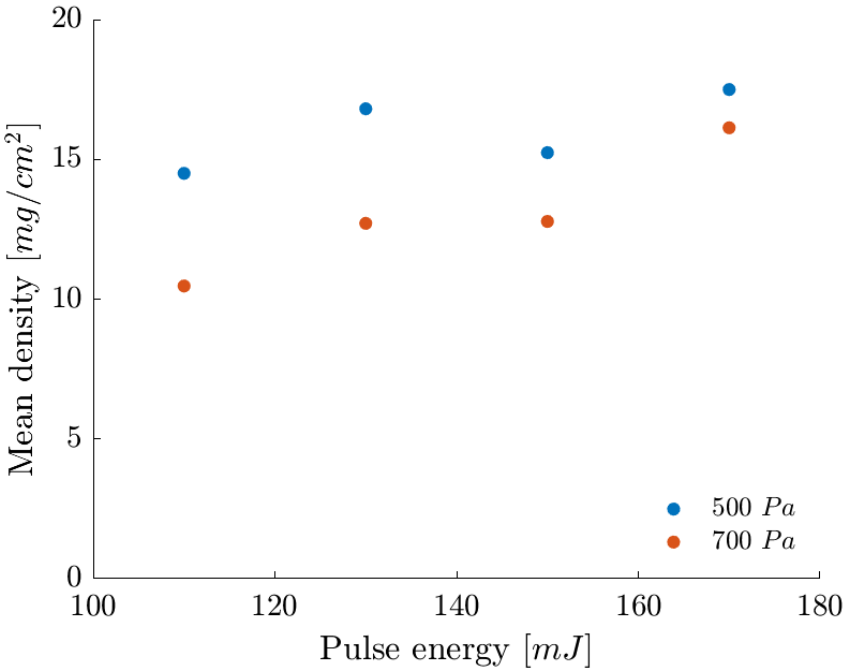

Figure 6.10: EDS-measured foam mean density as function of the pulse energy. Pulse spot diameter is fixed to $3.4\ mm$, deposition time to 5 minutes and gas pressure to $500\ Pa$ (in blue) and $700\ Pa$ (in orange).

Conversely, if all the above-mentioned parameters are fixed and the ambient gas pressure is changed (with 5 minutes as deposition time), a large density variation is observed in Figure 6.9. In detail, by changing the pressure from $60\ Pa$ to $1000\ Pa$, the density sensibly drops from $165\ mg/cm^3$ to $9\ mg/cm^3$, which is about 1.5 the critical density. Nanofoams can therefore be produced with a mean density range over one order of magnitude by simply regulating the gas pressure. It is also noticed that at high gas pressure the foam density tends to reach a plateau, which suggests that increasing further the Argon pressure is not a viable route to reduce further this foam property.

Finally, a last parametric scan with respect to the pulse energy is carried out. The pressure is fixed to $500\ Pa$ and $700\ Pa$, the deposition time to $5\ min$ while the pulse energy is changed from $110\ mJ$ to $170\ mJ$; the results, shown in Figure 6.10, highlight also a energy dependence onto the laser pulse energy (with fixed spot size), with lower density values obtained at lower energy. It should be pointed out that the ns-PLD Q-switch laser, present at the NanoLab, is not able to generate pulses with energy values lower than $110\ mJ$, hence it is not possible to observe if a plateau is reached with the energy as observed for the pressure scan.

In conclusion, this chapter describes the new method for film mass thickness and composition evaluation, and its application to nanofoams. A new capability to measure two-dimensional map can be useful to quantify the nanostructure uniformity, while the more accurate density measurement allowed to build a little database for ns-PLD-produced foams mean density, which can be realized from $1.5\ n_c$ to $30\ n_c$ by tuning the ambient gas pressure. Lower values of density are still not simply achievable; for this reason, a deep study onto

the nanofoam growth process is needed in order to better control the deposition process. The next chapter deals with this investigation and propose a new method to tune the foam density.

CHAPTER 7

Investigation on the nanofoam growth process

In this chapter the investigation on the ns-PLD-produced nanofoam growth process is described. The main aim of this study is to understand if the aggregation happens on the substrate surface or during the plasma plume expansion in the vacuum chamber. Secondly, the gained insights are used to obtain a better control on the nanofoam properties (i.e. density and uniformity).

Section 7.1 reports several experimental results from a PLD deposition campaign and proposes an interpretation of these with the so-called *Snowfall-like growth model*. It also introduces a new parameter to tune the foam density and uniformity, namely the laser *Repetition Rate* (RR); this new degree of freedom would allow enlarging the nanofoam properties space in the future.

In Section 7.2 the Snowfall-like model is used to justify the *Diffusion Limited Cluster-Cluster Aggregation* (DLCCA) model (Section 5.1); the DLCCA structure is compared to the real one both in a qualitative and quantitative way. A brief analysis also allows extracting informations about the materials features and the production limitations.

7.1 Snowfall-like growth model

7.1.1 First stages nanofoam growth

To study the nanofoam aggregation mechanism a first experimental investigation on the first stages growth is carried out. It consists in the deposition of samples with fixed PLD parameters ($150\ mJ$ pulse energy, $1.65\ J/cm^2$ fluence, $700\ Pa$ Argon) and variable deposition time; differently to the scan presented in Section 6.4, the time is chosen in order to have few laser shots and little deposited mass on the substrate. In particular, the PLD laser operates normally at $10\ Hz$ repetition rate, therefore to have number of shots equal to $N_s = 5-10-20-50-100-200$, the deposition time is set to $t_{dep} = 0.5-1-2-5-10-20\ s$.

Some of these produced samples are represented in Figure 7.1; the observed first stages foam growth is featured by the presence of separated micrometric aggregates which, at higher times, coalescence into a continuous film. These aggregates are composed by $10 - 20\ nm$ nanoparticles, as introduced in Section 3.1, and show a fractal structure (see Figure 7.2a). This fractal-like structure is frequently observed in colloids aggregates [126]; this resemblance enables to exploit all the yet-developed tools to analyse and describe them. First of all, fractal aggregates are scale invariant which means that, within proper limits, the structure appears the same over a wide range of scales. This concept can be written by a simple mathematical description, introduced by Hausdorff [127]:

$$N = k_0 \left(\frac{R_g}{a} \right)^{D_f} \tag{7.1}$$

Where N is number of particles with a radius, k_0 is a proportionality constant in the order of unity, R_g is the so-called gyration radius which quantifies the mean aggregate dimension (it is defined as $R_g^2 = 1/N^2 \sum_{n=1}^{N} |\mathbf{r_n} - \mathbf{r_{cm}}|^2$, with $\mathbf{r_n}$ the NP position vector and $\mathbf{r_{cm}}$ the centre of mass vector), while D_f is the Hausdorff number, also commonly called *fractal dimension*. This last parameter can be measured by several techniques, such as light scattering [128] or by the analysis of TEM/SEM images [129]; here the calculation of the so called *Structure Factor* S from SEM images is used to estimate D_f. $S(q)$ is the square of the Fourier transform of the density distribution of the aggregate; thus it is the q-space (reciprocal space with units of the length-inverse) description of the structure. Experimentally it describes scattered intensity as a function of scattering angle [128]. The crucial property of the structure factor for fractals is that:

$$\begin{aligned} S(q) &= 1, && qR_g < 1 \\ &= C(qR_g)^{-D_f}, && qR_g > 1 \end{aligned} \tag{7.2}$$

Where C is a proportionality constant. Thus, Equation 7.2 enables to calculate the fractal dimension of a single aggregate by taking the square of the Fourier transform of a SEM image, sum the intensity of it at the different radial directions (which is the so-called *Power Spectrum*) and calculating the exponent of the power fit. An example of the above calculation is given in Figure 7.2b; here, the estimated fractal dimension is equal to 1.87 which is a typical value for Diffusion Limited Cluster-Cluster Aggregation structures.

As described in Section 5.1, the DLCCA structure is generally formed from particles immersed in a fluid, undergoing to Brownian motion; in this context the only similar condition is given by NPs moving into the vacuum chamber ambient gas ($700\ Pa$ of Argon in this case). This suggests that the fractal aggregates are formed in the vacuum chamber and they later land onto the substrate with a mechanism similar to a snowfall: within this analogy, the fractal aggregate (the snowflake) increases its size by clustering of smaller nanoparticles (supercooled water droplets) while is free to float in a nanoparticle-rich atmosphere (supersaturated air masses); then, the nanofoam film (the snow blanket) grows because the DLCCA

aggregates (the snowflakes) deposit onto the substrate and stick together.

This *Snowfall-like* model is supported by several evidences, for example the tilted SEM image of Figure 7.2c shows three-dimensional features which could be difficulty explained by a surface aggregation, while they are predicted by an in-flight formation.

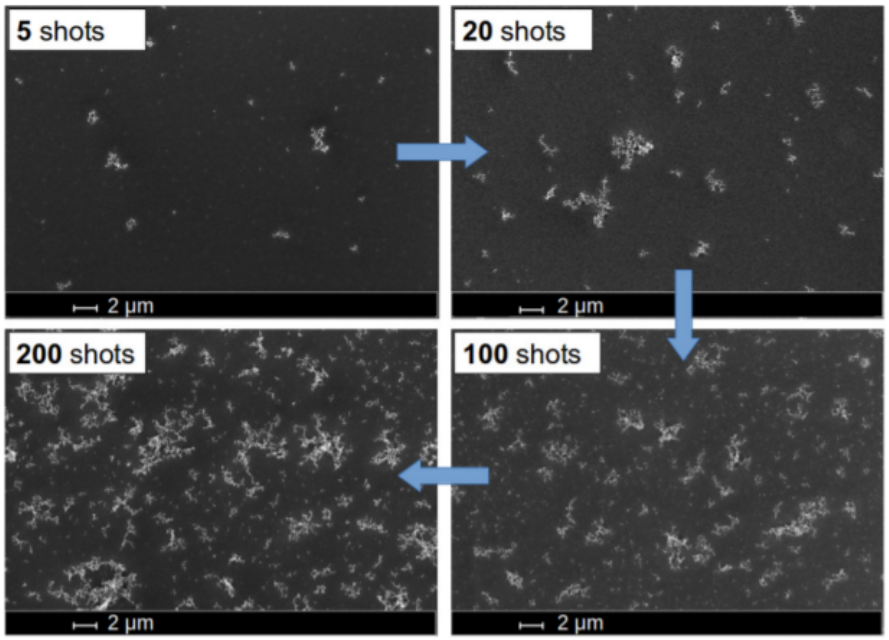

Figure 7.1: Evolution of nanofoam aggregates against the ns-PLD laser shots number; deposition parameter were 700 Pa pressure, 150 mJ pulse energy and 1.65 J/cm^2.

To additionally test this model an analysis onto the aggregates is carried out with respect to the different laser shots number samples. The area A of the single aggregate is calculated by the binarization of SEM images and the calculation of the number of the illuminated pixels; the equivalent radius, which is an estimation of R_g, is found by $R_{eq} = \sqrt{A/\pi}$. By doing this procedure for many aggregates from several SEM images an equivalent radius distribution is found, as shown for example in Figure 7.3a, for each of the above-mentioned shots number series. The results, represented in Figure 7.3b, show that at increasing laser shots number the aggregates mean radius is quite constant while the substrate coverage grows initially linearly and then tends to saturates, due to the coalescence of fractals into the foam structure. Again, this observation is well explained by the snowfall-like model, where aggregates with fixed dimension are formed in-flight and then deposited on the substrate surface.

7.1.2 Aggregates dimension and nanofoam properties

Since the snowfall-like model is reasonably confirmed, a question naturally arises: what the aggregates dimension depends on?

This question could be reformulated in a more proper form, due to the demonstration in the literature [130] that the gyration radius increases with the aggregation time τ_{agg}: which is the fractal aggregation characteristic time?

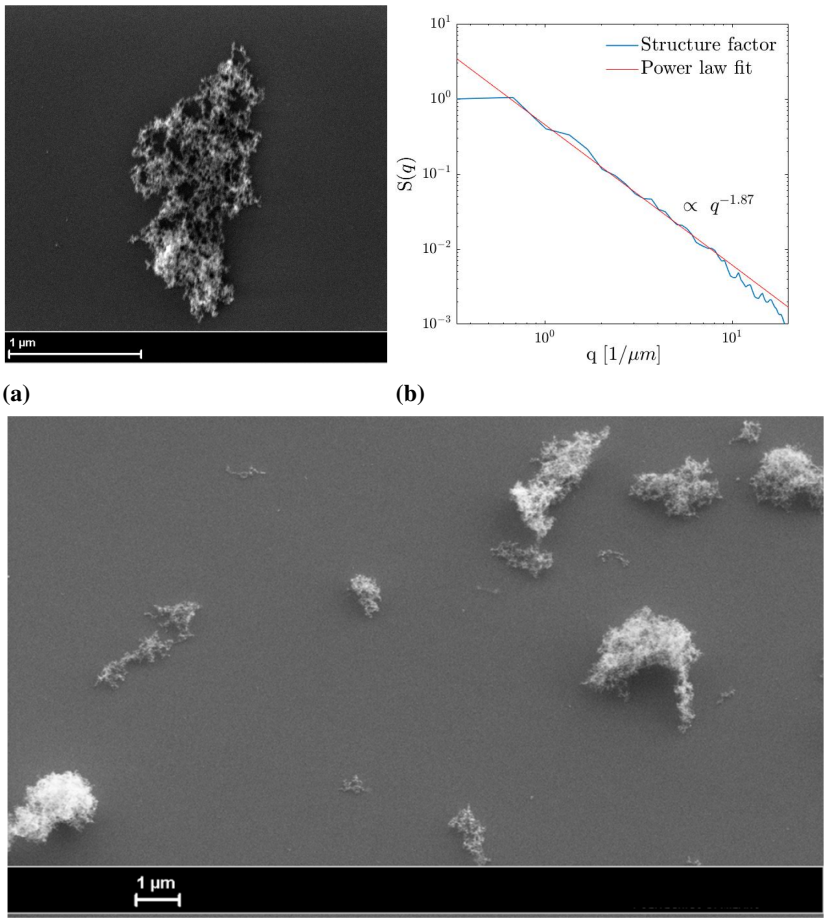

(a) (b)

(c)

Figure 7.2: (a) SEM image of a single aggregate. (b) Structure factor of the aggregate of figure (a); the power fit expontent is reported on the graph. (c) SEM image of several aggregates, taken with 25° tilt angle.

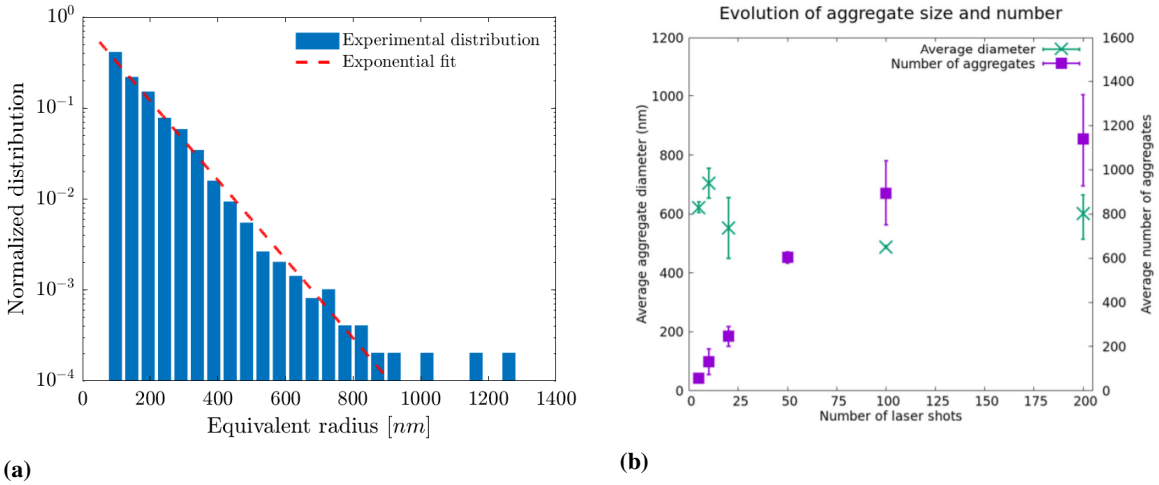

(a) (b)

Figure 7.3: (a) Normalized aggregates size distribution against the equivalent radius. (b) Evolution of aggregates mean size and substrate coverage against the shots number.

To answer this question two additional deposition series are realized; the first with fixed parameters and variable target-to-substrate distance and the second with variable shot-to-shot time (inverse of the RR) and the aggregates dimension in each condition is recorded.

The results are therefore compared to the literature theoretical predictions, in particular to the power law dependence valid for pure DLCCA aggregation, which reads:

$$R_g \propto {\tau_{agg}}^b \tag{7.3}$$

Where the b exponent is theoretically equal to $1/D_f \sim 0.54$. These new investigations aim in particular at observing the mean fractal gyration radius as a function of the different variables to find what is the aggregation time dependent on.

A reasonable hypothesis is to consider the characteristic time equal to the flight time τ_{flight} (in which the aggregates travel from the target to the substrate). Accordingly, this time should be dependent on the target-to-substrate distance d_{tts}; considering the increase of mass of the fractals during the aggregation and the decreasing speed of the plume expansion, τ_{flight} should increase more than linearly with the travelled distance. We can approximate this effects with a power law $\tau_{flight} \propto {d_{tts}}^c$, with $c > 1$. Substituting τ_{flight} into Equation 7.3 we find that $R_g \propto {d_{tts}}^{bc}$ ($bc > 0.54$); this theoretical finding must be compared with experimental results to test the hypothesis.

Figure 7.4a shows the mean equivalent diameter as a function of the target-to-substrate distance d_{tts}: the mean aggregate dimension depends weakly on this variable ($R_g \propto {d_{tts}}^{0.14}$), on the contrary the total substrate coverage remarkably reduced with d_{tts}. The fact that the theoretical prediction is highly incompatible with the experimental observations, demonstrates that the aggregation time can't be represented by the flight time.

Conversely, it is noticed in the shot-to-shot time τ_{sts} experimental series (see Figure 7.4b) that $R_g \propto {\tau_{sts}}^{0.27}$, which is a value more in agreement with the theoretical prediction. The fact that the mean fractal radius depends in a clear way on the laser RR, suggests that the DLCCA mechanism takes place into the ambient gas with a complex succession of phenomena: the laser pulses release in the vacuum chamber atmosphere a large amount of nanoparticles which reach a stable concentration, determined by the pumping flow and the NPs generation rate. When a laser pulse interacts with the target, it generates a strong shock wave in the ambient gas which forces large part of the aggregating fractals to land onto the substrate and releases new NPs in the atmosphere.

This picture is highly qualitative and it doesn't consider complex effects as the transport details, the variable NPs concentration in the vacuum chamber, the possible convective phenomena; this could be a reason for the deviation of the experimental exponent value from the theoretical one.

Despite this non-exhaustive interpretation, the mean gyration radius dependence onto the laser shot-to-shot time opens a new route to control the nanofoam film properties. Indeed, since the foam structure is formed by DLCCA aggregates, their properties determine the film ones, as the mean density and uniformity.

Exploiting Equation 7.1, we can estimate the mean density of the single fractal:

$$\rho_{agg} = \frac{N m_{NP}}{R_g^3} = \frac{k_0 m}{{r_{NP}}^{D_f}} {R_g}^{3-D_f} \tag{7.4}$$

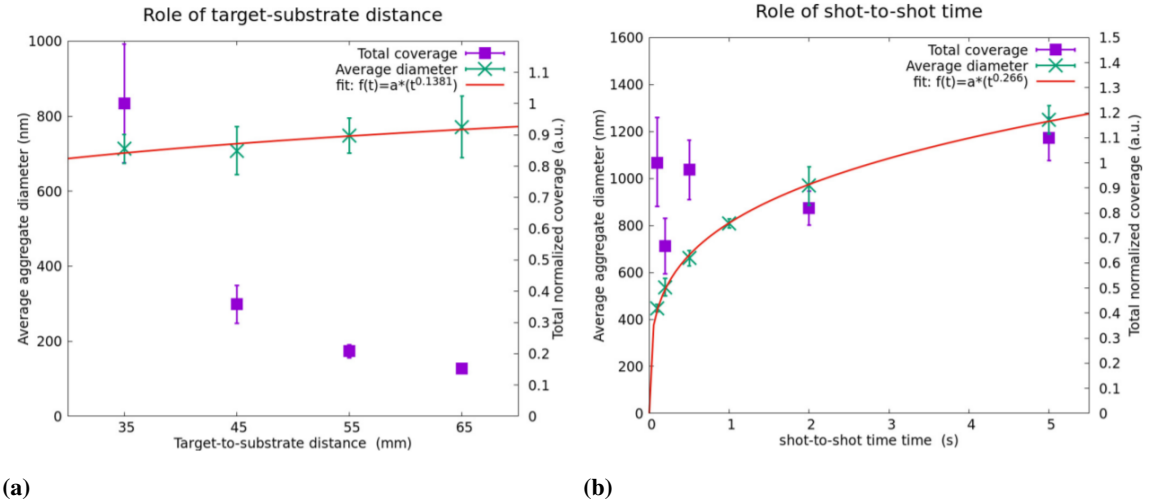

(a) **(b)**

Figure 7.4: (a) Dependence of aggregates mean size and substrate coverage against the target-to-substrate distance. (b) Dependence of aggregates mean size and substrate coverage against the shot-to-shot time.

Where m_{NP} is the nanoparticle mass. Equation 7.4 indicates that larger fractals are featured by lower density; consequently, we expect also lower density foams ρ_{nf} in this condition. At the same time it is reasonable to assume that the nanofoam uniformity characteristic length is given by R_g, which means that lower material density also results in a higher disuniformity.

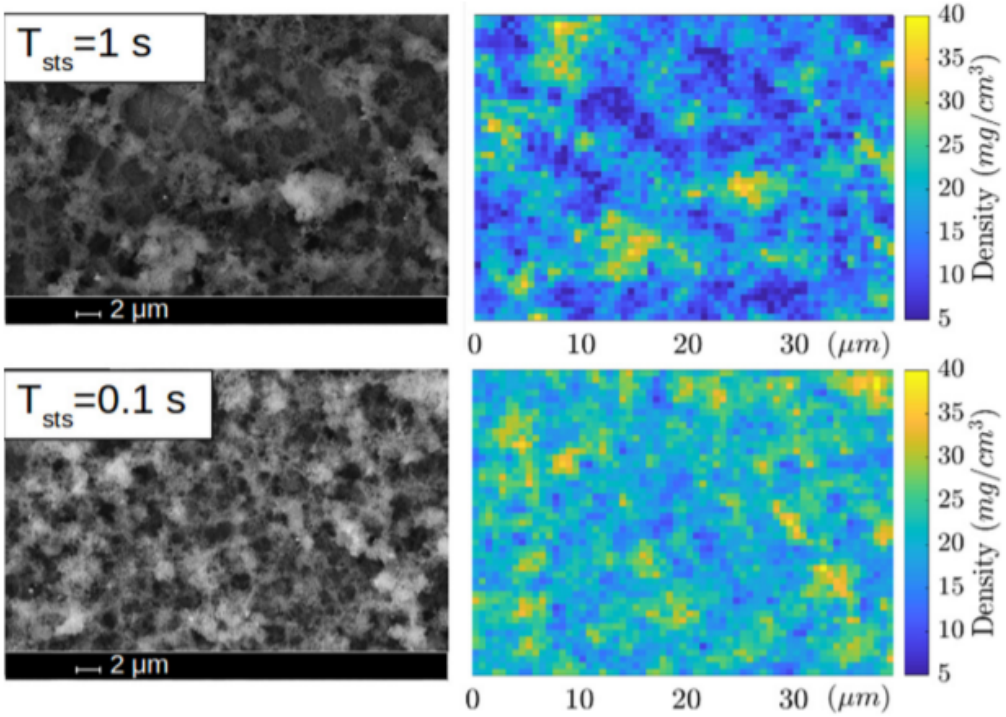

Figure 7.5: SEM images (left side) and EDS density maps (right side) of two Carbon nanofoams deposited with $\tau_{sts} = 1\ s$ (top) and $\tau_{sts} = 0.1\ s$ (bottom). Each deposition is performed with 7000 shots, Argon pressure of 1000 Pa, laser fluence 2.1 J/cm^2, target to substrate distance 4.5 cm.

This argument is tested by producing nanofoams with fixed parameters (200 mJ pulse energy, 2.1 J/cm^2 , 1000 Pa Argon, 7000 laser shots) and RR equal to 10 Hz and 1 Hz,

τ_{sts} $[s]$	$\bar{R}_{eq}^{exp}$ $[nm]$	$\bar{N}$ [Eq. 7.1]	ρ_{nf}^{exp} $[mg/cm^3]$	ρ_{nf}^{DLCCA} $[mg/cm^3]$
1	396	~ 900	14.3	13.4
0.1	247	~ 400	18.7	21.3

Table 7.1: Nanofoam aggregates parameters (equivalent radius $\bar{R}_{eq}^{exp}$ and size $\bar{N}$) in different deposition condition are reported with the relative measured (ρ_{nf}^{exp}) and simulated (ρ_{nf}^{DLCCA}) mean density.

corresponding to $\tau_{sts} = 0.1 - 1\ s$ respectively. The produced films and the relative mass density maps (retrieved with EDDIE, see Section 6.4) are reported in Figure 7.5. The images indicates that the higher τ_{sts} involves a more porous yet disuniform material ($\rho_{nf} = 14.3\ mg/cm^3$); conversely, lower shot-to-shot time allows increasing the film uniformity at the cost of a higher mean density ($\rho_{nf} = 18.7\ mg/cm^3$).

It should be pointed out that this new method to control the foam density and uniformity could be exploited in the future, combined with the standard methods of Section 6.4, to further enlarge the deposited material parameters space.

7.2 Virtual nanofoam structure validation

Experimental results presented in the previous Section suggest that the DLCCA mechanism represents a satisfactory description for the fractal aggregates formation, which are the building blocks of the nanofoam. The hypothesis underling the algorithm described in Section 5.1 are therefore justified. To further verify the goodness of the resulting virtual structure, it is compared to the real nanofoam in terms of visual resemblance and mean density.

The DLCCA algorithm is used to produce fractal aggregates which are deposited in the nanofoam virtual structure box; the fractals size (i.e. number of particles N) is chosen randomly from an exponential distribution with mean size $\bar{N}$. This size is experimentally fixed by the measurement of the mean equivalent radius of SEM images and by the inversion of fractal scaling law (Equation 7.1) with $D_f = 1.85$, $k_0 = 1$ and $r_{NP} = 10\ nm$. Table 7.1 reports the $\bar{N}$ values for two of the nanofoams described in the previous Section, in particular the ones of Figure 7.5: the foam produced with $\tau_{sts} = 1\ s$ has an experimental equivalent radius of about $400\ nm$ which corresponds to fractals with mean size $\bar{N} \sim 900$; on the other hand, the $\tau_{sts} = 0.1\ s$ deposition shows a $\bar{R}_{eq} \sim 250\ nm$ equivalent to $\bar{N} \sim 400$.

The two corresponding virtual foams with these size numbers are generated in a box with size $20\ \mu m\ \times 20\ \mu m\ \times 20\ \mu m$. 2000 fractal aggregates are generated and deposited for both the conditions. The final structures are rendered by the software Ovito [131] and represented in Figure 7.6, where they are compared to the corresponding SEM images. From the qualitative point of view the resemblance is sufficiently satisfactory, since not only the fractal structure is reconstructed, but always the mesoscale differences are reproduced. For example, the $\tau_{sts} = 0.1\ s$ nanofoam is featured by a more uniform structure both in the experimental and virtual images.

Additionally, a quantitative analysis is carried out: the DLCCA nanofoam structure mean density ρ_{nf}^{DLCCA} is calculated and compared to the experimental one. To calculate ρ_{nf}^{DLCCA}

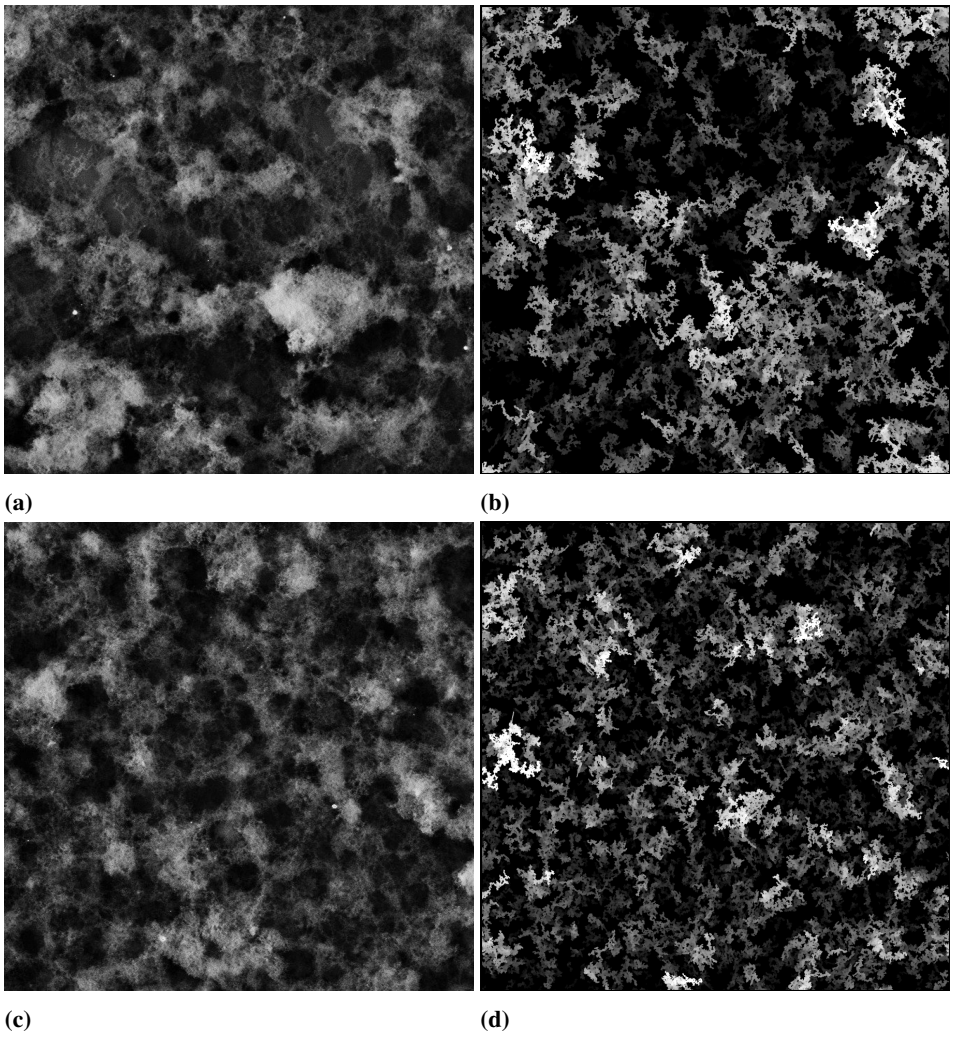

Figure 7.6: Comparison of the real and simulated nanofoams. Figure (a) and (c) show the SEM images of the nanofoams of Figure 7.5, produced with $\tau_{sts} = 1 - 0.1\ s$ respectively. Figure (b) and (d) show the DLCCA foam structure produced with the parameters of Table 7.1 and rendered with Ovito software. All the images are sized $20\ \mu m\ \times\ 20\ \mu m$.

we take the ratio of the mass of the single NP (m_{NP}) multiplied for the number of particles in the box N_{tot}, over the structure volume V: $\rho_{nf}^{DLCCA} = N_{tot}m/V$. It is more convenient to express this relation by normalizing the lengths to the particles diameter $2r_{NP}$, which reads:

$$\rho_{nf}^{DLCCA} = \frac{N_{tot}}{(D/2r_{NP})^2(h/2r_{NP})}\rho_{NP} \tag{7.5}$$

Where ρ_{NP} is the nanoparticle mean density, generally slightly inferior of the bulk one (e.g. for Carbon we take $\rho_{NP} = 2\ g/cm^3$) and h is the nanofoam thickness. Equation 7.5 solution is not as straightforward as it seems because the DLCCA foam thickness is not well defined. To show this point the local number density $n(x, y, z)$ is integrated along the transversal directions to obtain the mean density profile along the heigh z, $\sigma_{nf}(z) = \rho_{NP}\int_0^{D/2r_{NP}}\int_0^{D/2r_{NP}} n(x, y, z)dxdy$; this function is represented in Figure 7.7a for the two DLCCA foams. It is observed that this profile is not featured by a clear cut-off, hence the thickness is not determined in a trivial way; by convention we define the structure

thickness as $h = 2Z_{HM}$, where Z_{HM} is the nanofoam half-maximum thickness which meets the following condition $\sigma_{nf}(Z_{HM}) = 0.5 \max(\sigma_{nf})$.

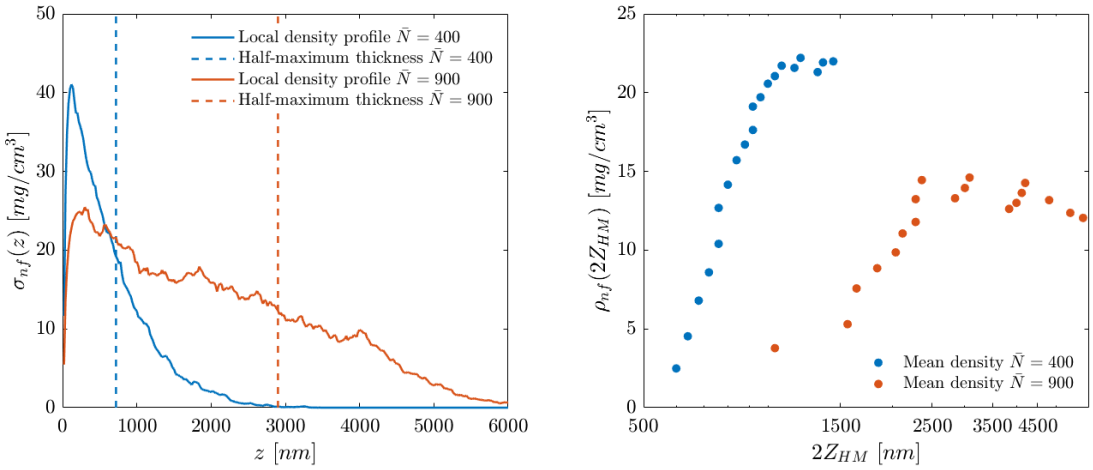

(a) **(b)**

Figure 7.7: (a) Local density profiles $\sigma_{nf}(z)$ for the DLCCA structures shown in Figure 7.6b, mean size $\bar{N} = 400$ (blue line), and Figure 7.6d, mean size $\bar{N} = 400$ (orange line). The dashed lines mark the half-maximum thickness. (b) DLCCA structure mean density ρ_{nf}^{DLCCA} as a function of the half-maximum thickness; the different points are obtained by calculating ρ_{nf}^{DLCCA} and Z_{HM} for different number of deposited aggregates (from 100 to 2000 with steps of 100). The blue and orange points refer to $\bar{N} = 400$ and $\bar{N} = 900$ respectively.

Using this method the DLCCA structure mean density is retrieved for increasing number of deposited fractal aggregates in steps of 100 and showed in Figure 7.7b. It is observed that the calculated values increase with the number of aggregates (and consequently also the thickness h) to reach a saturation value, which is the one reported in Table 7.1; this is due to the initial deposition of separated aggregates onto the substrate, which coalescence at increasing number of deposited units to form a continuous film.

It is worth mentioning that the retrieved values for ρ_{nf}^{DLCCA} are in agreement with the experimental ones within a 15% of error, which is a good results considering all the used approximations (for example, the gyration radius is approximated by the equivalent radius) and the experimental errors in measurement of the mean density and the equivalent radius distribution. This is another strong indication that the DLCCA structure is a satisfactory model of the nanofoam and it can be reasonably exploited in the PIC simulations, as done in Chapter 5.

Finally, thanks to the DLCCA model validation, some useful considerations onto the structure can be drawn. Firstly, the nanofoam is featured by an intrinsic slope in the density profile due to the fractals deposition (see Figure 7.7a), with the maximum values near the substrate; this feature could be beneficial for laser-plasma interaction, in particular if the foam is pre-uniformed by a proper per-pulse, because the low density at the top should reduce the pulse reflection at the start of the interaction and induce a strong self-focusing at higher propagation lengths. Secondly, it should be noticed from Figure 7.7b that the density saturation thickness (or the film-formation thickness) changes with the aggregates

mean gyration radius (about $1\ \mu m$ for the $\bar{R}_g \sim 250\ nm$ case and roughly $2.5\ \mu m$ for the $\bar{R}_g \sim 400\ nm$) with a not linear law. This effect imposes that a minimum foam thickness must be produced if a 'continuous' film is wanted; larger is ρ_{nf}, lower is this minimum thickness, as well higher the uniformity. These are important consequences to consider when the near-critical layer of a DLT is experimentally produced, since a trade-off between the theoretical optimal density and thickness and the experimentally achievable ones must be reached.

CHAPTER 8

Production of nanofoams by Pulsed Femtosecond Laser Deposition (fs-PLD)

This chapter describes the preliminary work in the nanofoams production with an innovative technique: the ultrafast Pulsed Laser Deposition. This consists in a PLD which exploits ultrashort laser pulses ($\tau < 100\ fs$) to ablate a target and deposit materials onto a substrate into a vacuum chamber; for this reason this technique is also referred as *fs-PLD*.

Fs-PLD experimental apparatus was implemented during this PhD thesis project; the technical characteristic are reported in Section 8.1. This Section also deals with the production of CNFs with fs-PLD and with their comparison with the standard ones produced by ns-PLD; in particular, it is shown that, thanks to the technique peculiarities, more fractal and porous structures can be realized and, consequently, lower mean densities can be achieved, keeping at the same time higher levels of uniformity.

On the other hand, Section 8.2 introduces the fs-PLD capability to generate nanofoams with controllable elemental composition; Carbon, Tungsten and Copper nanostructures are showed and the morphological differences are discussed with respect to the nanoparticles properties.

8.1 Comparison between fs- and ns-PLD Carbon nanofoams

During this PhD project a fs-PLD technique was implemented. The technique is based on two principal systems: an ultrafast laser source and an automated vacuum chamber. The first is a commercial CPA Ti:Sapphire laser (*Coherent Astrella*), which generates short pulses with temporal duration of about $80\ fs$, energy $5\ mJ$ and $1\ kHz$ repetition rate. The vacuum chamber is pumped with a double stage (scroll and turbo-molecular pumps) and it allows controlling the ambient gas pressure and moving the substrate and target positions with an automated system. A scheme of the controllable parameters is reported in Table 8.2 and an

	Chamber pressure $[Pa]$	**Pulse energy** $[mJ]$	**Intensity** $[W/cm^2]$	**Fluence** $[J/cm^2]$
Min	10^{-4}	0.1	~ 0	~ 0
Max	10^5	5	$2 \cdot 10^{16}$	$1.5 \cdot 10^3$

Table 8.1: Table summarizing the controllable parameters (with the inferior and upper values) of the Nanolab fs-PLD.

image of the experimental apparatus in Figure 8.1.

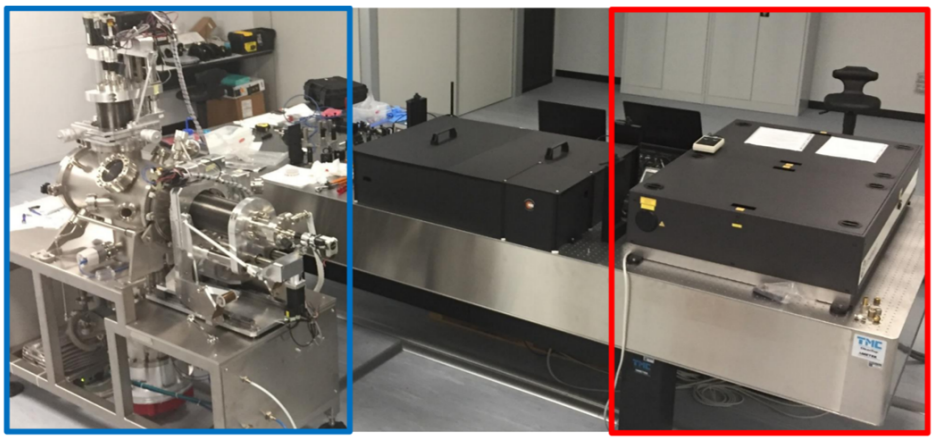

Figure 8.1: Image of the Nanolab fs-PLD setup. The blue box marks the interaction vacuum chamber, the red box the Astrella fs laser.

Ultrafast laser ablation has unique properties in terms of laser-target interaction which distinguishes it from the standard ns-duration one. The pulse temporal duration is lower than the typical ions motion characteristic time (tens of ps); for this reason the electromagnetic energy is transferred primarily to the target electrons and later, at end of the laser-target interaction, the energy is given to the material lattice through electron-phonon collisions, as opposite to the ns regime where the electron and ion populations have enough time to thermalize.

In the ultrafast regime the nanoparticles synthesis is particularly favoured, also in absence of an ambient gas atmosphere, in contrast of the ns-regime where NPs are formed by gas condensation, favoured by a slight ionization [67]. A currently accepted model suggests that nanoparticles are generated in the fs-regime by the following mechanism [132, 134]: since the laser is absorbed by the superficial electrons, it is quite reasonable to assume that, immediately after the end of the fs pulse, the surface region reaches high temperatures with almost constant density. This is depicted in Figure 8.2 in a thermodynamic (ρ, T) diagram; the condition for different depth layer of the target, after the pulse end, is represented by the vertical line (ρ_0, T_0). For increasing time, the material at the plasma state starts to expand adiabatically, reducing the temperature and density. Different initial conditions, which refer also to different depths, result in different thermodynamic paths, shown schematically in Figure 8.2; path 1 is characterized by a very high temperature and the plasma plume expansion never reaches the binodal curve. Along this path the plasma recombines into an atoms vapour. Conversely, nanoparticles are preferentially formed along the path 3, where

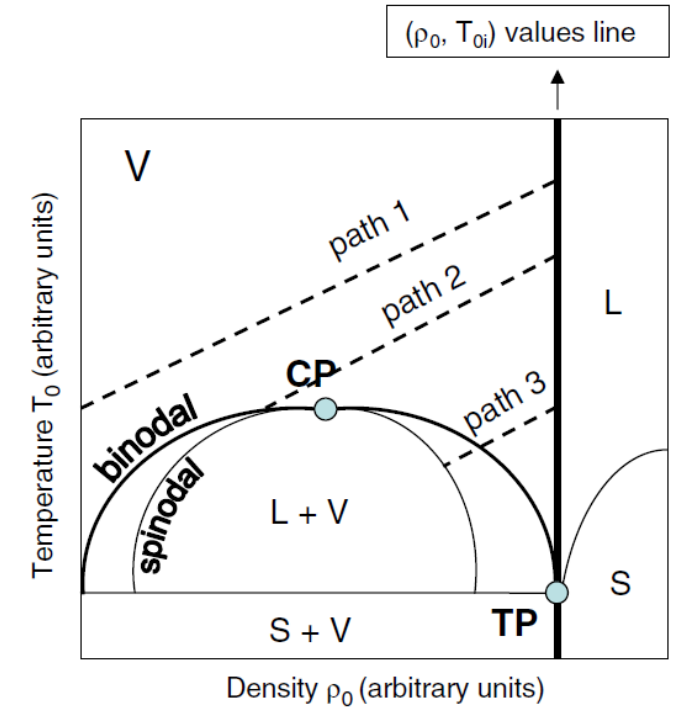

(a)

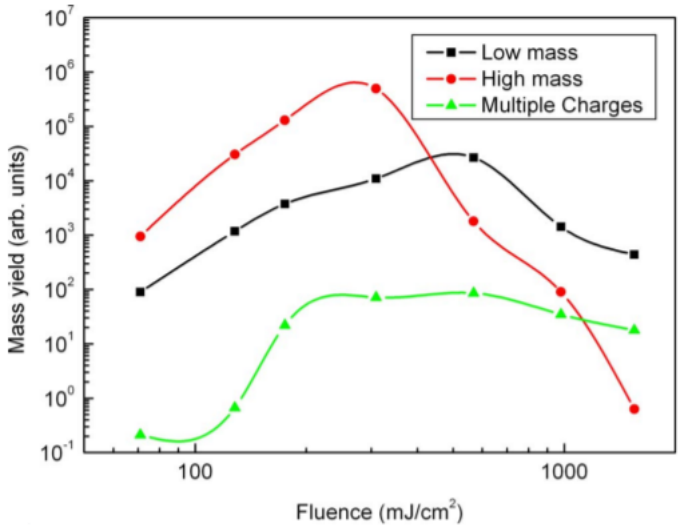

(b)

Figure 8.2: (a) Schematic (ρ, T) diagram with the various domain boundaries (solid S, liquid L and vapour V). CP and TP are the critical and triple points. The lines 1–3 show the various symbolic adiabatic trajectories for various initial temperature T_0 conditions. From [132]. (b) Ablated Carbon clusters mass (low mass, $1-29$ atoms; high mass, $30-550$ atoms) as a function of the laser fluence. The curves were obtained from the ToF spectra by appropriate transformation. From [133].

the spinodal curve is intercepted; indeed, at this threshold infinitesimally small fluctuations in composition and density will lead to phase separation via spinodal decomposition.

This simple yet effective model predicts a higher NPs synthesis, with respect to the vapour phase, for relatively low laser fluence, where path 3 is followed for all the target depth layers. In particular, in Reference [132] the highest amount of nanoparticles production is obtained for fluence lower than about $0.2\ J/cm^2$ for a Titanium target, while in Reference [133] a

large fraction of high mass Carbon clusters ($30 - 550$ atoms) over low mass ones ($1 - 29$ atoms) is reported in the fluence range $0.07 - 0.3\ J/cm^2$ (see Figure 8.2b). It was also demonstrated [135] that for Carbon target, the plasma plume is always composed of three different populations with atoms flying in front of the plume, followed by the C_3 radicals and then by a low-velocity population of Carbon clusters; at a laser fluence of $0.1\ J/cm^2$ the plume is composed principally of clusters, while increasing it to $3\ J/cm^2$ has the effect of producing more radicals and atoms.

It should be pointed out that nowadays no experimental results have been still reported onto the fractal nanofoam deposition onto a substrate, by fs laser ablation of a target; even if some recent work succeed in realising silica foams directly onto the irradiated target (e.g. a glassy nanofoam from a glass target [136]). For this reason we decided to exploit the great fs-PLD control over the NPs production to deposit Carbon nanofoams into an ambient gas atmosphere.

In the nanofoam deposition framework the NPs formation conditions are of high importance, since the Snowfall-like model (see Chapter 7) demonstrated that large number of particles results in bigger fractal aggregates and in more porous nanostructures; in order to maximize the NPs synthesis with respect to the atomic/little clusters phase, we chose to fix the fluence to $0.11\ J/cm^2$, using $5\ mJ$ of pulse energy and $2.4\ mm$ as spot diameter. The Snowfall-like model also indicated that a great role is played by the chamber atmospheric condition, because the aggregation of the nanoparticles is due to the Brownian motion, mediated by the collisions with the gas atoms. We therefore set in the chamber an Argon gas atmosphere, with variable pressure values.

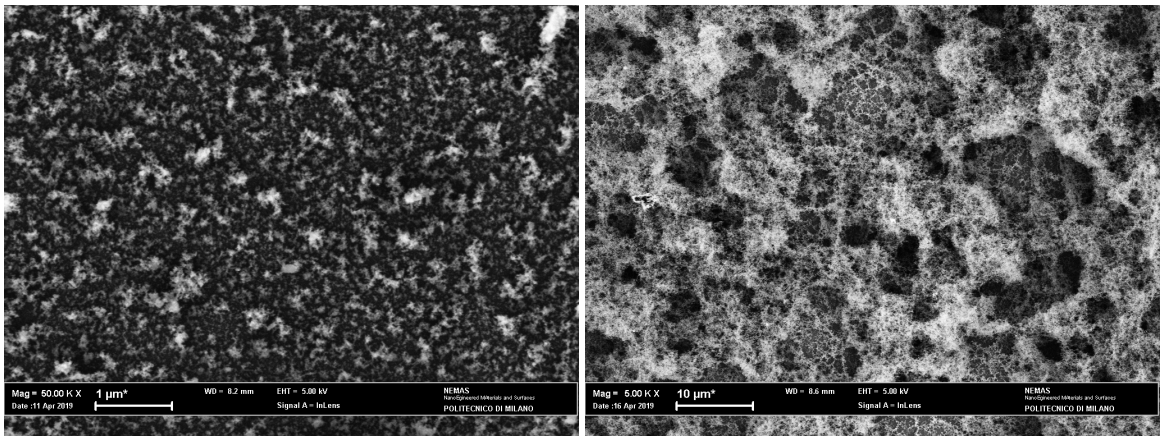

(a) **(b)**

Figure 8.3: SEM images of Carbon nanofoams deposited by fs-PLD, with $0.11\ J/cm^2$ fluence and $50\ Pa$ (a) and $100\ Pa$ (b) Argon pressure.

Carbon nanofoams are successfully deposited in an Argon atmosphere with different pressures ($50,\ 60\ , 80,\ 100,\ 120\ Pa$), fixing the target-to-substrate distance to $7\ cm$ and the deposition time to $5\ min$. Two of them (50 and $100\ Pa$) are represented in the SEM images of Figure 8.3, where the typical nanofoam fractal structure can be appreciated.

The mean density is measured through the EDS method (see Chapter 6) and it is reported

in Figure 8.4 against the Ar pressure. The so-produced CNFs are featured by density values well below the bulk one, even lower than the critical density threshold, which is a non-achievable result for the standard ns-PLD. Indeed the in the figure the measurements are compared to the ones of ns-PLD nanofoams (reported in Section 6.4); the fs-PLD enables to deposit less dense materials at even lower Ar pressure. It should be also observed that in both the regimes at low pressure values ($< 100\ Pa$ for fs-PLD, $< 200\ Pa$ for ns-PLD) the density points are aligned in the double logarithmic chart; this indicates that the density depends with a power law on the gas pressure $\rho_{nf} \propto p^{-b}$, where the higher slope is seen for the fs technique. After the above-mentioned pressure threshold the mean density tends to saturate to a plateau value which is almost two times higher for ns- to fs-PLD ($9\ mg/cm^3$ vs $5.1\ mg/cm^3$). We point out that the two trends are qualitative similar, thus we suggest that the aggregation phenomenon, even if it develops under very different regimes, is quite similar.

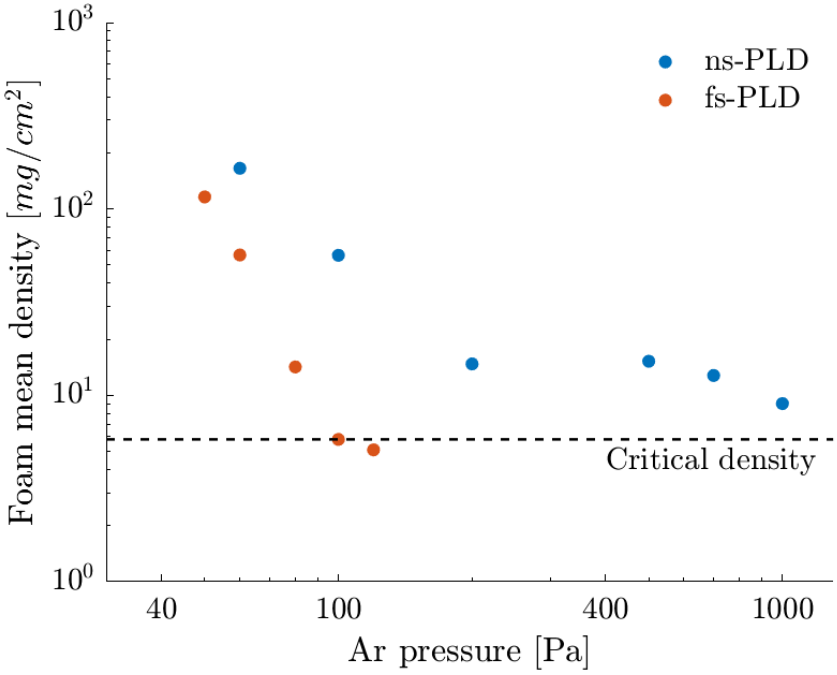

Figure 8.4: EDS-measured Carbon nanofoam mean density as function of the Argon gas pressure. Blue dots refer to foams produced with ns-PLD with $1.65\ J/cm^2$ pulse fluence and $5\ min$ of deposition time, while orange dots to fs-PLD with $0.11\ J/cm^2$ laser fluence and $5\ min$ deposition time. The critical density value for fully ionized Carbon is marked with the black dashed line.

To shed a light onto the reasons why different slopes and different saturation densities are seen, an analysis onto SEM images is carried out; similar density nanofoams produced with the different techniques are compared in Figure 8.5. Figure 8.5a shows a CNF produced by ns-PLD with $200\ Pa$ Argon pressure featured by a mean density of $14.7\ mg/cm^3$, while Figure 8.5b a fs-PLD nanofoam with $14.2\ mg/cm^3$, deposited in a $80\ Pa$ Argon atmosphere. From a qualitative point of view the ns-CNF appear less uniform: to quantitative retrieve informations from the images, the Structure Factor with the Fourier transform method is calculated (see Section 7.1) and it is represented in Figure 8.6. The obtained curves have similar

shapes, featured by a plateau at low q-vector till a threshold q_{th} and a power law trend for higher values. Section 7.1 showed that, for separated aggregates, q_{th} is an estimation for the inverse of the mean aggregate size R_g, while the exponent represents the fractal dimension. Here the interpretation must be adapted to the foam three-dimensional continuous structure; therefore q_{th} can be considered as the inverse of the uniformity scale length, while the power law exponent as the fractal dimension of all the structure projected over the 2D SEM image.

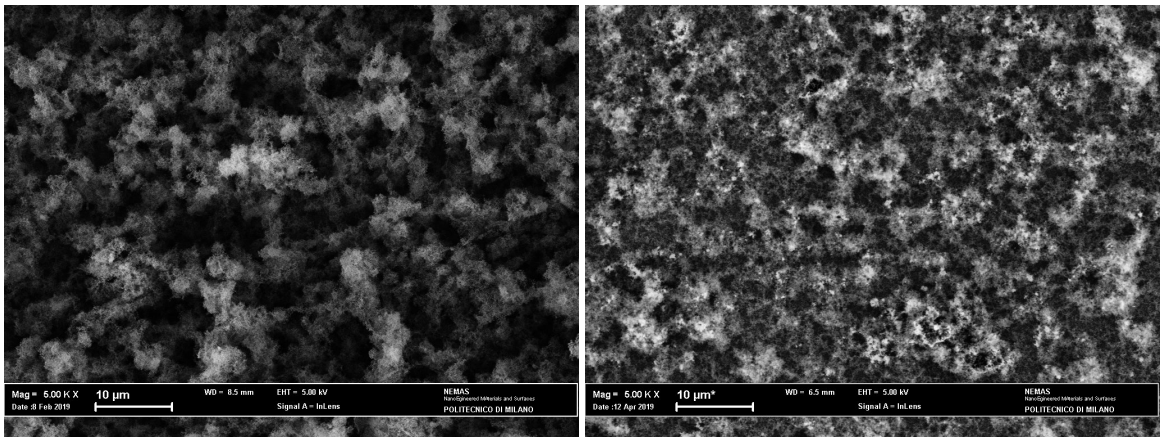

(a) **(b)**

Figure 8.5: SEM images of Carbon nanofoams with mean density about 14 mg/cm^3 produced with ns-PLD, 1.65 J/cm^2 fluence, 200 Pa Ar (a) and fs-PLD, 0.11 J/cm^2 fluence, 80 Pa Ar (b).

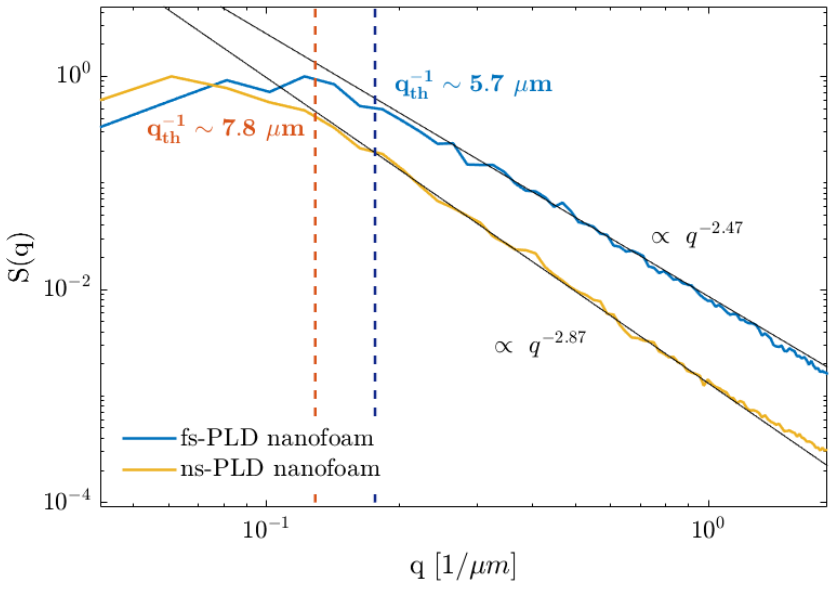

Figure 8.6: Structure factor calculated with the Fourier transform method (see Section 7.1) for the SEM images of Figure 8.5. On the grapth the power law dependence of the curve and the $q_t h^{-1}$ values are reported.

Thus the difference in the ns- and fs-nanofoams can be quantified by these two parameters: the ultrafast technique, at equal foam mean density, enables to realize more fractal ($D_f^{fs} = 2.47$ vs $D_f^{ns} = 2.87$) and more uniform ($q_{th,fs}{}^{-1} \sim 5.7\ \mu m$ vs $q_{th,ns}{}^{-1} \sim 7.8\ \mu m$) films with respect to the standard one. This is probably a consequence of the more efficient NPs synthesis by the ultrafast laser ablation; nevertheless, a deeper investigation in the future

could indicate which are the main mechanism underling these differences.

A last observable difference in the materials of Figure 8.5 is the presence of bright particles in the fs-foam. This peculiar effect is caused by the target condition during the deposition: fractal aggregates as well atoms and debrys are re-deposited onto the target, thus the target-ablation phenomenon is altered for long production times (indicatively over $20\ min$). Consequently, also the realized nanofoam begins to be contaminated from not-fractal Carbon particles, which are visible as bright spots in the SEM image of Figure 8.7a due to the different crystalline structure.

This 'contamination' effect can be mitigated by a laser pre-cleaning in vacuum of the target before the deposition (similarly to what done in Reference [137]). Figure 8.7b shows a nanofoam produced with the same parameters of Figure 8.7a, yet with the pre-cleaning; the resulting material is not affected by the bright particles and it is featured by a more neat structure.

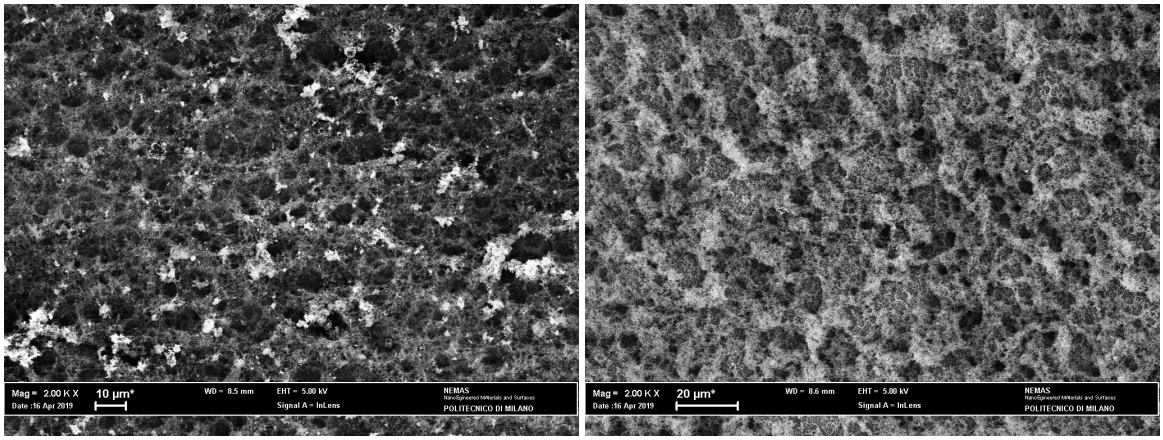

(a) **(b)**

Figure 8.7: SEM images of Carbon nanofoams produced by fs-PLD with $0.11\ J/cm^2$ laser pulse fluence and $100\ Pa$ of Argon pressure. Target laser-cleaning in vacuum before the deposition is not carried out in (a) while it is done in (b).

It should be highlighted that the presence of these bright particles is accompanied by a larger density: Figure 8.7a foam is $5.8\ mg/cm^3$ dense while the Figure 8.7b nanofoam has a $4.8\ mg/cm^3$ mean density. It therefore appears that the target laser-cleaning before each nanofoam deposition is a desirable procedure which keeps the laser-target interaction more similar to ideal conditions and consequently also more reproducible.

8.2 Production of nanofoams with controllable elemental composition

The fs-PLD capability to naturally generate NPs from theoretically any kind of target, can be exploited to produce nanoparticle-based fractal aggregates and therefore nanofoams, with controllable elemental composition.

During this PhD project, a preliminary work over this subject is carried out: nanofoams from Carbon, Tungsten and Copper targets are deposited and represented in Figure 8.8. The production conditions differ slightly in the shown cases, indeed a pulse fluence of $0.11\ J/cm^2$

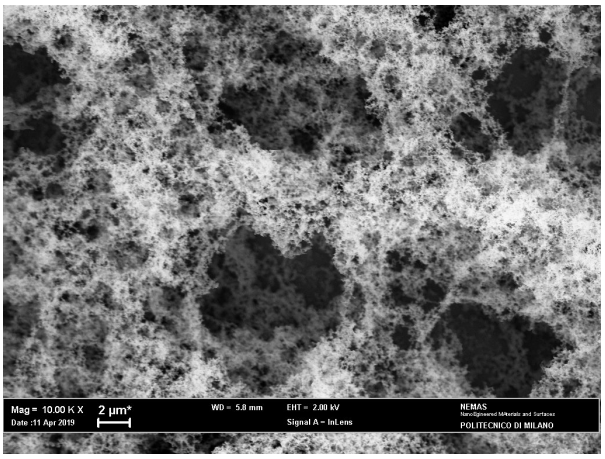

(a)

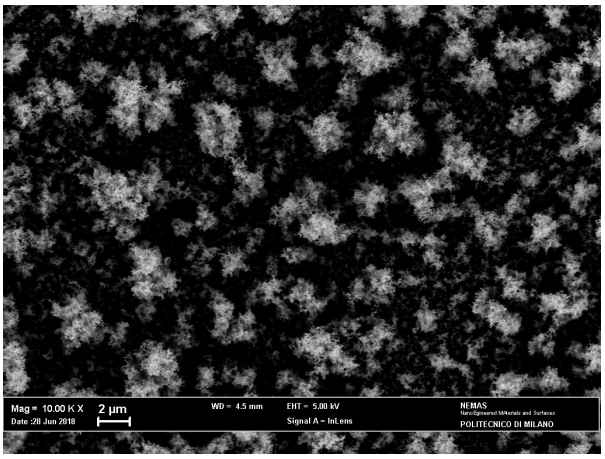

(b)

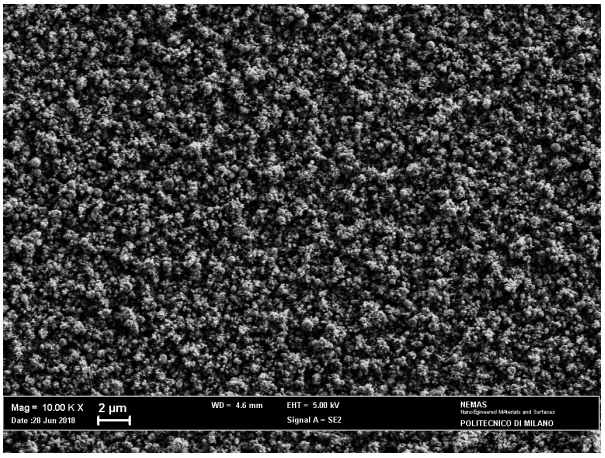

(c)

Figure 8.8: SEM images of Carbon (a), Tungsten (b) and Copper (c) nanofoams produced by fs-PLD. The laser fluence is $0.11\ J/cm^2$ for (a) and (b), while $0.19\ J/cm^2$ for (c); the Argon gas pressure is $100\ Pa$ for (a) and (c), while $500\ Pa$ for (b). Deposition time is $5\ min$ for all the cases.

is used for Carbon and Tungsten, while for the Copper sample it is set to $0.19\ J/cm^2$; the Argon ambient gas pressure is set to $100\ Pa$ for Carbon and Copper while $500\ Pa$ for Tungsten. These choices are made to have a plume dimension visually similar in the three cases; it should be pointed out that, even if the fluence and the pressure are slightly different, some useful observation can still be drawn.

Figure 8.8 shows the nanofoams realized with the above-mentioned conditions and $7\ cm$ target-to-substrate distance, $5\ min$ deposition time. The nanostructure strongly depends onto the elemental composition: Carbon foam is the more porous film, followed by the Tungsten one, while the Copper one is featured by the more compact structure. These differences are difficultly explainable by the different deposition conditions, for example the higher pressure gas for the Tungsten case should result in a more open structure, as opposite to what observed. The variation in porosity seems also not to be dependent onto the element atomic mass; indeed Tungsten has a much larger mass with respect to C and Cu, but its structure is intermediate between the two cases.

To study this effect, samples are deposited in the same conditions of Figure 8.8 but with lower deposition time (tens of seconds), in order to analyse the produced nanoparticles properties. The SEM images of Figure 8.9 show individual NPs and aggregates in the three cases. To quantitative analyse the samples, the software ImageJ is used [138]; in particular, the images are binarized with a proper threshold and the particles are analysed. The ones having circularity, defined as $4\pi(\text{area}/\text{perimeter}^2)$, in the $0.9-1$ range are selected to generate NPs size distribution, shown in Figure 8.10; the circularity value approaching one corresponds to almost circular objects, which allows filtering all the fractal aggregates or debrys from the analysis.

	Z	$\rho_b\ [g/cm^3]$	$\bar{r}_{NP}\ [nm]$	$\bar{m}_{NP}\ [amu]$	$(\Delta v/v)_{coll}$
C	6	2.3	7.9	$2.9 \cdot 10^6$	$2.5 \cdot 10^{-5}$
W	74	19.3	8.4	$2.9 \cdot 10^7$	$2.5 \cdot 10^{-6}$
Cu	29	9.0	16.5	$1.0 \cdot 10^8$	$7.1 \cdot 10^{-7}$

Table 8.2: The table reports, for Carbon, Tungsten and Copper elements, the atomic number Z, the bulk material density ρ_b, the medium NPs radius $\bar{r}_{NP}$ calculated from the distributions of Figure 8.10, the mean NPs mass calculated as $\bar{m}_{NP} = \rho_b \frac{4}{3}\pi \bar{r}^3_{NP}$ and the NPs relative momentum variation in a head-on collision with an Argon atom at rest (Equation 8.1).

The NPs radius distributions shown in Figure 8.10 are featured by an almost-exponential trend with a cut-off at few nanometers diameter (probably due to the SEM resolution $\sim nm$); the Carbon and Tungsten histograms are quite similar, indeed mean NPs radia (reported in Table 8.2) are $7.9\ nm$ and $8.4\ nm$ respectively. The copper NPs are conversely characterized by a broader distribution with a higher mean radius, $16.5\ nm$. These differences could be interpreted in several ways (for example by the different laser fluence or the different material thermal properties), thus a deeper study is needed to justify this point. Nevertheless, the experimentally measured NPs properties can be exploited to unfold the observed nanostructures of Figure 8.8: it appears that the particles inertia is correlated with the material porosity. Table 8.2 summarizes the mean nanoparticles mass for the analysed distributions (calculated using the bulk density), showing the highest value for the Copper case and the lower one for Carbon; the different inertia results in a different diffusion process into the Argon ambient gas. For example, in head-on elastic collision between a moving NPs and an Argon atom at

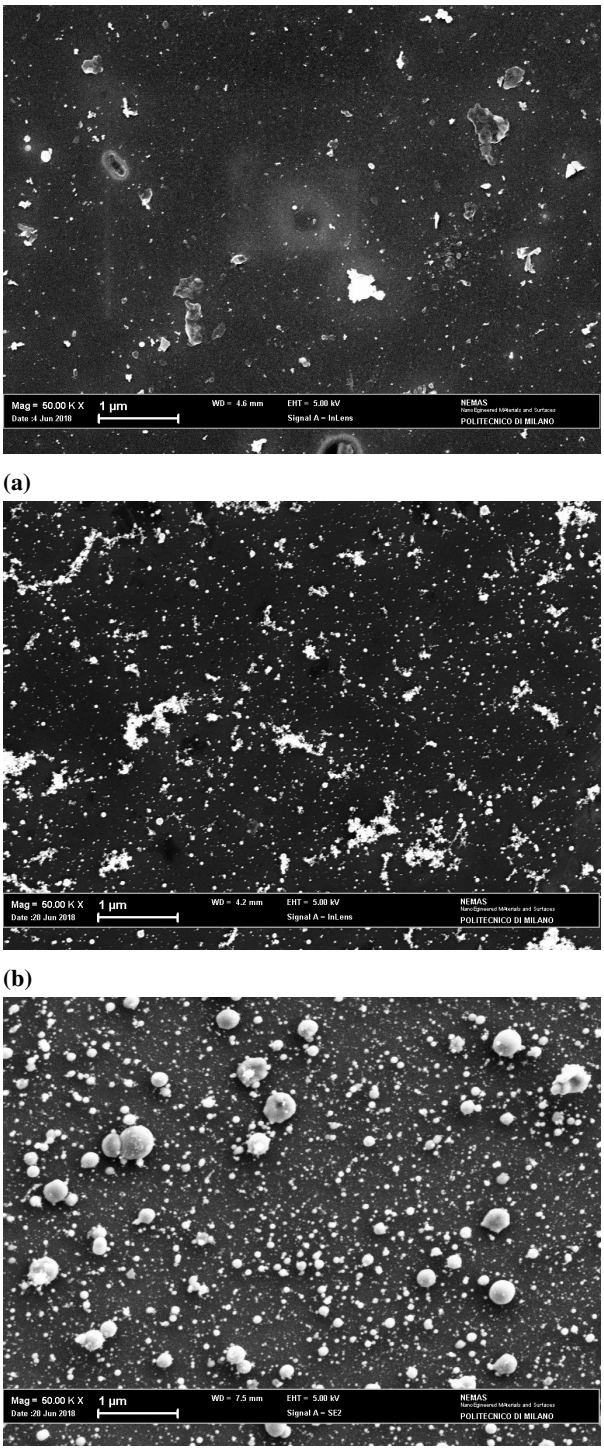

Figure 8.9: SEM images of Carbon (a), Tungsten (b) and Copper (c) nanoparticles produced by fs-PLD. The deposition condition are the same of Figure 8.9, except for deposition time which is about ten seconds.

rest, the relative variation in velocity is given by:

$$\left(\frac{\Delta v}{v}\right)_{coll} \sim \frac{2m_{Ar}}{m_{NP}} \tag{8.1}$$

Which is valid when the nanoparticle mass m_{NP} is much higher than the Argon atomic

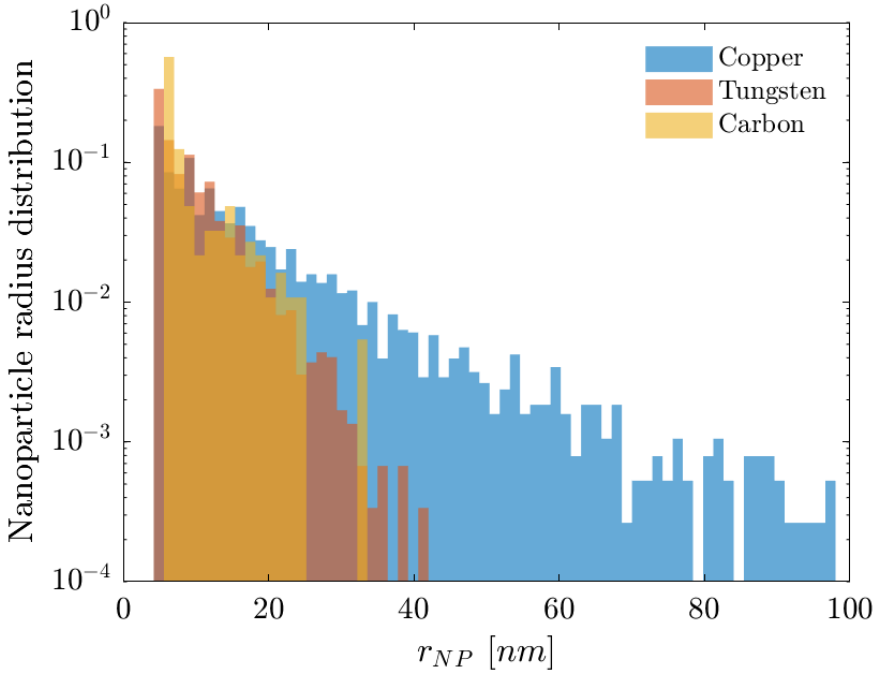

Figure 8.10: Normalized nanoparticles radius distributions retrieved from the SEM images of Figure 8.9. The analysis is obtained by ImageJ, by setting a proper image binarization and looking for circular objects, to filter fractal aggregates and debrys.

mass (always respected since $m_{Ar} \sim 40$ uma and $m_{NP} > 10^6$ uma). Equation 8.1 trivially predicts a lower momentum variation for the higher mass NPs, which is the Copper case; the highly directional particles ejected from the target are therefore more slowed down by the gas for Carbon and Tungsten. In the latter condition the particles are able to stay in the vacuum chamber for longer times and therefore generate larger fractal aggregates, as predicted by Equation 7.3. Since bigger aggregates are less dense, as stated by Equation 7.4, the resulting structure is more porous.

In conclusion, nanofoams can be produced with tunable density and controllable elemental composition, but the structure is strongly dependent onto the nanoparticles size distribution and on the ambient gas conditions. In particular the NP size plays an important role both in the mean fractal aggregate density (Equation 7.5) and in the aggregation dynamics; it is shown that, when the radius is larger, little fractals are formed and the deposited nanofoam is more compact. Thus a further investigation over the control of the NPs size through the laser parameter is very desirable in the future.

Part IV

Experimental investigation on ion acceleration from nanofoam-based DLTs

CHAPTER 9

Production of nanofoam-based DLTs

This chapter describes the production of Double-Layer Targets for a specific laser acceleration experimental campaign, carried out at the laser facility of the *Helmoltz-Zentrum-Dresden-Russeldorf* (HZDR) in Germany. Section 9.1 deals with the experimental production at NanoLab of the DLT, consisting in the substrate attaching to the target holder and the subsequent deposition of a near-critical Carbon nanofoam. While in Section 9.2 the target damaging issues are considered, in particular it is analysed the effect of the target holder geometry onto the DLT damaging by the laser.

9.1 Target realization

The near-critical Double-Layer Targets production is carried out at the Nanolab and consists in the assembling of the system represented in Figure 9.1.

To realize this assembly, firstly a thin Aluminum foil ($1.5\ \mu m$) is glued to the foil holder, as shown in Figure 9.2a; the latter is inserted into the ns-PLD vacuum chamber to deposit a Carbon foam onto it and finally, the target holder is clamped over the system to obtain the final assembly of Figure 9.2b.

The Carbon nanofoam is produced by the ns-PLD with the following parameters: $200\ mJ$ pulse energy, $1000\ Pa$ Ar pressure, spot diameter $3.4\ mm$. The choice of using the ns-PLD instead of the fs-PLD is driven by the fact that the latter technique, even if it is capable to produce foams with a larger range of densities (see Chapter 8), is still not optimized for the deposition of uniform thickness over large areas. Conversely, the ns-PLD allows producing nanostructured material with constant thickness over several cm^2 areas by simply rotating the substrate with the axis shifted to the one of the target.

The ns-PLD deposition parameters are selected to produce a quite uniform material (shown in Figure 9.3a), a mean density around $3n_c$ and tunable thickness down to few μm (see Fig-

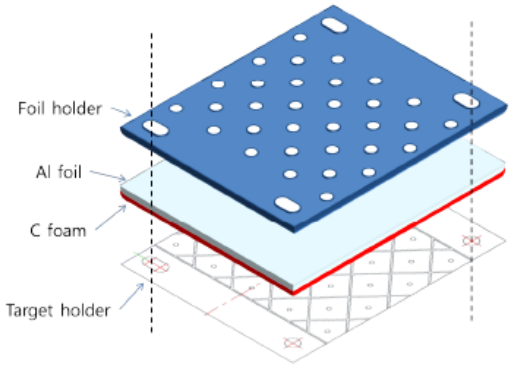

Figure 9.1: Scheme of the DLT assembly.

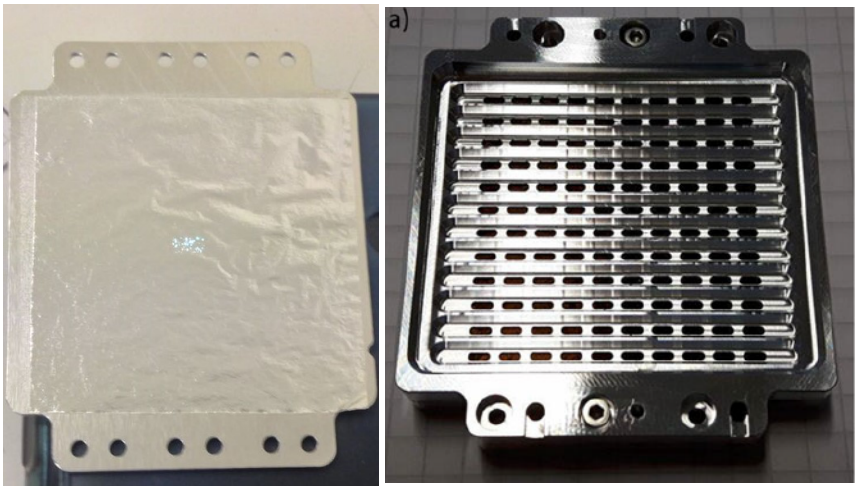

(a) **(b)**

Figure 9.2: (a) Image of the foil holder with the attached thin Aluminum substrate; the centre of the foil is back illuminated and the light propagates through the micrometric holes. (b) Image of the DLT assembly.

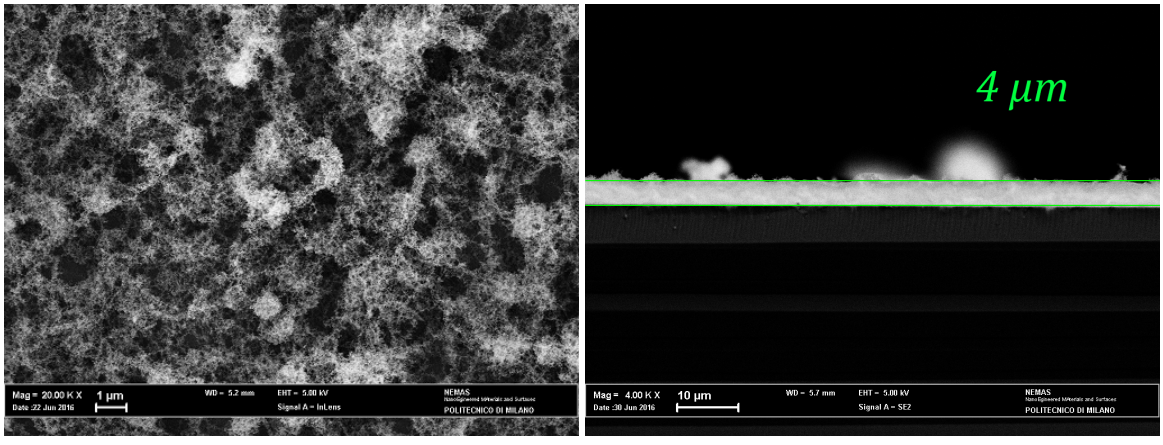

(a) **(b)**

Figure 9.3: SEM top (a) and cross-section (b) images of a Carbon nanofoam used for the HZDR experimental campaign.

ure 9.3b). The mean density value is chosen in order to obtain high enhancement values with the specific ultra-intense laser exploited in the experiment, as described in detail in the next

Voltage $[kV]$	K_α^C/K_α^{Si}	K_α^O/K_α^{Si}	**% C**	**% O**	**Mean density** $[mg/cm^3]$	**Fraction of bulk density**	**Normalized density** $[n_e/n_c]$
5	0.3967	0.0267	96	4	18.2	0.0079	3.14
7	0.1188	0.0090	96	4	19.1	0.0083	3.29
10	0.0412	0.0035	96	4	18.9	0.0082	3.26

Table 9.1: The table summarizes the EDS-based density measurements. The analysed nanofoam is deposited with ns-PLD with 200 mJ pulse energy and 1000 Pa Ar pressure, the SEM measured thickness is 8 μm. The EDS measurements are carried out at $5,\ 7,\ 10\ kV$ with 120 s acquisition time; the characteristic X-rays counts from Carbon, Oxygen and Silicon are used to calculate the K-ratios reported in the second an third column. The results of the method described in Chapter 6 are reported in columns $4-8$.

Chapter; the density measurement is carried out by the EDS method explained in Chapter 6. In particular, it has been observed in Section 6.4 that the mean density does not depend onto the film thickness, thus the measurement is carried out onto only one foam, with $8\ \mu m$ thickness at three electron accelerating voltage values. As reported in Table 9.1, the EDS technique shows stable density measurements with respect to the different voltage conditions, with a mean density of $18.7\ mg/cm^3$, which corresponds to about $3.2\ n_c$ for a fully ionized material. The measurement error with these condition is theoretically expected to be under $10\ \%$, in fact the data acquired at different voltages maximally deviate $5\ \%$, one from each other.

The film thickness is controlled by simply linearly scaling the deposition time; nanofoams with constant density ($\sim 3n_c$) are deposited onto the thin Aluminum foils attached to the foil holder, with $4\ \mu m$ thickness ($3'20''$ deposition time), $8\ \mu m$ thickness ($6'40''$ deposition time), $12\ \mu m$ thickness ($10'00''$ deposition time) and $16\ \mu m$ thickness ($13'20''$ deposition time).

9.2 Damaging issues

The foam-based DLT is an advanced target which suffers from some damaging issues, both from the production method and the stability to laser irradiation.

Considering the production, the handmade method is sensible to human and not-human errors; for example the Al foil, which is fragile due to its low thickness, can be damage during the attaching procedure. In addition, this kind of thin foils presents a high defects density, like micrometric holes and creaks [139]. These issues can be dealt with an accurate post-production characterization (e.g. with optical and electron microscopes), aimed at ensuring good target properties.

More complex are the damaging issues related to the laser irradiation: the ultra-intense pulse, after the interaction and the ion acceleration process, can affect the properties of the target for long spatial scales ($\sim\ cm$) through different mechanisms. The laser generally completely destroys the target with mm extension from the interaction point, in addition fast debris and mechanical/thermal shocks are produced, which can damage the target at larger distances.

To study such issues, related in particular to DLTs, a first test was conducted few months

before the main experimental campaign: few laser shots are fired onto a DLT with a thick C nanofoam ($32\ \mu m$), appositely prepared for the test, and the target is characterized after the irradiation. Figure 9.4 shows an image of the irradiated DLT after the removal of the target holder, where several damaging can be observed.

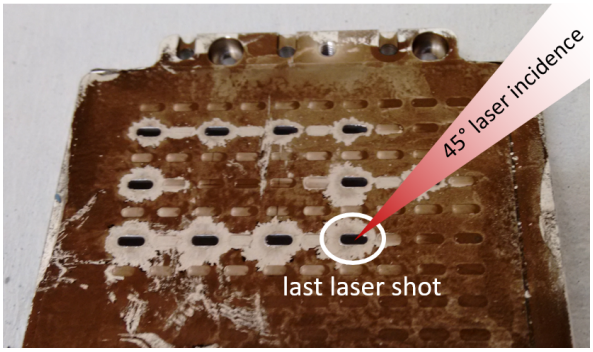

Figure 9.4: Image of a DLT after the laser irradiation; a scheme of the laser incidence condition is depicted over the image.

The ultra-intense pulse completely destroys the target within the foil holder holes, probably due to mechanical and thermal shocks; in addition, the fast debris, produced during the plasma explosion, are projected in all directions wiping out the nanofoam layer for several mm around the hole. A last damaging effect should be also noticed at even larger distance ($\sim cm$): the nanofoam is partially removed only in correspondence of the target holder holes.

To investigate this particular damaging effect the irradiated target is characterized by the SEM. From the acquired images, reported in Figure 9.5, a particular shape is observed in the nanofoam removal. For all the first neighbours holes, the nanostructured material is completely wiped out at the left side of the hole, while the right side foam is preserved. In addition also the second neighbours holes are damaged, in particular at the left side, with a seagull-wings shape.

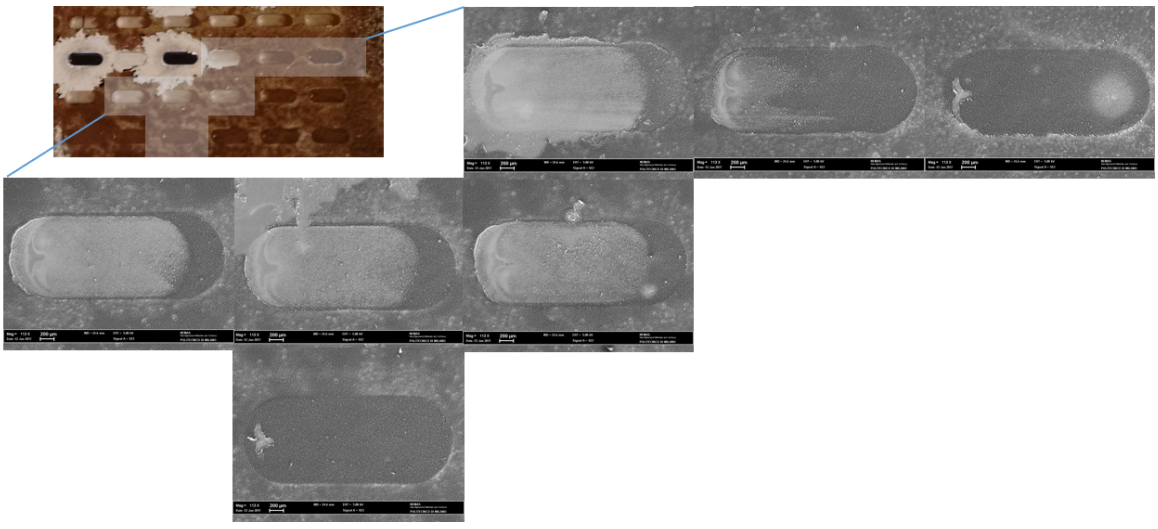

Figure 9.5: The holes near the last laser shot are characterized by SEM with top images.

These observations are consistent with a damaging effect due to the low intensity laser

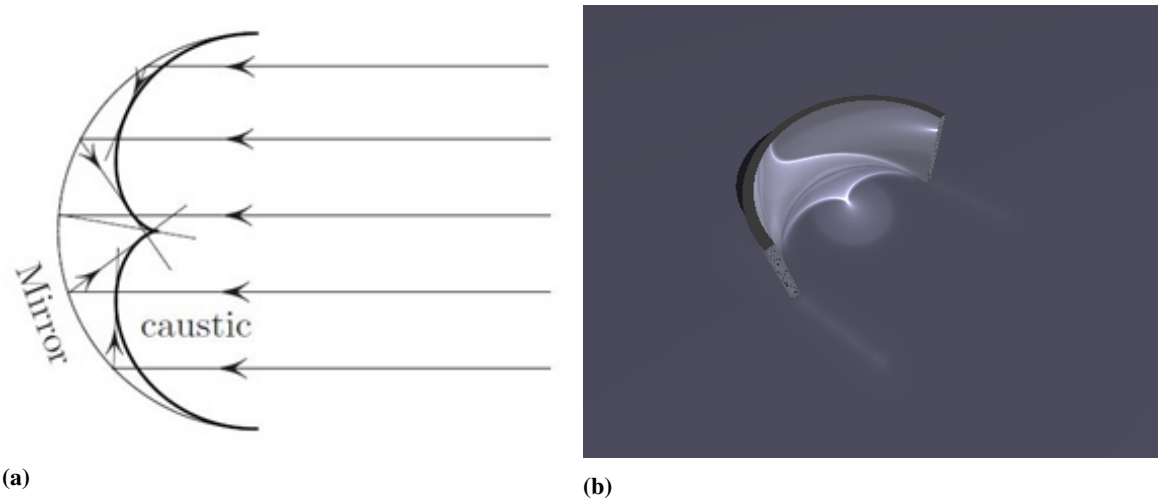

(a) (b)

Figure 9.6: Scheme (a) and rendering by POV-ray [140] (b) of the caustic phenomenon due to light reflection by a cylindrical mirror.

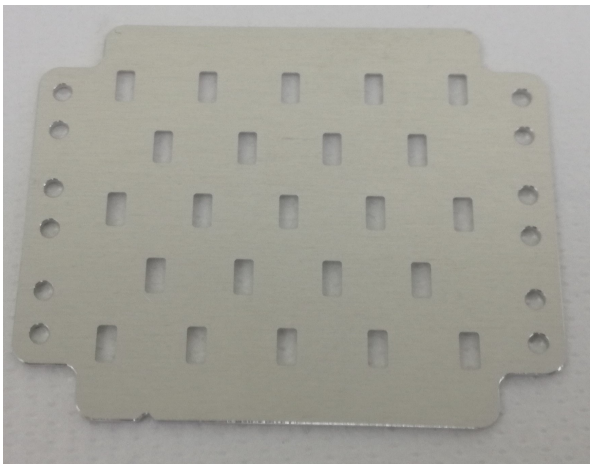

Figure 9.7: Image of the re-designed holder; the number of holes is reduced and the shape is rectangular.

fringes, extending at high distances from the focal point; indeed, the seagull-wings shape is very similar to the caustic of a cylindrical mirror, as shown in Figure 9.6. Therefore, the light fringes are reflected and focused by the target holder circular edges onto the nanofoam, which is ablated. In this picture, the not-destroyed part at the right of the hole corresponds to the target holder shadow due to the 45° angle of incidence.

To avoid all these issues the foil and target holder are re-designed as shown in Figure 9.7. The hole shape is rectangular in order to reduce the caustic effect, while the number of holes is reduced. With this solution the shot-to-shot distance is sufficiently high to reduce also the debris damaging effects; as a conclusion, sub-sequent laser shots onto the DLT can be considered as fully independent on damaging effects.

CHAPTER 10

Laser-driver ion acceleration campaign at the Helmoltz-Zentrum-Dresden-Russeldorf

The chapter describes the laser-driven ion acceleration experimental results achieved during a two-weeks campaign at the *Helmoltz-Zentrum-Dresden-Russeldorf* (HZDR) in Dresden, Germany. The first section is dedicated to the description of the ultra-intense laser parameters, the experimental apparatus and the set of diagnostics used to characterize the acceleration process with standard and Double-Layer Targets. In Section 10.2, the experimental evidences of an enhanced laser absorption into the nanostructured near-critical layer are reported, while Section 10.3 gives an interpretation of these results based on the concept of relativistic transparency and the theoretical insights introduced in Part II.

10.1 Experimental apparatus

The HZDR is a German research laboratory based in Dresden that conducts research in three of the Helmholtz Association's areas: matter, health, and energy. It has an ultra-intese laser facility featured by $150\,TW$ power, called *Draco*, based on the Ti:Sapphire technology introduced in Chapter 1. The pulses are generated by a regenerative amplifier and three stages of multipass amplifiers and they can be delivered with $2\,J$ energy, a FWHM duration of $30\,fs$ and $10\,Hz$ repetition rate; the laser has a low intrinsic contrast level due to the *cross-polarized wave* (XPW) technology [141], which is further increased with a plasma mirror system [142] inside the interaction chamber (see Figure 10.1a) which enables to eliminate the pre-pulses and the *amplified spontaneous emission* (ASE) [143]. The pulse is focused by a deformable parabolic mirror [144] which enables to achieve a spot FWHM diameter of about $3\,\mu m$.

The pulse peak intensity on target is about $5 \cdot 10^{20}\,W/cm^2$, corresponding to a normalized amplitude of $a_0 = 16$, with a contrast level of 10^{-7} at about $2\,ps$ before the main peak arrival

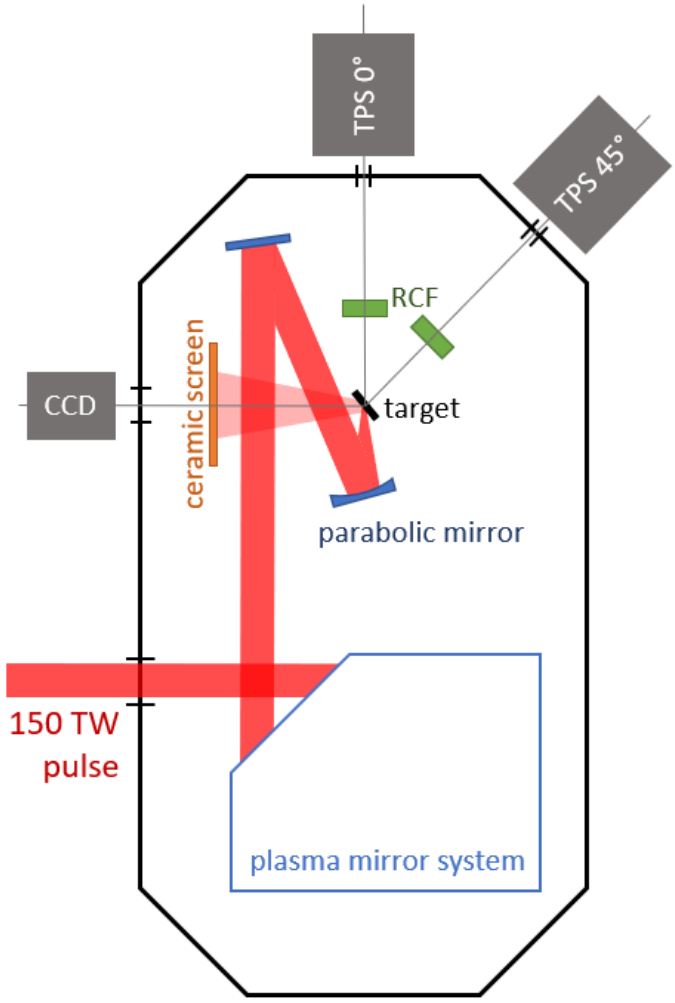

(a)

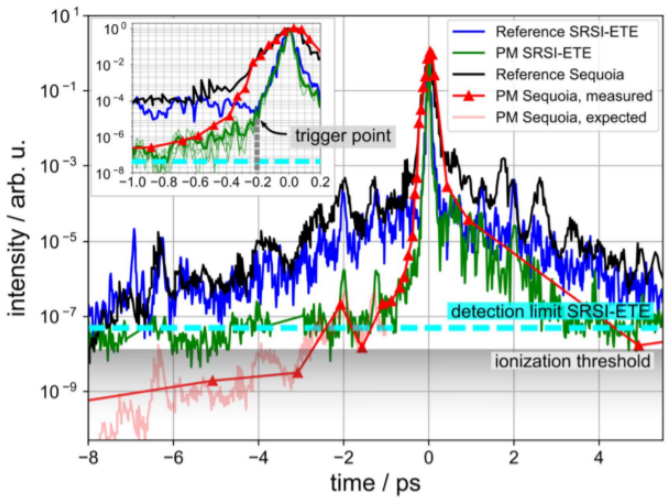

(b)

Figure 10.1: (a) Scheme of the interaction chamber and the set of the used diagnostic systems, RCF stands for Radiochromic Film stack, TPS for Thomson Parabola Spectrometer. (b) Measured pulse contrast level with and without the plasma mirror; from [143].

(see Figure 10.1b); this high contrast value enables to preserve the target to expand before the peak pulse interaction (see Section 2.1). The polarization is linear in the interaction plane (P-polarization) and the incidence angle can be equal to $45°$ and to $0°$.

The laser-driven ions can be characterized both along the laser direction and in the $45°$ one by two standard techniques: Radiochromic Film stacks (RCF) [145], and two Thomson Parabola Spectrometers (TPS) [77]. In particular we call TPS $0°$ the one along the laser direction and TPS $45°$ the other one. The two diagnosis systems can be used at the same time when the RCF are perforated, while in the opposite situation they must be used one at shot. It should be remarked that RCF are capable to determine with high spatial resolution the ion beam at the cost of low energy spectrum resolution; in addition, it should remarked that RCF stacks are passive detectors, which means that the measurements can be obtained only few hours after the interaction. Conversely, TPS are active detectors with high energy resolution (which nevertheless decreases at high energy) but low spatial resolution, since the TPS measurement is taken only at a tiny solid angle of the ion bunch.

In addition to the these diagnostics, it is also characterized the laser light reflected by the target; the system consists in a ceramic (MACOR) screen positioned at the $90°$ direction with respect to the laser one. A CCD camera, filtered at the laser wavelength, observes the scattered light imaged from the ceramic screen along the same line of sight by using a dichroic mirror. It should be pointed out that this active detector can be exploited only for $45°$ incidence due to the chamber geometry.

10.2 Evidences of enhanced ion acceleration and laser absorption

To investigate the DLT effect, ions energy is measured by irradiating the different targets (see Chapter 9) with variable pulse energy and incidence angle. Due to the chamber geometry and diagnostics, the incidence angle is varied in two conditions, normal and $45°$, with constant linear P-polarization.

A number of ions species are recorded by the Thomson Parabola spectrometers along the normal of the target (TPS $0°$ for the normal incidence condition and TPS $45°$ for the other one); an example of the spectra observed during the experiment is shown in Figure 10.2. In particular Figure 10.2a reports the proton spectra for bare Al target and DLT with $4\ \mu m$ foam in the highest achieved intensity condition and for different incidence angle; fully ionized Carbon ions spectra for the same conditions are shown in Figure 10.2b.

The reported ions spectra exhibit an exponential-like trend, in agreement with the experimental and theoretical knowledge about the TNSA mechanism, with a cut-off energy which reaches the highest values ($20\ MeV$ for protons and $100\ MeV$ for C^{6+}) for the DLT in the normal incidence condition. It is quite surprising that for the standard target the incidence angle weakly affects the maximum ions energy, since it is widely believed that TNSA reaches the highest performances at not-normal incidence. Indeed, higher energy proton measurements at oblique incidence were reported in the literature [42], yet at lower intensity values ($2.5 \cdot 10^{19}\ W/cm^2$); this effect depends on the Brunel electron heating mechanism

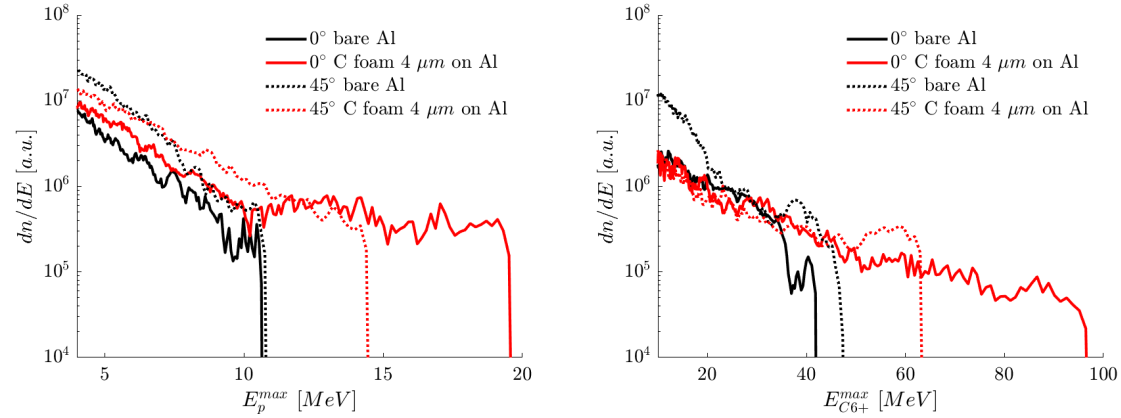

(a) **(b)**

Figure 10.2: Examples of Proton (a) and fully ionized Carbon ions (b) spectra obtained with the Thomson Parabola Spectrometers at normal (full lines) and oblique incidence (broken lines). The spectra are obtained by irradiating standard Al target (in black) and DLTs (in red), composed by an Al substrate and a $4\ \mu m$ thick and $3\ n_c$ dense nanofoam.

(see Chapter 1) which is damped when the polarization is circular or the incidence angle is 0. Nevertheless, it have also been theoretically predicted (see Section 1.1) that the Brunel effect plays a marginal role in the electron heating, with respect to $\mathbf{j} \times \mathbf{B}$, when ultra-high intensity ($> 10^{20}\ W/cm^2$) are used; in this picture, the Brunel mechanism damping in normal incidence could be compensated by the advantage of increasing the intensity value of a factor of $\sqrt{2}$ with respect to $45°$ angle. It should be also mentioned that the high power laser pulse is capable to bend the target due to radiation pressure, automatically inducing a little incidence angle [146]; one last possible interpretation is reported in Reference [147], where it is mentioned that, even at normal condition, the pulse spatial chirp can induce a tilted envelope with results similar to oblique incidence.

Since high ions energies are measured exploiting DLTs, it is deeper investigated the dependence of the thickness and intensity onto the proton energy, using both the Thomson Parabola and the RCF. DLTs with nanofoam mean density equal to about $3.2\ n_c$ (see Chapter 9) and $4 - 8 - 12 - 16\ \mu m$ thickness are irradiated at both the incidence conditions, with variable intensity controlled by the pulse energy, and compared to the reference Aluminium target.

Figure 10.3a shows the cut-off proton energy at normal incidence and Figure 10.3b at oblique one. Two different behaviour are observed in the different conditions, since for $0°$ angle the DLT enables to increase the laser absorption and, consequently, the proton maximum energy up to a factor of two (for the thinnest foam, $4\ \mu m$) for all the investigated intensity range (from $5 \cdot 10^{20}\ W/cm^2$ to $1.75 \cdot 10^{20}\ W/cm^2$), while the $45°$ case is featured by a very low enhancement at 100% intensity and even a worse performance for 50% and 10% energy. It should be noted that the data can be considered quite robust because the two different diagnostics, TPS and RCF, measure similar values within the limits of the large error bars (probably due to the intrinsic instability of the acceleration phenomenon or even the thickness inhomogeneities of the nanostructured material).

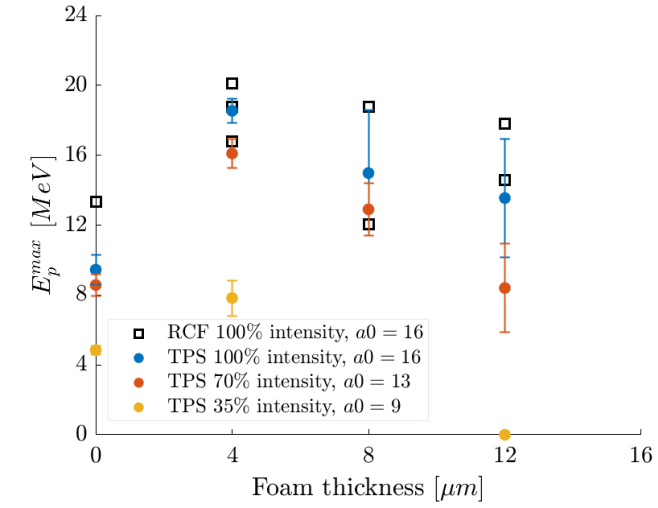

(a)

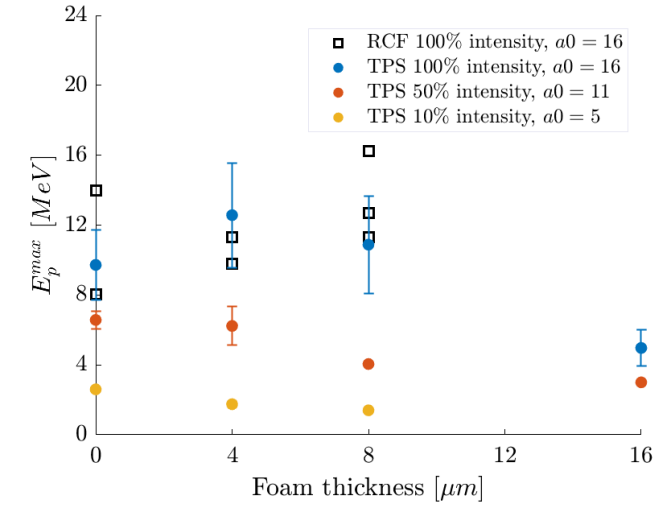

(b)

Figure 10.3: Cut-off proton energies measured by TPS (full points) and RCF (empty squares) as a function of the nanofoam thickness at different pulse intensity; the $0\ \mu m$ value corresponds to bare Al target. Since the RCF measurement are few for each condition, each data is represented, while the TPS measurements are sufficiently high (in the order of 10) to represent the mean and standard deviation values. In (a) the laser incidence angle is $0°$, while in (b) it is $45°$.

DLTs with foam thickness higher than $4\ \mu m$ are featured by a reduced energy, which means that the at larger propagation depth the laser energy is impoverished and large fraction of low temperature electrons are accelerated; this effect should dilute the highest energy electrons, hence reducing the TNSA sheath field (as explained by the model of Chapter 4). In this picture the oblique incidence has the effect of increasing by a factor of roughly $\sqrt{2}$ the laser path inside the foam and consequently further reducing the proton energy, even if the same DLT is irradiated. This interpretation is further discussed in the next Section.

A deeper analysis onto the RCF stacks enables to recover the proton spectra with spatial resolution (see Figure 10.4a); the picture reveals that the ions spot obtained by the $4\ \mu m$ DLT is wider and smoother with respect to the one from standard target, suggesting that a bigger

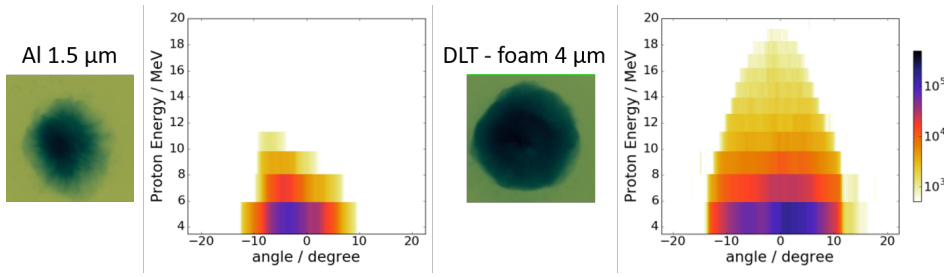

(a)

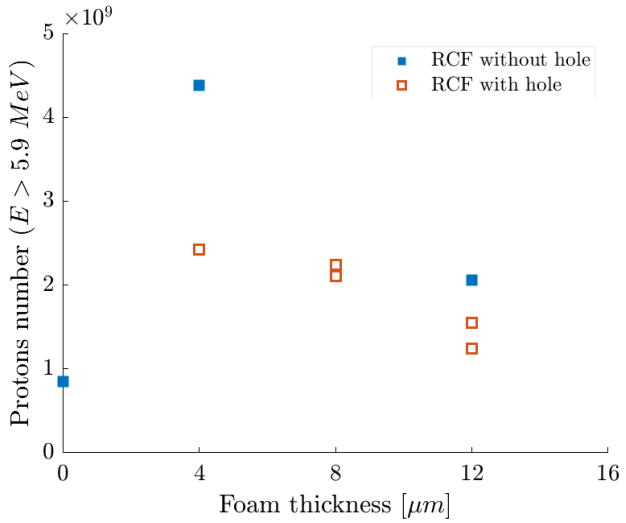

(b)

Figure 10.4: (a) Images of the first RCF layer and the angle-energy distribution of the proton bunch. (b) Protons total number for energy higher than $5.9\ MeV$, as a function of the DLT foam thickness; the 0 value corresponds to bare Al target. The blue full squares are relative to unaltered RCF stacks, the empty red squares to perforated RCF stacks, used to carry out measurements both on the RCF and the TPS.

and stronger hot electron sheath is established with the near-critical layer. In addition, this diagnostic allows measuring the total number of the accelerated particles, which are reported in Figure 10.4b; the protons number is reduced for the perforated RCF stacks because the central part of the accelerated particles are free to propagate in the TPS direction. The graph reveals that not only the proton cut-off energy is increased with the proper DLT, but also the ions number is sensibly enhanced; in particular a factor of about 4 is observable for the $4\ \mu m$ foam DLT (considering the RCF without hole which is the more accurate measurement).

RCF can be also exploited to obtain information about the laser energy conversion to other forms of secondary radiation, such as electrons and gamma rays; indeed, the top part of the stack is not affected by the proton beam, which propagates in straight direction, but only by the more diffused radiations. The measured dose in this part of the RCF is shown in Figure 10.5 with respect to the stack layer (for the normal incidence condition); the dose profile with the depth can't be used alone to determine if the dose contribution is more dependent onto gamma rays or electrons, nevertheless it should be observed that the total dose is enhanced by a factor about 6 for the $4\ \mu m$ foam DLT, with a trend very similar to the one observed in the TPS data at normal incidence.

A last indication of the improved laser energy absorption is given by the reflected light

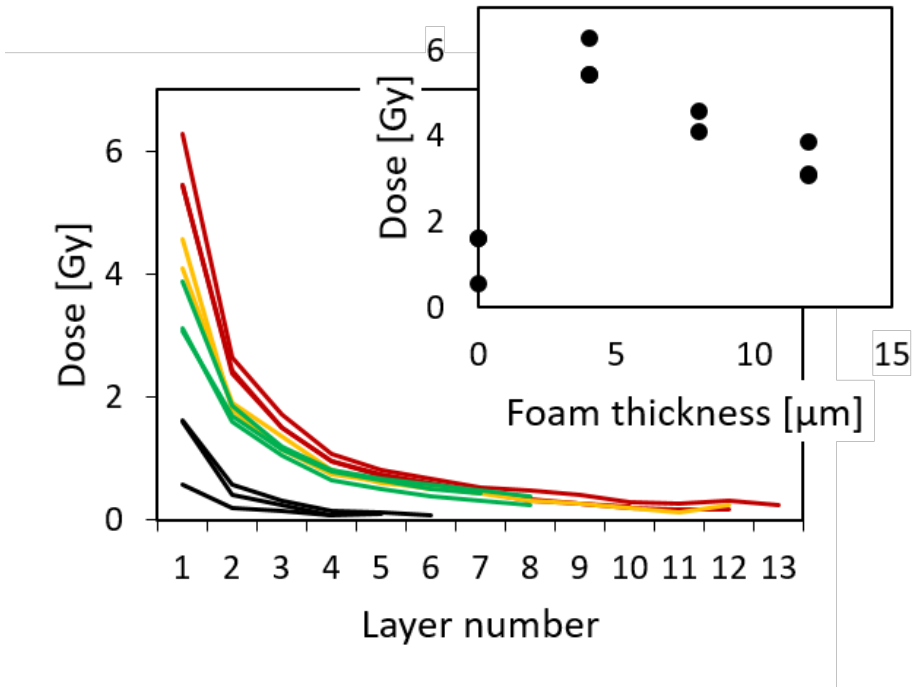

Figure 10.5: Measured dose in the RCF with respect to the stack layer number for DLTs with $4\ \mu m$ thick foam (in red), $8\ \mu m$ (in yellow), $12\ \mu m$ (in green) and for bare Al target (in black). The inset shows the total dose as function of the foam thickness.

data recorded at oblique incidence condition only; Figure 10.6a immediately reveals that the pulse energy reflected by the bare Aluminium target is much larger than the one measured in the presence of the DLT. Figure 10.6b summarizes the quantitative analysis consisting in integrating the total signal measured by the CCD (in arbitrary units) for different foam thickness and intensity. In all the cases a similar pseudo-exponential attenuation trend is seen, where thicker foams absorb the highest amount of laser energy.

It should be also noted that, when the DLT is irradiated, the reflected laser pattern is featured by higher and lower brightness spots with a spatial scale independent onto the foam thickness; this observation can be interpreted by the well-known *speckle pattern* phenomenon [148]. A speckle pattern is produced by the mutual interference of a set of incoherent wavefronts and it typically occurs in diffuse reflections of monochromatic light. Such reflections may happen on disordered materials such as paper, white paint, rough surfaces or media with a large number of scattering particles, which is exactly the nanofoam case. The speckles presence therefore suggests that the foam is maintaining its nanostructure at the moment of the main pulse interaction; as a consequence, the pre-expansion due to the pre-pulse can be reasonably considered negligible.

Another clue of a surviving nanostructure can be observed in the off-normal TPS spectra; sings of protons accelerated at $45°$ with respect to the normal are measured (using the TPS $0°$ for oblique incidence and the TPS $45°$ for normal one) and the cut-off energies are reported in Figure 10.7. These ions can't be explained by TNSA, because this acceleration process accelerate directional particles; conversely, *Coulomb Explosion* (CE) [149] of nanoparticles

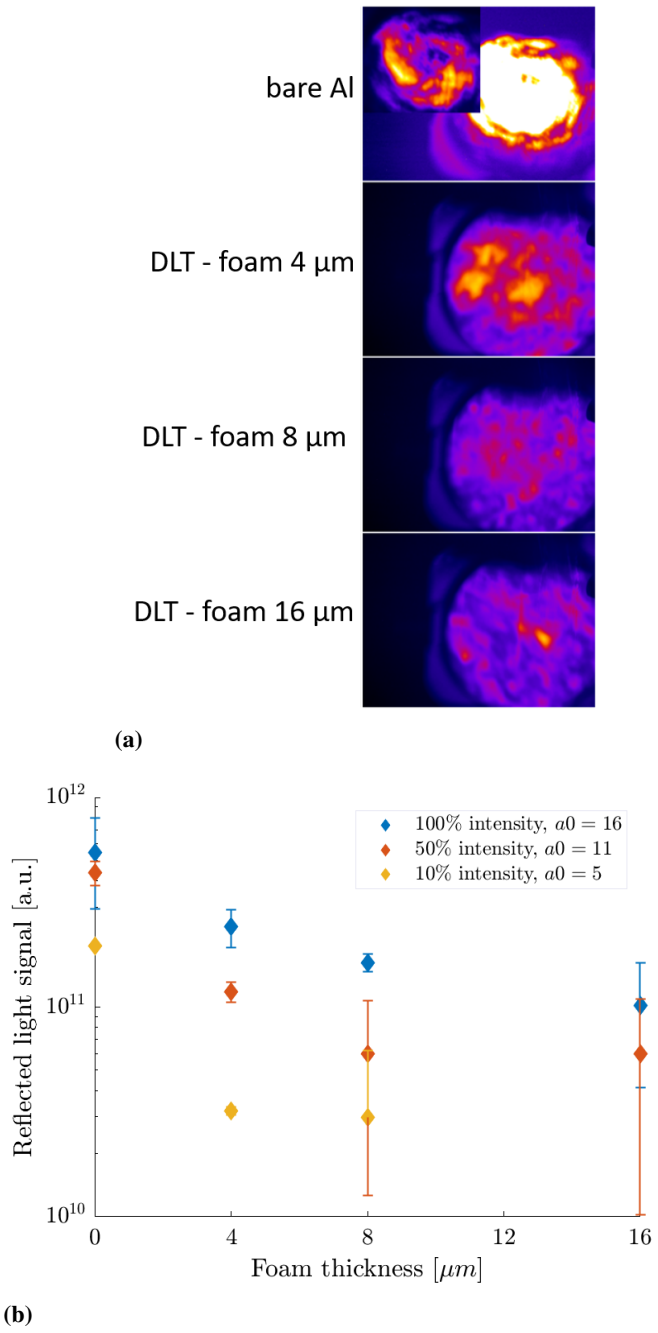

Figure 10.6: (a) Images of the reflected light measured for bare Al target and different foam thickness DLTs for oblique incidence; the inset in the upper figure shows the same image with adjusted contrast and brightness values. (b) Total measured reflected light signal (in arbitrary units) with respect to the foam thickness at different pulse intensity.

is a good candidate for the interpretation of the results. As yet introuced in Section 5.2, this acceleration mechanism consists in the nanoparticle ions explosion due to electrostatic repulsion, thanks to the almost completely removal of the electrons from the nanoparticle by the high laser ponderomotive force. The phenomenon is featured by an isotropic ions acceleration and by a continuum spectrum with a cut-off energy, dependent onto the charge density and the radius which can be considered fixed in all the irradiation conditions.

Indeed, both in Figure 10.7a (normal incidence) and in Figure 10.7b (oblique incidence),

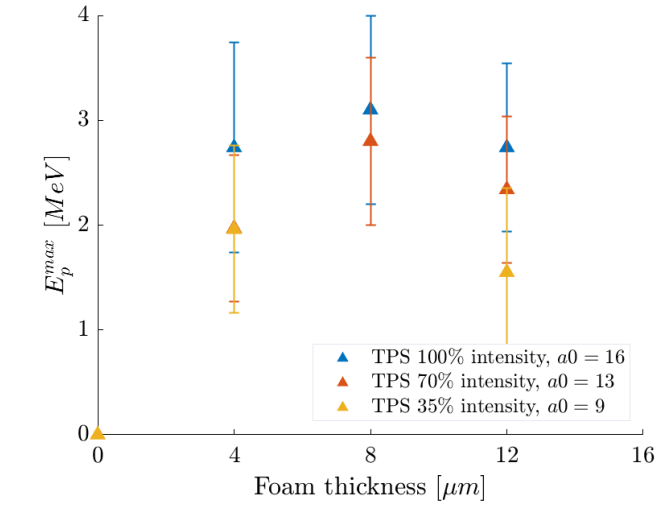

(a)

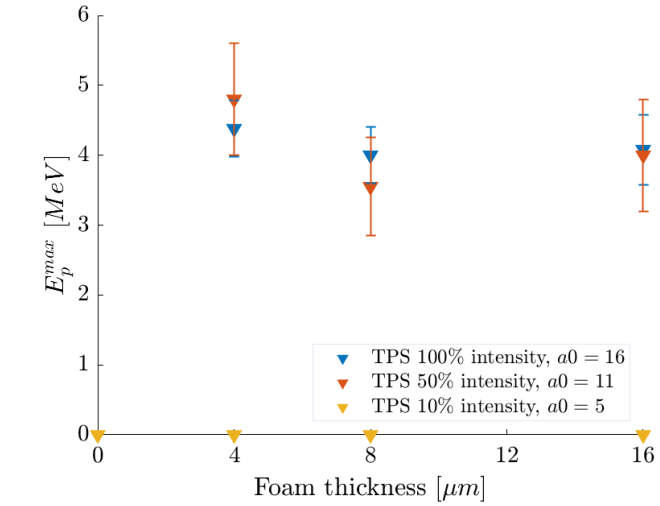

(b)

Figure 10.7: Cut-off proton energies measured by the off-normal TPS as a function of the nanofoam thickness at different pulse intensity; the $0\ \mu m$ value corresponds to bare Al target. In (a) the laser incidence angle is $0°$, while in (b) it is $45°$.

the maximum energy is almost independent onto the foam thickness and even the laser intensity; while no ions signal is measured in the presence of the standard bare target. The fact that the cut-off proton energy in the normal incidence case is lower than in the $45°$ incidence is probably due to the different instrument sensitivity together with the low CE signal, which decreases with the inverse of the squared distance between the source and the spectrometer.

It should be also noted that in the oblique incidence and 10% intensity case ($a_0 = 5$), no CE protons are visible; this is consistent with the low electron Lorentz factor $\gamma = \sqrt{1 + a_0^2/2} \sim 3.7$ which is comparable to the nanofoam density ($n_e \sim 3.2 n_c$). In this condition the relativistic transparency factor $\bar{n} \sim 0.87$ approaches one and the nanostructured plasma tends to be not very transparent and highly reflective, hindering the laser propagation (see Chapter 4); since only a little pulse energy is given to the nanostructure, it is reasonable to assume that only a little part of the nanoparticles are cleared by electrons, hence highly

damping the Coulomb Explosion signal.

10.3 Interpretation based on the relativistic transparency factor

The data described in the previous section show that the foam-based DLT is effective in enhancing the laser energy absorption and the accelerated ions energy and total charge; nevertheless, it appears that some target conditions (4 μm foam and normal incidence) lead to much higher performances compared to the others. To shed a light on these observations the results are compared to the model described in Chapter 4.

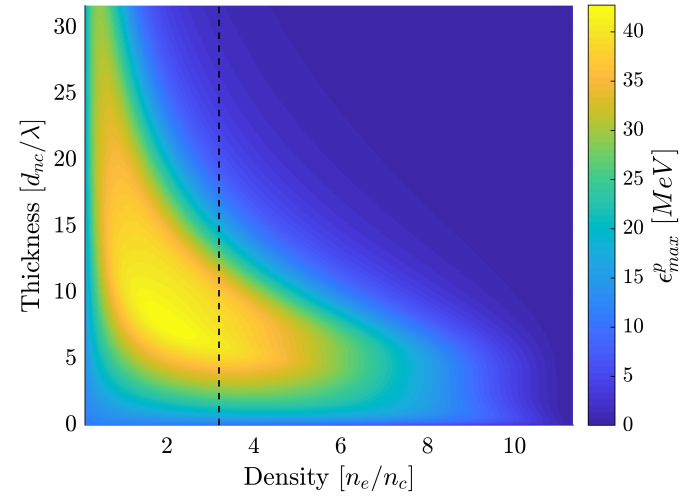

(a)

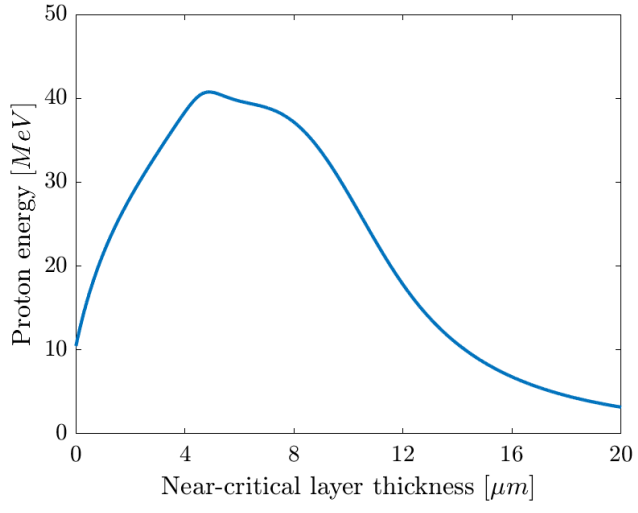

(b)

Figure 10.8: (a) Heat map representing DLTs cut-off proton energy (numerically calculated from the model described in Chapter 4) as a function of the near-critical layer thickness and density. The vertical black line corresponds to the density value (3.2 n_c) of the foams produced for the acceleration experiment. (b) Line-out of the heat map represented in (a) at the density value 3.2 n_c.

Firstly, the model is numerically solved for the specific laser parameters adopted in the experiment ($a_0 = 16$, $w_0 = 3\ \mu m$, $\tau = 30\ fs$) to find the heat map of Figure 10.8a, representing the proton energy as a function of the near-critical layer thickness and density.

It should be noted that the foam used for the DLTs has a density near the highest energy island (see the black dashed line), which means that high enhancement can be obtained if the proper thickness is adopted. A line-out of the heat map in correspondence of the $3.2\ n_c$ density value is shown in Figure 10.8b in order to theoretically determine the best thickness.

High enhancement values are predicted for both $4\ \mu m$ and $8\ \mu m$ thickness, which is consistent with the experimental findings; nevertheless, these energy values (up to $40\ MeV$) are much higher than the observed ones. This is probably due to the Direct Laser Acceleration damping effect described in Chapter 5: while in uniform near-critical plasmas, the electrons are resonant accelerated in the channel to high energies, the nanostructure breaks the channel symmetry and reduces the hot electrons temperature. As a consequence, the TNSA field strength is diminished and protons reach lower energies.

As yet introduced in Section 5.3, this damping effect can be taken into account by simply multiplying the near-critical layer hot electron temperature (see Equation 4.15) by a free parameter α_{ns} included between 0 and 1, which takes into account the inhomogeneity of the nanostructure:

$$E_{ns}(x) = \alpha_{ns} E_{nc}(x) \tag{10.1}$$

By solving the model with $\alpha_{ns} = 0.40$ (which is in agreement to the observed value of about 0.3 in the PIC electrons spectra, see Chapter 5) the predicted proton energies agree with the experimental data within the model validity range and the error bars, as shown in Figure 10.9.

One interesting feature is that the theoretical model of Chapter 4 justifies the highest enhancement factor obtained with the $4\ \mu m$ foam, which is near the self-focusing length and consequently the theoretical optimum thickness. In addition, it should be noted that the 35% intensity data are characterized by lower DLTs proton energies (normalized to the ponderomotive scaling), accordingly to the higher normalized density $\bar{n} = 0.44$ with respect to the 100% and 75% cases (with $\bar{n} = 0.26$ and $\bar{n} = 0.32$ respectively). As deeper described in Chapter 4, this is due to the higher reflectivity and the lower amplitude amplification at high $\bar{n}$.

It should be pointed out that more uniform foams should therefore increase the α_{ns} factor and higher enhancement factor up to the theoretical maximum (about 4) could be observed. In particular, not to suppress the Direct Laser Acceleration mechanism, the inhomogeneity nanostructure scale should be inferior than the laser wavelength, which could be realized in future experiments through nanofoamms produced by the fs-PLD, as decribed in Chapter 8.

Since the model predictions are reasonably in agreement with the experimental data, the model assumptions and the theoretical phenomenon description can be considered as justified. In this framework, it was analytically demonstrated in Section 4.2 that the near-critical layer electrons have a predominant weight in determining the TNSA field properties, due to their larger number and temperature. For this reason the incidence angle should play a role not for the alteration of the interaction mechanism (as for the flat solid target case), but for the different effective path length of the laser pulse propagating inside the transparent

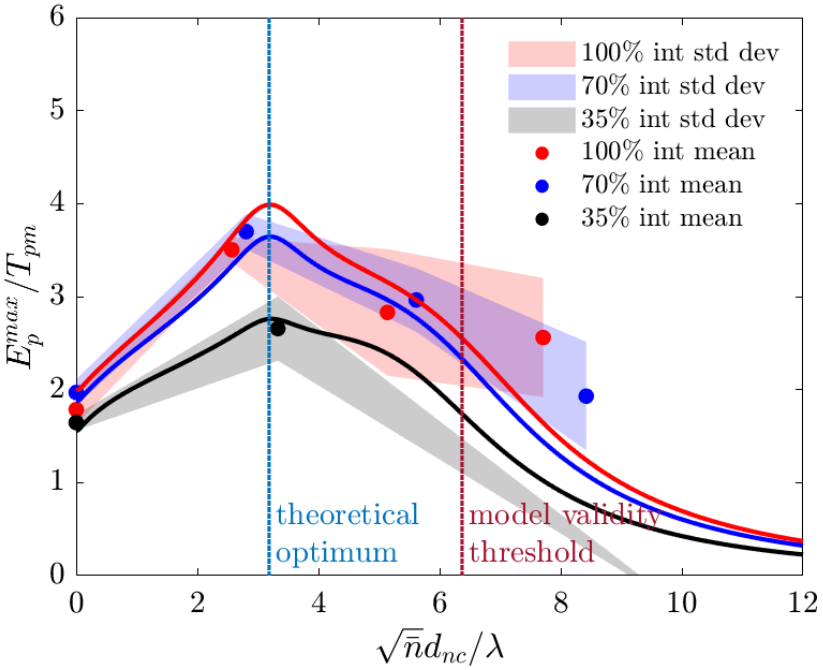

Figure 10.9: Comparison between the experimental TPS cut-off proton energies obtained at normal incidence and the theoretical predictions of the model described in Chapter 4 (modified to include the nanostructure effect with Equation 10.1). The proton cut-off energy is normalized to the ponderomotive scaling $T_{pm} = 0.511(\gamma - 1)\ MeV$, while the foam thickness is normalized to the laser wavelength and the square root of the relativistic transparency factor $\bar{n}$. The vertical blue line corresponds to the self-focusing length ($\sqrt{\bar{n}}l_f/\lambda \sim w_0/\lambda \sim 3.2$); the vertical red line corresponds to the maximum thickness value admitted from the model.

near-critical layer, as shown in the scheme of Figure 10.10.

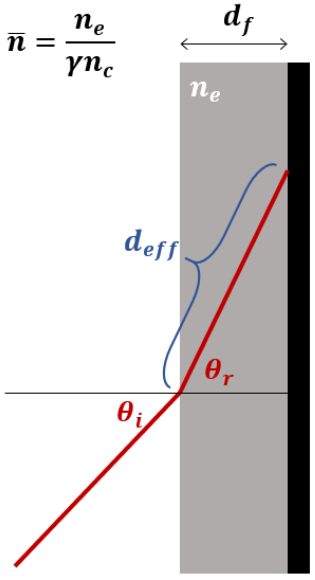

Figure 10.10: Scheme of the laser refraction phenomenon due to the near-critical plasma refractive index, lower than 1. θ_i and θ_r are respectively the incidence and refraction angles; n_e, d_f and $\bar{n}$ are respectively the near-critical layer density, thickness and relativistic transparency factor. The pulse propagation length inside the plasma is given by the effective thickness d_{eff}.

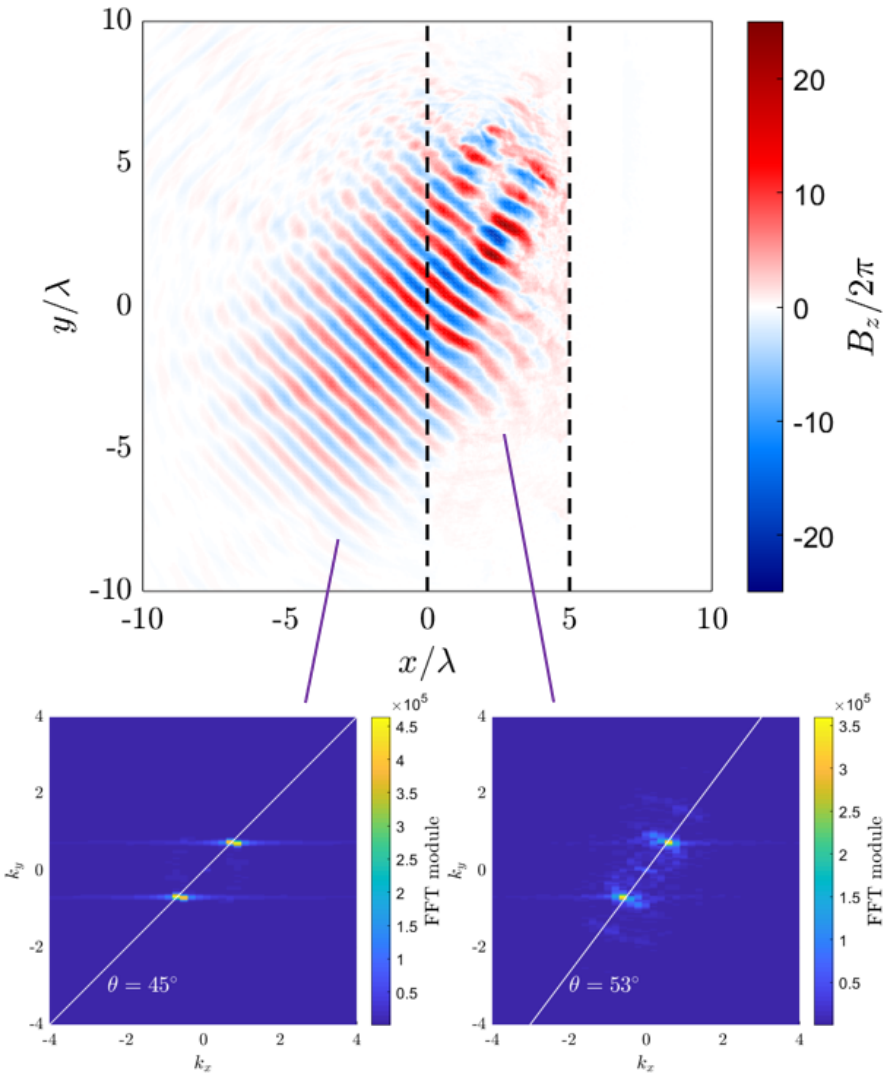

Figure 10.11: The blue-to-red color map represents the transverse component of the laser magnetic field B_z in the $z = 0$ plane, obtained from a 3D PIC simulation at time $15\lambda/c$ after the start of the interaction. The two insets report the Fast Fourier Transform evaluated in vacuum zone ($-10 < x < 0$) and in the near-critical layer ($0 < x < 5$). The angle between the FFT peaks is reported on the graphs.

The effective thickness of the near-critical layer hence depends on the foam thickness d_f, the incidence angle θ_i and the refraction angle θ_r; indeed, the near-critical layer acts as a transparent slab featured by a refractive index lower than one, which further deflects the laser pulse. A simple way to determine this angle consists in solving the Snell law: $\mathrm{n}_1 sin(\theta_i) = \mathrm{n}_2 sin(\theta_r)$, where $\mathrm{n}_1 = 1$ is the vacuum refractive index, while $\mathrm{n}_2 = \sqrt{1-\bar{n}}$ is the foam refractive index calculated in the cold relativistic plasma approximation. The angle of refraction is then calculated by:

$$\theta_r = asin\left[\frac{1}{\sqrt{1-\bar{n}}} sin(\theta_i)\right] \tag{10.2}$$

Therefore, the effective near-critical layer thickness assumes the following form:

$$d_{eff} = \frac{d_f}{cos\,(\theta_r)} \tag{10.3}$$

To test the goodness of the relativistic cold plasma refraction approximation, a 3D PIC simulation with the laser experimental parameters ($a_0 = 16$, $w_0 = 3\ \mu m$, $\tau = 30\ fs$, P polarization) and the DLCCA nanostructured plasma ($d_f = 4\ \mu m$, $n_e = 3\ n_c$) is carried out, using the same methodology exploited in Chapter 5.

In detail, the PIC simulation exploits an idealized cos^2 temporal profile for the laser pulse and a Gaussian transverse profile, which is focused at the vacuum-plasma boundary. The waist is 3.2λ, while the temporal duration is $15\ \lambda/c$ (FWHM of the fields). A $90\ \lambda \times 70\ \lambda \times 60\ \lambda$ box is used, with a resolution of 20 points per wavelength. The nanostructured DLCCA plasma fills a $5\ \lambda \times 70\ \lambda \times 60\ \lambda$ region with an average density of $3\ n_c$ and a local density of $\sim 40\ n_c$. 40 macro-electrons per cell, sufficient to resolve the critical density, are used. In the simulation the plasma is fully pre-ionized and the the charge/mass ratio of the ions is equal to 0.5 (e.g. C^{6+}). The electron population is initialized with a temperature of few hundreds of eVs to avoid numerical artefacts and to consider the effect of a little pre-heating.

Figure 10.11 shows a cut of the pulse transverse magnetic field B_z over the $z = 0$ plane, showing that the laser propagating inside the foam layer undergoes self-focusing and it is also refracted. To quantitative determine the tilt angle, the two-dimensional *Fast Fourier Transform* (FFT) is evaluated both in the vacuum zone and in the near-critical layer. As expected, the vacuum FFT peaks are tilted to $45°$, while they are aligned to about $53°$ in the foam case, which is reasonably in agreement with the angle of refraction calculated from Equation 10.2 ($\theta_r = 55°$).

The concept of effective thickness is tested with the experimental data: the reflected light collected at $45°$ incidence is normalized to the fraction of the maximum intensity on the ordinate (1 and 0.5 for the $a_0 = 16$ and $a_0 = 11$ cases, respectively) and the abscissa values are normalized with the effective thickness and the square root of the relativistic transparency factor $\bar{n}$, for the reasons explained in Chapter 4. Figure 10.12a represents these data and indicates a self-similar trend in the reflected light with respect to the normalized effective thickness; this observation suggests that the pulse is absorbed and reflected self-similarly within the observed intensity and density ranges.

Finally, the same normalization approach is adopted for the TPS proton energy data, measured at different intensities and angle of incidence; in particular, Figure 10.12b represents the maximum proton energy normalized to the ponderomotive scaling as a function of the normalized effective foam thickness $\bar{d}_{eff} = \sqrt{\bar{n}} d_f / cos(\theta_r)\lambda$. Again all the measured cut-off proton energies collapse to a single self-similar curve, where the highest values are obtained near the self-focusing length (which is about 3.2 in the normalized units). It should be also noted that higher $\bar{n}$ points are characterized by little lower energies, since higher pulse reflection and absorption is expected.

This TPS proton energy normalization could be particularly useful because, not only val-

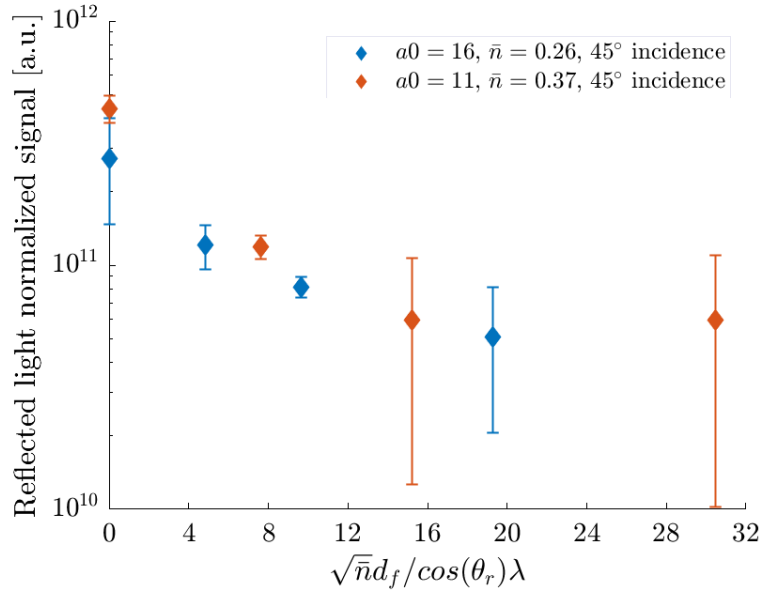

(a)

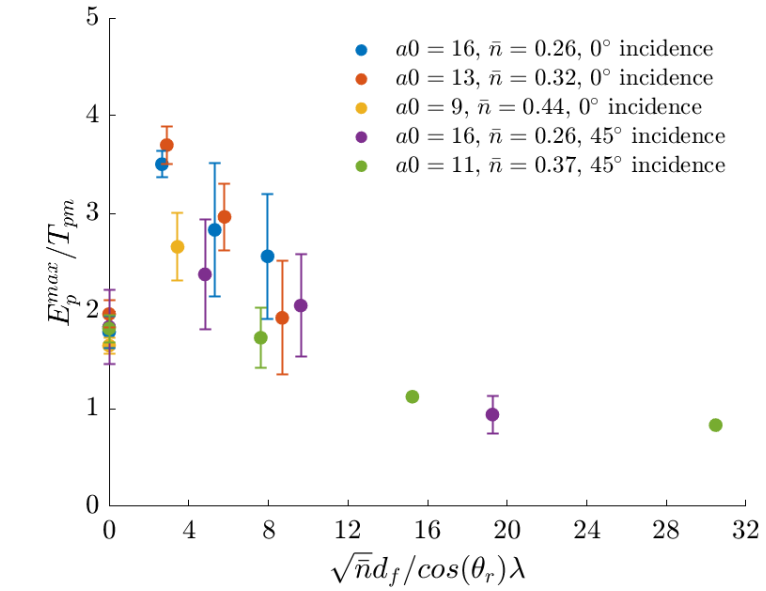

(b)

Figure 10.12: (a) Reflected light total signal measured at oblique incidence as a function of the normalized effective foam thickness $\bar{d}_{eff}$; the ordinate is normalized to the maximum intensity fraction. (b) Cut-off proton energies measured by TPS at normal and oblique incidence at different pulse intensity; the ordinate is normalized to the ponderomotive scaling ($T_{pm} = 0.511(\gamma - 1)\ MeV$) while the abscissa represents the relativistically normalized effective thickness $\bar{d}_{eff}$.

idates the theoretical framework of Chapter 4, but also puts the basis for future experimental work: even if the laser parameters are changed, for example the pulse energy is increased or the angle of incidence is chosen to an intermediate value between $0°$ and $45°$, the self-similar behaviour should be respected. Thus the nanofoam parameters can be proper selected near the maximum enhancement conditions.

Part V

Conclusions and future perspectives

Conclusions and future perspectives

In this PhD thesis, near-critical Double-Layer Targets (DLT) for the enhanced ion acceleration, driven by ultra intense ($> 10^{19}\ W/cm^2$) ultra short ($10s\ fs$) laser pulses, were investigated through the analysis of numerical simulations, the development of suitable advanced material science techniques for target manufacturing and a laser driven ion acceleration experiment performed in an external laser facility.

As introduced in Chapter 1, laser-driven ion acceleration is a peculiar phenomenon occurring when an ultra-intense and ultra-short laser pulse is focused over a thin solid target; the accelerated ions are featured by a broad exponential distribution with a cut-off energy in the order of $MeVs$ and by a directional emission along the normal of the target. The phenomenon can be interpreted by the Target Normal Sheath Acceleration model (described in Section 1.3): in this framework the ions are pushed by strong electrostatic fields generated by the charge separation of hot electrons expanding in the vacuum.

A laser-driven ion source could be exploited for several application in the near future, due to its cheapness and compactness with respect to standard accelerators; nevertheless, to take the best advantage of it, the TNSA process should be further optimized by increasing the laser conversion efficiency to fast ions. As explained in Section 2.2, a promising strategy consists in irradiating advanced Double-Layer Targets, composed by a standard solid foil with an ultra-low density front layer which matches the plasma transparency condition (called critical density); in this regime the pulse is better absorbed into hot electrons and results into more energetic and numerous ions.

The last introductory chapter (Chapter 3) described the state of the art in producing and characterizing near-critical DLTs based on a particular nanostructured material, called Carbon nanofoam, which is produced by a particular technique, the Pulsed Nanosecond Laser Deposition (ns-PLD); the nanostructured material, thanks to its fractal structure, has a high porosity and an ultra-low density, capable to increase the laser absorption and the ions energy, as demonstrated in the reported laser acceleration experiments.

In this framework, this PhD thesis aimed to bring off several goals: to investigate with

simulations and analytical tools the enhanced acceleration process with DLTs (Part II), to experimentally improve the production and characterization of the C nanofoam (Part III) and, finally, to exploit the gained insights on DLTs to perform a laser-acceleration experiment with better ion energy enhancements (Part IV).

In more detail, Chapter 4 dealt with the numerical simulation of DLTs (with the Particle-In-Cell method) with ideal conditions, namely uniform near-critical layer, normal incidence and P linear polarization. The simulation results were used to build a theoretical model which describes the laser-DLT interaction, the hot electrons heating and the resulting ion acceleration; the model was analytically solved to find the optimal thickness and density that a near-critical layer should have, for the best performances. Moreover, in Chapter 5 more realistic simulations were carried out (with nanostructured plasmas and other polarizations) and the results showed differences with respect to the ideal case; these non-idealities were discussed and integrated in the above-mentioned theoretical framework.

Chapter 6 described an improved method for the C nanofoam density and uniformity characterization, validated with benchmark techniques; while in Chapter 7 the foam growth process was experimentally analysed and the Snowfall-like model was proposed. This model described the nanofoam production as the deposition on the substrate of micro-metric fractal aggregates, composed by nanoparticles and formed in the ns-PLD vacuum chamber; the gained insights enabled to obtain a better control over the deposited nanofoam density. In addition, a new technique was implemented and presented in Chapter 8, the Pulsed Femtosecond Laser Deposition (fs-PLD); the fs-PLD was exploited to produce C nanofoams featured by lower densities and higher uniformity, as well to investigate the capability to deposit nanofoams from different elemental composition (Copper and Tungsten).

Finally, Chapter 9 illustrated the manufacturing method for the DLTs production and the related damaging issues, which can be avoided with proper precautions. The produced DLTs were used in an enhanced laser-driven ion acceleration experiment, in collaboration with the Helmoltz-Zentrum-Dresden-Russeldorf in Germany. The results, reported in Chapter 10, showed a higher proton energy enhancement with respect the foam-based DLT state of the art; in addition, the experimental evidences were quantitatively interpreted with the theoretical framework, developed in Chapters 4 and 5.

Owing to these results, this PhD thesis paves the way for new future research: it has been theoretically demonstrated in Chapter 5 that the nanofoam non-uniformity has a detrimental effect on the ion acceleration process, thus it should be highly beneficial for further increasing the DLT performances to take advantage of the fs-PLD technique to produce more homogeneous foams, with density and thickness specified by the theoretical model of Chapter 4. In addition, more complex phenomena occurring in the laser-DLT interaction could be deepened; for example, it is well known that the laser pulses undergoes to phase self-modulation (i.e. light spectrum broadening and chirping) during the propagation in under-critical plasmas. The study of this effect through PIC simulations could be used to pre-compensate the phenomenon, inducing a laser anti-chirp or third-order dispersion, and to reduced the pulse

temporal duration. Also the use of high atomic number nanofoams could be an interesting field of research, since they can be efficiently produced by the fs-PLD and studied with proper PIC simulations. Indeed, it is known that the ionization rate, in high atomic number materials, is very sensible to the local laser intensity; a DLT with this property should have the effect of increasing the number of hot electrons where the pulse intensity is higher, with the result of forming a more dense and energetic electron cloud and, consequently, a stronger accelerating sheath field. Finally, the high atomic number nanofoams could be also exploited to increase the conversion of hot electrons into energetic photons through the bremsstrahlung mechanism; this kind of bright gamma rays source could be used in several application, as the photon activation analysis or the detection of illicit radioactive materials.

Bibliography

[1] A Einstein. Zur quantentheorie der strahlung. *Phys. Z.*, 18:121–128, 1917.

[2] TH Maiman et al. Stimulated optical radiation in ruby. 1960.

[3] FJ McClung and RW Hellwarth. Giant optical pulsations from ruby. *Journal of Applied Physics*, 33(3):828–829, 1962.

[4] LE Hargrove, Richard L Fork, and MA Pollack. Locking of he–ne laser modes induced by synchronous intracavity modulation. *Applied Physics Letters*, 5(1):4–5, 1964.

[5] PA Franken, AE Hill, CW Peters, and G Weinreich. Generation of optical harmonics. *Physical Review Letters*, 7(4):118, 1961.

[6] D Strickland and G Mourou. Compression of amplified chirped optical pulses. *Optics communications*, 55(6):447–449, 1985.

[7] S-W Bahk, P Rousseau, TA Planchon, V Chvykov, G Kalintchenko, A Maksimchuk, GA Mourou, and V Yanovsky. Generation and characterization of the highest laser intensities (10 22 w/cm 2). *Optics letters*, 29(24):2837–2839, 2004.

[8] JW Yoon, C Jeon, J Shin, SK Lee, HW Lee, IW Choi, HT Kim, JH Sung, and CH Nam. Achieving the laser intensity of 5.5× 10 22 w/cm 2 with a wavefront-corrected multi-pw laser. *Optics express*, 27(15):20412–20420, 2019.

[9] X-M Tong, ZX Zhao, and C-D Lin. Theory of molecular tunneling ionization. *Physical Review A*, 66(3):033402, 2002.

[10] RJ Goldston and PH Rutherford. *Introduction to plasma physics*. CRC Press, 1995.

[11] G Malka and JL Miquel. Experimental confirmation of ponderomotive-force electrons produced by an ultrarelativistic laser pulse on a solid target. *Physical review letters*, 77(1):75, 1996.

[12] L Cialfi, L Fedeli, and M Passoni. Electron heating in subpicosecond laser interaction with overdense and near-critical plasmas. *Physical Review E*, 94(5):053201, 2016.

[13] A Maksimchuk, S Gu, K Flippo, D Umstadter, and VY Bychenkov. Forward ion acceleration in thin films driven by a high-intensity laser. *Physical Review Letters*, 84(18):4108, 2000.

[14] RA Snavely, MH Key, SP Hatchett, TE Cowan, M Roth, TW Phillips, MA Stoyer, EA Henry, TC Sangster, MS Singh, et al. Intense high-energy proton beams from petawatt-laser irradiation of solids. *Physical review letters*, 85(14):2945, 2000.

[15] SP Hatchett, CG Brown, TE Cowan, EA Henry, JS Johnson, MH Key, JA Koch, AB Langdon, BF Lasinski, RW Lee, et al. Electron, photon, and ion beams from the relativistic interaction of petawatt laser pulses with solid targets. *Physics of Plasmas*, 7(5):2076–2082, 2000.

[16] A Macchi, M Borghesi, and M Passoni. Ion acceleration by superintense laser-plasma interaction. *Reviews of Modern Physics*, 85(2):751, 2013.

[17] J Schreiber, PR Bolton, and K Parodi. Invited review article:"hands-on" laser-driven ion acceleration: A primer for laser-driven source development and potential applications. *Review of Scientific Instruments*, 87(7):071101, 2016.

[18] V Malka, J Faure, YA Gauduel, E Lefebvre, A Rousse, and KT Phuoc. Principles and applications of compact laser–plasma accelerators. *Nature physics*, 4(6):447, 2008.

[19] SC Wilks, AB Langdon, TE Cowan, M Roth, M Singh, S Hatchett, MH Key, D Pennington, A MacKinnon, and RA Snavely. Energetic proton generation in ultra-intense laser–solid interactions. *Physics of plasmas*, 8(2):542–549, 2001.

[20] D Neely, P Foster, A Robinson, F Lindau, O Lundh, A Persson, C-G Wahlström, and P McKenna. Enhanced proton beams from ultrathin targets driven by high contrast laser pulses. *Applied Physics Letters*, 89(2):021502, 2006.

[21] JS Green, APL Robinson, N Booth, DC Carroll, RJ Dance, RJ Gray, DA MacLellan, P McKenna, CD Murphy, D Rusby, et al. High efficiency proton beam generation through target thickness control in femtosecond laser-plasma interactions. *Applied Physics Letters*, 104(21):214101, 2014.

[22] JH Bin, WJ Ma, HY Wang, MJV Streeter, C Kreuzer, D Kiefer, M Yeung, S Cousens, PS Foster, B Dromey, et al. Ion acceleration using relativistic pulse shaping in near-critical-density plasmas. *Physical review letters*, 115(6):064801, 2015.

[23] M Passoni, L Bertagna, T Ceccotti, and P Martin. Proton maximum energy cutoff scaling laws for bulk targets. In *AIP Conference Proceedings*, volume 1153, pages 159–163. AIP, 2009.

[24] K Zeil, SD Kraft, S Bock, M Bussmann, TE Cowan, T Kluge, J Metzkes, T Richter, R Sauerbrey, and U Schramm. The scaling of proton energies in ultrashort pulse laser plasma acceleration. *New Journal of Physics*, 12(4):045015, 2010.

[25] J Metzkes, T Kluge, K Zeil, M Bussmann, SD Kraft, TE Cowan, and U Schramm. Experimental observation of transverse modulations in laser-driven proton beams. *New Journal of Physics*, 16(2):023008, 2014.

[26] M Passoni, A Sgattoni, I Prencipe, L Fedeli, D Dellasega, L Cialfi, IW Choi, IJ Kim, KA Janulewicz, HW Lee, et al. Toward high-energy laser-driven ion beams: Nanostructured double-layer targets. *Physical Review Accelerators and Beams*, 19(6):061301, 2016.

[27] D Margarone, IJ Kim, J Psikal, J Kaufman, T Mocek, IW Choi, L Stolcova, J Proska, A Choukourov, I Melnichuk, et al. Laser-driven high-energy proton beam with homogeneous spatial profile from a nanosphere target. *Physical Review Special Topics-Accelerators and Beams*, 18(7):071304, 2015.

[28] IJ Kim, KH Pae, CM Kim, HT Kim, JH Sung, SK Lee, TJ Yu, IW Choi, C-L Lee, KH Nam, et al. Transition of proton energy scaling using an ultrathin target irradiated by linearly polarized femtosecond laser pulses. *Physical review letters*, 111(16):165003, 2013.

[29] KA Flippo, J Workman, DC Gautier, S Letzring, RP Johnson, and T Shimada. Scaling laws for energetic ions from the commissioning of the new los alamos national laboratory 200 tw trident laser. *Review of Scientific Instruments*, 79(10):10E534, 2008.

[30] L Robson, PT Simpson, RJ Clarke, KWD Ledingham, F Lindau, O Lundh, T McCanny, P Mora, D Neely, C-G Wahlström, et al. Scaling of proton acceleration driven by petawatt-laser–plasma interactions. *Nature physics*, 3(1):58, 2007.

[31] J Fuchs, P Antici, E d'Humières, E Lefebvre, M Borghesi, E Brambrink, CA Cecchetti, M Kaluza, V Malka, M Manclossi, et al. Laser-driven proton scaling laws and new paths towards energy increase. *Nature physics*, 2(1):48, 2006.

[32] M Lontano and M Passoni. Electrostatic field distribution at the sharp interface between high density matter and vacuum. *Physics of plasmas*, 13(4):042102, 2006.

[33] M Passoni and M Lontano. Theory of light-ion acceleration driven by a strong charge separation. *Physical review letters*, 101(11):115001, 2008.

[34] M Passoni, C Perego, A Sgattoni, and D Batani. Advances in target normal sheath acceleration theory. *Physics of Plasmas*, 20(6):060701, 2013.

[35] J Fuchs, P Antici, E d'Humières, E Lefebvre, M Borghesi, E Brambrink, CA Cecchetti, Ma Kaluza, V Malka, M Manclossi, et al. Laser-driven proton scaling laws and new paths towards energy increase. *Nature physics*, 2(1):48, 2006.

[36] S Betti, F Ceccherini, F Cornolti, and F Pegoraro. Expansion of a finite-size plasma in vacuum. *Plasma physics and controlled fusion*, 47(3):521, 2005.

[37] P Mora. Thin-foil expansion into a vacuum. *Physical Review E*, 72(5):056401, 2005.

[38] RR Freeman, D Batani, S Baton, M Key, and R Stephens. The generation and transport of large currents in dense materials: The physics of electron transport relative to fast ignition. *Fusion science and technology*, 49(3):297–315, 2006.

[39] T Ceccotti, A Lévy, H Popescu, F Réau, P d'Oliveira, P Monot, JP Geindre, E Lefebvre, and Ph Martin. Proton acceleration with high-intensity ultrahigh-contrast laser pulses. *Physical review letters*, 99(18):185002, 2007.

[40] K Zeil, J Metzkes, T Kluge, M Bussmann, TE Cowan, SD Kraft, R Sauerbrey, B Schmidt, M Zier, and U Schramm. Robust energy enhancement of ultrashort pulse laser accelerated protons from reduced mass targets. *Plasma Physics and Controlled Fusion*, 56(8):084004, 2014.

[41] L Fedeli, A Sgattoni, G Cantono, D Garzella, F Réau, I Prencipe, M Passoni, M Raynaud, M Květoň, J Proska, et al. Electron acceleration by relativistic surface plasmons in laser-grating interaction. *Physical review letters*, 116(1):015001, 2016.

[42] T Ceccotti, V Floquet, A Sgattoni, A Bigongiari, O Klimo, M Raynaud, C Riconda, A Heron, F Baffigi, L Labate, et al. Evidence of resonant surface-wave excitation in the relativistic regime through measurements of proton acceleration from grating targets. *Physical review letters*, 111(18):185001, 2013.

[43] D Margarone, O Klimo, IJ Kim, J Prokupek, J Limpouch, TM Jeong, T Mocek, J Psikal, HT Kim, J Proska, et al. Laser-driven proton acceleration enhancement by nanostructured foils. *Physical review letters*, 109(23):234801, 2012.

[44] V Floquet, O Klimo, J Psikal, A Velyhan, J Limpouch, J Proska, F Novotny, L Stolcova, A Macchi, A Sgattoni, et al. Micro-sphere layered targets efficiency in laser driven proton acceleration. *Journal of Applied Physics*, 114(8):083305, 2013.

[45] SA Gaillard, T Kluge, KA Flippo, M Bussmann, B Gall, T Lockard, M Geissel, DT Offermann, M Schollmeier, Y Sentoku, et al. Increased laser-accelerated proton energies via direct laser-light-pressure acceleration of electrons in microcone targets. *Physics of Plasmas*, 18(5):056710, 2011.

[46] A Higginson, RJ Gray, M King, RJ Dance, SDR Williamson, NMH Butler, R Wilson, R Capdessus, C Armstrong, JS Green, et al. Near-100 mev protons via a laser-driven transparency-enhanced hybrid acceleration scheme. *Nature communications*, 9(1):724, 2018.

[47] A Pukhov and J Meyer-ter Vehn. Relativistic magnetic self-channeling of light in near-critical plasma: three-dimensional particle-in-cell simulation. *Physical review letters*, 76(21):3975, 1996.

[48] A Pukhov, Z-M Sheng, and J Meyer-ter Vehn. Particle acceleration in relativistic laser channels. *Physics of Plasmas*, 6(7):2847–2854, 1999.

[49] HY Wang, C Lin, ZM Sheng, B Liu, S Zhao, ZY Guo, YR Lu, XT He, JE Chen, and XQ Yan. Laser shaping of a relativistic intense, short gaussian pulse by a plasma lens. *Physical review letters*, 107(26):265002, 2011.

[50] F Sylla, A Flacco, S Kahaly, M Veltcheva, A Lifschitz, V Malka, E d'Humières, I Andriyash, and V Tikhonchuk. Short intense laser pulse collapse in near-critical plasma. *Physical review letters*, 110(8):085001, 2013.

[51] T Nakamura, SV Bulanov, TZ Esirkepov, and M Kando. High-energy ions from near-critical density plasmas via magnetic vortex acceleration. *Physical review letters*, 105(13):135002, 2010.

[52] A Sgattoni, P Londrillo, A Macchi, and M Passoni. Laser ion acceleration using a solid target coupled with a low-density layer. *Physical Review E*, 85(3):036405, 2012.

[53] ON Rosmej, NE Andreev, S Zaehter, N Zahn, P Christ, B Borm, T Radon, A Sokolov, LP Pugachev, D Khaghani, et al. Interaction of relativistically intense laser pulses with long-scale near critical plasmas for optimization of laser based sources of mev electrons and gamma-rays. *New Journal of Physics*, 21(4):043044, 2019.

[54] M Passoni, A Zani, A Sgattoni, D Dellasega, A Macchi, I Prencipe, V Floquet, P Martin, TV Liseykina, and T Ceccotti. Energetic ions at moderate laser intensities using foam-based multi-layered targets. *Plasma Physics and Controlled Fusion*, 56(4):045001, 2014.

[55] I Prencipe, A Sgattoni, D Dellasega, L Fedeli, L Cialfi, Il Woo Choi, IJ Kim, KA Janulewicz, KF Kakolee, HW Lee, et al. Development of foam-based layered targets for laser-driven ion beam production. *Plasma Physics and Controlled Fusion*, 58(3):034019, 2016.

[56] JH Bin, M Yeung, Z Gong, HY Wang, C Kreuzer, ML Zhou, MJV Streeter, PS Foster, S Cousens, B Dromey, et al. Enhanced laser-driven ion acceleration by superponderomotive electrons generated from near-critical-density plasma. *Physical review letters*, 120(7):074801, 2018.

[57] JH Bin, WJ Ma, HY Wang, MJV Streeter, C Kreuzer, D Kiefer, M Yeung, S Cousens, PS Foster, B Dromey, et al. Ion acceleration using relativistic pulse shaping in near-critical-density plasmas. *Physical review letters*, 115(6):064801, 2015.

[58] WJ Ma, I Jong Kim, JQ Yu, Il Woo Choi, PK Singh, HW Lee, Jae Hee Sung, SK Lee, C Lin, Q Liao, et al. Laser acceleration of highly energetic carbon ions using a double-layer target composed of slightly underdense plasma and ultrathin foil. *Physical review letters*, 122(1):014803, 2019.

[59] A Macchi, S Veghini, TV Liseykina, and F Pegoraro. Radiation pressure acceleration of ultrathin foils. *New Journal of Physics*, 12(4):045013, 2010.

[60] F Sylla, M Veltcheva, S Kahaly, A Flacco, and V Malka. Development and characterization of very dense submillimetric gas jets for laser-plasma interaction. *Review of Scientific Instruments*, 83(3):033507, 2012.

[61] AM Khalenkov, NG Borisenko, VN Kondrashov, Yu A Merkuliev, J Limpouch, and VG Pimenov. Experience of micro-heterogeneous target fabrication to study energy transport in plasma near critical density. *Laser and Particle Beams*, 24(2):283–290, 2006.

[62] W Ma, L Song, R Yang, T Zhang, Y Zhao, L Sun, Y Ren, D Liu, L Liu, J Shen, et al. Directly synthesized strong, highly conducting, transparent single-walled carbon nanotube films. *Nano Letters*, 7(8):2307–2311, 2007.

[63] A Zani, D Dellasega, V Russo, and M Passoni. Ultra-low density carbon foams produced by pulsed laser deposition. *Carbon*, 56:358–365, 2013.

[64] NG Borisenko, IV Akimova, AI Gromov, AM Khalenkov, Yu A Merkuliev, VN Kondrashov, J Limpouch, J Kuba, E Krousky, K Masek, et al. Regular 3-d networks with clusters for controlled energy transport studies in laser plasma near critical density. *Fusion science and technology*, 49(4):676–685, 2006.

[65] NG Borisenko, AM Khalenkov, V Kmetik, J Limpouch, Yu A Merkuliev, and VG Pimenov. Plastic aerogel targets and optical transparency of undercritical microheterogeneous plasma. *Fusion science and technology*, 51(4):655–664, 2007.

[66] DB Geohegan, AA Puretzky, G Duscher, and SJ Pennycook. Time-resolved imaging of gas phase nanoparticle synthesis by laser ablation. *Applied Physics Letters*, 72(23):2987–2989, 1998.

[67] MS Tillack, DW Blair, and SS Harilal. The effect of ionization on cluster formation in laser ablation plumes. *Nanotechnology*, 15(3):390, 2004.

[68] AJ d'Alfonso, B Freitag, D Klenov, and LJ Allen. Atomic-resolution chemical mapping using energy-dispersive x-ray spectroscopy. *Physical Review B*, 81(10):100101, 2010.

[69] WE Sweeney Jr, RE Seebold, and LS Birks. Electron probe measurements of evaporated metal films. *Journal of Applied Physics*, 31(6):1061–1064, 1960.

[70] GH Cockett and CD Davis. Coating thickness measurement by electron probe microanalysis. *British Journal of Applied Physics*, 14(11):813, 1963.

[71] I Prencipe, D Dellasega, A Zani, D Rizzo, and M Passoni. Energy dispersive x-ray spectroscopy for nanostructured thin film density evaluation. *Science and technology of advanced materials*, 16(2):025007, 2015.

[72] P Willich, D Obertop, and HJ Tolle. Quantitative electron microprobe determination of oxygen in metal layers covered by surface oxide films. *X-Ray Spectrometry*, 14(2):84–88, 1985.

[73] JL Pouchou. X-ray microanalysis of stratified specimens. *Analytica chimica acta*, 283(1):81–97, 1993.

[74] C Merlet. A new quantitative procedure for stratified samples in epma. In *Proceedings of the 29th annual conference of the Microbeam Analysis Society*, pages 203–204, 1995.

[75] YG Lavrent'Ev, VN Korolyuk, and LV Usova. Second generation of correction methods in electron probe x-ray microanalysis: Approximation models for emission depth distribution functions. *Journal of Analytical Chemistry*, 59(7):600–616, 2004.

[76] P Karduck and W Rehbach. Microbeam analysis, 1988.

[77] K Harres, M Schollmeier, E Brambrink, P Audebert, A Blažević, K Flippo, DC Gautier, M Geißel, BM Hegelich, F Nürnberg, et al. Development and calibration of a thomson parabola with microchannel plate for the detection of laser-accelerated mev ions. *Review of Scientific Instruments*, 79(9):093306, 2008.

[78] S Eliezer. *The interaction of high-power lasers with plasmas*. CRC press, 2002.

[79] John Dawson. One-dimensional plasma model. *The Physics of Fluids*, 5(4):445–459, 1962.

[80] CK Birdsall and AB Langdon. *Plasma physics via computer simulation*. CRC press, 2018.

[81] R Courant, K Friedrichs, and H Lewy. On the partial difference equations of mathematical physics. *IBM journal of Research and Development*, 11(2):215–234, 1967.

[82] EV Stenson, J Horn-Stanja, MR Stoneking, and TS Pedersen. Debye length and plasma skin depth: two length scales of interest in the creation and diagnosis of laboratory pair plasmas. *Journal of Plasma Physics*, 83(1), 2017.

[83] A Sgattoni, L Fedeli, S Sinigardi, A Marocchino, A Macchi, V Weinberg, and A Karmakar. Optimising piccante-an open source particle-in-cell code for advanced simulations on tier-0 systems. *arXiv preprint arXiv:1503.02464*, 2015.

[84] J Babaei, LA Gizzi, P Londrillo, S Mirzanejad, T Rovelli, S Sinigardi, and G Turchetti. Rise time of proton cut-off energy in 2d and 3d pic simulations. *Physics of Plasmas*, 24(4):043106, 2017.

[85] A Macchi. *A Superintense Laser-Plasma Interaction Theory Primer*. Springer Science & Business Media, 2013.

[86] DT Moore. Gradient-index optics: a review. *Applied Optics*, 19(7):1035–1038, 1980.

[87] HY Wang, XQ Yan, JE Chen, XT He, WJ Ma, JH Bin, J Schreiber, T Tajima, and D Habs. Efficient and stable proton acceleration by irradiating a two-layer target with a linearly polarized laser pulse. *Physics of Plasmas*, 20(1):013101, 2013.

[88] S Gordienko and A Pukhov. Scalings for ultrarelativistic laser plasmas and quasimonoenergetic electrons. *Physics of Plasmas*, 12(4):043109, 2005.

[89] SS Bulanov, VY Bychenkov, V Chvykov, G Kalinchenko, DW Litzenberg, T Matsuoka, AGR Thomas, L Willingale, V Yanovsky, K Krushelnick, et al. Generation of gev protons from 1 pw laser interaction with near critical density targets. *Physics of plasmas*, 17(4):043105, 2010.

[90] JR Davies. Laser absorption by overdense plasmas in the relativistic regime. *Plasma Physics and Controlled Fusion*, 51(1):014006, 2008.

[91] P Gibbon, AA Andreev, and KY Platonov. A kinematic model of relativistic laser absorption in an overdense plasma. *Plasma Physics and Controlled Fusion*, 54(4):045001, 2012.

[92] YQ Cui, WM Wang, ZM Sheng, YT Li, and Jie Zhang. Laser absorption and hot electron temperature scalings in laser–plasma interactions. *Plasma Physics and Controlled Fusion*, 55(8):085008, 2013.

[93] T Liseykina, P Mulser, and M Murakami. Collisionless absorption, hot electron generation, and energy scaling in intense laser-target interaction. *Physics of Plasmas*, 22(3):033302, 2015.

[94] DB Zou, HB Zhuo, XH Yang, FQ Shao, YY Ma, TP Yu, HC Wu, Y Yin, ZY Ge, and XH Li. Enhanced target normal sheath acceleration based on the laser relativistic self-focusing. *Physics of Plasmas*, 21(6):063103, 2014.

[95] TA Witten Jr and LM Sander. Diffusion-limited aggregation, a kinetic critical phenomenon. *Physical review letters*, 47(19):1400, 1981.

[96] P Meakin and HE Stanley. Spectral dimension for the diffusion-limited aggregation model of colloid growth. *Physical review letters*, 51(16):1457, 1983.

[97] CM Sorensen, WB Hageman, TJ Rush, H Huang, and C Oh. Aerogelation in a flame soot aerosol. *Physical Review Letters*, 80(8):1782, 1998.

[98] MY Lin, HM Lindsay, DA Weitz, RCBR Klein, RC Ball, and P Meakin. Universal diffusion-limited colloid aggregation. *Journal of Physics: Condensed Matter*, 2(13):3093, 1990.

[99] S Tolman and P Meakin. Off-lattice and hypercubic-lattice models for diffusion-limited aggregation in dimensionalities 2–8. *Physical Review A*, 40(1):428, 1989.

[100] T Vicsek. *Fractal growth phenomena*. World scientific, 1992.

[101] P Meakin. Formation of fractal clusters and networks by irreversible diffusion-limited aggregation. *Physical Review Letters*, 51(13):1119, 1983.

[102] L Fedeli, A Formenti, CE Bottani, and M Passoni. Parametric investigation of laser interaction with uniform and nanostructured near-critical plasmas. *The European Physical Journal D*, 71(8):202, 2017.

[103] K Nishihara, H Amitani, M Murakami, SV Bulanov, and T Zh Esirkepov. High energy ions generated by laser driven coulomb explosion of cluster. *Nuclear Instruments and Methods in Physics Research Section A: Accelerators, Spectrometers, Detectors and Associated Equipment*, 464(1-3):98–102, 2001.

[104] TW Huang, APL Robinson, CT Zhou, Bin Qiao, Bin Liu, SC Ruan, XT He, and PA Norreys. Characteristics of betatron radiation from direct-laser-accelerated electrons. *Physical Review E*, 93(6):063203, 2016.

[105] H Iskef, JW Cunningham, and DE Watt. Projected ranges and effective stopping powers of electrons with energy between 20 ev and 10 kev. *Physics in Medicine & Biology*, 28(5):535, 1983.

[106] WSM Werner. Electron transport in solids for quantitative surface analysis. *Surface and Interface Analysis: An International Journal devoted to the development and application of techniques for the analysis of surfaces, interfaces and thin films*, 31(3):141–176, 2001.

[107] G Moliere. Theorie der streuung schneller geladener teilchen ii mehrfach-und vielfachstreuung. *Zeitschrift für Naturforschung A*, 3(2):78–97, 1948.

[108] H Bichsel and RP Saxon. Comparison of calculational methods for straggling in thin absorbers. *Physical Review A*, 11(4):1286, 1975.

[109] LN Trefethen. Finite difference and spectral methods for ordinary and partial differential equations. 1996.

[110] X Llovet and F Salvat. Penepma: A monte carlo program for the simulation of x-ray emission in electron probe microanalysis. *Microscopy and Microanalysis*, 23(3):634–646, 2017.

[111] J Barzilai and JM Borwein. Two-point step size gradient methods. *IMA journal of numerical analysis*, 8(1):141–148, 1988.

[112] A Jablonski, F Salvat, and CJ Powell. Comparison of electron elastic-scattering cross sections calculated from two commonly used atomic potentials. *Journal of physical and chemical reference data*, 33(2):409–451, 2004.

[113] F Salvat, A Jablonski, and CJ Powell. Elsepa—dirac partial-wave calculation of elastic scattering of electrons and positrons by atoms, positive ions and molecules. *Computer physics communications*, 165(2):157–190, 2005.

[114] CJ Powell, A Jablonski, F Salvat, and AY Lee. Nist electron elastic-scattering cross-section database, version 4.0. Technical report, 2016.

[115] J Lindhard, A Winther, et al. *Stopping power of electron gas and equipartition rule*. Munksgaard, 1964.

[116] F Salvat and JM Fernández-Varea. Semiempirical cross sections for the simulation of the energy loss of electrons and positrons in matter. *Nuclear Instruments and Methods in Physics Research Section B: Beam Interactions with Materials and Atoms*, 63(3):255–269, 1992.

[117] D Bote, F Salvat, A Jablonski, and CJ Powell. Cross sections for ionization of k, l and m shells of atoms by impact of electrons and positrons with energies up to 1 gev: Analytical formulas. *Atomic Data and Nuclear Data Tables*, 95(6):871–909, 2009.

[118] WT Elam, BD Ravel, and JR Sieber. A new atomic database for x-ray spectroscopic calculations. *Radiation Physics and Chemistry*, 63(2):121–128, 2002.

[119] JH Hubbell, PN Trehan, Nirmal Singh, B Chand, D Mehta, ML Garg, RR Garg, Surinder Singh, and S Puri. A review, bibliography, and tabulation of k, l, and higher atomic shell x-ray fluorescence yields. *Journal of Physical and Chemical Reference Data*, 23(2):339–364, 1994.

[120] W Hink and H Paschke. K-shell-fluorescence yield for carbon and other light elements. *Physical Review A*, 4(2):507, 1971.

[121] K Feser. K-shell fluorescence yield for beryllium, boron, and carbon. *Physical Review Letters*, 28(16):1013, 1972.

[122] BL Henke, EM Gullikson, and JC Davis. X-ray interactions: photoabsorption, scattering, transmission, and reflection at e= 50-30,000 ev, z= 1-92. *Atomic data and nuclear data tables*, 54(2):181–342, 1993.

[123] A Saltelli, M Ratto, T Andres, F Campolongo, J Cariboni, D Gatelli, M Saisana, and S Tarantola. *Global sensitivity analysis: the primer*. John Wiley & Sons, 2008.

[124] NP Barradas, C Jeynes, M Jenkin, and PK Marriott. Bayesian error analysis of rutherford backscattering spectra. *Thin Solid Films*, 343:31–34, 1999.

[125] J Jokinen, J Keinonen, P Tikkanen, A Kuronen, T Ahlgren, and K Nordlund. Comparison of tof-erda and nuclear resonance reaction techniques for range profile measurements of kev energy implants. *Nuclear Instruments and Methods in Physics Research Section B: Beam Interactions with Materials and Atoms*, 119(4):533–542, 1996.

[126] DA Weitz and M Oliveria. Fractal structures formed by kinetic aggregation of aqueous gold colloids. *Physical Review Letters*, 52(16):1433, 1984.

[127] F Hausdorff. Dimension und äußeres maß. *Mathematische Annalen*, 79(1-2):157–179, 1918.

[128] CM Sorensen. Light scattering by fractal aggregates: a review. *Aerosol Science & Technology*, 35(2):648–687, 2001.

[129] N Almqvist. Fractal analysis of scanning probe microscopy images. *Surface Science*, 355(1-3):221–228, 1996.

[130] P Meakin. Aggregation kinetics. *Physica Scripta*, 46(4):295, 1992.

[131] A Stukowski. Visualization and analysis of atomistic simulation data with OVITO-the Open Visualization Tool. *Modelling and Simulation in Materials Science and Engeneering*, 18(1), JAN 2010.

[132] J Perrière, C Boulmer-Leborgne, R Benzerga, and S Tricot. Nanoparticle formation by femtosecond laser ablation. *Journal of Physics D: Applied Physics*, 40(22):7069, 2007.

[133] M Lenner, A Kaplan, C Huchon, and RE Palmer. Ultrafast laser ablation of graphite. *Physical Review B*, 79(18):184105, 2009.

[134] S Eliezer, N Eliaz, E Grossman, D Fisher, I Gouzman, Z Henis, S Pecker, Y Horovitz, M Fraenkel, S Maman, et al. Synthesis of nanoparticles with femtosecond laser pulses. *Physical Review B*, 69(14):144119, 2004.

[135] S Amoruso, G Ausanio, M Vitiello, and X Wang. Infrared femtosecond laser ablation of graphite in high vacuum probed by optical emission spectroscopy. *Applied Physics A*, 81(5):981–986, 2005.

[136] JA Grant-Jacob, B Mills, and RW Eason. Parametric study of the rapid fabrication of glass nanofoam via femtosecond laser irradiation. *Journal of Physics D: Applied Physics*, 47(5):055105, 2014.

[137] A Uccello, A Maffini, D Dellasega, and M Passoni. Laser cleaning of pulsed laser deposited rhodium films for fusion diagnostic mirrors. *Fusion Engineering and Design*, 88(6-8):1347–1351, 2013.

[138] CA Schneider, WS Rasband, and KW Eliceiri. Nih image to imagej: 25 years of image analysis. *Nature methods*, 9(7):671–675, 2012.

[139] D Vavassori. Production of optimized targets for enhanced laser-driven ion acceleration. 2019.

[140] Persistence of vision pty. ltd. (2004) persistence of vision raytracer (version 3.6). http://www.povray.org/.

[141] A Jullien, O Albert, F Burgy, G Hamoniaux, JP Rousseau, JP Chambaret, F Augé-Rochereau, G Chériaux, J Etchepare, N Minkovski, et al. 10? 10 temporal contrast for femtosecond ultraintense lasers by cross-polarized wave generation. *Optics letters*, 30(8):920–922, 2005.

[142] B Dromey, S Kar, M Zepf, and P Foster. The plasma mirror—a subpicosecond optical switch for ultrahigh power lasers. *Review of Scientific Instruments*, 75(3):645–649, 2004.

[143] L Obst, J Metzkes-Ng, S Bock, GE Cochran, TE Cowan, T Oksenhendler, PL Poole, I Prencipe, M Rehwald, C Rödel, et al. On-shot characterization of single plasma mirror temporal contrast improvement. *Plasma Physics and Controlled Fusion*, 60(5):054007, 2018.

[144] F Druon, G Chériaux, J Faure, J Nees, M Nantel, A Maksimchuk, G Mourou, JC Chanteloup, and G Vdovin. Wave-front correction of femtosecond terawatt lasers by deformable mirrors. *Optics letters*, 23(13):1043–1045, 1998.

[145] DS Hey, MH Key, AJ Mackinnon, AG MacPhee, PK Patel, RR Freeman, LD Van Woerkom, and CM Castaneda. Use of gafchromic film to diagnose laser generated proton beams. *Review of Scientific Instruments*, 79(5):053501, 2008.

[146] K Zeil, SD Kraft, S Bock, M Bussmann, TE Cowan, T Kluge, J Metzkes, T Richter, R Sauerbrey, and U Schramm. The scaling of proton energies in ultrashort pulse laser plasma acceleration. *New Journal of Physics*, 12(4):045015, 2010.

[147] K Zeil, J Metzkes, T Kluge, M Bussmann, TE Cowan, SD Kraft, R Sauerbrey, and U Schramm. Direct observation of prompt pre-thermal laser ion sheath acceleration. *Nature communications*, 3:874, 2012.

[148] JW Goodman. Some fundamental properties of speckle. *JOSA*, 66(11):1145–1150, 1976.

[149] EM Bringa and RE Johnson. Coulomb explosion and thermal spikes. *Physical review letters*, 88(16):165501, 2002.